Investigation of the structural properties of GaAs layers grown by molecular-beam epitaxy at low temperatures

G. B. Galiev, R. M. Imamov, B. K. Medvedev, V. G. Mokerov, É. Kh. Mukhamedzhanov, E. M. Pashaev, and V. B. Cheglakov

Institute of Radio Engineering and Electronics, Russian Academy of Sciences, 103907 Moscow, Russia
(Submitted March 20, 1996; accepted for publication February 17, 1997)
Fiz. Tekh. Poluprovodn. **31**, 1168–1170 (October 1997)

The results of an investigation of the structural perfection of GaAs epitaxial films grown by molecular-beam epitaxy at low growth temperatures (240–300 °C) and various As/Ga flux ratios (from 3 to 13) are presented. Diffraction reflection curves display characteristic features for the samples before and after annealing in the temperature range from 300 to 800 °C. Hypotheses which account for these features are advanced. The range of variation of the arsenic/gallium flux ratio, in which low-temperature growth takes place under nearly stoichiometric conditions, is established. © *1997 American Institute of Physics.* [S1063-7826(97)00410-9]

1. INTRODUCTION

There has recently been heightened interest in GaAs epitaxial layers obtained by molecular-beam epitaxy (MBE) in a low-temperature (LT) growth regime. Gallium arsenide layers grown by MBE at substrate temperatures $T_S \sim 200-300$ °C are called LT layers. Such layers are characterized by a high concentration of point defects, an arsenic excess that exceeds the homogeneity region, and mismatch between the lattice constant of the LT layer and the substrate.[1–3] X-ray diffraction studies of the properties of LT layers following heat treatments have shown that annealing leads to increased perfection of the crystal structure.[1–4] According to Refs. 5–8, the use of LT GaAs layers in device structures and elements of integrated microcircuits leads to improvement of their parameters and characteristics. Another important area of research into the properties of LT GaAs layers is the investigation of the mechanism for the appearance of As precipitates and the dynamics of their behavior as the annealing temperature T_A is raised.[9–11]

The purpose of the present work is to thoroughly investigate the features of the crystal structure of LT GaAs layers grown at different growth temperatures with different arsenic/gallium flux ratios, as well as the influence of subsequent annealing on the degree of perfection of the crystal structure of LT GaAs films.

2. SAMPLE PREPARATION AND INVESTIGATIVE METHODS

Wafers of (100)-oriented single-crystal GaAs served as substrates. After heat treatment at 660 °C, the substrate temperature T_S was lowered to the growth temperature (240, 270, or, 300 °C in our case), and LT GaAs layers with a thickness of ~ 0.3 μm were grown at various values of γ (where $\gamma = P_{As_4}/P_{Ga}$ is the ratio between the pressures of the As_4 and Ga vapors). The annealing was carried out in the growth chamber of an MBE machine in a stream of As at $T_A = 300$, 400, 600, 700, and 800 °C over the course of 10 min.

Diffraction reflection curves were recorded on a double-crystal spectrometer using Cu $K\alpha$ radiation. The characteristics of the spectrometer were presented in Ref. 12.

Photoluminescence (PL) spectra were recorded on an automatic spectrometer using an MDR-23 monochromator. The luminescence was excited by an argon laser ($\lambda_{exc} = 514$), and the excitation power density impinging on the sample was 100 W/cm^2.

3. MEASUREMENT RESULTS AND DISCUSSION

Figure 1 presents the measured diffraction reflection curves for samples *1–3*, which were grown at $T_S = 240$ (*1*), 270 (*2*), and 300 °C (*3*) and $\gamma = 12$. It is seen that the curves have an additional peak (I_{add}), which is characteristic of a distorted lattice. (Here I_0 is the principal peak on the diffraction reflection curve from the substrate, i.e., from single-crystal GaAs). In Fig. 1, which presents the results of the x-ray diffraction measurements, it is seen that I_{add} is small compared with I_0. The values of the relative reflection intensity P_R and the full-width at half-maximum (FWHM) W'' of I_0 were 0.53, 0.6, 0.62 and 12″, 10.8″, 10.8″ for samples *1*, *2*, and *3*, respectively. Since these values refer to the substrates, we attribute the slight differences from one sample to another to the quality of the substrates used for growth.

One characteristic feature of the diffraction reflection curves for samples *1–3* is an increase in I_{add} with increasing T_S. Since the thickness of the epitaxial film $d \sim 0.36$ μm and the angular positions of the peaks ($-170''$) are identical for all three samples, the small value of I_{add1} in comparison to $I_{add2,3}$ attests to the more perfect crystal structure of that sample, which may be caused by different mechanisms for incorporating As into the GaAs matrix at different values of T_S. We also note the appearance of oscillations with a period $\Delta\Theta \sim 57''$ on the diffraction reflection curve for sample *3* (Fig. 1), which indicate the formation of a sharper film/substrate interface under these growth conditions.[12] The thickness $d = 0.36$ μm determined from $\Delta\Theta$ is in good agreement with the film thickness determined from the growth rate. All the formulas needed to treat the diffraction reflection curves were presented in Ref. 12.

Figure 2 presents the measured diffraction reflection curves for sample *1* after annealing at $T_A = 300$, 600, 700, and 800 °C (samples *4–7*). As is seen from Fig. 2, beginning

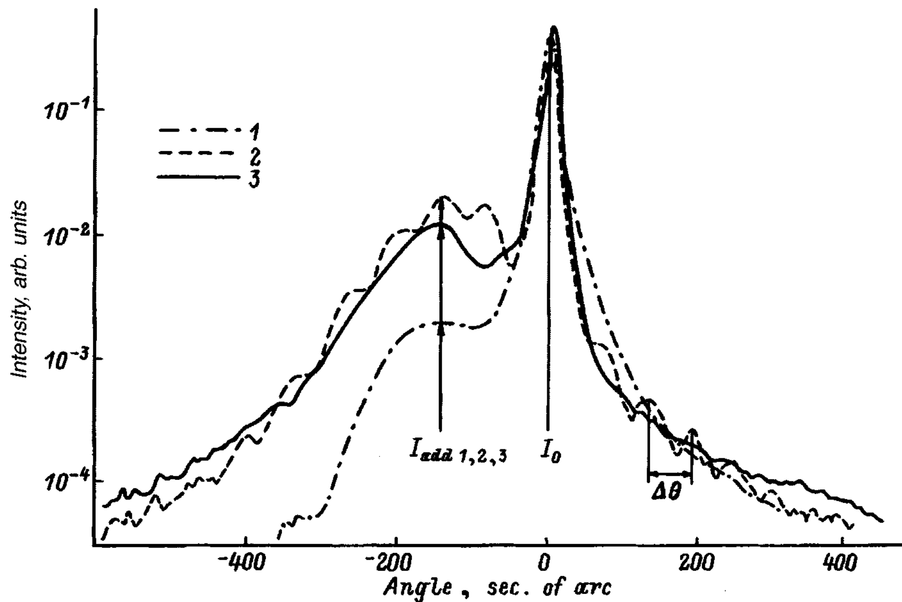

FIG. 1. Diffraction reflection curves for samples *1–3*, which were obtained at $\gamma=13$.

at $T_A=300$ °C, annealing alters the form of the diffraction reflection curve. As a result, I_{add1} increases by a factor of about 3, and this peak undergoes displacement from its original position at $-170''$ for sample *1* to $-90''$ for sample *4*, indicating some variation of $\Delta a/a$.[12] (Here a is the lattice constant of GaAs.) In addition, the value of W'' for the principal peak increases to 20″. The increase in W'' for sample *4* is probably attributable to redistribution of the excess As in the LT GaAs layer. Such redistribution can occur between different types of point defects, whose nature and concentration for a sample grown at $T_S=250$ °C (i.e., at a substrate temperature very close to our value $T_S=240$ °C) were presented in Ref. 13. Further annealing of the samples at higher values of T_A leads to increased perfection of the crystal lattice in the LT layer, and the lattice constants of the film become the same as in single-crystal GaAs.

These data are confirmed by the results of the measurements of the PL spectra. In our case, as in Refs. 14–16, there is no PL signal for the original sample grown at $T_S=240$ °C. However, subsequent annealing at $T_A>300$ °C leads to the appearance of a signal at $\lambda=0.825$ nm, whose intensity is equal to 700, 175, 240, and 370 relative units and whose FWHM is equal to 40, 20, 12, and 9 meV for samples *4*, *5*, *6*, and *7*, respectively (the PL spectra were recorded at $T=77$ K, and the numbers of the samples correspond to the numbers in Fig. 2). These data, i.e., the increase in the amplitude and the decrease in the FWHM of the PL signal with increasing T_A also attest to the increasing perfection of the crystal lattice of the LT GaAs layer.

For the purpose of studying the influence of γ on the crystal structure of LT GaAs layers, samples were grown at $T_S=240$ °C, but with $\gamma=8$. The additional peak on the diffraction reflection curve observed in Fig. 1 was not detected for such a sample. It was found that the values of W'' for the as-grown sample and the samples after annealing at $T_A=400$, 600, and 700 °C are equal to $10-11''$, i.e., they vary only slightly, and only a slight increase in the intensity of the principal peak is observed. This attests to the good correspondence between the crystal lattice parameters of the substrate and the epitaxial film.

The formation of an LT GaAs layer without the appearance of I_{add} on the diffraction reflection curve was also reported in Ref. 13, but at $\gamma=3-4$. Missous and O'Hagan[13] attributed this to the fact that there is no excess arsenic in the LT layer at such values of γ. The difference between these values and the value ($\gamma\sim8$), at which we no longer observe the additional peak on the diffraction reflection curve, is apparently due to design features of the apparatus used. This is also indicated by the fact that we were unable to grow LT GaAs layers at $\gamma=3-4$.

Thus, summarizing the results of this investigation, we note the following.

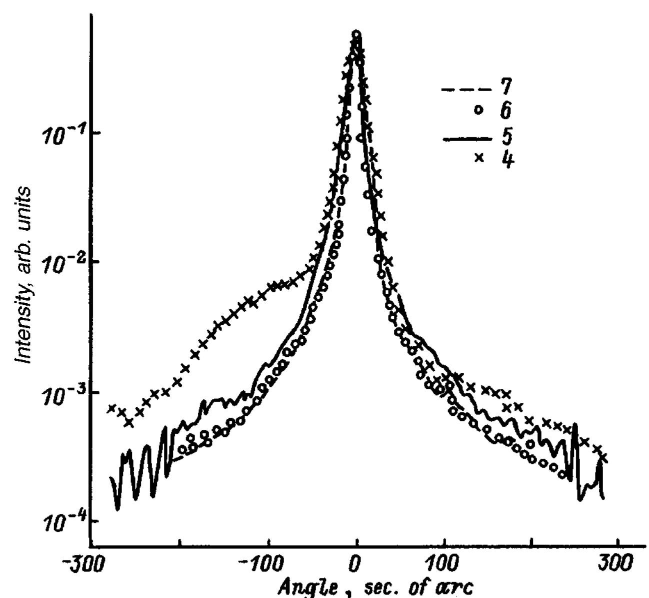

FIG. 2. Diffraction reflection cures for sample *1* after annealing at 300, 600, 700, and 800 °C (samples *4–7*, respectively).

1. Low-temperature GaAs epitaxial layers have been grown and investigated. It has been found that an additional peak caused by the differences between the lattice constants of the LT layer and the substrate is observed on the diffraction reflection curves of structures with an LT layer when $\gamma = 13$. The intensity of I_{add} is smallest for $T_S = 240$ °C and increases with increasing T_S (270–300 °C). In our opinion, this is because the excess As occupies a different position in the GaAs lattice.

2. The additional oscillations discovered on the diffraction reflection curve for $T_S = 300$ °C attest to a sharp film/substrate interface with different lattice constants.

3. Subsequent annealing of LT GaAs layers at $T_A > 500$ °C leads to disappearance of the additional peak on the diffraction reflection curve. This attests to an increase in the perfection of the crystal lattice in the film, as is confirmed by measurements of the PL spectra.

4. A sharp increase in the FWHM of the principal peak I_0 has been observed at $T_A \sim 300$ °C. In our opinion, this occurs because the most intense redistribution of the excess As, which causes the greatest variation of the lattice constant of the LT layer, takes place at these values of T_A.

[1] M. Kaminska, Z. Liliental-Weber, E. R. Weber, T. George, J. B. Kortright, F. M. Smith, B. Y. Tsaur, and A. R. Calawa, Appl. Phys. Lett. **54**, 1881 (1989).
[2] D. C. Look, J. Appl. Phys. **70**, 3148 (1991).
[3] N. A. Bert, A. I. Veĭnger, M. D. Vilisova, S. I. Goloshchapov, I. V. Ivonin, S. V. Kozyrev, A. E. Kunitsyn, L. G. Lavrent'eva, D. I. Lubyshev, V. V. Preobrazhenskiĭ, B. R. Semyagin, V. V. Tret'yakov, V. V. Chaldyshev, and M. P. Yakubenya, Fiz. Tverd. Tela (St. Petersburg) **35**, 2609 (1993) [Phys. Solid State **35**, 1289 (1993)].
[4] J. K. Luo, H. Thomas, D. V. Morgan, and D. Westwood, Appl. Phys. Lett. **64**, 3614 (1994).
[5] B. Nabet, A. Paolella, P. Cooke, M. L. Lemuene, P. R. Moerkirk, and L.-C. Lion, Appl. Phys. Lett. **64**, 3151 (1994).
[6] L.-W. Yin, Y. Hwang, J. H. Lee, R. J. Trew, and U. K. Mishra, IEEE Trans. Electron Devices Lett. **11**, 561 (1990).
[7] M. R. Melloch, D. C. Miller, and B. Das, Appl. Phys. Lett. **54**, 943 (1989).
[8] J.-F. B. Lin, C. P. Kocot, D. E. Mars, and R. Jaeger, IEEE Trans. Electron Devices **37**, 46 (1990).
[9] T. M. Cheng, C. Y. Chang, T. C. Chang, J. H. Huang, and M. F. Huang, Appl. Phys. Lett. **64**, 3626 (1994).
[10] T. M. Cheng, C. Y. Chang, A. Chin, M. F. Huang, and J. H. Huang, Appl. Phys. Lett. **64**, 2517 (1994).
[11] T. M. Cheng, A. Chin, C. Y. Chang, M. F. Huang, K. Y. Hsien, and J. H. Huang, Appl. Phys. Lett. **64**, 1546 (1994).
[12] A. M. Afanas'ev, R. M. Imamov, V. G. Mokerov, A. V. Maslov, É. Kh. Mukhamedzhanov, D. V. Novikov, É. M. Pashaev, V. S. Ignat'ev, and A. A. Zaĭtsev, Tr. FTIAN **63**, (1993).
[13] M. Missous and S. O'Hagan, J. Appl. Phys. **75**, 3396 (1994).
[14] F. W. Smith, H. Q. Le, V. Diadiuk, M. A. Hollis, A. R. Calawa, S. Gupta, M. Frankel, D. R. Dykaar, G. A. Mourou, and T. Y. Hsiang, Appl. Phys. Lett. **54**, 890 (1989).
[15] D. C. Look, D. S. Walters, M. O. Manasreh, J. R. Sizelove, and C. E. Stutz, Phys. Rev. B **42**, 3578 (1990).
[16] A. C. Warren, J. M. Woodall, J. L. Freeouf, D. Grischkowsky, D. T. Mclnturff, M. R. Melloch, and N. Otsuka, Appl. Phys. Lett. **57**, 1331 (1990).

Translated by P. Shelnitz

Influence of fast-neutron irradiation on the intensity of the copper-related luminescence band at $h\nu_m = 1.01$ eV in n-type GaAs

K. D. Glinchuk and A. V. Prokhorovich

Institute of Semiconductor Physics, Ukrainian National Academy of Sciences, 252028 Kiev, Ukraine
(Submitted September 24, 1996; accepted for publication February 3, 1997)
Fiz. Tekh. Poluprovodn. **31**, 1171–1173 (October 1997)

The influence of neutron irradiation (the energy $E=2$ MeV and the dose $\Phi=10^{13}-10^{15}\mathrm{cm}^{-2}$) and subsequent anneals (the annealing temperature T_a=400–700 °C and the annealing time is 30 min) of n-type GaAs(Te,Cu) crystals with an initial carrier concentration $n_0=2\times10^{18}$ cm^{-3} on the intensity of the copper-related luminescence band with an emission maximum at $h\nu_m=1.01$ eV is studied. A significant irradiation-induced increase in the intensity of the band is observed. It is attributed to a radiation-stimulated increase in the concentration of emitting centers ($\mathrm{Cu_{Ga}}V_{\mathrm{As}}$ pairs) as a result of the effective interaction of interstitial copper atoms with irradiation-induced gallium (V_{Ga}) and arsenic (V_{As}) vacancies, as well as $V_{\mathrm{Ga}}V_{\mathrm{As}}$ divacancies. © *1997 American Institute of Physics.* [S1063-7826(97)00510-3]

1. INTRODUCTION

Studying the influence of fast-neutron irradiation and subsequent anneals on the photoluminescence (PL) of n-type GaAs(Te,Cu), we discovered an increase induced by radiation-heat treatment in the intensity of the copper-related luminescence band with a position of the emission maximum $h\nu_m$ near 1.01 eV. We shall dwell below on this observation, as a well as on a model which accounts for it.

2. METHOD

The original samples for the experiments were tellurium-doped n-GaAs crystals with a concentration of tellurium atoms $N_{\mathrm{Te}}=2\times10^{18}$ cm^{-3} and a concentration of equilibrium electrons $n_0=2\times10^{18}$ cm^{-3}. The crystals were irradiated by fast neutrons at 20 °C (the mean energy $E=2$ MeV, the integral dose $\Phi=10^{13}-10^{15}$ cm^{-2}, and the concentration of radiation defects introduced $n_d(0)\simeq50\,[\mathrm{cm}^{-1}]\cdot\Phi$). Such neutron irradiation scarcely altered the value of n_0, since $n_d(0)\ll N_{\mathrm{Te}}$.

The diffusion of copper atoms from a thin layer deposited on the surface into unirradiated and neutron-irradiated n-GaAs(Te) crystals was allowed to proceed at T=400–700 °C for 30 min and was followed by rapid cooling (the copper concentration is denoted by N_{Cu}, and the maximum penetration depth of the copper atoms was 100 μm). The diffusion of copper atoms scarcely altered the value of n_0, since $N_{\mathrm{Cu}}\ll N_{\mathrm{Te}}$. However, during the diffusion of copper atoms, most of the radiation defects annihilated in various drains [their concentration in the annealed crystals was $n_d\simeq0.2n_d(0)-0.3n_d(0)$].

The photoluminescence was measured at 77 K. It was excited by the strongly absorbed output of a He-Ne laser with a quantum energy equal to 1.96 eV (the absorption coefficient was 4×10^4 cm^{-1}, and the excitation intensity $L=10^{18}$ cm$^{-2}\cdot$s^{-1}). The PL source was a thin layer of the order of several microns near the GaAs surface. At the values of L used the intensity of the copper-related luminescence band with a maximum at $h\nu_m=1.01$ eV ($I_{1.01}$) increased linearly with increasing L; i.e., the variations in $I_{1.01}$ in response to radiation-heat treatment reflected the corresponding variations in the concentrations of the centers causing it $N_{1.01}$ ($I_{1.01}\sim N_{1.01}$).[1] The relative values of $N_{1.01}$ in the unirradiated and irradiated crystals were found (to within $\pm15\%$) by comparing the corresponding changes in the integrated intensity of the copper-related luminescence band with a maximum at $h\nu_m=1.01$ eV ($I_{1.01}$) and the intensity of the intrinsic luminescence band with a maximum at $h\nu_m=1.52$ eV ($I_{1.52}$): clearly, $N_{1.01}\sim I_{1.01}/I_{1.52}$.[2,3]

3. RESULTS

Figure 1 presents the low-temperature ($T=77$ K) PL spectra of unirradiated and neutron-irradiated n-type GaAs crystals after the diffusion of copper atoms in them. As expected, a) the diffusion of copper atoms leads to the appearance of a luminescence band with a maximum at $h\nu_m=1.01$ eV [$I_{1.01}=0$ for any value of T, if $N_{\mathrm{Cu}}=0$ (Ref. 3)]; b) the intensity of the intrinsic luminescence band is approximately identical in the unirradiated and irradiated crystals after an-

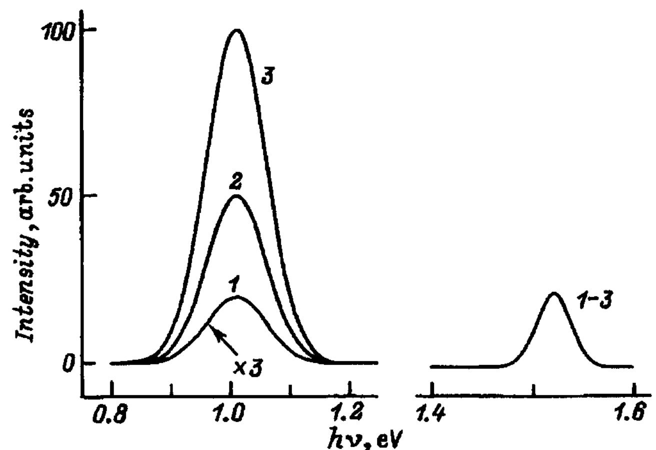

FIG. 1. Photoluminescence spectra of unirradiated n-type GaAs crystals (*1*), as well as crystals irradiated by doses of fast neutrons $\Phi=10^{14}$ (*2*) and 10^{15} cm^{-2} (*3*). Left-hand curves — without annealing; right-hand curve — after annealing at T_a=700 °C for 30 min with a copper layer on the surface.

 1063-7826/97/101006-02$10.00 © 1997 American Institute of Physics

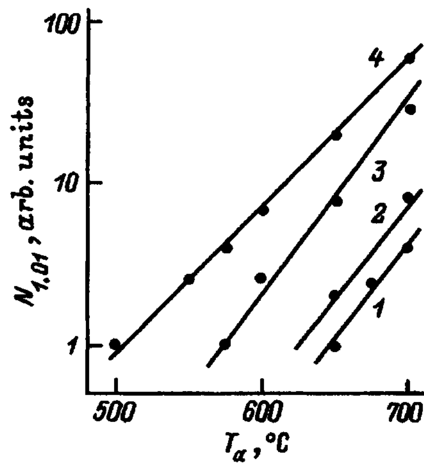

FIG. 2. Dependence of the relative concentration of the copper-related emitting centers in n-type GaAs crystals on the annealing temperature T_a for an annealing time of 30 min with a copper layer on the surface: *1* — unirradiated crystal; *2–3* — crystals irradiated by doses of fast neutrons $\Phi = 10^{13}$, 10^{14}, and 10^{15} cm^{-2}, respectively.

nealing (at the high annealing temperatures employed most of the radiation defects, some of which are effective recombination centers for excess electrons and holes, annihilated in various drains[2,4–6]). The significant increase induced by neutron irradiation in the intensity of the luminescence band with $h\nu_m = 1.01$ eV was unexpected ($I_{1.01} = 0$ for any value of Φ, if $N_{Cu} = 0$).

Figure 2 presents the dependence of the concentration of the copper-related emitting centers on the annealing temperature T_a in unirradiated n-GaAs crystals and crystals irradiated by various doses of fast neutrons. As we see, a) fast-neutron irradiation significantly increases the concentration of the copper-related emitting centers $N_{1.01}$ and shifts the region for their significant generation to lower temperatures; b) the increase in $N_{1.01}$ is stronger, the higher is the irradiation dose (this confirms the radiation-stimulated nature of the increase in the concentration of the copper-related emitting centers).

4. DISCUSSION

As we know,[3] the luminescence with a maximum at $h\nu_m = 1.01$ eV in n-type GaAs crystals is caused by the radiative recombination of electrons in $Cu_{Ga}V_{As}$ pairs (Cu_{Ga} is a copper atom in the gallium sublattice of gallium arsenide, and V_{As} is an arsenic vacancy). They appear as a result of the successive interaction of interstitial copper atoms with isolated gallium (V_{Ga}) and arsenic (V_{As}) vacancies or as a result of the trapping of interstitial copper atoms by $V_{Ga}V_{As}$ divacancies.[3] Therefore, the observed radiation-stimulated increase in the intensity of the absorption band with a maximum at $h\nu_m = 1.01$ eV is associated with an increase in the concentration of the $Cu_{Ga}V_{As}$ pairs in the neutron-irradiated n-GaAs crystals as a result of the radiation-induced increase in the concentrations of V_{Ga}, V_{As}, and $V_{Ga}V_{As}$.[1)]

5. CONCLUSIONS

The neutron irradiation of n-GaAs(Te,Cu) crystals leads to a significant increase in the concentration of $Cu_{Ga}V_{As}$ pairs in them. This increase is due to the effective interaction of interstitial copper atoms with the irradiation-induced isolated gallium and arsenic vacancies and $V_{Ga}V_{As}$ divacancies. The results obtained are important for understanding the defect-defect interaction in irradiated semiconductors.[4–6]

[1)] As our estimates show (the estimation method was described in Ref. 7, and its accuracy is $\pm 50\%$), $N_{1.01} \simeq 1 \times 10^{14}$ cm^{-3} in unirradiated crystals annealed at 700 °C, and $N_{1.01} \simeq 2 \times 10^{15}$ cm^{-3} in crystals irradiated by the maximum neutron dose $\Phi = 10^{15}$ cm^{-2} and then annealed at 700 °C.

[1] K. D. Glinchuk, V. I. Guroshev, and A. V. Prokhorovich, Fiz. Tekh. Poluprovodn. **27**, 1030 (1993) [Semiconductors **27**, 560 (1993)].

[2] E. V. Vinnik, K. D. Glinchuk, V. I. Guroshev, and A. V. Prokhorovich, Fiz. Tekh. Poluprovodn. **25**, 82 (1991) [Sov. Phys. Semicond. **25**, 48 (1991)].

[3] F. M. Vorobkalo, K. D. Glinchuk, B. K. Gapchin, and A. V. Prokhorovich, Fiz. Tekh. Poluprovodn. **7**, 2047 (1973) [Sov. Phys. Semicond. **7**, 1370 (1974)].

[4] *A Survey of Semiconductor Radiation Techniques*, L. S. Smirnov (Ed.), Mir, Moscow (1983).

[5] V. V. Emtsev and T. V. Mashovets, *Native Defects and Impurities in Semiconductors*, The Institute of Physics, Bristol (1993).

[6] G. Dlubek, A. Dlubek, R. Krause, and R. Brummer, Phys. Status Solidi A **107**, 111 (1988).

[7] K. D. Glinchuk, K. Lukat, and V. E. Rodionov, Fiz. Tekh. Poluprovodn. **15**, 1337 (1981) [Sov. Phys. Semicond. **15**, 772 (1981)].

Translated by P. Shelnitz

Thermopower of transmutation-doped Ge:Ga in the region for hopping conductivity

A. G. Andreev, A. G. Zabrodskiĭ, and S. V. Egorov

A. F. Ioffe Physicotechnical Institute, Russian Academy of Sciences, 194021 St. Petersburg, Russia

I. P. Zvyagin

Physics Faculty, Moscow State University, 119899 Moscow, Russia

(Submitted December 23, 1996; accepted for publication February 24, 1997)
Fiz. Tekh. Poluprovodn. **31**, 1174–1179 (October 1997)

The low-temperature thermopower of transmutation-doped Ge:Ga is investigated experimentally and theoretically. The large values of the thermopower observed in the region for ε_1 conduction and its sharp drop upon the transition to conduction between impurities are interpreted as manifestations of the phonon drag of free holes and its suppression in the region for hopping transport. The positive sign of the thermopower and its magnitude in the hopping-conduction saturation region can be explained theoretically under the assumption that the classical ε_2 conduction channel, which is not manifested explicitly in the electrical conductivity, makes a contribution to the thermopower in the narrow temperature range associated with the transition from ε_1 conduction to hopping conduction. After the transition to variable-range hopping ($T \leqslant 2$ K), the thermopower decreases sharply and takes anomalous, vanishingly small values. They can be explained within the standard theory of hopping thermopower only under the condition that the contribution caused by the asymmetry of the density of states of the impurity band in the vicinity of the Fermi level and the correlation contribution are compensated. © *1997 American Institute of Physics.* [S1063-7826(97)00610-8]

1. INTRODUCTION

Transmutation-doped germanium Ge:Ga is a thoroughly characterized model system for studying hopping transport.[1–3] It is a moderately compensated p-type semiconductor with uniformly distributed Ga, As, and Se transmutation impurity atoms in a ratio which depends on the hardness of the reactor neutrons used.[4] According to Fritzsche and Cuevas,[1] in transmutation-doped Ge:Ga the classical transport of free holes in the valence band (ε_1 conduction) is replaced at sufficiently low temperatures by hopping conductivity among the localized ground states of the shallow Ga acceptors, which is described by the expression

$$\sigma = \sigma_{01} \exp(-\varepsilon_1/kT) + \sigma_{03} \exp(-\varepsilon_3/kT), \tag{1}$$

where the second term is associated with ε_3 hopping conductivity [so-called nearest-neighbor hopping (NNH) conductivity].

Zabrodskiĭ, Andreev, and Alekseenko showed[2] that transmutation-doped Ge:Ga has a saturation region near the high-temperature boundary for hopping conductivity, where the conductivity depends weakly on the temperature, and the activation energy ε_3 for NNH conduction is manifested only when the thermal energy kT becomes smaller than the width of the impurity band. At lower temperatures there is variable-range hopping (VRH) among states of the parabolic Coulomb gap,[3] which corresponds to the following temperature dependence of the resistivity:

$$\rho = \sigma^{-1} = \rho_{03} \exp(T_\Delta/T)^x, \tag{2}$$

where $x = 1/2$.

Zabrodskiĭ and Andreev, showed,[3] however, that the gap in transmutation-doped Ge:Ga is considerably narrower than the gap following from the single-electron Éfros–Shklovskiĭ model.[5] This was interpreted in Ref. 3 as a manifestation of many-electron hops. As the doping level is increased, the beginning of VRH conduction shifts toward higher temperatures, and the interval for NNH conduction narrows accordingly[2] and practically vanishes when $N > 0.1N_c$ ($N_c = 2 \times 10^{17}$ cm^{-3} is the critical Ga concentration corresponding to the metal-insulator transition).

Another characteristic which is sensitive to the features of the spectrum of electron states is the thermopower. The data from measurements of the hopping thermopower of noncrystalline semiconductors are comparatively sparse.[6,7] The thermopower of doped semiconductors at low temperatures has been studied to a small extent. For example, Geballe and Hull[8] performed measurements of the thermopower for p-type Ge at comparatively high temperatures (exceeding 20 K) in the region for ε_1 conduction.[8] The increase in the thermopower that they observed when the temperature was lowered was attributed to the phonon drag of free holes.[8,9]

Our purpose here was to investigate the low-temperature thermopower in transmutation-doped Ge:Ga at the transition from classical to hopping transport and in the region for hopping conductivity.

2. MEASUREMENT MATERIAL AND METHOD

One of the reasons for selecting transmutation-doped Ge:Ga as the object of investigation is that its electrical parameters were determined with a high accuracy in Refs. 2 and 4. We carried out a very thorough investigation of a sample of transmutation-doped Ge:Ga with a degree of compensation $K = 0.35$, which was obtained by bombardment with reactor neutrons having a sufficiently hard spectrum.[4]

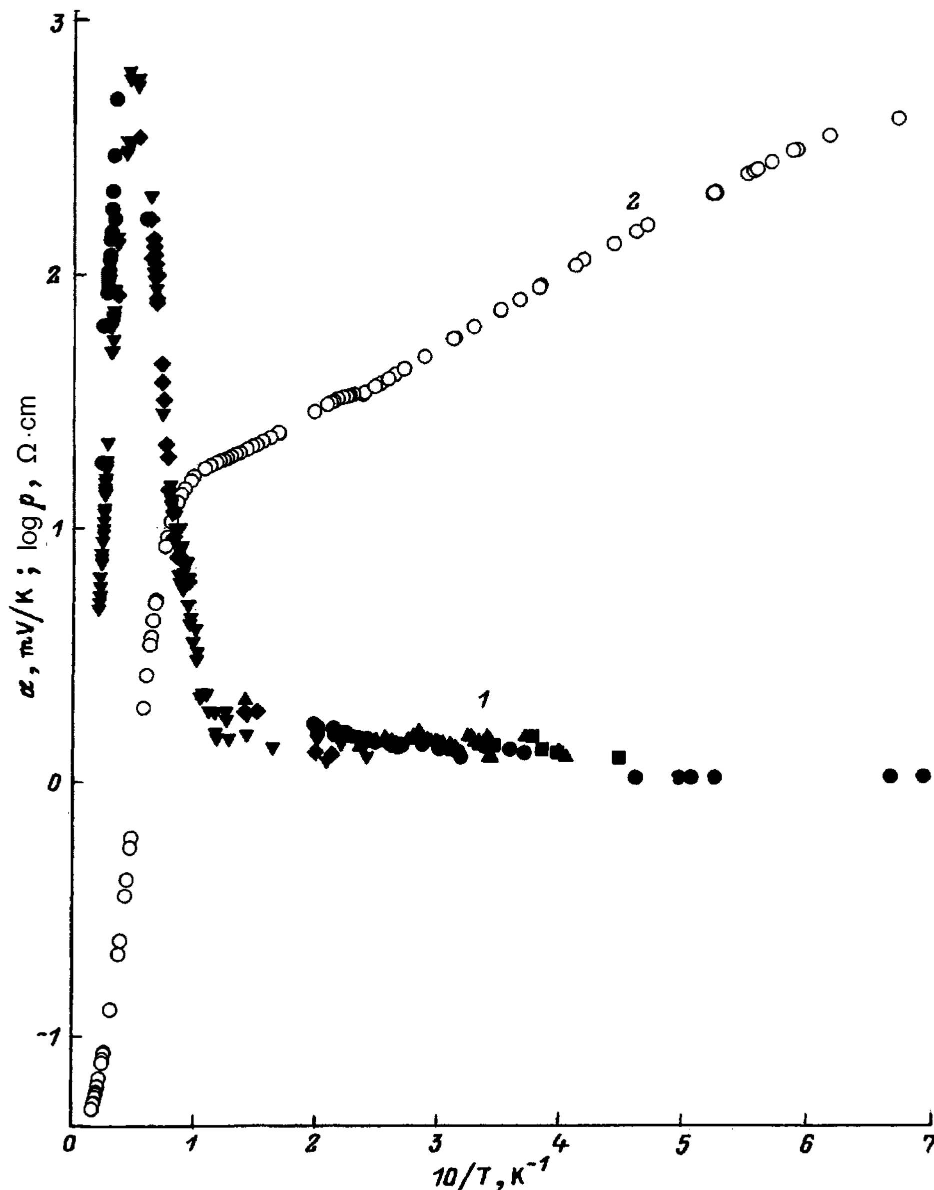

FIG. 1. Dependence of the logarithm of the resistivity (*1*) and the thermopower (*2*) for transmutation-doped Ge:Ga on the reciprocal temperature.

The neutron flux provided a concentration of the principal dopant gallium is $N=3\times10^{16}$ cm^{-3}. The impurity concentration was measured using the calibration curves for the Hall factor in p-Ge taken from Ref. 2. Such a doping level seems optimal for investigating hopping thermopower for the following reasons, which follow from the results in Refs. 2 and 3. First, the increase in the radius of the localized states as the metal-insulator transition is approached is still insignificant here, and the value for the Bohr radius of a light hole $a=90$ Å can be used for qualitative estimates in calculating the rates of hopping transitions (the exact value $a=94$ Å is obtained from the data in Ref. 3). Second, at these doping levels we still see a small saturation region, from which hopping conductivity similar to the NNH regime that was thoroughly characterized in Refs. 2 and 3 begins. Third, VRH conduction begins here at very high temperatures ($T\sim2-3$ K).

The sample investigated had the shape of a parallelepiped measuring $13\times2.5\times0.5$ mm^3, whose longest side was oriented perpendicular to the [111] growth axis of the crystal. The fact that the $\rho(T)$ curve for the sample studied was exponential, i.e., the sample itself was a good thermometer, was utilized to measure the temperature difference between the probes. Two pairs of In point contacts with a diameter of 0.4 mm were made on its broad lateral plane at a distance of 8 mm from one another. The temperature dependence of the resistance of each pair was measured, so that two "internal" thermometers would be obtained for determining the temperature difference. Temperature differences of the order of 0.1 K could be measured at liquid-helium temperatures.

3. MEASUREMENT RESULTS

The results of the conductivity and thermopower measurements are presented in Figs. 1 and 2. The measured thermopower remains positive at all temperatures. In the temperature range $T\leqslant50$ K, which corresponds to the classical hole transport among delocalized states, the thermopower in-

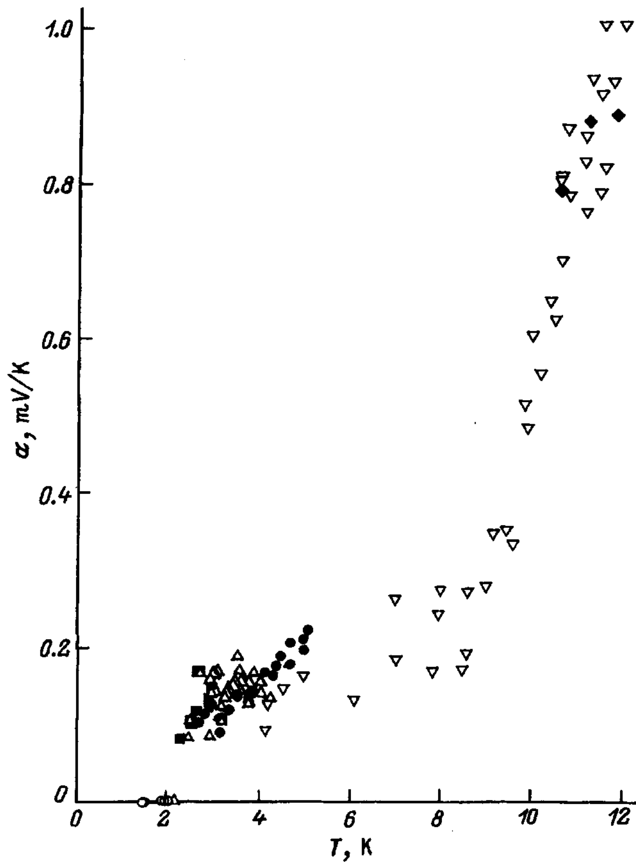

FIG. 2. Temperature dependence of the hopping thermopower of transmutation-doped Ge:Ga.

creases sharply with increasing temperature and reaches its maximum values of about 3 mV/K at $T \cong 25$ K, after which it decreases rapidly. In the hopping-conduction saturation region at $5-8$ K the values of the thermopower are of the order of 0.2 mV/K. As the temperature is lowered further (in the region of the highest observable values of the activation energy for hops), the thermopower decreases smoothly. This decrease becomes more abrupt after passage into the VRH region. As a result, below 2 K the thermopower takes very small values, which are not subject to measurement.

4. DISCUSSION OF RESULTS

Let us consider the three characteristic regions for electron transport: the transition from classical to hopping transport, the saturation region for nearest-neighbor hopping conductivity, and the transition to variable-range hopping conductivity.

4.1. Phonon drag. Here we shall discuss the thermopower maximum observed in the region of classical hole transport. As we know,[9] the thermopower is determined by the expression

$$\alpha = -\frac{k}{e}\frac{Q-\mu}{kT}, \tag{3}$$

where Q is the transport energy, which is equal to the energy flux density per unit flux density of the particles, and μ is the Fermi level. In the case of the activation of holes to the mobility threshold in the valence band, we have $Q \approx \varepsilon_1 + Q^*$, where Q^* is the mean transport kinetic energy. According to the data for the sample in Figs. 1 and 2, $\varepsilon_1 = 8$ meV, and at the characteristic temperature $T = 25$ K we obtain $\alpha \approx 250$ μV/K from (3). We see that this value is significantly smaller than the measured values of the thermopower in the region of the maximum. As in Ref. 8, we associate the magnitude and behavior of the thermopower in this temperature range with the phonon drag of free holes.

The sharp decrease in the thermopower upon the transition to hopping transport in the impurity band is apparently a consequence of the suppression of phonon drag in this case, which was previously predicted by Zvyagin.[10] However, the behavior of the thermopower at temperatures below 8 K, at which the conductivity is determined mainly by hops among localized states in the impurity band, is far from trivial.

4.2. Behavior of the thermopower in the hopping-conduction saturation region. According to (3), the position of the Fermi level relative to the impurity band and its temperature shift should be found before calculating the thermopower. Let us discuss the temperature dependence of the Fermi level. When the correlation of the holes impinging on the same local center is taken into account, the filling function of the acceptors differs from the Fermi function and has the form

$$\begin{aligned} f(E) &= \{1 + g_a^{-1} \exp[-(E-\mu)/kT]\}^{-1} \\ &= \{1 + \exp[-(E-\tilde{\mu})/kT]\}^{-1}, \end{aligned} \tag{4}$$

where g_a is the degeneracy factor of the acceptor level, and $\tilde{\mu} = \mu + kT \ln g_a$. For an infinitely narrow impurity band (with a width $w \ll kT$) the temperature shift of the Fermi level is specified by the expression

$$\mu(T) = \mu_0 - kT \ln\{(1-K)/(g_a K)\}, \tag{5}$$

where μ_0 is the position of the Fermi level at $T=0$. Hence it follows that the Fermi level shifts downward toward the valence band when $K > K_c = 1/(g_a+1)$. The data from measurements of the hole concentration in p-type Ge are more faithfully described, if the conventional value $g_a = 2$ is replaced by $g_a = 4$,[11] and then $K_c = 1/5$ (for $g_a = 2$ we would have $K_c = 1/3$). The degree of compensation $K = 0.35 > K_c$ for the test samples of transmutation-doped Ge:Ga, and when the temperature is raised, the Fermi level shifts upward relative to the impurity band.

Let us discuss the role of the finite width w of the impurity band in the simple model of a ''rectangular'' density of states $g(E) = (N/w)\theta[(w/2) - |E - E_a|]$, where θ is the Heaviside function corresponding to an impurity band centered at $E = E_a$. Using (4), for the temperature dependence of the Fermi level in this case, instead of (5), we obtain

$$\mu = E_A + w/2 - kT \ln\frac{\exp\{w(1-K)/kT\} - 1}{g_a\{1 - \exp(-wK/kT)\}}. \tag{6}$$

This dependence is shown in Fig. 3. It is seen that in the temperature region which interests us now the Fermi level does not extend beyond the impurity band. This means that $|\mu - Q|$ in Eq. (3) is smaller than $w/2$, and the corresponding contribution to the thermopower in the temperature range

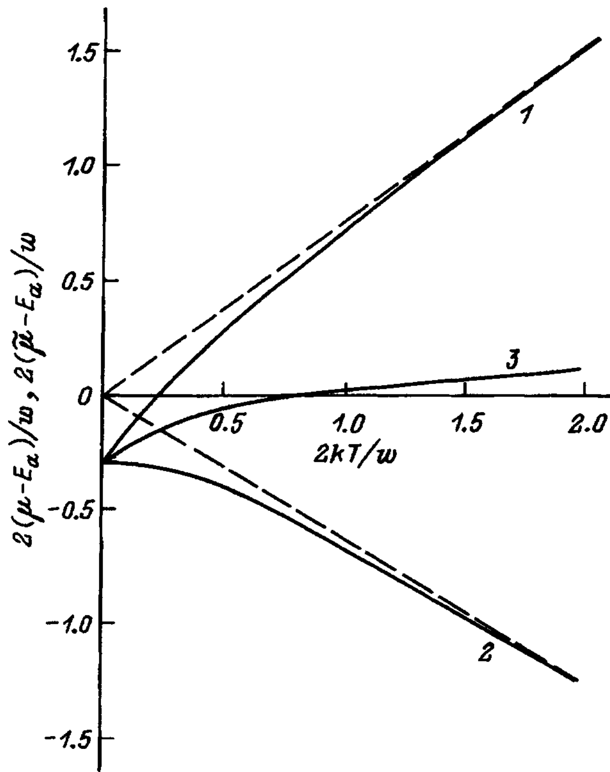

FIG. 3. Temperature dependence of the Fermi level μ and $\tilde{\mu}$: *1* — $2(\mu-E_a)/w$ ($g_a=4$), *2* — $2(\tilde{\mu}-E_a)/w$ ($g_a=4$), *3* — $2(\mu-E_a)/w$ ($g_a=2$). The dashed lines describe the asymptotic behavior of μ and $\tilde{\mu}$ for $kT \gg w$ [Eq. (5)].

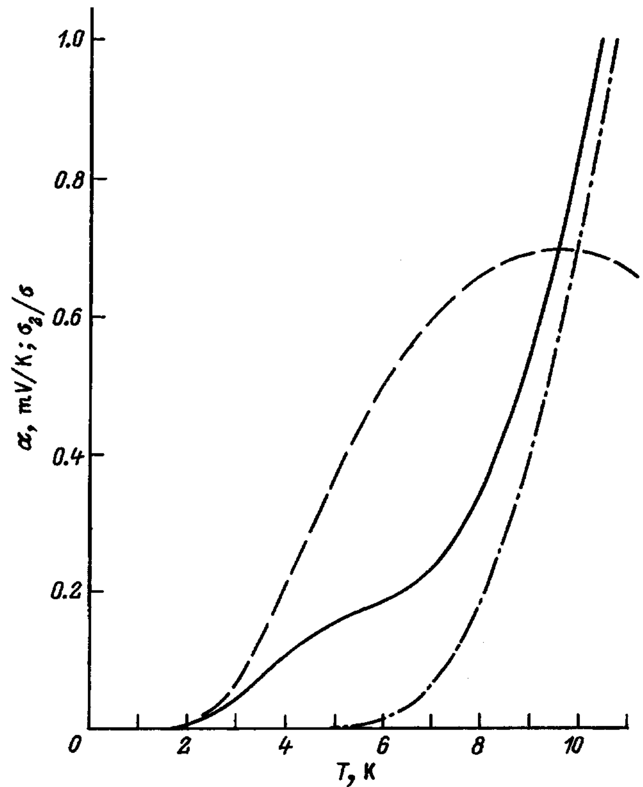

FIG. 4. Thermopower calculated with allowance for the ε_2 conduction channel [for ε_2 conduction $Q-\mu \approx \varepsilon_2 = 2$ meV, and the hopping conductivity $\sigma=\sigma_{0m}\exp(-\varepsilon_m/kT)$] is characterized by the maximum activation energy for hopping conduction $\varepsilon_m=0.6$ meV (for the difference between ε_m and ε_3 see Ref. 2), the ratios between the pre-exponential factors for the different conduction channels are $\sigma_{02}/\sigma_{01}=10^{-2}$ and $\sigma_{0m}/\sigma_{01}=6.3\times10^{-4}$, the contribution of the band holes to the thermopower was simulated with consideration of phonon drag,[9] and the thermopower associated with hopping transport in the band of free acceptor states was assumed to be small]. The dot-dashed line shows the result of a calculation without consideration of the ε_2 conduction, and the dashed curve is the relative contribution of the ε_2 channel to the total conductivity.

$8-10$ K is at least $1.5-2$ times smaller than the observed value of the order of 200 μV/K. It is significant that at low temperatures the corresponding contribution to the thermopower must be negative, since at these temperatures the Fermi level lies below the middle of the impurity band for the degree of compensation considered.

On the other hand, the measured thermopower is positive. Scrutiny of the positive contribution of the valence-band holes reveals that at the measured values of ε_1 it decreases rapidly and cannot account for maintenance of the sign of the thermopower and its observed values at temperatures below 8 K.

We can attempt to explain the behavior of the thermopower by assuming that, along with ε_1 conduction and hopping conduction in the band of acceptor ground states, there is another channel for electron transport among states lying below the Fermi level, which makes a positive contribution to the thermopower. This channel can be the ε_2 conduction observed in Ge at intermediate doping levels and small degrees of compensation (ε_2 conduction is usually associated with transport in a band of doubly occupied states separated by a Hubbard gap from a band of singly occupied states; see Ref. 15). When there are several conduction channels labeled by i, the total thermopower is given by the expression $\alpha=\Sigma\alpha_i\sigma_i/\Sigma\sigma_i$. Figure 4 demonstrates the possibility of describing thermopower behavior similar to that observed experimentally when the significant contribution from the channel considered above is taken into account. Since the values of the activation energies for different channels and the corresponding temperature dependences of the conductivity differ appreciably, as shown by the results of our analysis in Fig. 4, the contribution of the ε_2 channel to the thermopower is significant only in the narrow transition region from ε_1 conduction to hopping condition.

4.3. Behavior of the thermopower upon the transition to variable-range hopping conduction. Let us now consider the VRH region, where the measured thermopower is anomalously small, and attempt to explain our results on the basis of the existing theory of hopping thermopower. In the case of hopping transport in the impurity band corresponding to the ground state of the acceptors, the energy $\mu-Q$ can be found by utilizing the relation[7]

$$\mu-Q=kT\ln g_a+\frac{\int d\varepsilon(\tilde{\mu}-\varepsilon)g(\varepsilon)\nu(\varepsilon,\tilde{\mu})}{\int d\varepsilon g(\varepsilon)\nu(\varepsilon,\tilde{\mu})}, \tag{7}$$

where $\nu(\varepsilon,\tilde{\mu})$ is the mean number of bonds per site which

belongs to the infinite percolation cluster. The usual expression[7] for $\nu(\varepsilon,\widetilde{\mu})$ holds, but $\widetilde{\mu}$ now appears in it instead of μ; for one-phonon hops we have

$$\nu(\varepsilon,\widetilde{\mu})=(4\pi/3)(2/a)^3\int d\varepsilon' d(\varepsilon') \times\left(\eta-\frac{|\varepsilon-\widetilde{\mu}|+|\varepsilon'-\widetilde{\mu}|+|\varepsilon-\varepsilon'|}{2kT}\right)^3, \tag{8}$$

where η is the critical percolation value of the exponent in the expression for the hopping rate. The first term in (7) is the Hubbard correlation contribution associated with the features of the electron distribution function (4), and the second term depends on the symmetry of the density of states relative to $\widetilde{\mu}$.

For a density of states which is symmetric relative to $\widetilde{\mu}$ [in particular, for $g(\varepsilon)=\text{const}$ or a Coulomb gap which is symmetric relative to $\widetilde{\mu}$] the second term vanishes, and only the term $\alpha_{\text{corr}}=(k/e)\ln 4\approx 120\ \mu\text{V/K}$ remains in the thermopower. In general, the sign and the temperature dependence of α_{dos}, which is associated with the second term, depend on the form of the density of states (it can be shown that the energy dependence of the localization radius of the states is insignificant). It is seen from Fig. 4 that in our case $\alpha_{\text{dos}}<0$.

In the absence of a Coulomb gap, at extremely low temperatures we would have $\alpha_{\text{dos}}=-\xi a(T_0/T)^{1/2}$, where ξ is a number of order unity, T_0 is a parameter of Mott VRH, and $a=[d\ \ln g(\varepsilon)/d\varepsilon]_{\varepsilon=\widetilde{\mu}}<0$ is a parameter which characterizes the asymmetry of the contributions to the fluxes from states lying on different sides of $\widetilde{\mu}$ (at the degree of compensation under consideration $a>0$).[10]

The appearance of a parabolic Coulomb gap at $\varepsilon=\widetilde{\mu}$ at low temperatures should cause the contribution of conduction among gap states to the thermopower to tend to the constant value $\alpha_{\text{dos}}=-(k/e)\xi_\Delta b_\Delta kT_\Delta$, where $\xi_\Delta\approx0.34$, T_Δ is the parameter in the expression for the exponential factor of VRH conduction among gap states (2), and b_Δ is the cubic asymmetry parameter of the Coulomb gap ($b_\Delta>0$ when $K=0.35$; see Ref. 12). Thus the contributions α_{corr} and α_{dos} to the thermopower have opposite signs. In such a case the nearly zero values of the hopping thermopower indicate that these contributions are of the same order and compensate one another. Since $kT_\Delta\approx7.5$ meV under our conditions,[3] we can hence obtain the estimate $b_\Delta\approx0.3\ \text{meV}^{-1}$. For such an interpretation it can be assumed that α_{dos} depends on the degree of compensation, and that at small degrees of compensation the low-temperature thermopower becomes negative.

Thus, the anomalously small values of the thermopower at low temperatures might have been caused, in principle, by mutual compensation of the correlation contribution and the contribution due to the asymmetry of the density of states of the impurity band (in the region of the Coulomb gap near $\widetilde{\mu}$). Such a ''compensation'' explanation should have been very sensitive to the characteristics of the object investigated (particularly to the degree of compensation). This explanation, however, seems unlikely. In fact, we discovered anomalously small thermopower values at low temperatures even in moderately compensated, nitrogen-doped n-type $6H$-SiC. This allows us to regard such behavior as fairly common.

On the other hand, the small value of the hopping thermopower can be an indication that in the low-temperature region we go over to a ballistic phonon transport regime, in which the standard theory of thermoelectric phenomena based on the use of a local equilibrium distribution is, in general, inapplicable. It is known, for example, that in doped Ge:Ga, where phonon drag is clearly expressed, an appreciable dependence of the effect on the sample thickness, which attests to a significant contribution of the scattering of phonons at the boundaries, is observed already at temperatures below 80 K.[8,9] The role of the scattering on boundaries increases with decreasing temperature, and in the temperature range that we considered it also determines the phonon distribution. Under these conditions the phonon distribution function in a system adjoining two temperature-control stages held at different temperatures is not dependent on the coordinates. Accordingly, in the region for hopping conduction, despite the presence of a directed phonon flux, no carrier flux appears, and the thermopower vanishes.

5. PRINCIPAL RESULTS AND CONCLUSIONS

The thermopower of moderately compensated transmutation-doped Ge:Ga exhibits the following interesting features as the temperature is lowered and the system passes from classical to hopping transport.

The positive thermopower caused by the phonon drag of free holes drops sharply (by more than an order of magnitude) upon the transition to the region for hopping conduction. This can be regarded as experimental confirmation of the theoretically predicted[10] suppression of phonon drag under hopping carrier transport.

However, the behavior of the thermopower in the region for hopping conduction differs from the picture that follows from the standard theory of hopping thermopower. For example, upon the transition from the ε_1 conduction of free holes to hopping conduction, the behavior of the thermopower can be described under the assumption that in this narrow temperature range a significant contribution to the thermopower is made by an additional channel of classical transport (presumably, ε_2 conduction), which is not manifested explicitly in the electrical conductivity. Upon the transition to variable-range hopping ($T\leqslant2$ K), the thermopower decreases sharply and takes anomalous, vanishingly small values. They can be explained within the standard theory of hopping thermopower only under the condition that there is compensation of the contribution caused by the asymmetry of the density of states of the impurity band in the vicinity of the Fermi level and the correlation contribution to it. However, since such compensation is very sensitive to the characteristics of the object investigated, the small value of the hopping thermopower, which we also observed in nitrogen-doped $6H$-SiC, apparently points to another possible explanation: a transition to a ballistic phonon transport regime.

We thank M. V. Alekseenko for preparing the Ge:Ga samples, as well as the participants in the seminar of the Laboratory for Nonequilibrium Processes in Semiconductors

of the A. F. Ioffe Physicotechnical Institute of the Russian Academy of Sciences for a discussion of the results of our study.

This research was performed with support from the Russian Fund for Fundamental Research (Grant 96-17936) and INTAS (Grant 94-4435).

[1] H. Fritzsche and M. Cuevas, Phys. Rev. **119**, 1239 (1960).
[2] A. G. Zabrodskiĭ, A. G. Andreev, and M. V. Alekseenko, Fiz. Tekh. Poluprovodn. **26**, 431 (1992) [Sov. Phys. Semicond. **26**, 244 (1992)].
[3] A. G. Zabrodskiĭ and A. G. Andreev, Pis'ma Zh. Éksp. Teor. Fiz. **58**, 809 (1993) [JETP Lett. **58**, 756 (1993)].
[4] A. G. Zabrodskiĭ and M. V. Alekseenko, Fiz. Tekh. Poluprovodn. **27**, 2033 (1993) [Semiconductors **27**, 1116 (1993)]; **28**, 168 (1994) [Semiconductors **28**, 101 (1994)].
[5] B. I. Shklovskii and A. L. Efros, *Electronic Properties of Doped Semiconductors*, Springer-Verlag, Berlin (1984).
[6] N. F. Mott and E. A. Davis, *Electronic Processes in Non-Crystalline Materials*, 2nd ed., Clarendon Press, Oxford (1979) [Russian trans., Mir, Moscow (1982)].
[7] I. P. Zvyagin, in *Hopping Transport in Solids*, M. Pollak and B. Shklovskii (Eds.), Elsevier (1991), p. 144.
[8] T. H. Geballe and G. W. Hull, Phys. Rev. **94**, 1134 (1954).
[9] J. Tauc, *Photo- and Thermoelectric Effects in Semiconductors*, Pergamon Press, Oxford (1962) [Russian trans., IL, Moscow (1962)].
[10] I. P. Zvyagin, Phys. Status Solidi B **58**, 443 (1973).
[11] J. S. Blakemore, *Semiconductor Statistics*, Pergamon, Oxford (1962) [Russ. trans., Mir, Moscow (1964)].
[12] I. P. Zvyagin, Fiz. Tekh. Poluprovodn. **20**, 1527 (1986) [Sov. Phys. Semicond. **20**, 959 (1986)].

Translated by P. Shelnitz

Resonance acceptor states in uniaxially strained semiconductors

M. A. Odnoblyudov, A. A. Pakhomov, V. M. Chistyakov, and I. N. Yassievich

A. F. Ioffe Physicotechnical Institute, Russian Academy of Sciences, 194021 St. Petersburg, Russia
(Submitted March 4, 1997; accepted for publication April 15, 1997)
Fiz. Tekh. Poluprovodn. **31**, 1180–1186 (October 1997)

The energies and lifetimes of resonance states that arise in a uniaxially strained semiconductor are considered in the framework of the zero-radius potential model. The results obtained can be used directly for A^+ states and for the qualitative analysis of the behavior of the ground state of a Coulomb acceptor in a strained semiconductor. Numerical results obtained for Ge and GeSi are presented. The oscillator strengths of optical transitions between the resonance state and the ground state in strained germanium are calculated. © *1997 American Institute of Physics.* [S1063-7826(97)01010-7]

1. INTRODUCTION

The Γ_8^+ or Γ_8 representation corresponds to the top of the valence band in Ge, Si, and in most of the III–V compounds. The four-fold degeneracy of the top of the valence band is removed in the strained semiconductor. There is also a corresponding splitting of the acceptor ground state that transforms under the same representation.[1] When a particular strain is reached, one of the levels (doubly degenerate) falls into the valence-band continuum and becomes a quasistationary (resonance) level.

The advent of the far-infrared laser that relies on intracenter transitions in a shallow acceptor in stressed Ge (Refs. 2 and 3) has stimulated interest in calculating the energy levels, wave functions, and lifetimes of resonance states that arise in this case. Experiments on laser generation have been carried out with uniaxially strained Ge crystals to which electric-field pulses with durations between 0.2 and 1 μm were applied. The pulses depleted the ground state of the shallow acceptor in the bandgap and transferred holes to the valence band. A sharp increase in the radiation intensity emerging from the sample was observed at a certain pressure ($P \approx 4$ kbar for $\mathbf{P}\|[111]$ and $P \approx 3$ kbar for $\mathbf{P}\|[001]$). The observed phenomenon was regarded as being due to stimulated transitions of holes from the resonance state with inverted population, through which they passed in that case, to localized acceptor states in the bandgap. Stimulated radiation was observed in the pressure range $P = 4$ kbar to $P = 12$ kbar for $\mathbf{P}\|[111]$ and $P = 3$ kbar to $P = 8$ kbar for $\mathbf{P}\|[001]$. The upper limit of P corresponds to a 48-meV splitting of the top of the valence band. Detailed analysis of the experimental data requires a knowledge of the binding energy and of the splitting of the acceptor ground state in this pressure range.

The effect of strain on shallow acceptor states heretofore has been considered only for two limiting cases:[1] (1) small deformations, for which the splitting of the valence band is much smaller than the binding energy of the acceptor state in the undeformed material and for which perturbation-theory problem can be solved and (2) large deformations, for which each of the split subbands and the associated levels can be examined independently. The decay of the resonance states was not considered at all.

In this paper, we consider the problem in terms of the zero-radius-potential model, when the undeformed crystal has only one localized fourfold degenerate level. This model enables us to derive analytic expressions for wave functions, and simple equations for the energies and lifetimes of split states in the entire pressure range. Obviously, the model cannot claim high precision when acceptor states in the a strained semiconductor are calculated because the zero-radius potential is a relatively coarse approximation to the actual Coulomb potential. The model can nevertheless be used to derive an equation for the lifetimes of resonance acceptor states. We note that this problem cannot be solved by other existing methods, e. g., variational method, so that even qualitative information relating to resonance states is of considerable interest for practical applications of strain-split acceptor states in the far-infrared laser.

2. THEORETICAL MODEL

In the spherical approximation with uniaxial strain, the valence band is described by the 4×4 Lattinger Hamiltonian[4]

$$H(\mathbf{k},\zeta) = -\frac{\hbar^2}{2m_0}\begin{bmatrix} a_+ & b & c & 0 \\ b^* & a_- & 0 & c \\ c^* & 0 & a_- & -b \\ 0 & c^* & -b^* & a_+ \end{bmatrix}, \tag{1}$$

where

$$a_+ = -(\gamma_1 - 2\gamma)k_Z^2 - (\gamma_1+\gamma)(k_X^2+k_Y^2) - \zeta,$$

$$a_- = -(\gamma_1 + 2\gamma)k_Z^2 - (\gamma_1-\gamma)(k_X^2+k_Y^2) + \zeta,$$

$$b = 2\sqrt{3}\gamma(k_X - ik_Y)k_z,$$

$$c = \sqrt{3}\gamma(k_X - ik_Y)^2,$$

$$\gamma = (2\gamma_3 + 3\gamma_3)/5. \tag{1a}$$

Here $\hat{\mathbf{k}} = -i\nabla$, the Z axis lies along the strain axis, and γ_1, γ_2, and γ_3 are the Lattinger parameters. The parameter ζ is related to the splitting of the top of the valence band in the strained material:

$$E_{\text{def}} = \frac{\hbar^2\zeta}{m_0} = bX, \tag{2}$$

where b is the deformation potential, and X is the applied pressure. In the case of Ge, $b=6$ meV/kbar when the strain along the [111] axis is 4 meV/kbar (Ref. 1). The following set of Bloch basis vectors was chosen for (1):

$$u_{3/2}=\frac{1}{\sqrt{2}}(X+iY)\uparrow,\quad u_{1/2}=\frac{1}{\sqrt{6}}[(X+iY)\downarrow-2Z\uparrow],$$

$$u_{-3/2}=\frac{1}{\sqrt{2}}(X-iY)\downarrow,\quad u_{-1/2}=\frac{1}{\sqrt{6}}[(X-iY)\uparrow+2Z\downarrow]. \tag{3}$$

The acceptor wave function can be characterized by the values of the Z-component of the angular momentum, namely, $M=\pm 1/2,\pm 3/2$. We shall use the following notation for the states $M=\pm 1/2,\pm 3/2$:

$$E^M=\frac{\hbar^2\alpha_M^2}{2m_0}. \tag{4}$$

In the zero-radius potential model, the acceptor wave function takes the form[5]

$$\Psi^M(\mathbf{r})=\frac{A_M}{\sqrt{V}}\sum_{k,m=\pm 3/2,\pm 1/2}\hat{G}_{Mm}(E^M,\mathbf{k},\zeta)e^{i\mathbf{kr}}u_m, \tag{5}$$

where $M=\pm 1/2,\pm 3/2$, and u_m are the Bloch amplitudes, given by (3),

$$\hat{G}_{Mm}(E^M,\mathbf{k},\zeta)=[\hat{H}(\mathbf{k},\zeta)-E^M\hat{I}]^{-1}_{Mm} \tag{6}$$

is the Green's function of the Lattinger Hamiltonian for the deformed material, $\hat{I}$ is the unit matrix, and A_M is a normalizing constant. The precise form of the matrix $\hat{G}_{Mm}(E^M,\mathbf{k})$ and of the normalizing constants A_M is given in Appendix I. The form of the acceptor wave function of the undeformed material is analogous to (5):

$$\tilde{\Psi}^M(\mathbf{r})=\frac{A_M}{\sqrt{V}}\sum_{k,m=\pm 3/2,\pm 1/2}\hat{\tilde{G}}_{Mm}(E,\mathbf{k},\zeta=0)e^{i\mathbf{kr}}u_m, \tag{7}$$

where $\hat{\tilde{G}}_{Mm}(E,\mathbf{k},\zeta=0)$ is the Green's function of the Lattinger Hamiltonian for zero strain (see Appendix I).

We now introduce the ionization energies of states with $M=\pm 1/2$ and $\pm 3/2$ in the strained material, which we define as the separations of the $M=\pm 1/2$ and $\pm 3/2$ levels from the top of the corresponding subbands:

$$\varepsilon_{b_{\pm 1/2}}(\zeta)=-E_{\pm 1/2}-0.5E_{\rm def}\equiv\frac{\hbar^2\delta^2_{\pm 1/2}}{2m_0} \tag{8}$$

and

$$\varepsilon_{b_{\pm 3/2}}(\zeta)=-E_{\pm 3/2}+0.5E_{\rm def}\equiv\frac{\hbar^2\delta^2_{\pm 3/2}}{2m_0}. \tag{9}$$

The quantities δ_M^2 are positive. Accordingly, the binding energy of the acceptor state in the undeformed crystal, which is regarded as a known parameter in the zero-radius-potential model, is written in the form

$$E=-\frac{\hbar^2\kappa^2}{2m_0}. \tag{10}$$

Thus the energy level problem involves calculation of $\delta^2_{\pm 1/2}$ and $\delta^2_{\pm 3/2}$ as functions of κ^2 and the strain parameter ζ. The equations for these calculations can be obtained from the boundary condition for the wave function envelopes with $|\mathbf{r}|\to 0$:

$$\lim_{|\mathbf{r}|\to 0}[\langle u_M|\Psi^M\rangle\langle u_M|\tilde{\Psi}^M\rangle]=0, \tag{11}$$

where the angle brackets denote integration over the unit cell. This condition corresponds to the assumption that strain does not affect the behavior of the wave function within the range of the potential. Substituting the wave functions (5) and (7) in (11), and using Eqs. (8)–(10), we obtain the equations for δ_M^2 $(M=\pm 1/2,\pm 3/2)$

$$I(\delta_M^2,\kappa^2,\zeta)=0, \tag{12}$$

where

$$I(\delta_M^2,\kappa^2,\zeta)=\sum_{\mathbf{k}}\left\{\frac{a_\pm(\mathbf{k},\zeta)-\delta_M^2\mp\zeta}{A_\delta B_\delta-D}-\frac{a_\pm(\mathbf{k},\zeta)-\kappa^2\pm\zeta}{A_\kappa B_\kappa-D}\right\},$$

$$A_\delta=a_-(\mathbf{k},\zeta)-\delta_M^2\pm\zeta,\quad B_\delta=a_+(\mathbf{k},\zeta)-\delta_M^2\pm\zeta,$$

$$A_\kappa=a_-(\mathbf{k},\zeta)-\kappa^2-\zeta,\quad B_\kappa=a_+(\mathbf{k},\zeta)-\kappa^2+\zeta,$$

$$D=b(\mathbf{k})b^*(\mathbf{k})+c(\mathbf{k})c^*(\mathbf{k}). \tag{13}$$

In these expressions, the upper sign refers to $M=\pm 1/2$ and the lower sign refers to $M=\pm 3/2$; the expressions for $a_\pm(\mathbf{k},\zeta),b(\mathbf{k}),c(\mathbf{k})$ are obtained from (1a) by replacing the operator $\hat{\mathbf{k}}$ with the vector $\mathbf{k}$.

For compressive strain, the quantity ζ is positive, the top of the light-hole subband $(M=\pm 1/2)$ is shifted downward from the heavy-hole subband $(M=\pm 3/2)$, and the spectrum becomes asymmetric (see Fig. 1). The acceptor level undergoes the corresponding splitting. For a particular strain, the level with $M=\pm 3/2$ is pushed into the continuous spectrum of the light subband. The state thus becomes quasistationary and the energy acquires an imaginary term:

$$\varepsilon_{b,\pm 3/2}(\zeta)=-E_{\pm 3/2}-i\frac{\Gamma}{2}+0.5E_{\rm def}=\frac{\hbar^2(\delta^2_{\pm 3/2}-i\delta')}{2m_0},$$

which is related to the lifetime of the resonance state by

$$\tau=\frac{\hbar}{\Gamma}=\frac{m_0}{\hbar\delta'}.$$

For tensile strain, ζ is negative and the top of the heavy subband $(M=\pm 3/2)$ shifts downward from the subband of light holes $(M=\pm 1/2)$. The level with $M=\pm 1/2$ can become a resonant state in this case. This situation is encountered, for example, when a GeSi layer is grown between Si layers.

The detailed solution of (12) for $M=\pm 1/2,\pm 3/2$ is discussed in Appendix II.

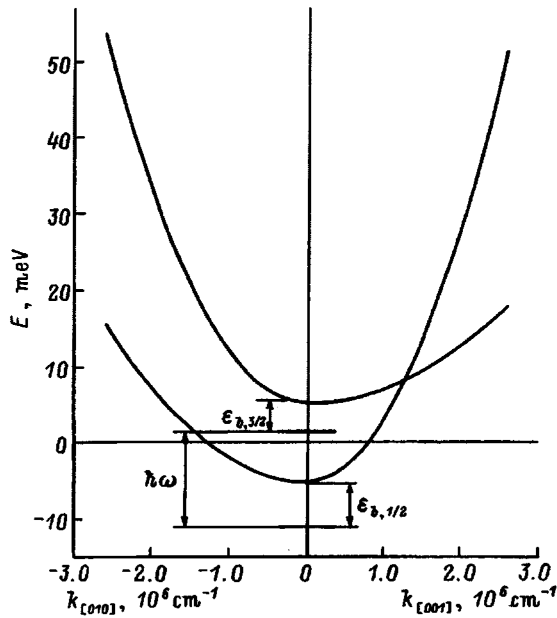

FIG. 1. Schematic representation of the valence band of Ge for uniaxial strain along the [001] axis.

3. DISCUSSION OF NUMERICAL RESULTS FOR Ge AND GeSi

Within the framework of the zero-radius potential model, the equation in (5), with allowance for (A.I.1)–(A.I.4), determines the wave functions of the localized and resonant states in the strained crystal for different level energies $\varepsilon_{b,\pm 3/2}$ and $\varepsilon_{b,\pm 1/2}$, which can be obtained by numerical solution of (12).

Let us begin by considering the case of an acceptor state for a Ga impurity in uniaxially compressed germanium. The procedure for solving (12) is described in Appendix II. We assumed that the binding energy in the undeformed material (8) is $E=11.3$ meV, which corresponds to the Ga impurity in Ge (Ref. 6). Figure 2 shows the ionization energy in the ground state of the acceptor impurity ($M=\pm 1/2$) and the

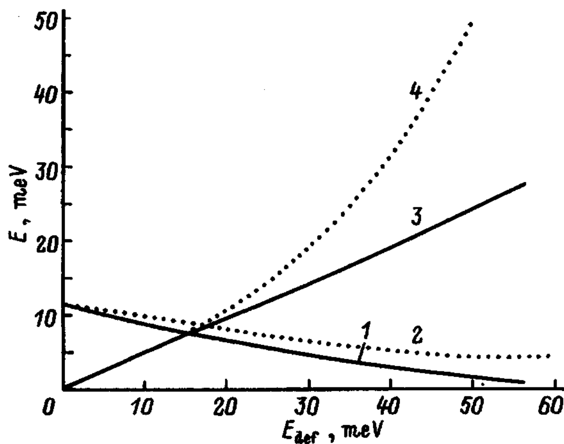

FIG. 2. Ionization energy $\varepsilon_{b,\pm 1/2}$ and the gorund-state splitting $\hbar\omega=\varepsilon_{b,\pm 1/2}-\varepsilon_{b,\pm 3/2}+E_{\mathrm{def}}$ (*3,4*) in the shallow acceptor Ga as functions of the strain splitting of the top of the valence band E_{def} in uniaxially compressed Ge: *1,3*—short-range potential, *2,4*—Coulomb potential.

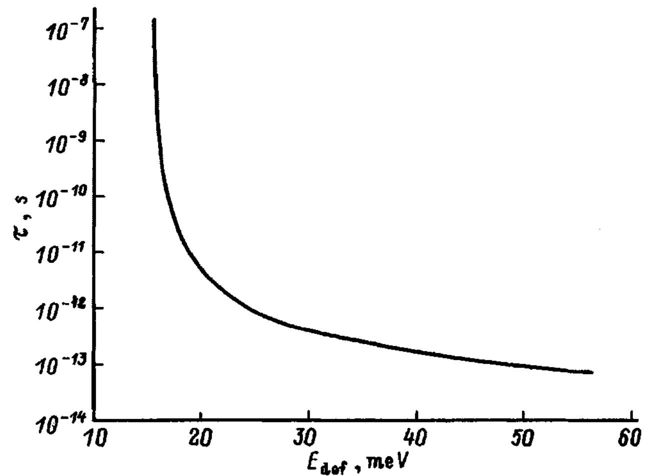

FIG. 3. Lifetime τ of the $M=\pm 3/2$ state on the Ga impurity as a function of splitting at the top of the valence band E_{def} of uniaxially compressed Ge.

ground-state splitting energy of uniaxially compressed germanium ($E_{\pm 3/2}-E_{\pm 1/2}$) as functions of the splitting of the valence band (curves *1* and *3*), which in turn is related to the applied pressure by (2). It is clear from Fig. 2 that the threshold value of the strain splitting energy at the top of the valence band, for which the resonance state appears, is 15.68 meV, which corresponds to the threshold pressure of 2.6 kbar for [001] strain and 3.92 kbar for [111]. This threshold corresponds to the point of intersection of curves *1* and *3*. For any other acceptor impurity, it is sufficient to have the binding energy in the undeformed material in order to obtain the threshold energy for the strain-split valence band, since the critical value of the ratio $E/0.5E_{\mathrm{def}}$ for Ge is 1.441 and is independent of the binding energy of the impurity state. The threshold splitting energy at the top of the valence band, for which the resonance state appears in Ge, is therefore $E_{\mathrm{def,crit}}=1.388E$. To estimate the precision of the zero-radius- potential model used in these calculations, we can compare graphs analogous to curves *1* and *3* in Fig. 2, which were calculated for the true Coulomb potential of the acceptor impurity (curves *2* and *4*). Curves 2 and 4 were calculated at high pressures from Eq. (27.18) in Ref. 1 and were determined approximately at low pressures. Comparison of curves *1* and *3* with *2* and *4* shows that the zero-radius-potential model provides a reasonable description of the splitting of the ground state of a shallow acceptor impurity as a function of the applied pressure in the pressure range in which the splitting energy at the top of the valence band can exceed the the binding energy of the acceptor state in the undeformed crystal by a factor of 2–2.5.

As already noted, when the pressure corresponds to a splitting of 15.68 meV at the top of the valence band, the $M=\pm 3/2$ state falls into the continous spectrum of the light subband ($M=\pm 1/2$) and becomes quasistationary. Figure 3 shows the lifetime of the resonance state plotted as a function of the splitting at the top of the valence band. It is clear that the lifetime falls rapidly as the resonance level moves into the continuum of the subband, which corresponds to a strong reduction in the quasistationary level width. Notice-

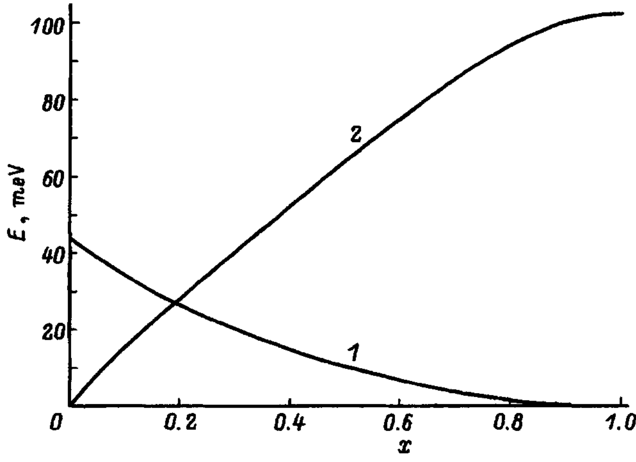

FIG. 4. Ionization energy $\varepsilon_{b,\pm 3/2}$ (*1*) and splitting $\hbar\bar{\omega}=\varepsilon_{b,\pm 3/2}-\varepsilon_{b,\pm 1/2}+E_{\rm def}$ (*2*) of the ground state of a shallow boron acceptor impurity as functions of the concentration x of the solid solution Ge_xSi_{1-x} grown on Si.

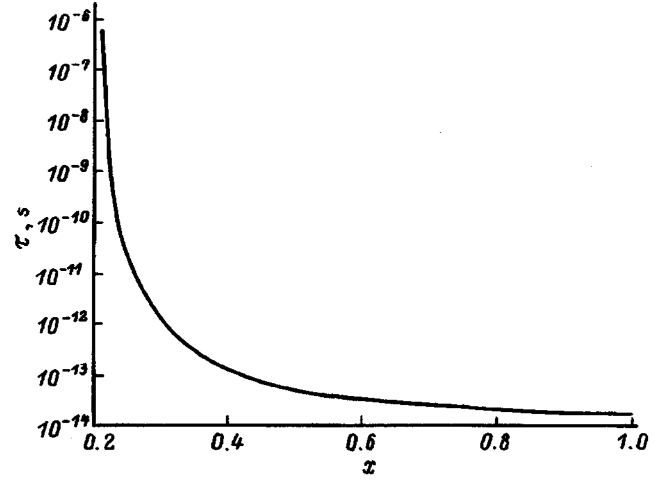

FIG. 5. Lifetime τ of the resonance state $M=\pm 1/2$ on the boron impurity plotted as a function of the concentration x of the solid solution Ge_xSi_{1-x}/Si.

able hole localization occurs only when $|E_{\rm def}-E_{\rm def,crit}|\leq 0.1$ meV. At high pressures, the bound state decays nearly instantaneously, because the lifetime τ in this case is on the order of several nanoseconds.

Sufficiently thick Ge_xSi_{1-x} layers that may be considered three dimensional can be produced by growing the Ge_xSi_{1-x} solid solution with a low Ge concentration x on Si substrate. These layers are stressed because Si and Ge_xSi_{1-x} have different lattice constants. The stress is tensile ($\zeta<0$), so that the ground state has $M=\pm 3/2$, whereas a resonant state has $M=\pm 1/2$. The tensile strain is a function of the concentration x. We used the known splitting at the top of the valence band in strained Ge_xSi_{1-x} and the binding energy of the ground state of the shallow acceptor on the boron impurity in undeformed Ge_xSi_{1-x} to calculate the ionization energy $\varepsilon_{b,\pm 3/2}$, the splitting $\bar{h}\omega=\varepsilon_{b,\pm 3/2}-\varepsilon_{b,\pm 1/2}+E_{\rm def}$ of the ground state in this impurity, and the lifetime of the $M=\pm 1/2$ resonant state as a function of the concentration x of the solid solution. These plots are shown in Figs. 4 and 5. The required binding energy of the acceptor ground state for the boron impurity, the Lattinger parameters, and the splitting of the top of the valence band in the strained crystal as a function of the concentration x in the solid solution Ge_xSi_{1-x} were taken from Refs. 7 and 8. It is clear from Figs. 4 and 5 that when the concentration of Ge in the solid solution Ge_xSi_{1-x} is greater than 20%, the fourfold degenerate ground state of the shallow acceptor is split to such an extent that the $M=\pm 1/2$ state becomes a resonant state.

4. OPTICAL TRANSITIONS

In cubic semiconductors, transitions between $M=\pm 1/2$ and $M=\pm 3/2$ are forbidden in the dipole approximation because the two states have the same parity. The transition becomes allowed when a parity-violating pertubation, e.g., an external electric field, is introduced. The presence of this field is a necessary condition for the operation of the infrared laser using intracenter transitions in the shallow acceptor.[2,3] When the electric field points in the direction of the strain axis, the emitted radiation is polarized at right angles to this direction. By using second-order perturbation theory we can show that the oscillator strength of the $3/2\leftrightarrow 1/2$ transition is given by

$$f_{3/2,1/2}=\frac{m_0}{\hbar^2\gamma_1}(E_{3/2}-E_{1/2})\sum_{M_f=\pm 1/2}\sum_{M_i=\pm 3/2}\times\left|\sum_{\eta\nu\mathbf{k}}\frac{\left\langle\frac{1}{2},M_i\middle|\mathbf{er}\middle|\eta\nu\mathbf{k}\right\rangle\left\langle\eta\nu\mathbf{k}\middle|e\mathscr{E}\mathbf{z}\middle|\frac{3}{2},M_f\right\rangle}{E_i-\varepsilon_\eta(\mathbf{k})+i\Gamma}\right|^2. \tag{14}$$

Here $\mathscr{E}$ is the electric field, and $\mathbf{e}$ is the polarization unit vector. The dependence of the oscillator strength on the applied pressure has a singularity that corresponds to a particular pressure for which the $M=\pm 3/2$ level coincides with the top of the light subband. The behavior of the oscillator strength in this energy range can be determined by using (14) in the form

$$f_{3/2,1/2}=\frac{m_0}{\hbar^2\gamma_1}(E_{3/2}-E_{1/2})\sum_{M_f=\pm 1/2}\sum_{M_i=\pm 3/2}\times\left|\sum_{\mathbf{k}}\left\langle\frac{1}{2},M_f\middle|\mathbf{er}\hat{G}(E_i,\mathbf{k},\zeta)e\mathscr{E}\mathbf{z}\middle|\frac{3}{2},M_i\right\rangle\right|^2. \tag{15}$$

If we now use (5), we obtain the expression for the matrix element

$$\sum_{\mathbf{k}}\left\langle\frac{1}{2},M_f\middle|\mathbf{er}\hat{G}(E_{3/2},\mathbf{k},\zeta)e\mathscr{E}\mathbf{z}\middle|\frac{3}{2},M_i\right\rangle=A_iA_fe\mathscr{E}\int\frac{d^3k}{(2\pi)^3}\sum_{\alpha\beta}G_{M_f\beta}(E_i,\mathbf{k},\zeta)\times\left(\mathbf{e}\frac{\partial}{\partial\mathbf{k}}\right)G_{\beta\alpha}(E_f,\mathbf{k},\zeta)\frac{\partial}{\partial k_z}G_{\alpha M_i}(E_f,\mathbf{k},\zeta). \tag{16}$$

If the level with $M_f=\pm 3/2$ is close to the top of the light subband, then $|\varepsilon_{b,3/2}\sim E_{\rm def}|<E_{\rm def}$ and the matrix element

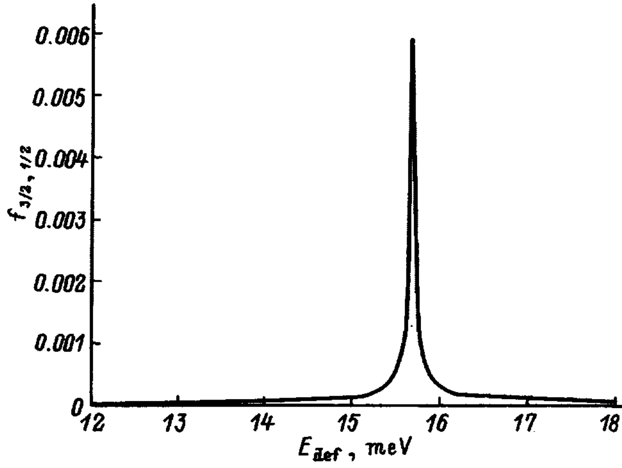

FIG. 6. Oscillator strength $f_{1/2,3/2}$ of the $M=\pm 3/2 \rightarrow M=\pm 1/2$ transition between the strained states of a shallow acceptor on the Ga impurity as a function of splitting at the top of the valence band E_{def} in uniaxially compressed Ge.

(16) can be evaluated analytically. Using the expression for the Green's function of the Lattinger Hamiltonian (see Appendix I) for small k, i.e., $\varepsilon_1(\mathbf{k}) < E_{\text{def}}$, we obtain the following expression for the oscillator strength of the $M=\pm 3/2 - M \leftrightarrow \pm 1/2$ transition:

$$f = 1.2\times 10^{-3}[\text{meV}]^3 C(E_{\text{def}}, \varepsilon_{b,1/2}\varepsilon_{b,3/2})\mathscr{E}^2 \times \frac{\varepsilon_{b,1/2}-\varepsilon_{b,3/2}+E_{\text{def}}}{E_{\text{def}}\varepsilon^2_{b,1/2}} \frac{1}{|\varepsilon_{b,3/2}-E_{\text{def}}|}, \tag{17}$$

where $C(E_{\text{def}}, \varepsilon_{b,1/2}, \varepsilon_{b,3/2})$ is a dimensionless function of energy of the order of 1. It shows that the oscillator strength of the optical transition rises sharply as the $M_i = \pm 3/2$ level approaches the top of the light subband. Figure 6 shows the oscillator strength of the $M=\pm 3/2 \leftrightarrow M=\pm 1/2$ transition for the acceptor impurity Ga in Ge as a function of the splitting at the top of the valence band. This function has a narrow peak near the threshold splitting, but falls to values of the order of 10^{-5} as the splitting departs from its typical value. It is important to note that the resulting expression is valid only for $|\varepsilon_{b,3/2} \ll E_{\text{def}}| \ll E_{\text{def}}$, i.e., when the separation between the $M_i = \pm 3/2$ level and the top of the light subband is much less than the splitting at the top of the valence band.

5. CONCLUSIONS

We have used the zero-radius-potential model to obtain the equation for the energy levels in the ground state and resonance state of an acceptor in a strained crystal. This equation was also used to calculate the lifetime of resonance states. The results of a numerical calculation performed for Ge and SiGe are presented. It is shown that this model can also be used to describe the splitting of the ground state of a Coulumb acceptor at moderate pressures. The oscillator strength was calculated for an optical transition between resonance and ground states.

The authors wish to thank Volkswagen-Stiftung and the Russian Fund for Fundamental Research (grant No. 97-02-16820) for partial support of this research.

APPENDIX I

We now reproduce the precise form of the Green's matrix for the Lattinger Hamiltonian $\hat{G}(E^M,\mathbf{k})$ and the expressions for the normalizing constants A_M:

$$\hat{G}(E^M,\mathbf{k},\zeta) = (\hat{H}(\mathbf{k},\zeta) - E^M\hat{I})^{-1} = \frac{1}{\det(\hat{H}(\mathbf{k},\zeta)-E^M\hat{I})} \times \begin{bmatrix} B_{11} & B_{12} & B_{13} & B_{14} \\ B_{21} & B_{22} & B_{23} & B_{24} \\ B_{31} & B_{32} & B_{33} & B_{34} \\ B_{41} & B_{42} & B_{43} & B_{44} \end{bmatrix}^T, \tag{A.I.1}$$

where B_{Mm} is the algebraic complement of the element $[\hat{H}(\mathbf{k},\zeta)-E^M\hat{I}]^{-1}_{Mm}$, and $\hat{I}$ is the unit matrix. Finally, we have

$$\hat{G}(E^M,\mathbf{k}) = -\frac{2m}{\hbar^2}\frac{1}{(a_-+\alpha_M^2)(a_++\alpha_M^2)-bb^*-cc^*} \times \begin{bmatrix} a_-+\alpha_M^2 & -b & -c & 0 \\ -b^* & a_++\alpha_M^2 & 0 & -c \\ -c^* & 0 & a_++\alpha_M^2 & b \\ 0 & -c^* & b^* & a_-+\alpha_M^2 \end{bmatrix}. \tag{A.I.2}$$

The normalizing constants A_M are given by

$$A_M^{-2} = \sum_{k,m=\pm 1/2,\pm 3/2} |\hat{G}(E^M,\mathbf{k})_{Mm}|^2, \tag{A.I.3}$$

Finally, we have

$$A^{-2}_{\pm 3/2} = \sum_{\mathbf{k}} \frac{(a_-+\alpha^2_{\pm 3/2})^2 + |b|^2 + |c|^2}{[(a_-+\alpha^2_{\pm 3/2})(a_++\alpha^2_{\pm 3/2}) - bb^* - cc^*]^2},$$

$$A^{-2}_{\pm 1/2} = \sum_{\mathbf{k}} \frac{(a_++\alpha^2_{\pm 1/2})^2 + |b|^2 + |c|^2}{[(a_-+\alpha^2_{\pm 1/2})(a_++\alpha^2_{\pm 1/2}) - bb^* - cc^*]^2}. \tag{A.I.4}$$

APPENDIX II

Lets us now consider the equation describing the behavior of the $M=\pm 1/2$ level. The expressions below are used for the case of compressive stress $(\zeta > 0)$. To calculate $I(E_{1/2}, E, \zeta)$ from (12), we transform to the dimensionless variables

$$\eta = \frac{\sqrt{k_x^2+k_y^2+k_z^2}}{\zeta} \quad \text{and} \quad x = \frac{k_z}{\sqrt{k_x^2+k_y^2+k_z^2}}. \tag{A.II.1}$$

We thus find that (13) transforms to

$$I(\varepsilon_{b,\pm 1/2}, E, E_{\text{def}}) = \sqrt{\zeta}\int_0^1 dx \int_{-\infty}^{+\infty} \eta^2 d\eta L_{1/2}(x,\eta), \tag{A.II.2}$$

where

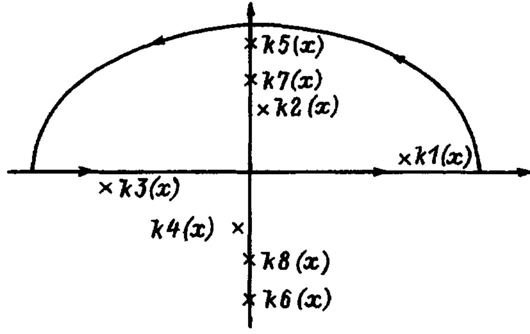

FIG. 7. Disposition of the poles of the integrand and the integration contour for (A.II.3) and (A.II.5) for energies $\varepsilon_{b,\pm 3/2}$ and $\varepsilon_{b,\pm 1/2}$ corresponding to the bound states of the acceptor impurity with $M=\pm 3/2$ and $M=\pm 1/2$.

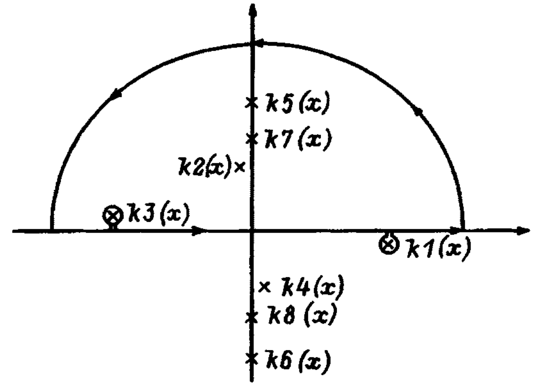

FIG. 8. Disposition of the poles of the integrand and the integration contour for (A.II.5) for the complex energy $\varepsilon_{b,\pm 3/2}$ corresponding to the quasistationary states of the acceptor impurity with $M=\pm 3/2$.

$$L_{1/2}(x,\eta)=\frac{A_{1/2}^{+}-1}{(A_{1/2}^{-}-1)(A_{1/2}^{+}-1)-D_1}-\frac{B_{+}+1}{(B_{-}-1)(B_{+}+1)-D_1},$$

$$A_{1/2}^{-}=a_{-}(\eta,x)-\varepsilon_{b,\pm 1/2}/0.5E_{\rm def},$$

$$A_{1/2}^{+}=a_{+}(\eta,x)-\varepsilon_{b,+1/2}/0.5E_{\rm def},$$

$$B_{-}=a_{-}(\eta,x)-E/0.5E_{\rm def},$$

$$B_{+}=a_{+}(\eta,x)-E/0.5E_{\rm def},$$

$$D_1=b(\eta,x)b^{*}(\eta,x)+c(\eta,x)c^{*}(\eta,x).$$

Equation (12) becomes

$$I=\sqrt{\zeta}F_{1/2}\left(\frac{\varepsilon_{b,\pm 1/2}}{0.5E_{\rm def}},\frac{E}{0.5E_{\rm def}}\right)=0 \tag{A.II.3}$$

and gives $\varepsilon_{b,\pm 1/2}/0.5E_{\rm def}$ as a function of $E/0.5E_{\rm def}$.

We note that the integrand in (A.II.2) consists of a difference of two terms which tend to the same constant as $\eta\to\infty$, so that the integrals diverge for infinite limits, but the difference itself tends to $1/\eta^2$ in the limit $\eta\to\infty$ and the integral of the difference is finite. We now reduce the integrands to a common denominator. The resulting rational fraction has purely imaginary poles that are functions of x. To evaluate the integral with respect to η, we close the contour in the upper half-space, as shown in Fig. 7, and use the residue theorem. The integral with respect to x between finite limits can be readily evaluated numerically. Solving (A.II.3), we obtain the quantity $\varepsilon_{b\pm 1/2}$ as a function of $E_{\rm def}$.

Let us now consider the equation for the energy of a level with $M=\pm 3/2$. If we apply the transformations defined by (A.II.1) to (13). We finally obtain the expression for $I(\varepsilon_{b\pm 3/2},E,\zeta)$ of the form of (A.II.2):

$$I(\varepsilon_{b\pm 3/2},E,E_{\rm def})=\sqrt{\zeta}\int_0^1 dx\int_{-\infty}^{+\infty}\eta^2 d\eta L_{3/2}(x,\eta), \tag{A.II.4}$$

where

$$L_{3/2}(x,\eta)=\frac{A_{3/2}^{-}+1}{(A_{3/2}^{-}+1)(A_{3/2}^{+}+1)-D_1}-\frac{B_{-}-1}{(B_{-}-1)(B_{+}+1)-D_1},$$

$$A_{3/2}^{-}=a_{-}(\eta,x)-\varepsilon_{b,\pm 3/2}/0.5E_{\rm def},$$

$$A_{3/2}^{+}=a_{+}(\eta,x)-\varepsilon_{b,\pm 3/2}/0.5E_{\rm def},$$

and the quantities B_{-}, B_{+}, and D_1 were defined earlier. The result is that (12) assumes the form

$$I=\sqrt{\zeta}F_{3/2}\left(\frac{\varepsilon_{b,\pm 3/2}}{0.5E_{\rm def}},\frac{E}{0.5E_{\rm def}}\right)=0. \tag{A.II.5}$$

When the ratio $E/0.5E_{\rm def}$ is greater than $(E/0.5E_{\rm def})_{cr}$, which is determined by the Lattinger parameters for the given material, the solution of (A.II.5) by the method described for $M=\pm 1/2$ gives the values of $\varepsilon_{b,+3/2}/0.5E_{\rm def}$ corresponding to the bound states with $M=\pm 3/2$ in the bandgap. As $E/0.5E_{\rm def}\to(E/0.5E_{\rm def})_{cr}$, the bound state approaches the bottom of the light subband and for $E/0.5E_{\rm def}<(E/0.5E_{\rm def})_{cr}$, it falls into the continuum of this subband. The poles of the integrand in (A.II.4) then become real and remain real for any $x\in[0,1]$. If we evaluate the integral in this case, we obtain the complex function

$$I=U\left(\frac{\varepsilon_{b,\pm 3/2}}{0.5E_{\rm def}},\frac{E}{0.5E_{\rm def}}\right)+iV\left(\frac{\varepsilon_{b,\pm 3/2}}{0.5E_{\rm def}}\right), \tag{A.II.6}$$

which can vanish only for complex values of $\varepsilon_{b,\pm 3/2}$ and, correspondingly, $\delta^2_{\pm 3/2}$. We now write

$$\varepsilon_{b,\pm 3/2}(\zeta)\to\varepsilon_{b,\pm 3/2}(\zeta)-i\Gamma=-E_{\pm 3/2}-i\Gamma+0.5E_{\rm def}=\frac{\hbar^2(\delta^2_{b,\pm 3/2}-i\delta')}{m_0}. \tag{A.II.7}$$

After this substitution, the poles of the integrand in (A.II.4) become complex and when the integral with respect to η is evaluated, the contour must be closed as shown in Fig. 8. Solving (A.II.5), we obtain $\varepsilon_{b,\pm 3/2}$ and Γ as functions of $E_{\rm def}$.

[1] G. L. Bir and G. E. Pikus, *Symmetry and Strain Effects in Semiconductors* [in Russian], Nauka, Moscow, 1972.

[2] I. V. Altukhov, M. S. Kagan, K. A. Korolev, and V. P. Sinis, JETP Lett. **59**, 476 (1994).
[3] I. V. Altukhov, E. G. Chirkova, M. S. Kagan, K. A. Korolev, V. P. Sinis, and I. N. Yassievich, Phys. Status Solidi B **198**, 35 (1996).
[4] J. M. Luttinger and W. Kohn, Phys. Rev. **97**, 869 (1955).
[5] A. A. Pakhomov and I. N. Yassievich, Fiz. Tekh. Poluprovodn. **27**, 482 (1993) [Semiconductors **27**, 270 (1993)].
[6] Landolt-Bornstein, *Group II Semiconductors, New Series*, Berlin, 1989, Vol. 22, subvol. b.
[7] R. R. Buczko, Sol. St. Commun. **93**, 367 (1995).
[8] T. Fromhertz, E. Koppensteiner, M. Helm, G. Bauer, J. F. Nutzel, and G. Abstreiter, Phys. Rev. B **50**, 15073 (1994).

Translated by S. Chomet

Nuclear magnetic resonance spectra of ^{119}Sn and ^{125}Te in SnTe and SnTe:Mn

V. V. Slyn'ko, E. I. Slyn'ko, A. G. Khandozhko, and Yu. K. Vygranenko

Institute for Materials Science, National Academy of Sciences, 274001 Chernovtsy, Ukraine
(Submitted April 13, 1996; accepted for publication January 13, 1997)
Fiz. Tekh. Poluprovodn. **31**, 1187–1191 (October 1997)

A study is reported of the nuclear magnetic resonance spectra of ^{119}Sn and ^{125}Te in SnTe with hole concentrations $p_{77}=1.42\times10^{20}-2.3\times10^{21}$ cm^{-3} and in SnTe:Mn ($N_{\mathrm{Mn}}=0.5$ and 5 at. %, $p_{77}=8\times10^{20}$ cm^{-3}) at $T=4.2-300$ K. Considerable broadening of NMR lines due to hyperfine magnetic interactions between nuclear and electron spins was observed in SnTe with $p_{77}>2\times^{20}$ cm^{-3}. Asymmetric broadening of the resonance lines was observed in the rhombohedral phase of SnTe and SnTe:Mn. The temperature dependence of the NMR line width of ^{125}Te in SnTe:Mn is in agreement with the magnetic phase diagram for $N_{\mathrm{Mn}}=5$ at. %. The superparamagnetic phase of SnTe:Mn is formed at $T=20\pm2$ K and the ferromagnetic phase is formed at $T=4.2$ K. © *1997 American Institute of Physics.* [S1063-7826(97)01210-6]

1. INTRODUCTION

The NMR spectra of ^{119}Sn in SnTe crystals with hole concentrations $p_{77}=6\times10^{19}-8\times10^{20}$ cm^{-3} were investigated in Ref. 1. An investigation was made there of the effect of the electron subsystem on the ferroelectric phase transition, and the ferroelectric point was found to be $T_c=145$ K at the lowest hole concentration $p_{77}=6\times10^{19}$ cm^{-3}.

In this paper we report a study of the effect of the electronic and magnetic subsystems of SnTe:Mn crystals on NMR spectra. We have examined the dynamics of the shape and width of the NMR lines of ^{119}Sn and ^{125}Te (and also the Knight shift) as functions of the concentration p in SnTe. We have recorded the NMR spectra and the magnetic susceptibility of SnTe:Mn with different impurity concentrations. The results were then used to analyze the state of the doped system SnTe:Mn.

2. EXPERIMENTAL PROCEDURE

The resonance spectra were recorded in a NMR spectrometer, using an inductive probe at the resonance frequency 13.495 MHz. The signal was detected by a standard method, using differential scans and digital signal averaging.[1]

The SnTe crystals were grown by Bridgman's method. The hole concentration in them ($p_{77}1/eR_{77}$) was usually $7\times10^{20}-8\times10^{20}$ cm^{-3}. These values are attributable to the properties of the phase diagram, i. e., a deviation of the equilibrium composition of SnTe from stoichiometry toward an excess of Te. The concentration p was therefore determined by the number of electrically active tin vacancies.[2]

To produce samples with concentrations in the broad range $p_{77}=1.42\times10^{20}-2.3\times10^{21}$ cm^{-3}, the original material (single crystal and powder samples) was subjected to isothermal annealing in saturated vapor of the components at different tempertures for $240-600$ h (Ref. 2). X-ray diffraction studies at $T=300$ K have shown that the annealing process does not alter the cubic structure of SnTe, but, according to Ref. 3, it does facilitate the more uniform distribution of free carriers in the sample.

The doped material was produced by adding Mn to the material.

NMR was investigated in powder samples with grain diameters in the range $50-100$ μm and sample volume of 0.25 cm^3. The grain dimensions did not have any appreciable effect of the resonance spectra. The magnetic susceptibility of single-crystal SnTe:Mn was measured by the Faraday method.

3. EXPERIMENTAL RESULTS

A. NMR spectra of ^{119}Sn and ^{125}Te in SnTe

We have investigated the NMR spectra of tin and tellurium in SnTe with $p_{77}=1.42\times10^{20}-2.3\times10^{21}$ cm^{-3} in the temperature range $T=4.2-300$ K. The line width was determined at half-height of the resonance absorption curve.

Since SnTe is a low-temperature ferroelectric, the concentration dependence of the width of the resonance lines of ^{119}Sn and ^{125}Te $[\Delta B=f(p)]$ was measured at $T=300$ K. The lines broaden as p increases, and the effect is particularly noticeable for ^{119}Sn (Fig. 1). The lineshape is nearly Gaussian for $p_{77}<2\times10^{20}$ cm^{-3}, found from the ratio of the second to fourth moments. For higher values of p, the line shape departs appreciably from the Gaussian shape. When the concentration dependence is well defined, the line width is found to be a slowly varying function of temperature (see Table I).

For $p_{77}<8\times10^{20}$ cm^{-3}, the SnTe samples showed asymmetric NMR line broadening at low temperatures. The temperature T_c at which asymmetry disappears is a function of the concentration p. Figure 2 shows the transformation of the shape of the NMR line of ^{119}Sn in a sample with $p_{77}=2\times10^{20}$ cm^{-3} . (The derivative of the NMR signal was recorded in order to exhibit more clearly any features present on the line.) It is clear that, for $T<100$ K, the shift of the peak is accompanied by asymmetric line broadening. These features of the resonance lines were less well defined in the case of ^{125}Te. According to Ref. 4, the symmetry of the low-temperature phase of SnTe ($T<150$ K) is a function of the concentration p. In samples with $p<5\times10^{20}$ cm^{-3} (we recall that $p=0.6\times p_{77}$), a ferroelectric phase transition oc-

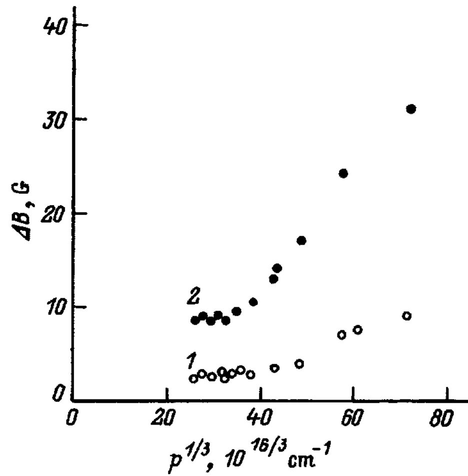

FIG. 1. Width of the resonance lines of ^{119}Sn (*2*) and ^{125}Te (*1*) plotted as a function of the hole concentration at $T=300$ K.

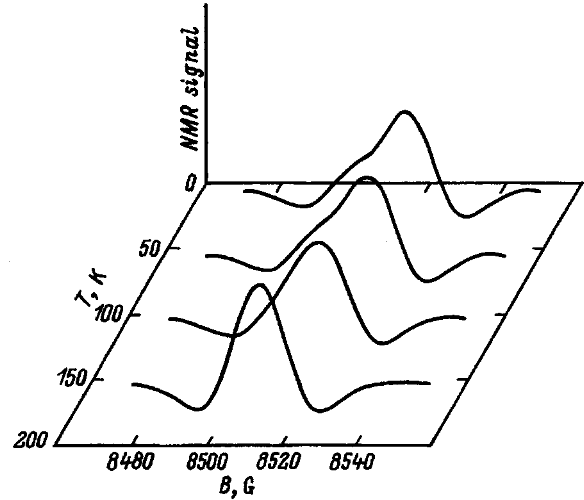

FIG. 2. Width of the ^{119}Te NMR line in SnTe with $p_{77}=2\times10^{20}$ cm^{-3} as a function of temperature.

curs as p is reduced, and in the rhombohedral phase of SnTe is formed. Thus, $T_c=98$ and ~150 K for $p=8\times10^{19}$ and 4×10^{19} cm^{-3}, respectively.

It follows from the foregoing discussion that the asymmetric broadening of the NMR lines of ^{119}Sn and ^{125}Te is typical for concentration and temperature ranges corresponding to the rhombohedral phase of SnTe. This conclusion is confirmed by the following arguments. In SnTe samples with $p_{77}\geq8\times10^{20}$ cm^{-3}, in which the cubic structure persists down to the lowest temperatures,[4] the resonance lines due to both nuclei are symmetrically broadened in the temperature range $T=4.2-300$ K. Computer analysis of the lineshape shows that it can be described by the sum of two lines with almost Gaussian shape in roughly equal amplitude.

B. NMR spectra of ^{119}Sn and ^{125}Te in SnTe:Mn and magnetic susceptibility

The NMR spectra were investigated using SnTe:Mn samples with impurity concentrations $N_{Mn}=0.5$ and 5 at. %, and $p_{77}=8\times10^{20}$ cm^{-3}, for which their structure remained cubic throughout the temperature range $4.2-300$ K. This excluded the possibility of asymmetric line broadening due to the ferroelectric phase of SnTe.

The introduction of the Mn impurity has no effect on hole concentration in SnTe, but does have a significant effect on the shape and width of the resonance lines. For $N_{Mn}=0.5$ at. %, resonance absorption is observed for both nuclei. For $N_{Mn}=5$ at. %, the NMR width of ^{119}Sn exceeds 150 Hz and becomes difficult to detect by continuous scanning techniques. The dynamics of the lineshape as a function of N_{Mn} is therefore reproduced only for ^{125}Te (Fig. 3).

Figure 4 shows the temperature dependence of the NMR line width of ^{125}Te for $N_{Mm}=5$ at. %. A reduction in temperature from 300 to 22 K has no appreciable effect on the lineshape or width. However, at $T=20\pm2$ K, the line broadens abruptly and a further reduction to 4.2 K produces no detectable resonance absorption.

To obtain additional information on the state of the impurity system in SnTe:Mn, we have measured the magnetic

TABLE I. NMR line width, G

p_{77}, cm^{-3}	line type	T, K 300	77	4.2
1.42×10^{20}	^{119}Sn	8.5	9.8	11.5
	^{125}Te	2.5	4.5	6.0
1.0×10^{21}	^{119}Sn	17.0	10.0	19.5
	^{125}Te	4.0	6.8	7.5
2.3×10^{21}	^{119}Sn	31.0	33.0	34.0
	^{125}Te	9.0	11.6	13.4

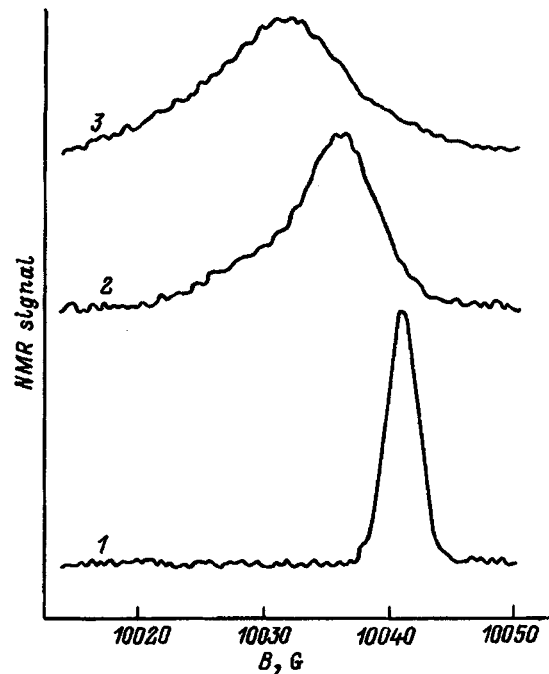

FIG. 3. Shape of the NMR liners of ^{125}Te NMR line in SnTe:Mn as a function of the impurity concentration N_{Mn} at $T=300$ K: *1* — undoped SnTe, *2,3* — $N_{Mn}=0.5$ and 5 at. %, respectively.

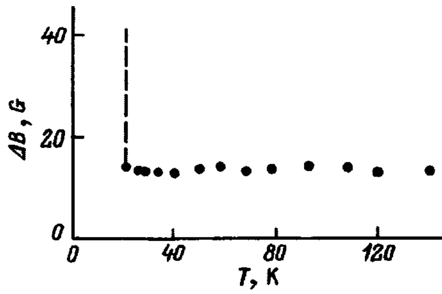

FIG. 4. Width of the ^{125}Te NMR line as a function of temperature for $N_{\mathrm{Mn}}=5$ at. %, $p_{77}=8\times10^{20}$ cm^{-3}.

susceptibility of samples with $N_{\mathrm{Mn}}=0.5$, and 10 at. % and $p_{77}=8\times10^{20}$ cm^{-3}.

The paramagnetic component of susceptibility increases with increasing N_{Mn} and the function $\chi_p^{-1}(T)$ satisfies the Curie-Weiss law (Fig. 5). Since the Mn^{2+} ions are in the S-state in SnTe, the fact that the Curie-Weiss law is satisfied confirms the presence of the exchange interaction between them. For $N_{\mathrm{Mn}}=0.5$ and 5 at. %, the characteristic temperture is $\theta=-20$ and -54 K, respectively, i. e., the exchange interaction is antiferromagnetic (Fig. 5, curves *1* and *2*). It was found that $\theta=+29$ K for $N_{\mathrm{Mn}}=10$ at. %, which suggests a ferromagnetic interaction. We observed not only a nonmonotonic variation of θ with increasing N_{Mn} in SnTe (as in PbTe:Mn and PbTe:Eu; Ref. 5), but also a change in the mechanisms responsible for the interaction.

4. DISCUSSION OF THE RESULTS

The NMR spectra of solids exhibit in most cases a broadening of the Gaussian line due to the dipole-dipole interaction between the nuclear magnetic moments. The additional local magnetic field induced on the nuclei produces the resonance-line broadening, but is too weak to affect the resonance frequency. The shape of the spectra is also affected by the electric and magnetic interaction of the nuclei with their environment.[6,7]

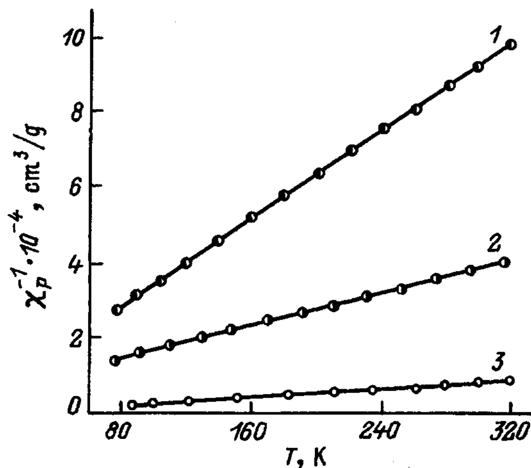

FIG. 5. Temperature dependence of the paramagnetic susceptibility χ_p of SnTe:Mn for the following values of N_{Mn}, at. %: *1* — 0.5, *2* — 5, *3* — 10.

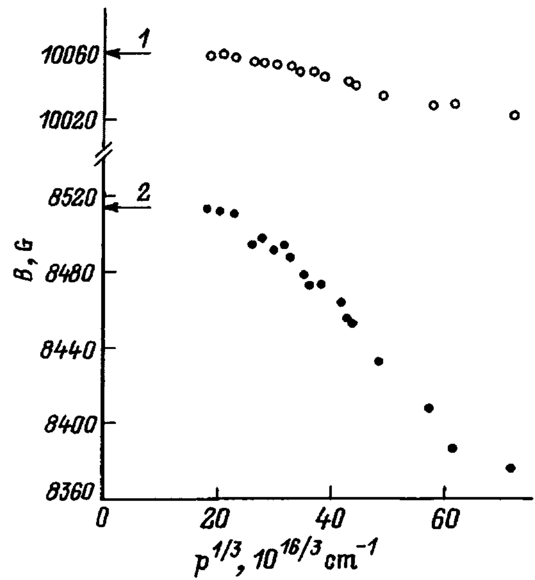

FIG. 6. Concentration dependence of the resonance field on the nuclei ^{119}Sn (*2*) and ^{125}Te (*1*) at 13.495 mHz (arrows show the chemical shifts) at $T=300$ K.

In degenerate SnTe, the zero quadropole moments of the ^{119}Sn and ^{125}Te nuclei ensure that the magnetic electron-nuclear interaction is the dominant feature. To detect it, we have measured the resonance fields on ^{119}Sn and ^{125}Te as functions of the hole concentration (Fig. 6). The resonance field on nuclei is the resultant field shift consisting of the chemical and Knight components S_c and S_K shifts, respectively. Since the chemical shift is independent of hole concentration, we may consider that our curves reflect the character of the concentration dependence of the Knight shift. The arrows in the figure show the values of S_c in the corresponding nuclei, obtained as in Ref. 3 by extrapolating the measured dependence to zero hole concentration.

It is clear from Fig. 6 that both nuclei have positive S_K (resonance field shifted toward lower value) for $p_{77}>2\times10^{20}$ cm^{-3}, which increases with increasing p. Symmetric broadening of the NMR lines (Fig. 1) was observed in parallel and was much greater than the pure dipole broadening. At the same time, S_K and ΔB were greater for ^{119}Sn than for ^{125}Te.

The recorded S_K shows that there is magnetic hyperfine interaction between nuclear and electron spins. The additional magnetic field generated by this interaction on the nuclei (the field is parallel to the external field because $S_K>0$) produces not only a line broadening, but also a shift of the resonance frequency.

Comparison of Figs. 1 and 6 shows that the concentration dependence of ΔB and S_K is the same for ^{119}Sn (or ^{125}Te). This means that there is a relationship between ΔB and S_K. To verify this assertion, we have plotted the function $\Delta B=f(S_K)$ for ^{119}Sn in the concentration range $p_{77}=4\times10^{20}-2\times10^{21}$ cm^{-3}. We found that this function is a linear relationship that can be described by

$$\Delta B=\Delta B_0+c\cdot S_K, \tag{1}$$

where $\Delta B_0 = 1.5$ G is the line width obtained by extrapolating the experimental curve to $S_K = 0$ and $c = 0.22$ is the slope. The linear relationship between ΔB and S_K for ^{207}Pb in p-type PbTe was obtained for the first time (Ref. 3).

We may therefore conclude that the weak temperature dependence of the line width (see Table I) reflects the temperature dependence of S_K in the degenerate material.[3,8]

We now turn to the discussion of the results obtained for the SnTe:Mn samples. The paramagnetic ions Mn^{2+} produce a considerable enhancement of the effective magnetic field H_e, on the nuclei. This leads to a broadening of the resonance lines that is particularly appreciable in the case of ^{119}Sm. The line width of ^{119}Sn is greater by a factor of nearly 10 than the line width of ^{125}Te for $N_{\mathrm{Mn}} = 5$ at. %. The significant difference between the values of H_e for these nuclei is obviously the reason for the asymmetric broadening of the NMR lines in SnTe:Mn (Fig. 3).

The functions $\chi_p^{-1}(T)$ and $\Delta B = f(T)$, shown in Figs. 3 and 4, are in agreement with one another and are consistent with the magnetic phase diagram of SnTe:Mn (Fig. 1 in Ref. 9).

According to Ref. 9, the exchange interaction between the Mn ions is conveyed by holes (Ruderman-Kittel-Kasuya-Iosida mechanism). Depending on N_{Mn}, this mechanism gives rise to anti- or ferromagnetic interaction between the impurity ions in SnTe (Fig. 5).

The functions $\chi_p^{-1}(T)$ satisfy the Curie-Weiss law

$$\chi_p = \frac{N_{\mathrm{Mn}} \cdot \mu_e^2}{3k(T-\theta)}, \quad (2)$$

where μ_e is the effective magnetic moment of the Mn ions. This means that for SnTe:Mn with $N_{\mathrm{Mn}} = 0.5$, 5, and 10 at. %, there are no regions with long-range magnetic order in the temperature range $T = 77 - 300$ K. An analogous conclusion can be drawn from the plot of $\Delta B = f(T)$ in Fig. 4. The fact that ΔB is independent of T in the range $22 - 300$ K shows that the field H_e on ^{125}Te does not change down to 22 K. The abrupt broadening of the lines at $T = 20 \pm 2$ K is a reflection of the change in the state of the impurity system SnTe:Mn and of the associated sharp increase in μ_e (and, consequently in H_e).

This fact can be explained in terms of the magnetic phase diagram[9] according to which the superparamagnetic phase of SnTe:Mn is observed at this temperature when $N_{\mathrm{Mn}} = 5$ at. %. The considerable increase in μ_e in the superparamagnetic phase is due to a ferromagnetic cloud formed around each Mn ion as a result of the spin polarization of free carriers. The resonance is difficult to observe near $T < 22$ K because of the strong line broadening.

The vanishing of the NMR signal at 4.2 K can be attributed to the ferromagnetic phase of SnTe:Mn that is formed as a result of the overlap of the ferromagnetic clouds.[9]

We note that our results are in conflict with the conclusions reported in Ref. 10, according to which ΔB should be a linear function of N_{Mn} and of $1/T$. To verify this assertion, we have used the data from Ref. 10 to plot a graph of $\Delta B = f(T)$ for ^{125}Te with $N_{\mathrm{Mn}} = 0.5$ at. % (the values of ΔB for $N_{\mathrm{Mn}} = 5$ at. % are shown only for $T = 330$ and 77 K). As expected, the Curie law is not satisfied: strong line broadening is observed at $T = 4.2$ K. Again, in contrast to Ref. 10, we have not detected any changes in the NMR line width of ^{125}Te in the temperature range $77 - 300$ K for $N_{\mathrm{Mn}} = 5$ at. %

Our results lead us to the following conclusions. The broadening of the NMR lines of ^{119}Sn and ^{125}Te in SnTe is due to the magnetic hyperfine interaction between the nuclear and electron spins. The line shape is definitely non-Gaussian for $p_{77} > 2 \times 10^{20}$ cm^{-3}. The asymmetric broadening of the lines occurs in the rhombohedral phase of SnTe. The temperature dependence $\Delta B = f(T)$ for ^{125}Te in SnTe:Mn with $N_{\mathrm{Mn}} = 5$ at. % is a reflection of the presence of the superparamagnetic phase at $T = 20 \pm 2$ K and the ferromagnetic phase at $T = 4.2$ K. The asymmetric broadening of the resonance lines of SnTe:Mn is due to the different values of H_e for the nuclei ^{125}Te and ^{119}Sn.

[1] E. I. Slyn'ko, A. G. Khandozhko, S. D. Letyuchenko, and A. I. Izv. AN SSSR, Ser. Fiz. **51**, 2136 (1987).
[2] R. F. Brebrick, J. Electron. Mater. **6**, 659 (1977).
[3] S. D. Senturia, A. C. Smith, C. R. Newes, J. A. Hofmann, and P. L. Sagalyn, Phys. Rev. B **1**, 4045 (1970).
[4] O. E. Kvyatkovskii, Fiz. Tverd. Tela **32**, 2862 (1990)[Sov. Phys. Solid State **32**, 1990].
[5] V. I. Fistul (ed.), *Physics and Material Properties of Semiconductors with Deep Levels* [in Rusian], Metallurgiya, Moscow, 1987, Chap. 3, p. 56.
[6] J. Winter, *Magnetic Resonance in Metals*, Clarendon Press, Oxford (1971).
[7] M. L. Afanas'ev, E. P. Zeer, and Yu. G. Kubarev, *Magnetic Resonance and Electron-Nuclear Interactions in Crystals* [in Russian], Nauka, Novosibirsk (1983).
[8] Lee Kenneth, J. Liesegang, and P. B. P. Phipps, Phys. Rev. **161**, 322 (1967).
[9] A. Mauger and M. Escorne, Phys. Rev. B **35**, 1902 (1987).
[10] B. Perrin and F. T. Hedgcock, Can. J. Phys. **60**, 1783 (1982).

Translated by S. Chomet

Characterization of macrodefects in pure silcon carbide films using X-ray topography and Raman scattering

A. M. Danishevskii, A. S. Tregubova, and A. A. Lebedev

A. F. Ioffe Physicotechnical Insititute, Russian Academy of Sciences, 194021 St. Petersburg. Russia
(Submitted September 2, 1996; accepted for publication February 13, 1997)
Fiz. Tekh. Poluprovodn. **31**, 1192–1197 (October 1997)

Raman and X-ray topographic measurements were carried out on epitaxial films of silicon carbide grown at Cree Research Inc. by vapor-phase epitaxy on bulk 6*H*-SiC substrates. The objective was to identify ranges of the Raman spectrum of 6*H*-SiC that were particularly sensitive to macrostructural defects (dislocations, inclusions, etc.) in these films, and to determine what conclusions could be drawn about the properties of the corresponding portions of the films. © *1997 American Institute of Physics.* [S1063-7826(97)01310-0]

Single-crystal films of *n*-type silcon carbide grown by Cree Research Inc. on bulk 6*H*-SiC crystals 30 mm in diameter are at present practically the only product of this kind available commercially on the world market. They have a relatively low free-carrier concentration $N_d - N_a \simeq 10^{14} - 10^{16}$ cm^{-3} and can be used in a variety of electronic devices such as high-voltage diodes, MOSFETs, and other devices. However, the structural perfection of these films is still inadequate, and this is reflected among other things in the relatively low breakdown voltage of the diodes employing these films,[1)] in the dependence of this parameter on the area of the $p-n$ junction, and in its significant variation over the area of the film. In view of the foregoing, we have carried out a comprehensive study of structural defects in the crystal lattice of these films, and of the reasons for them.

The structural properties of the above SiC films were investigated by X-ray topography in Bragg reflection geometry. The topograms were recorded in symmetric reflections such as (000.12), (000.18), and asymmetric reflections such as (101.10) in Cu$K\alpha$ radiation. This corresponded to diffraction images at different depths, defined by the absorption of the X-rays. Thus, topograms obtained in (101.10) reflections contained information about defects in a layer of ~ 15 μm, which approximately corresponds to the film thickness in our film samples. Figures 1–3 show topograms obtained for three samples, on which X-ray and Raman measurements were performed.

These topograms enabled us to establish that the epitaxial layers contained fine structures with dislocation densities of $N_D \simeq 10^2 - 10^5$ cm^{-2} in the basal plain. Many of the observed dislocations were found to emerge on the surface. The samples contained particle inclusions of different size and shape, surrounded by local microstresses and higher dislocation densities ($N_D > 10^5$ cm^{-2}). We have shown that the formation of the dislocation structure in the film and the distribution of defects over the sample area are due to structural imperfections in the substrates on which the films were grown.

The Raman spectra of the SiC crystals of different polytypes were investigated[1–4] in a number of publications. Studies of silcon carbide films can yield a variety of data silicon on the crystal symmetry (polytype) of the films and on their structural defects, as well as inclusions of other chemical elements. Careful light-scattering measurements were therefore performed in spectral regions in which different phonon branches of SiC were active on different portions of the samples.

1. EXPERIMENTAL METHOD

The scattered spectra were examined with the DFS-52 spectrometer and the FU-79 photomultiplier working as a photon counter. The excitation source was the 5145–Å line from an argon laser.[2)] Since both the film and the 6*H*-SiC substrate are transparent to this radiation, we used glancing-incidence geometry (angle of incidence 75–80°) with the electric vector polarized in the plane perpendicular to the plane of incidence. Less than 10% of the incident radiation in this case passes through the film, because most of it is reflected and because scattering occurs largely in the surface layer of the film

The photon spectrum of hexagonal SiC polytypes contains a large number of bands, but some of them are relatively weak and were not used in this investigation. We shall now enumerate and characterize segments of the Raman spectrum that were investigated in some detail in the above films.

1. The frequency of the acoustic phonon with symmetry E_2 varies significantly (by tens of cm^{-1}) from one polytype to another. It can therefore be concluded that this branch of the vibrational spectrum is associated with the Si and C layer packing structure in the SiC lattice. The spectrum recorded in the neighborhood of the above phonon frequency yields information on the film polytype and also on structural defects at the point at which the spectrum was recorded. For 6*H*-SiC, the maximum of this band should lie near 149 cm^{-1}.

2. The TO and LO branches in all the hexagonal and rhombohedral SiC polytypes show practically no variation with energy among the polytypes. The TO branch splits into the bands at 768 ± 2 cm^{-1} and 790 ± 2 cm^{-1}, whereas the LO branch frequency is $970-971$ cm^{-1}. The TO phonon of the cubic phase has a frequency of 796 ± 2 cm^{-1}, whereas the corresponding figure for the LO phonon is 972 ± 2 cm^{-1}. The appearance next to the TO-phonon band (790 cm^{-1}) of

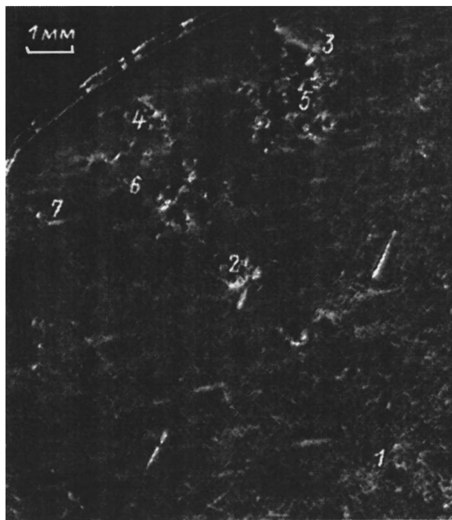

FIG. 1. X-ray topogram of the E0464-11 sample, (101.10) reflection. Cu$K\alpha$ radiation. Numbers identify portions of the film with different dislocation densities N_D.

the hexagonal crystal of the additional band at 796−798 cm^{-1} in our geometry shows that there were inclusions of cubic SiC at this point in the film.

Raman scattering experiments with nanoporous SiC layers deposited on crystals and films of 6*H*-SiC (Ref. 5) have shown that the shape and amplitude of the LO-phonon band is much more sensitive to defects in the SiC lattice than the TO-phonon band. It may therefore be assumed that, in many cases, information about structure defects can be extracted from the spread in the ratio $A_{\mathrm{LO}}/A_{\mathrm{TO}}$ of these bands, measured at different points on the sample (of course, the same light beam configuration and polarization relative to the crystal axes must be preserved in all cases).

3. When vapor-phase epitaxy (CVD) is used, the SiC films are often produced when there is a considerable excess

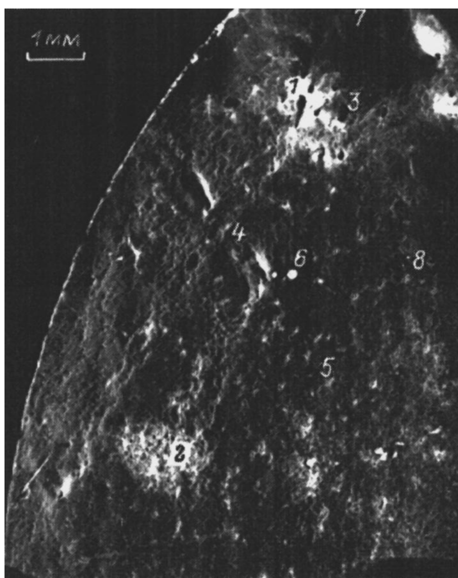

FIG. 2. X-ray topogram of the B0853-7 sample, (101.10) reflection. Cu$K\alpha$ radiation. Numbers identify portions of the film with different dislocation densities N_D.

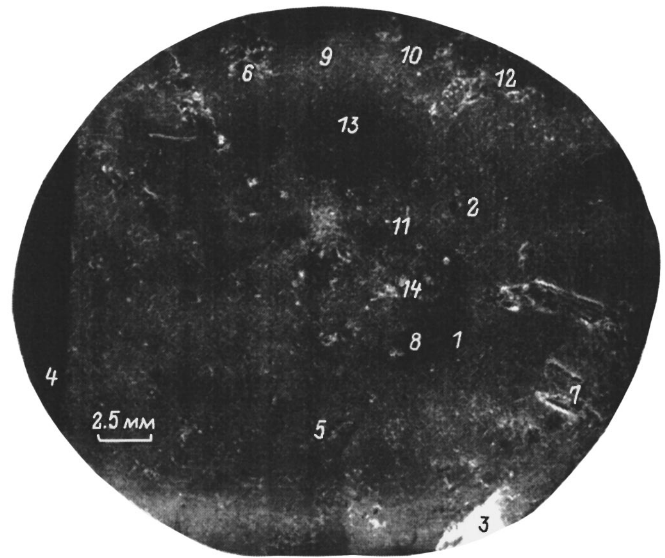

FIG. 3. X-ray topogram of the E0464-14 sample, (101.10) reflection. Cu$K\alpha$ radiation. Numbers identify portions of the film with different dislocation densities N_D.

of silcon in the vapor phase. It follows that in the crystalline state these films can contain excess silcon in the form of fine pure-silicon clusters, or the silcon atoms form some excess Si–Si bonds while being bonded to carbon at the same time. In the former case one observes the 522 to 524 cm^{-1} mode, whereas in the latter there are weak bands with frequencies of 531, 536, and 542 cm^{-1} (Ref. 6). When the dimensions of the silicon nanocrystals are less than 20−30 nm, the silcon band frequency can be slightly lower (512−514 cm^{-1}) and, at the same time, it is usually inhomogeneously broadened in nanocrystalline and porous sillicon. We note that the same part of the spectrum suggests the presence of 6*H*-SiC lattice vibrations with A_1 symmetry (504 and 508 cm^{-1}), and the Si–Si modes are seen against this background.

4. The surplus carbon in SiC can be in diamond-like (sp^3) or graphite-like (sp^2) configurations. In the first case, the Raman spectrum contains a band with a maximum at 1330−1335 cm^{-1} whereas in the second case the maximum is at 1570−1580 cm^{-1} and occasionally at 1350 cm^{-1}. Other bands are observed in the range 1500−1600 cm^{-1} (Ref. 6) and are attributed to rings of carbon bonds.

We note that the same region of the Raman spectrum of SiC contains two-phonon bands of SiC (1518, 1533, 1543, 1568, and 1616 cm^{-1}), which complicates identification based on Raman spectra of small clusters of carbon that, in principle, can be present in the film. On the other hand, the intensity of bands in the two-phonon spectrum is a measure of the structural imperfection of the SiC lattice and, in this sense, the spectrum can be a useful source of information.

2. EXPERIMENTAL RESULTS

The Raman spectroscopy was largely confined to detect containing regions that are readily identified on X-ray topograms. In particular, we wanted to identify the part of the Raman spectrum that was most sensitive to the above structure effects. On the other hand, it was interesting to establish

the dislocation density for which distortions of local lattice symmetry lead to significant deformation of the phonon spectrum of the crystal.

Figure 4 shows the Raman spectra in the range 120−180 cm^{-1} recorded at different points on the E0464-11 and E0464-14 films. The planes of polarization of the incident and scattered radiation were orthogonal in this case. There is a well-defined peak in Fig. 4a at 150 cm^{-1} and a small 'shoulder' near 142−145 cm^{-1}. In Fig. 4b, this peak falls to the level of the 'shoulder', suggesting the onset of local structural disorder. In Fig. 4c, the above band is absent altogether, and in Fig. 4d the spectrum contains three well-defined bands: 138.5, 148, and 166 cm^{-1}. These results suggest a significant distortion of the lattice at the above points. Figure 4e shows for comparison the spectrum recorded at a point with relatively low dislocation density ($N_D < 10^2$ cm^{-2}).

The spectra near the TO- and LO-phonon frequencies were investigated from the standpoint of (1) detection of the cubic phase and (2) the effect of structure defects on the spectra. Cubic phase inclusions were found to be relatively unimportant, although they were noticeable at some points on the samples. As noted above, structure defects have a greater effect on the amplitude and shape of the LO-phonon band. Taking the foregoing as our starting point, we recorded the Raman spectra in this range and determined the amplitude ratio A_{LO}/A_{TO} and the width of the LO-phonon band $\Delta h\nu_{LO}$ (see Table I). At point *I* on sample B0853-7 with dislocation density $N_D > 10^6$ cm^{-2}, the considerable broadening of the LO-phonon band corresponds to an appreciable reduction in the ratio A_{LO}/A_{TO}. At other points, with lower dislocation density, the ratio is nearer to 0.56. As can be seen, there is a clear spread in the values (in some cases, the values are greater than in the case of an undamaged part of the sample; this probably requires a special investigation).[3)]

It is clear from the data shown in Table I that there is only partial correlation between results obtained from the Raman spectra of LO and TO phonons, on the one hand, and the distribution of structure defects on the X-ray patterns. Raman spectra of the above samples were also used to detect the presence of excess Si in the 6*H*-SiC. Bands corresponding to Si inclusions were seen in a number of these spectra. Their positions, amplitudes and widths were different at different points on the samples. In some cases, there were even two or three bands that seemed likely to be associated with Si–Si vibrations.

Figure 5 shows the spectra recorded for the E0464-14 sample. Trace (a) has three bands (521, 525, and 532 cm^{-1}) that are clearly due to excess Si in different structure configurations. The 510-cm^{-1} band is due to SiC lattice vibrations. The origin of the 485-cm^{-1} band is unclear.

On trace (b), the crystalline Si line predominates over all other modes. There are also SiC phonon bands: 504 and 507.5 cm^{-1}. The strongest band in the structure of trace (c) has its peak at 505.5 cm^{-1}. Excess Si appears to be absent at this point on the sample. We note that the peaks due to SiC lattice vibrations that were recorded in this spectral range at different points on the sample are shifted slightly relative to one another. One of these peaks was found to predominate in different spectra, probably because of the lattice defects associated with dislocation clusters.

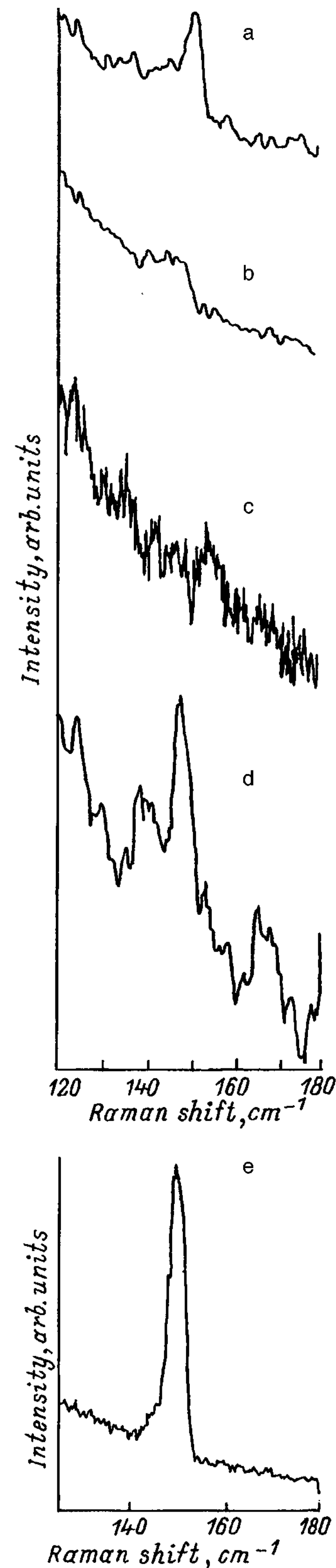

FIG. 4. Raman scattering spectra. The polarizations of the incident and scattered radiations are orthogonal. (a,b,e) — E0464-11 sample, points at which measurements were made: a — 1, b — 3, e — low dislocation density. (c,d) — sample E0464-14, d — point 7 (Fig. 3).

Figure 6 shows the region of the two-phonon Raman

TABLE I.

Sample	$N_d - N_a$, cm^{-2}	Point number	$\Delta\hbar\nu_{LO}$, cm^{-1}	A_{TO}/A_{TO}	N_D, cm^{-2}
B 0853-7		*8*	6	0.556	$\sim 10^2$
n-layer	$\sim 10^{15}$	*2*	6	0.557	$\sim 10^5$
$d = 15$ μm		*3*	6	0.559	$\sim 10^4$
		1	9.9	0.321	$> 10^6$
E 0464-14,		*5*	6	0.545	$10^2 - 10^3$
n-layer	$(3-4)\times 10^{16}$	*4*	7.6	0.608	$\sim 10^5$
$d = 25$ μm;		*3*	6.5	0.551	$\sim 10^4$
p-layer	$\approx 10^{19}$	*7*	7.8	0.545	$\sim 10^5$
$d = 1$ μm		*12*	7.8	0.495	$> 10^5$
E 0464-11		*3*	6.5	0.615	$\sim 10^5$
n-layer	$(2-3)\times 10^{16}$	*4*	6.0	0.836	$\sim 10^5$
$d = 25$ μm					

Note. d-Layer thickness.

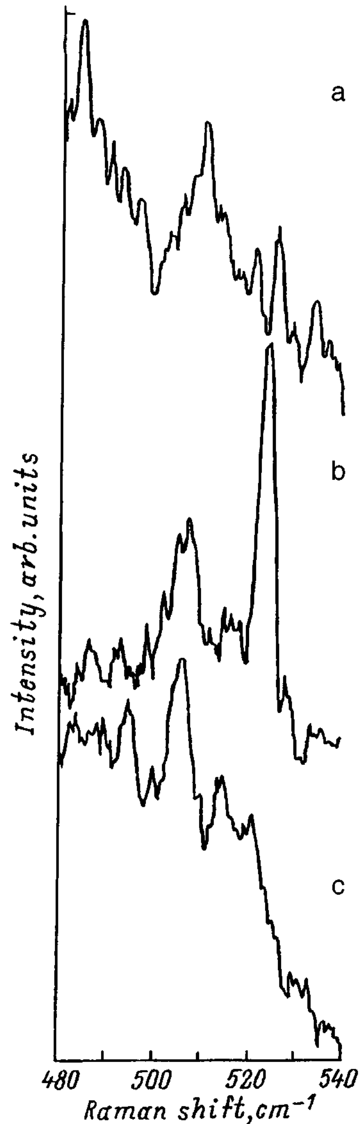

FIG. 5. Raman scattering spectra. The polarizations of the incident and scattered radiations are parallel. (a,b,e) - E0464-14 sample, points at which measurements were made: a — 4, b — 14, c — 12 (Fig. 3).

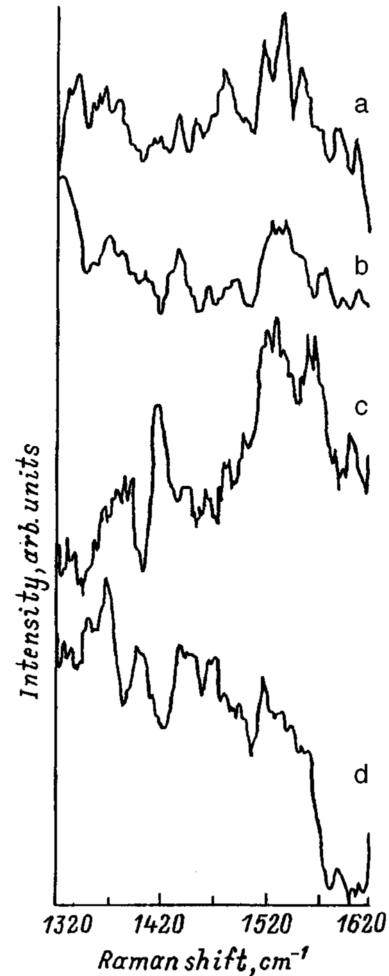

FIG. 6. Raman scattering spectra. a — E0464-11 sample, point 4 (Fig. 1). (b,c,d) — B0853-7 sample, measurement points (Fig. 2): b — 8, c — 7, d — 3.

spectrum in which spectral features associated with carbon inclusions ($1320-1620$ cm^{-1}) could be expected. Trace (a) clearly shows the presence of the two-phonon bands of $6H$-SiC (1380, 1480, 1518, 1533, 1546, and 1568 cm^{-1}). The spectrum also contains two poorly resolved bands (1332 and 1341 cm^{-1}) that are probably due to carbon present at this point in the sample in the sp^3 configuration. The 1590 cm^{-1} peak is usually attributed to carbon in the glassy state. The origin of the 1604-cm^{-1} peak is unclear.

Figure 6 also shows the analogous spectrum (b) recorded for sample B0853-7. The bands of the two-phonon spectrum here partially overlap, forming a broad band around $1515-1560$ cm^{-1}. The peak at 1480 cm^{-1} is weaker than on trace (a). There are also peaks due to carbon in the sp^3 and sp^2 configurations. Two other spectra obtained for the same sample are also reproduced in Fig. 6. Trace (c) clearly shows the bands of the two-phonon spectrum of SiC, with the 1568 cm^{-1} band much stronger than in the preceding spectra. There are no clear indications of the presence of excess Si in this spectrum. Conversely, in spectrum (d), the two-phonon bands are poorly defined. The 1380-cm^{-1} band is shifted and is now at 1370 cm^{-1}. It would appear that the lattice is greatly distorted at this point in the sample. Analo-

gous measurements were performed at other defect-containing points, which are clearly represented in the X-ray patterns.

In summary, we can say that analysis of all these data reveals that there are very considerable variations among the Raman acoustic-phonon and two-phonon spectra recorded for different defect-containing regions with dislocation densities $N_D > 10^{14}$ cm^{-2}. Indeed, Raman spectra can be used as indicators of the presence of macroscopic defects in SiC films. A systematic study of these variations will be necessary before the reasons for them can be specifically established.

We note in conclusion that the SiC films grown at Cree Research Inc., which we have investigated on the basis of Raman scattering, have the symmetry of the $6H$ polytype. The defect-containing regions of these films are often characterized by distortions of lattice symmetry and disturbed interlayer bonding. The acoustic phonon region and the two-phon region of the Raman spectrum of SiC are particularly sensitive to these effects. The behavior of the relatively weak bands at 504 and 508 cm^{-1} can also provide useful information. Small inclusions of cubic SiC were present at some points in the samples that were investigated. Inclusions of excess Si and, in some cases, of carbon were also detected in the films. Our investigation has shown that the structure of the $6H$-SiC films grown by vapor-phase epitaxy on bulk 6 H-SiC substrates is subject to some imperfections and that further efforts will be necessary to optimize the technology used to grow both films and substrates.

We wish to thank V. E. Chelnokov for interest and support.

This research was carried out under an INTAS Grant (No. 93-543) and with the partial support of the University of Arizona, USA.

[1)]The maximum published breakdown voltages of such diodes is 4.5 kV, which, in general, is also much lower than the theoretical limit. In the case of commercially available films, one cannot generally obtain values in excess of 1.00–1.5 kV or often significantly lower values. Moreover, these breakdown voltages refer to structures in which the area of the $p-n$ junction is less than 4×10^{-4} cm^2.

[2)]In order to exclude the laser 'plasma line' which was shifted from the main line by 530 cm^{-1}, the laser beam was first passed through a dispersive system and a final selecting slit.

[3)]The difference between the mean values of A_{LO}/A_{TO} obtained for different samples can be disregarded because the position of the crystal axes relative to the polarization vector of the laser beam is arbitrary in each case. Measurements at different points on a given sample were carried out for the same configuration of the polarization vector relative to the crystal axes in the (0001) plane.

[1] D. W. Feldman, J. H. Parker, W. J. Choyke, and L. Patrick, Phys. Rev. **170**, 698 (1968); Phys. Rev. **173**, 787 (1968).
[2] I. S. Gorban' and V. I. Lugovoi, Zh. Prikl. Spektrosk. XXIV, 333 (1976).
[3] S. Nakashima, Y. Nakakura, and Z. Inoue, J. Phys. Soc. Jpn. **56**, 359 (1987).
[4] S. Nakashima and K. Tahara, Phys. Rev. B **40**, 6339 (1989).
[5] A. M Danishevskii, V. B. Shuman, A. Yu. Rigachev, and P. A. Ivanov, Fiz. Tekh. Poluprovodn. **29**, 2122 (1995) [Semiconductors **29**, 1106 (1995)].
[6] Pham. V. Huong, Diamond and Related Mater., **1**, 33 (1991).

Translated by S. Chomet

Hole boil-off and the magnetoresitance of the semimagnetic semiconductor $Hg_{1-x}Mn_xTe_{1-y}Se_y$

N. K. Lerinman, P. D. Mar'yanchuk,[1)] A. I. Ponomarev, L. D. Sabirzyanova, and N. G. Shelushinina

Institute of Metal Physics, Urals Division, Russian Academy Of Sciences, 620219 Ekaterinburg, Russia
(Submitted July 31, 1996; accepted for publication February 25, 1997)
Fiz. Tekh. Poluprovodn. **31**, 1198–1205 (October 1997)

Galvanomagnetic effects were investigated in gapless and narrow-gap semiconductors of the form $Hg_{1-x}Mn_xTe_{1-y}Se_y$ with $x=0.03-0.11$, $y=0.01-0.10$ $(-150<\varepsilon_g<190)$meV and acceptor concentration $5.4\times10^{16}<N_A<4.3\times10^{18}$ cm^{-3}. In magnetic fields $H=5-50$ kOe and at $T=1.3-4.2$ K, the observed hole concentration $p=1/eR$ was found to increase by a substantial factor (of up to 500). This was accompanied by a fall in the longitudinal (ρ_{zz}) and transverse (ρ_{xx}) magnetoresistivities. The hole ''boil-off'' is assumed to be a consequence of the existence at $H=0$ of a bound magnetic polaron and the delocalization of carriers when these states are destroyed by the external magnetic field. The anomalous ratio of longitudinal-to-transverse resistivities ($\rho_{zz}>\rho_{xx}$), observed at liquid-helium temperatures and in magnetic fields $H>10$ kOe, is explained in terms of the properties of the energy spectrum of the valence band of semimagnetic semiconductors in quantizing magnetic fields. © *1997 American Institute of Physics.* [S1063-7826(97)01410-5]

1. INTRODUCTION

In the semimagnetic semiconductors $Hg_{1-x}Mn_xTe$ and $Hg_{1-x}Mn_xSe$, the exchange interaction between free electrons in the Γ_6 and Γ_8 bands, on the one hand, and localized electrons in the unfilled d shell of the Mn^{2+} ion ($s-d$ and $p-d$ intearctions, respectively), on the other hand, leads to a significant rearrangement in the energy spectrum of carriers in a magnetic field. In a previous paper[1] we reported a study of the magnetic and transport properties of the semimagnetic semiconductor $Hg_{1-x}Mn_xTe_{1-y}Se_y$ with p-type conductivity in the Γ_8 valence band. Galvanomagnetic properties clearly display effects due to the $p-d$ exchange interaction, namely, the boil-off of holes in a magnetic field, the associated negative magnetoresistivity effect, and the anomalous ratio of longitudinal-to-transverse magnetoresistivities. In this paper, we report a more detailed examination of these phenomena for an extended set of samples.

2. EXPERIMENTAL RESULTS

We have investigated the longitudinal (ρ_{zz}) and transverse (ρ_{xx}) magnetoresistivities and the Hall coefficient R of gapless ($x<0.07$) and narrow-gap ($x>0.07$) crystals of the little-studied semimagnetic semiconductor $Hg_{1-x}Mn_xTe_{1-y}Se_y$ in a wide range of compositions ($0.03<x<0.11$, $y=0.01-0.10$) at $T=1.3-300$ K and magnetic fields H up to 60 kOe. The sample parameters are listed in Table I. The Mn concentration was determined by measuring the magnetic susceptibility (see Ref. 1). The gap width ε_g and the Mn concentration of the narrow-gap crystals were also estimated from the intrinsic electron concentration at $T=300$ K. The acceptor-donor concentration difference N_A-N_D was determined from values of R in a strong magnetic field ($H=50$ kOe) at $T=77$ K. All the samples under investigation had p-type conductivities. Table I also lists typical hole mobilities μ_p at $T=1.4$ K in magnetic fields $H\cong10$ kOe, for which $R(H)$ reaches its maximum value.

In the nonmagnetic semiconductor $Hg_{1-x}Gd_xTe$, which has the analogous valence-band structure, the overlap of hole wave functions at the neighboring acceptors leads, as we know, to the dielectric-metal transition (Mott transition) for $N_A=N_M=2\times10^{17}$ cm^{-3} (Ref. 2). The samples which we have investigated can be divided into three groups according to the value of N_M:

Group I: $N_A<N_M$ samples 1–3 ($N_A<2\times10^{17}$ cm^{-3})

Group II: $N_A>N_M$ samples 4–9 ($N_A\sim10^{18}$ cm^{-3})

Group III: $N_A\gg N_M$ samples 10–12 ($N_A>3\times10^{18}$ cm^{-3})

Figures 1 and 2 show for a few temperatures the longitudinal ($\Delta\rho_{zz}$) and transverse ($\Delta\rho_{zz}$) magnetoresistivities and the Hall coefficient R plotted as functions of the magnetic field H for sample I (see Table I) with the minimum impurity concentration difference $N_A-N_D=5.4\times10^{16}$ cm^{-3}. The shape of the $R(H)$ curves at liquid-helium temperatures shows that the transport process involves the participation of two types of carrier, namely, electrons and holes. The electron contribution to $R(H)$, observed in low magnetic fields in p-type semiconductors with gap width $\varepsilon_g>100$ meV for $T<10$ K cannot be due to band carriers. This type of anomalous electron contribution has frequently been seen in $Hg_{1-x}Cd_xTe$ with $x\approx0.2$ (Ref. 2). By analogy with $Hg_{1-x}Cd_xTe$, we may assume that the samples that we examined contained a continuous n-type cluster which lies along the dislocation boundaries and which shunts conduction by the p-type volume at low temperatures in low magnetic fields.[3] The rise in hole concentration with increasing field (see later) and the Lorentz spiralling of the electron trajectories [electron mobility $\mu_n\approx10^4-10^5$ cm^2/(V·s)] lead to a change in the sign of R in $H\approx10$ kOe. At $H>10$ kOe, for which transport processes are wholly determined by

 1063-7826/97/101030-07$10.00 © 1997 American Institute of Physics

TABLE I. Parameters of the test samples $Hg_{1-x}Mn_xTe_{1-y}Se_y$.

Groups	Samples	y	x	ε_g, meV	(N_A-N_D), 10^{17} cm^{-3}	μ_p, cm^2/(V·s)
I	1	0.01	0.095	165	0.54	4500
	2	0.05	0.11	190	1.3	2300
	3	0.10	0.09	150	1.6	20.50
II	4	0.01	0.04	−150	13	800
	5	0.01	0.04	−120	9.3	1500
	6	0.01	0.05	−100	10	3100
	7	0.05	0.08	110	10	4400
	8	0.01	0.08	110	13	3800
	9	0.01	0.09	150	13	3600
III	10	0.10			31	75
	11	0.01	<0.07	<0	41	120
	12	0.10			43	50

holes (Figs. 1 and 2), there is a sharp reduction in the Hall coefficient and in resistivity: $R_{\max}/R(50\ \text{kOe})\approx 200$ and $\rho_{\max}/\rho(50\ \text{kOe})\approx 10^3$ at $T=1.3$ K.

Figures 3 and 4 show the functions $\Delta\rho_{zz}(H)$, $\Delta\rho_{xx}(H)$, and $R(H)$ for the narrow-gap sample 7 with intermediate impurity concentration difference $N_A-N_D=10^{18}$ cm^{-3}. The overall shape of these graphs is similar to that obtained for sample 1. The difference between them lies exclusively in the reduction in the Hall coefficient and resistivity ρ for $H>10$ kOe. For sample 7, they are much lower: $R_{\max}/R(50\ \text{kOe})\approx 6$, $\rho_{\max}/\rho(50\ \text{kOe})\approx 4$ at $T=1.3$ K. It is clear from Figs. 2 and 4 that at temperatures of $10-12$ K the Hall coefficient R is positive and practically independent of H. When we analyze the functions $\Delta\rho_{xx}(H))$ and $\Delta\rho_{zz}(H)$ for the samples under investigation (see Figs. 1 and 3), we have to bear in mind the unusual ratio of $\Delta\rho_{zz}$ to $\Delta\rho_{xx}$ in the region of p-type conductivity: ρ_{zz} becomes significantly greater than ρ_{xx} for $T<4.2$ K and $H\geqslant 5$ kOe.

For highly-doped crystals with $N_A-N_D\approx 3\times 10^{18}-4\times 10^{18}$ cm^{-3}, the behavior of the transport coefficients at low temperatures is entirely determined by holes, and varies little with increasing magnetic field.

3. DISCUSSION OF EXPERIMENTAL RESULTS

a. The hole boil-off effect. The substantial reduction in $R(H)$ for $H>5-10$ kOe is naturally related to the increase in the concentration of valence holes with increasing magnetic field. The hole boil-off, which is the inverse of the

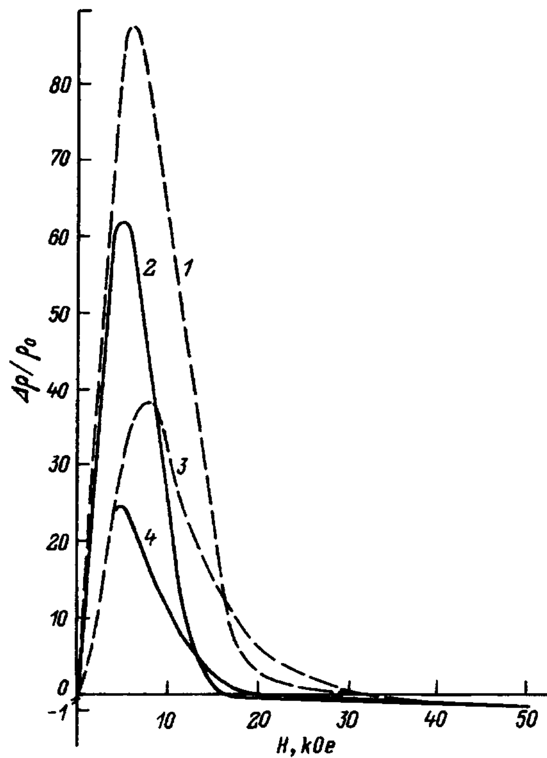

FIG. 1. Longitudinal (*1,3*) and transverse (*2,4*) magnetoresistivities $\Delta\rho/\rho_0$ as functions of the magnetic field H for sample 1 (see Table I) at the following temperatures (in K): *1,2*—1.6, *3,4*—4.2.

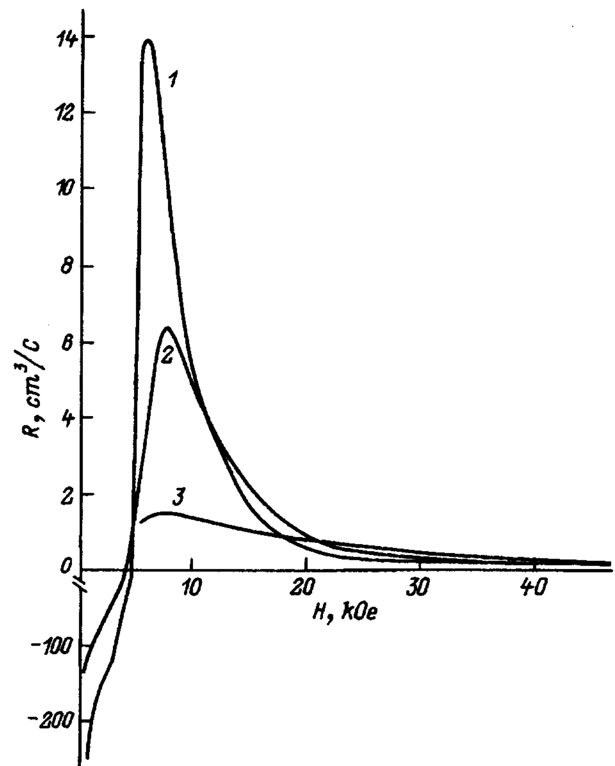

FIG. 2. Hall coefficient plotted as a function of the magnetic field in sample 1 at the following temperatures (in K): *1*—1.6, *2*—4.2, *3*—12.

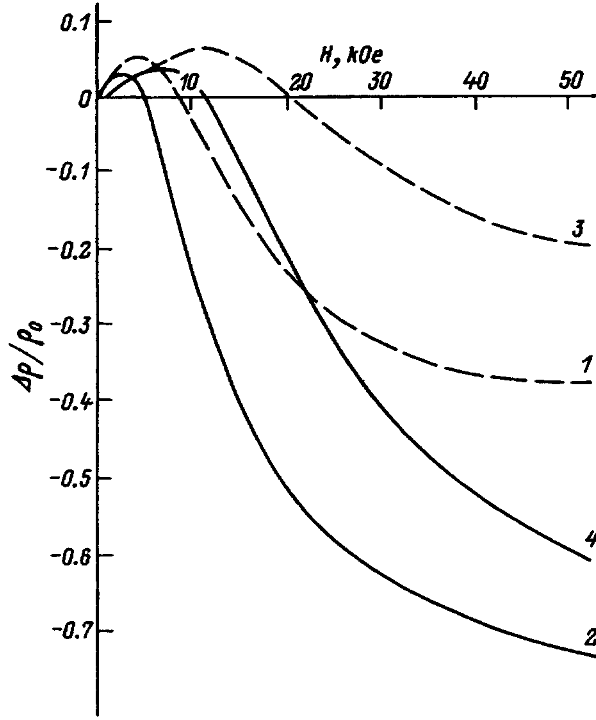

FIG. 3. Longitudinal (*1,3*) and transverse (*2,4*) magnetoresistivities $\Delta\rho/\rho_0$ as functions of the magnetic field H for sample 7 at the following temperatures (in K): *1,2*—1.3, *3,4*—4.2.

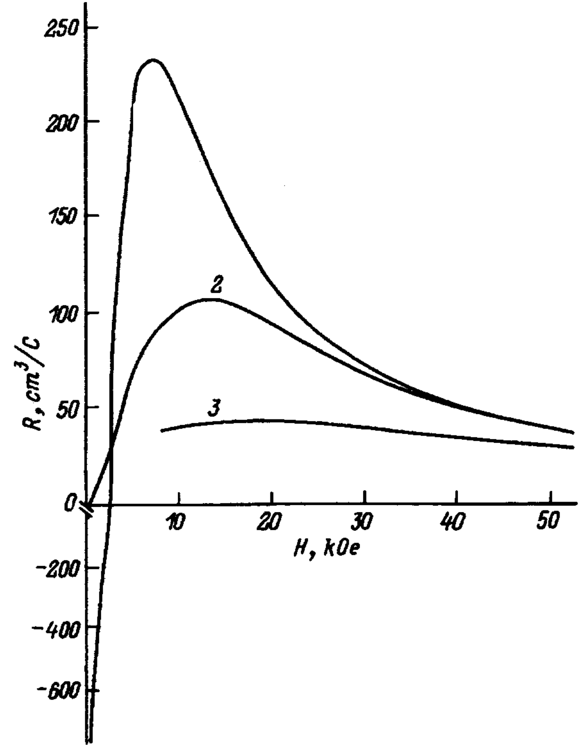

FIG. 4. Hall coefficient as a function of the magnetic field in sample 7 at the following temperatures (in K): *1*—1.3, *2*—4.2, *3*—10.

freeze-out, had previously been observed in narrow-gap[4] and gapless[5,6] crystals of p-type HgMnTe and is explained in terms of a reduction in the acceptor activation energy[7] or by the destruction of the states of the bound magnetic polaron[8] in a magnetic field.

Figure 5 shows $p(H)$ for samples 1 and 2 at $T=1.6$ K. It is clear that, up to $H\approx 20$ kOe, the observed dependence can be described by the expression $p(H)\sim\exp[E_A(H)/kT]$, where

$$E_A(H)=E_A^0-\gamma H \tag{1}$$

with $E_A^0=1.5$ meV, $\gamma=2.9\times10^{-2}$ meV/kOe for sample 1 and $E_A^0=2$ meV, $\gamma=4.8\times10^{-2}$ meV/kOe for sample 2. Extrapolating the linear function to $H=0$, we obtain an estimate for the hole concentration in the absence of the magnetic field: at $T=1.6$ K, we found that $p(H=0)=1.1\times10^{14}$ cm^{-3} for sample 1 and $p(H=0)=3.8\times10^{13}$ cm^{-3} for sample 2. The same figure shows $\sigma_{zz}=1/\rho_{zz}$ and $\sigma_\perp=1/\rho_{xx}$ as functions of H for sample 2 at $T=1.6$ K (the results for sample 1 are similar). It is clear that the plots of $\sigma_{zz}(H)$ and $\sigma_\perp(H)$ also have activation-type portions for $H<20$ kOe. Comparison of $p(H)$ with $\sigma_{zz}(H)$ and $\sigma_\perp(H)$ leads to the conclusion that the observed rapid fall in resistance for $H>5$ kOe at liquid-helium temperatures (Figs. 1 and 3) is largely due to the hole boil-off.

We now compare (1) with the theoretical result that predicts a reduction in the activation energy in a magnetic field and is valid for wide-gap semiconductors:[9]

$$E_A=E_A^0-\alpha B, \tag{2}$$

where

$$B=-(1/6)N_0\beta\langle S_z\rangle \tag{3}$$

is the exchange term added to the hole energy in the Γ_8 band. The quantity $\langle S_z\rangle$ is the mean value of the z-component of the spin of the Mn ion ($z\|\mathbf{H}$) and $N_0\beta$ is the exchange integral. In low enough magntic fields,

$$\langle S_z\rangle=S_0\,\frac{(S+1)g_{\mathrm{Mn}}\mu_B H}{3k(T+T_0)}, \tag{4}$$

where $S=5/2$, $g_{\mathrm{Mn}}=2$, μ_B is the Bohr magneton, S_0 and T_0 are the effective parameters describing the exchange interaction between the Mn spins, and γ is given by

$$\gamma_{ih}=\alpha\,\frac{1}{6}\,xN_0\beta\,\frac{S_0(S+1)g_{\mathrm{Mn}}\mu_B}{3k(T+T_0)}. \tag{5}$$

Using $N_0\beta=1.4$ eV, $S_0=1.02$, $T_0=9.9$ K (the same as for $\mathrm{Hg}_{1-x}\mathrm{Mn}_x\mathrm{Te}$ with $x=0.1$; Ref. 10), and $T=1.6$ K, we find that $\gamma_{th}=0.25\alpha$ meV/kOe. Comparison of γ_{th} with the measured values of γ yields $\alpha=0.12-0.2$, which is significantly lower than the theoretical value $\alpha=0.75$ for $\mathrm{Hg}_{1-x}\mathrm{Mn}_x\mathrm{Te}$ with $x\approx0.1$ (Ref. 9).

It is clear that the isolated acceptor model does lead to a satisfactory description of the hole boil-off. We also note that the value of the activation energy found for $H=0$, namely, $E_A^0=1.5-2$ meV is substantially lower than the theoretical estimate of the binding energy of the isolated acceptor, $E_A^0=6$ meV (Ref. 9). Values of E_A^0 close to this figure were actually observed for HgCdTe, but only for $N_A<10^{16}$ cm^{-3} (Ref. 11). The weak doping condition $N_A\ll N_M$ is not satisfied by our samples, not even for samples 1–3 with the lowest impurity concentrations. For

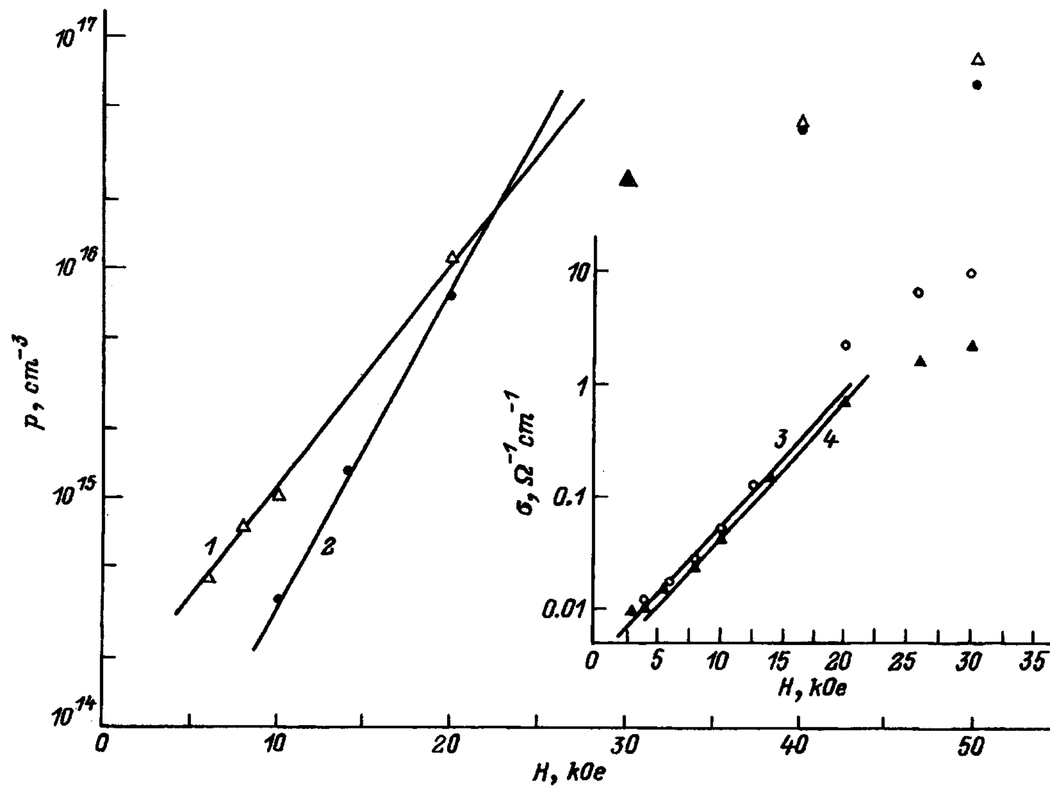

FIG. 5. Hall concentration p as a function of the magnetic field H at $T=1.6$ K for samples 1 and 2. The inset shows the transverse (3) and longitudinal (4) conductivities $\sigma_{\perp}=1/\rho_{xx}$ (3) and $\sigma_{zz}=1/\rho_{zz}$ as functions of the magnetic field for sample 2 at $T=1.6$ K.

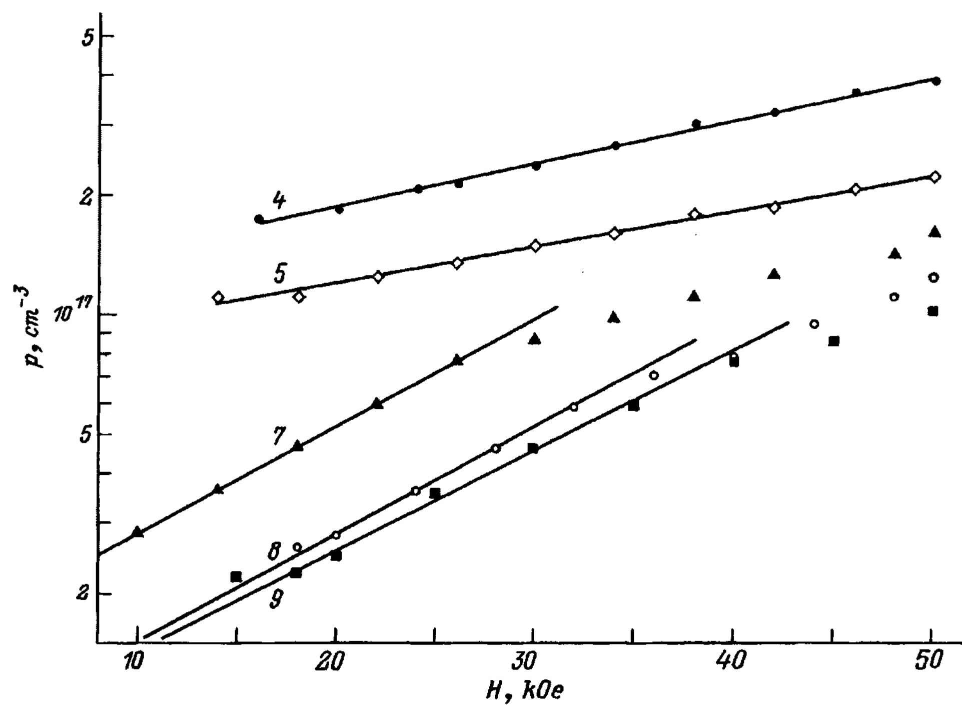

FIG. 6. Hole concentration p as a function of the magnetic field H at $T=1.4-1.7$ K. The labels on the curves correspond to the sample numbers (see Table I).

intermediate dopant concentrations, $N_A \lesssim N_M$, the overlap of the wave functions of neighboring acceptors cannot be neglected and the observed activation energy can be substantially lower than E_A^0.

Figure 6 shows $p(H)$ for $H>10$ kOe at $T=1.4-1.7$ K for samples 4–9 with $N_A \approx 10^{18}$ cm^{-3}. It is clear that these samples also display an appreciable dependence of hole concentration on H, although the dependence is weaker than for samples 1 and 2. For $N_A > N_M$, when the bound state of a hole and an acceptor, maintained by the Coulomb interaction, is absent, the rise in $p(H)$ cannot be explained by a reduction in the initial activation energy. It therefore seems necessary to use the idea of a bound magnetic polaron,[5] which is understood to be the bound state of a hole in a semimagnetic semiconductor, formed as result of the $p-d$ exchange interaction between hole on an acceptor and the surrounding Mn ion spins.[8] The addition of the magnetic (exchange) interaction to the electrostatic interaction can establish the necessary conditions for the localization of carriers even for $N_A > N_M$. Polaron effects may play a significant (and even the determining) role in the case of samples with $M_A < NM$ (samples 1–3). Actually, estimates of the polaron contribution to the binding energy of an isolated acceptor, based on the Dielt-Spalek theory[8] for our samples with $x \approx 0.1$ at $T=1.6$ K give $\Delta E_A \approx 4$ meV, which is comparable with the Coulomb binding energy of the isolated acceptor, $E_A^0 = 6$ meV.

The $p-d$ exchange ensures that the polarization of the Mn spin cloud (within the Bohr radius), $\langle S_z \rangle_{\rm loc}$, is nonzero even for $H=0$, where the long-range order is absent throughout the spin subsystem $(\rangle S_z \langle =0)$. All the Mn spins become polarized when the external magnetic field is turned on, and this leads to an increase in $\langle S_z \rangle$ and a reduction in the difference $\langle S_z \rangle - \langle S_z \rangle_{\rm loc}$, i.e., a gradual breakup of the states of the bound magnetic polaron. The carrier delocalization process during the breakup of the polaron states in the magnetic field finally leads to the hole boil-off.

In samples with $N_A > 3 \times 10^{18}$ cm^{-3} (samples 10–12), the overlap of wave functions on neighboring acceptors is considerable enough to ensure that localization due to exchange defects does not occur and the hole concentration is independent of both the magnetic field and temperature.

Thus, measurements on samples of the semimagnetic conductor p-HgMnTeSe in a broad range of acceptor concentrations N_A have shown that the increase in the concentration p during hole boil-off in a magnetic field becomes more significant with decreasing ratio of the concentration of acceptors to the concentrations N_M for the Mott transition in the nonmagnetic semiconductor. This emperical result is shown in Table II which also includes our data for eight gapless samples of HgMnTe with $M_A = 10^{17} - 2 \times 10^{17}$ cm^{-3} (Ref. 6).

If we assume that when p is independent of H and T, there is complete delocalization of holes, we may assume that the dielectric-metal transition occurs in the semimagnetic semiconductor that we have investigated for $N_A = N_M^* > 3 \times 10^{18}$ cm^{-3}. The effect of the exchange interaction between holes and the spin subsystem of the Mn^{2+} ions leads to the enhancement of the localization effects and

TABLE II. Hole boil-off in the range $10 \leq H \leq 50$ kOe for different sample groups.

Sample	x	$(N_A - N_D)$, 10^{17} cm^{-3}	$R_{\rm max}/R$ (50 kOe)
$Hg_{1-x}Mn_xTe_{1-y}Se_y$	$0.09-0.11$	$0.5-1.5$	$200-500$
$Hg_{1-x}Mn_xTe$	$0.05-0.07$	$1-2$	$10-20$
$Hg_{1-x}Mn_xTe_{1-y}Se_y$	$0.03-0.095$	$9-13$	$3-5$
$Hg_{1-x}Mn_xTe_{1-y}Se_y$	<0.07	$30-40$	1

Note: The data in the last column were obtained at $T=1.4-1.7$ K; $R_{\rm max}$ is the maximum value of $R(H)$ in the region of the hole conductivity at $H \simeq 10$ kOe.

to an increase by an order of magnitude in the concentration of the Mott transition as compared with a nonmagnetic semiconductor. We also note that the observed significant difference between the values of $R_{\rm max}/R$(50 kOe) for the HgMnTeSe and HgMnTeSe samples with a similar value $N_A \approx 10^{17}$ cm^{-3} (first and second rows in Table II) is most likely to be due to the natural enhancement of the hole boil-off with increasing x, i.e., with increasing exchange term that must be added to the hole energy.

b. Anomalous anisotropy of magnetoresistivity. We know that in semiconductors with a spherically symmetric band and isotropic scattering, the longitudinal magnetoresistivity is independent of the magnetic field in the classical range of magnetic fields. In the region of quantizing fields, ρ_{zz} depends on H, but for ordinary semiconductors, the ratio ρ_{zz}/ρ_{xx} is always less than one, both for the short-range and the long-range impurity potential.[12] In the semimagnetic semiconductor HgMnTe, the reverse situation is observed in a broad range of magnetic fields, namely, the longitudinal magnetoresistivity becomes greater by a substantial factor than the transverse magnetoresistivity.[4–6] In the $Hg_{1-x}Mn_xTe_{1-y}Se_y$ samples that we have investigated we have found anomalous anisotropy of magnetoresistivity: it is clear from Fig. 7 that for $H>10$ kOe, the resisitivity ρ_{zz} becomes greater than ρ_{xx}, and the ratio ρ_{zz}/ρ_{xx} increases significantly with increasing H and the concentration x of Mn, and also with decreasing temperature, beginning with values of the order of 10.

The exchange $p-d$ interaction in a magnetic field gives rise to the Zeeman splitting of the fourfold degenerate Γ_8 state into subbands with total angular momentum components $J_z = \pm 1/2$ and ± 3.2 (Ref. 13). The position of the top of each of these subbands relative to the top of the Γ_8 band for $H=0$ corresponds to energies $\varepsilon = \pm B$ and $\pm 3B$, where the exchange parameter B is given by (3). Since $\beta > 0$ and, consequently, $B<0$, the uppermost band is the valence band with $J_z = -3/2$, whose dispersion relation near the point Γ is $(\mathbf{H} \| z)$

$$\varepsilon_{-3/2}(k) = -\frac{\hbar^2}{2}\left[\left(\frac{3}{4m_l}+\frac{1}{4m_h}\right)k_\perp^2+\frac{k_z^2}{m_h}\right]-3B, \qquad (6)$$

where m_l and m_h are the masses of light and heavy holes, respectively, and $k_\perp$ is the component of the wave vector at right angles to the magnetic field. Since $m_l < m_h$, the isoenergy surface is an ellipsoid of revolution with its long axis along the magnetic field.

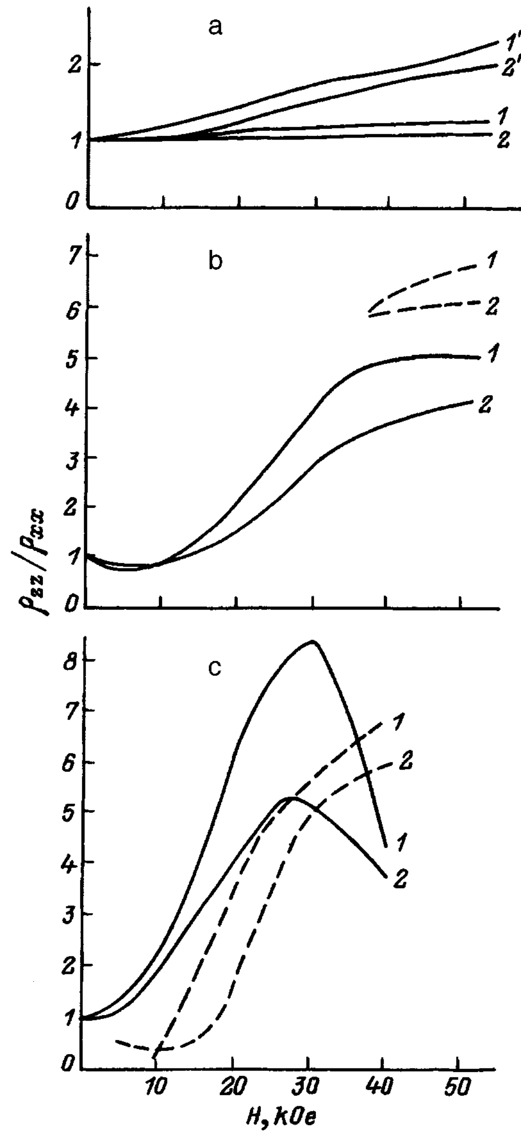

FIG. 7. The ratio ρ_{zz}/ρ_{xx} plotted as a function of the magnetic field H for the following samples (see Table I): a—No. 5 with $x=0.05$ (*1,2*) and No. 7 with $x=0.08(1',2')$ at the following temperatures (in K): *1,1'*—1.4, *2,2'*—4.2,; b—No. 3 with $x=0.09$ at the following temperatures: *1*—1,8, *2*—4.2,; c—No. 1 with $x=0.095$ at the following temperatures (in K): *1*—1.6, *2*—4.2. Dashed curves show ρ_{zz}/ρ_{xx} calculated from (9) using empirical $p(H)$.

In narrow-gap and gapless semimagnetic semiconductors with low effective light-hole mass ($m_l \sim |\varepsilon_g|$), we also must take into account the direct effect of the magnetic field on the orbital motion of carriers (Landau quantization).[14] For the usual parameter values, the highest Landau level in the valance band in the gapless and narrow-gap HgMnTe is the level b_{-1} (in the Pidgeon–Brown notation[15]), whose energy can be written in the following analytic form:

$$\varepsilon_{b-1} = -\frac{\hbar\omega_\perp}{2} + \frac{3}{2}\kappa\hbar\omega_0 - 3B - \frac{\hbar^2 k_z^2}{2m_h}, \tag{7}$$

where $\omega_\perp$ is the cyclotron frequency corresponding to the effective transverse mass $m_\perp \approx (4/3)m_l$, ω_0 is the free-electron cyclotron frequency, and κ is the Lattinger parameter defining the magnitude of the g-factor of carriers in the Γ_8 band in the absence of exchange effects.

It follows from (6) and (7) and from the form of the wave function[14] that the level b_{-1} is the first Landau level detached from the band $\varepsilon_{-3/2}(\mathbf{k})$. It is clear from (7) that the dependence of the energy $\varepsilon_{b-1}(\mathbf{k})$ on the component k_z is parabolic and is determined by the effective heavy-hole mass m_h. Numerical calculations performed for gapless[16] and narrow-gap[17] semiconductors HgMnTe show that the energy gap $\Delta\varepsilon$ between the top of the subband b_{-1} and the top of the nearest subband a_{-1} is of the order of B, i.e., $\Delta\varepsilon \approx B$. The gaps between the tops of the next Landau subbands (a_{-1}, b_1, b_2, etc.) are much smaller and decrease with increasing subband number, remaining of the order of the heavy-hole cyclotron energy $\hbar\omega_h$ ($\omega_h = eH/m_h c$). For typical values of the HgMnTe parameters, $\hbar\omega_h \ll B$ in a broad range of magnetic fields, so that the valence-band spectrum of a semimagnetic semiconductor in quantizing magnetic field is rather unusual: the uppermost level b_{-1} breaks off from the set of levels that lie nearby.

For this type of spectrum, the wave function describing a hole acceptor in a magnetic field is also found to change in an unusual way: the wave-function radius $a_\perp$ in the direction perpendicular to H increases with increasing fields.[7] In the region of hopping over impurities, the increase in the overlap of acceptor wave function with increasing H can lead to a reduction in resistance. Its effect is a maximum for transverse and a minimum for longitudinal magnetoresistances, respectively. This reduction in $\rho_{xx}(H)$ and $\rho_{zz}(H)$ for the anomalous ratio of these two quantitites ($\rho_{zz} > \rho_{xx}$) has been seen experimentally in compensated narrow-gap samples of HgMnTe in the region of hopping conduction.[4,7,18] The authors of Ref. 19 also associate the giant negative magnetoresistance, observed in strong magnetic fields $100 < H < 400$ kOe in HgMnTeSe as the impurity conductivity increases, with increasing overlap of the acceptor wave functions in the magnetic field.

We assume that the conductivity of the samples that we have investigated is due to band carriers. Actually, the hole mobility at 1.4–17 K is relatively high and its order of magnitude is in agreement with estimates based on the Brooks-Herring formula. For the crystals that we have investigated, $100 \lesssim |\varepsilon_g| \lesssim 200$ meV, estimates of the light-hole mass give $0.01m_0 \lesssim m_l \lesssim 0.02m_0$. According to (6), the anisotropic mass in the valence band $\varepsilon_{-3/2}(\mathbf{k})$ is $3m_h/4m_l = 15-30$ for $m_h = 0.4m_0$.

In the case of valence-band conductivity of gapless or narrow-gap semimagnetic semiconductors, the quantum limit is reached for $H = H_q$, when there is only the single Landau level b_{-1} above the Fermi level, i.e., $\varepsilon_F < \Delta\varepsilon$. When $\Delta\varepsilon \approx B$ and $B > \hbar\omega_h$, the quantum limit can be reached if the following condition is satisfied:

$$\varepsilon_F(H) > \hbar\omega_h. \tag{8}$$

We assume that it is precisely this unusual ratio of the kinetic-to-cyclotron energies of holes in the quantum limit that gives rise to the anisotropy in the magnetoresistivity which we have observed.[6] Actually, it was shown in Ref. 12

that, in a degenerate electron gas, the following relation is valid in the quantum limit for scattering by point defects:

$$\frac{\rho_{zz}}{\rho_{xx}}=4\ \frac{\varepsilon_F(H)}{\hbar\omega_c}\ , \tag{9}$$

where $\omega_c=eH/mc$ is the cyclotron frequency,

$$\varepsilon_F(H)=2\pi^4\hbar^2\lambda^4p^2/m \tag{10}$$

and $\lambda=(\cos\ \overline{h}/eH)^{1/2}$ is the magnetic length. We emphasize that, according to Ref. 12, both the cyclotron frequency and the expression given by (10) contain the effective mass m corresponding to the motion of carriers in the z-direction; i.e., in our case $m=m_h$ [see (7)]. As a result, the ratio given by (9) ensures that $\rho_{zz}>\rho_{xx}$ when (8) is taken into account. The enhancement of the effect with increasing x, H and decreasing T is naturally explained by an increase in the magnetization $\langle S_z\rangle$ of the subsystem of ions Mn^{++} and, as a consequence, an increase in the exchange term B that is added to the hole energy.

Using (10) for $\varepsilon_F(H)$ in the quantum limit, we find from (9) that

$$\rho_{zz}/\rho_{xx}=8\pi^4\lambda^6p^2\sim p^2/H^3. \tag{11}$$

The observed behavior of ρ_{zz}/ρ_{xx} with varying H is in qualitative agreement with (11). In particular, it is clear from Figs. 7b and 7c that the ratio ρ_{zz}/ρ_{xx} increases in the region of the rapid rise in the hole concentration, but in the region of the slow variation in $t(H)$ for $H>30-40$ kOe, the value of the ratio ρ_{zz}/ρ_{xx} reaches saturation or may even fall. Another important point is that values of the ratio ρ_{zz}/ρ_{xx} calculated from the simple expression given by (11) are close to the experimentally observed values.

4. CONCLUSIONS

We have used gapless and narrow-gap semiconductors $Hg_{1-x}Mn_xTe_{1-y}Se_y$ with $x=0.03-0.11$ $(-150<\varepsilon_g<190)$ meV and acceptor concentrations $5.4\times10^{16}\leqslant N_A\leqslant4.3\times10^{18}$ cm^{-3} to carry out a detailed investigation of the effects due to influence of the exchange $p-d$ interaction, which are typical for p-type semimagnetic semiconductors. These effects include hole boil-off in a magnetic field and the anomalous anisotropy of magnetoresistivity. We assumed that the rise in hole concentration with increasing H in these samples is a consequence of the existence at $H=0$ of the bound-polaron states and the gradual delocalization of carriers when these states are broken up by the magnetic field. On the other hand, the unusual ratio of the longitudinal-to-transverse magnetoresistivities, $\rho_{zz}>\rho_{xx}$, is essentially a consequence of the anisotropic (relative to the direction of the magnetic field) form of the isoenergy surfaces in the uppermost valence band $\varepsilon_{-3/2}\mathbf{k}$, which is detached by the exchange $p-d$ interaction from the Γ_8 band when Landau quantization in semiconductors with low $|\varepsilon_g|$ is taken into account. The substantial detachment of the uppermost Landau level b_{-1} from the other states in the valence band is due to the small transverse effective mass of the band $\varepsilon_{-3/2}(\mathbf{k})$ and the large value of the term B that is added to the energy on the Γ_8 band.

It is important to note that, within the framework of the model involving the bound magnetic polaron, the increase in hole concentration in the magnetic field occurs precisely because of the detachment (and upward shift in energy) of the band b_{-1}. On the other hand, the anomalous ratio of longitudinal-to-transverse magnetoresistivities is observed only in the quantum limit, i.e., when the conductivity is due to carriers in the band b_{-1}. The observed hole boil-off and anomalous anisotropy of magnetoresistivity are closely interconnected. They have a common cause, namely, the unusual form of the spectrum of Landau levels in the semimagnetic semiconductors that we have investigated.

[1)]Chernovtsy State University, 274012 Chernovtsy, Ukraine

[1] K. R. Krylov, N. K. Lerinman, L. D. Sabirzyanova, N. G. Shelushinina, N. P. Gavaleshko, and P. D. Mar'yanchuk, Fiz. Tekh. Poluprovodn. **28**, 1382 (1994) [Semiconductors **28**, 779 (1994)].
[2] I. M. Tsidil'kovskii, G. I. Harus, and N. G. Shelushinina, Adv. Phys. **34**, 43 (1985).
[3] A. I. Elizarov, V. I. Ivanov-Omskii, A. A. Korniyash, and V. I. Petrikov, Fiz. Tekh. Poluprovodn. **18**, 201 (1984) [Sov. Phys. Semicond. **18**, 125 (1984)].
[4] J. K. Furdyna, J. Vac. Sci. Technol. **27**, 220 (1982).
[5] A. V. Germanenko, L. P. Zverev, V. V. Kruzhaev, G. M. Min'kov, and O. E. Rut, Fiz. Tekh. Poluprovodn. **27**, 1857 (1995).
[6] N. G. Gluzman, A. B. Davydov, K. R. Krylov, N. K. Lerinman, B. B. Ponikarov, A. I. Ponomarov, L. D. Sabirzyanova, I. M. Tsidil'kovskii, N. G. Shelushinina, I. N. Gorbatyuk, and I. M. Rarenko, Fiz. Tekh. Poluprovodn. **20**, 1970 (1986) [Sov. Phys. Semicond. **20**, 1237 (1986)].
[7] J. Mycielski, in *Proceedings International Conference on High Magnetic Fields in Semiconductor Physics*, Grenoble, 1982, p. 431.
[8] T. Dietl and J. Spalek, Phys. Rev. B **28**, 1548 (1983).
[9] J. Mycielski, in *Diluted Magnetic Semiconductors*, ed. by J. K. Furdyna and J. Kossut, Academic Press, N.Y., (1988).
[10] W. Dobrowolski, M. von Ortenberg, A. M. Sandauer, R. R. Galazka, A. Mycielski, and R. Pauthenet, in *Proceedings 4th International Conference on Physics of Narrow Gap Semiconductors*, Linz, 1981, p. 302.
[11] A. V. Germanenko, V. V. Kruzhaev, G. M. Min'kov, and O. E. Rut, Fiz. Tekh. Poluprovodn. **22**, 992 (1988) [Sov. Phys. Semicond. **22**, 626 (1988)].
[12] E. Adams and T. Holstein, J. Phys. Chem. Solids **10**, 254 (1959).
[13] J. A. Gaj, J. Ginter, and R. R. Galazka, Phys. Status Solidi B **89**, 655 (1978).
[14] G. Bastard, C. Rigaux, Y. Guldner, J. Mycielski, and A. A. Mycielski, J. de Phys. **39**, 87 (1978).
[15] C. R. Pidgeon and R. N. Brown, Phys. Rev. **146**, 575 (1966).
[16] M. Dobrowolska, W. Dobrowolski, R. R. Galazka, and J. Kossut, Solid State Commun. **30**, 25 (1979).
[17] L. P. Zverev, V. V. Kruzhaev, G. M. Min'kov, O. E. Rut, N. P. Gavaleshko, and V. M. Frasunik, Fiz. Tverd. Tela **26**, 2943 (1984) [Sov. Phys. Solid State **26**, 1778 (1984)].
[18] J. R. Anderson, W. B. Johnson, and D. R. Stone, J. Vac. Sci. Techn. **A1**, 1761 (1983).
[19] V. A. Kul'bachanskii, P. D. Mar'yanchuk, and I. A. Churilov, Fiz. Tekh. Poluprovodn. **29**, 2007 (1995) [Semiconductors **29**, 1047 (1995)].

Translated by S. Chomet

Effect of infrared laser radiation on the structure and electrophysical properties of undoped single-crystal InAs

S. V. Plyatsko and V. P. Klad'ko

Institute of Semiconductor Physics, National Academy of Sciences, 252650 Kiev, Ukraine
(Submitted May 12, 1996; accepted for publication March 18, 1997)
Fiz. Tekh. Poluprovodn. **31**, 1206–1210 (October 1997)

Substantial changes have been found in the electrical properties and structural parameters of single-crystal InAs after exposure to infrared laser radiation with photon energy less than the energy gap of InAs and power density $W<50$ W/cm^2. The changes are due to the transformation and redistribution of intrinsic point defects in the field of the laser electromagnetic field.
© *1997 American Institute of Physics.* [S1063-7826(97)01510-X]

1. INTRODUCTION

One of the effective ways of controlling a semiconductor is to expose it to laser radiation which modifies its surface properties ($\hbar\omega>E_g$) (Ref. 1) or bulk properties ($\hbar\omega<E_g$) (Ref. 2), depending on the ratio of the laser photon energy $\hbar\omega$ to the energy gap E_g. However, despite many attempts, the mechanism responsible for the interaction between laser radiation and crystals has not yet been fully elucidated. We have therefore undertaken an investigation of laser-stimulated ($\hbar\omega<E_g$) transformation of structural and electrical properties of InAs crystals with a narrow homogeneity interval and a narrow energy gap.

2. EXPERIMENTAL METHOD

We used continuous CO_2-laser radiation with $\hbar\omega=0.0018$ eV. The transport coefficients were measured by standard methods and the stoichiometry of the samples was monitored by X-ray diffraction methods, using quasi-forbidden reflections.[3] This method is sensitive to changes in the sample and, if the intensity of the diffracted X-rays can be measured to better than 0.3%, it can be used to monitor changes in composition at the level of 10^{17} cm^{-3}. The change in the integrated intensity ΔR_1 is related to the change in the concentration c_i by

$$\Delta R_i/R_i=k(c_{\mathrm{In}}-c_{\mathrm{As}}), \tag{1}$$

where the constant k depends on the type of reflection and the form of radiation. Calculations show that for $CuK\alpha 1$ radiation and the (222) reflection, the difference $c_{\mathrm{In}}-c_{\mathrm{As}}$ can be detected at the level of 1.2×10^{-4}. The change in the relative volume fraction of the distorted lattice, ρ_0, was determined by measuring the increase in the integrated intensity due to the diffuse component of scattering by distortions in the (333) reflection, using the formula[4]

$$R_{ie}=(1-\rho_0)R_D+\rho_0 R_K, \tag{2}$$

where $R_{ie}R_D, R_K$ are the integrated intensities, respectively, measured and calculated from the dynamic and kinematic models of scattering.

We investigated undoped single-crystal InAs. The samples were cut from a single ingot and were polished and etched in order to remove the surface layer. The crystals had near-stoichiometric composition with a slight tendency toward the excess of As atoms or the metal component, and had p- and n-type conductivity, respectively.

3. RESULTS AND DISCUSSION

Samples cut from a single-crystal bulk plate were found to have different types of conductivity at 77 K. The carrier concentration in n-type samples was practically independent of temperature down to the region of instrinsic conduction. At low temperatures, the degree of concentration was probably determined by electroactive intrinsic defects, lying deep in the conduction band, so that they were not seen in the temperature dependence of the Hall constant R_H or the conductivity σ. Samples of the second type, whose conductivity at 77 K was $\sigma_{77}=0.25\times10^{-1}$ Om^{-1} cm^{-1}, had $R_H(T)$ typical for p-typical samples, i. e., the conduction type is inverted as the temperature is increased ($T=240-250$ K). For n-type conduction, the behavior of the Hall coefficient $R_H(T)$ is the same as in the first case.

The samples were then exposed to the laser radiation ($\hbar\omega=0.118$ eV, $E_g=0.35$ eV, $\hbar\omega<E_g$) . For low power densities ($W1=10$ Wcm^2), the measured concentration of electrons in type-1 samples decreases slightly with exposure time. An increase in the power density to $W_2=20$ W/cm^2 produces an appreciable rise in carrier concentration for a shorter exposure time as compared with W_1. Further exposure under the same conditions leads to a monotonic reduction in electron concentration to below the initial level (Fig. 1). The carrier mobility at $T=77$ K was found to increase during the exposure of the crystals to the laser radiation, and eventually exceeded the initial value by a factor of 2.

X-ray studies suggest that all this is accompanied by a change in the distribution of InAs atoms in the lattice. The integrated intensity R_i at first decreases from its initial value corresponding to a surplus of In atoms. This continues almost down to the stoichiometric value (Fig. 2), but then rises with increasing power density W_2 to a level greater than the initial value. Continuing exposure with $W_2=$const leads to a reduction in R_i below the level corresponding to the stoichiometric value (excess An).

In p-type crystals, the low power density $W_1=15$ W/cm^2 does not induce appreciable changes at room temperature, whereas at 77 K the hole concentration at first increases with time, but then tends to saturate (Fig. 3). As the

 1063-7826/97/101037-04$10.00 © 1997 American Institute of Physics

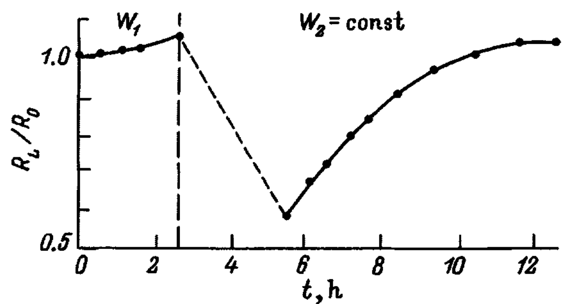

FIG. 1. Ratio of Hall coefficients R_L/R_0 as a function of exposure to the infrared radiation for InAs samples with excess In. R_0 is the Hall coefficient prior to exposure.

power density increases ($W_1 < W_2$), the hole concentration rises rapidly in a time $t = 30$ min, followed by a fall with increasing exposure time. When the power density is then increased to $W_2 = 25$ W/cm^2, the samples undergo a transition to the state with n-type conductivity and anomalously high mobility at 77 K $\mu_{77} = 6 \times 10^5$ cm^2/(V·s) (Fig. 4). However, this is an unstable state and the samples return to the state with p-type conductivity over a period of two days. Continuing illumination with the same power density produces a reduction in the hole concentration and, after a certain inverval of time, the crystals assume the n-type state throughout the temperature range that was investigated. The concentration of carriers with the characteristic temperature dependence is close to the electron concentration in n-type crystals in the original state (prior to illumination). After this transition, the crystal becomes stable and there are no changes in the electron concentration or their mobility as illumination continues with W = const. However, when the power density is stepped up to $W_3 = 40$ V/cm^2, the concen-

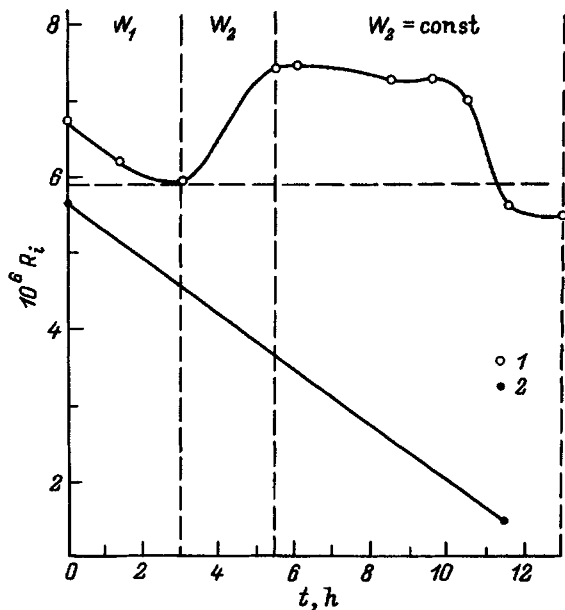

FIG. 2. Integrated reflection intensity R_i of quasi-forbidden (222) reflection as a function of exposure time for InAs samples: *1*—excess In, *2*—excess As.

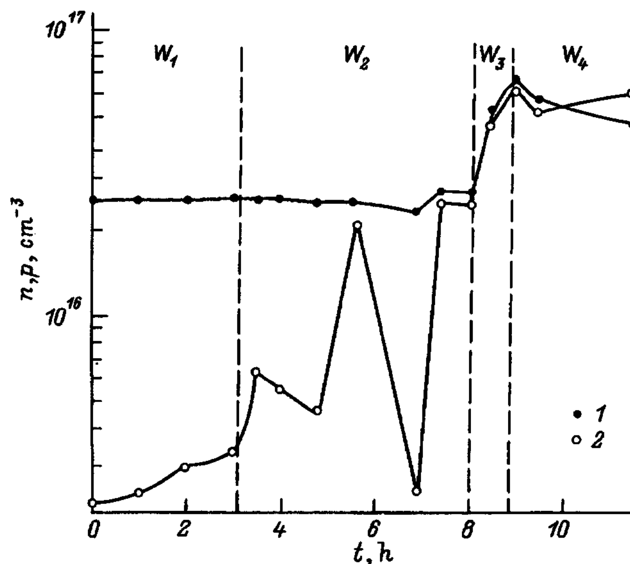

FIG. 3. Carrier concentration as a function of exposure time for InAs samples with excess As at the following temperatures (in K): *1*—300, *2*—77. Power densities (W/cm^2): $W_1 = 15$, $W_2 = 25$, $W_3 = 40$, $W_4 = 4$

tration at 77 K and at 300 K again increases, as it does in the case of crystals with initial n-type conductivity [Fig. 1, $t = 5.5$ h and Fig. 3, $t = 9$ (h)] but at higher values of W and

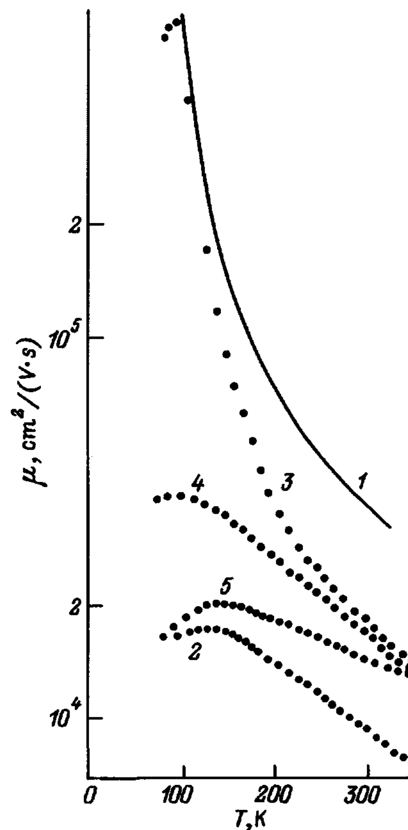

FIG. 4. Temperature dependence of electron mobility in InAs crystals: *1*—calculated for the case of scattering by lattice vibrations.[5] Crystal experiments: *2*—initial crystal with excess of In, *3–5*—excess of As. Measurements on n-type regions: *3*—unstable, *4*—stable, *5*—simultaneous application of constant electric field and laser radiation.

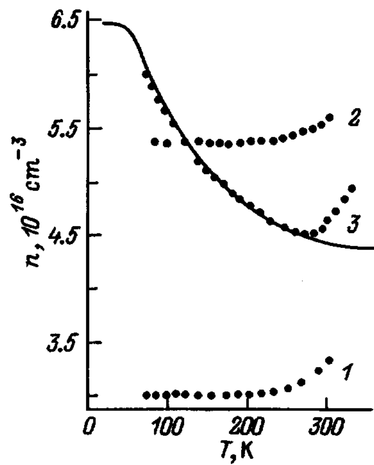

FIG. 5. Temperature dependence of carrier concentration for InAs samples: *1*—InAs sample with excess of In after a 13-hour exposure, *2*—InAs sample with excess As in a region with stable n-type conductivity prior to the simultaneous application of the electric field and laser radiation (9 h, 30 min), *3*—InAs sample with excess As in a region with stable n-type conductivity under the simultaneous application of the electric field and laser radiation (the solid curve is theoretical).

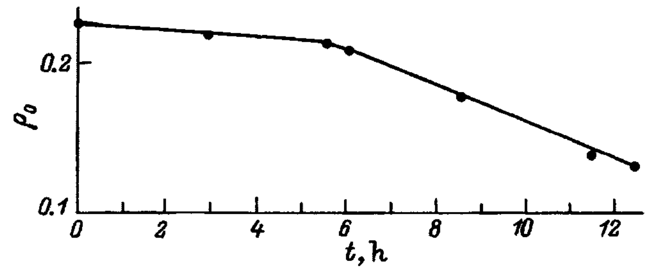

FIG. 6. Relative volume fraction of distorted lattice as a function of exposure time for InAs samples with excess In.

longer exposure. The power density is then substantially reduced to $W_4=4$ W/cm^2, and a constant electric field $E<0.1$ V/cm is applied to the sample parallel to the electric vector in the laser wave. It was shown in Ref. 6 that the laser-stimulated changes in the lattice in this case occur much more rapidly and, moreover, a directed migration of intrinsic and impurity components occurs with increasing exposure to the simultaneous action of the fields. In InAs, the electron concentration begins to fall in the presence of these fields (Fig. 5).

The results of these experiments can be explained by assuming that the changes in the crystal are not thermal, but are related to the laser-stimulated tranformations in the set of intrinsic point defects.

As in other semiconducting compounds such as GaAs, PbSnTe, and PbSnSe (Refs. 6 and 7), the laser-stimulated transformations of InAs occur in both sub-lattices, but at different rates. The metal component usually reacts more actively to a change in the laser power density than to changes in the dose, which is in fact confirmed experimentally.

The same mechanism for laser transformation of defects is typical for samples with excess As. The particular form of the function $R_H(T)$ that is observed only when the electric field and the laser radiation are applied to InAs (Fig. 5) is unusual and may be connected with a resonance level in the conduction band that transfers electrons to this band when the temperature is reduced. By analyzing the form of $R_H(T)$ we were able to calculate the position of this hypothetical level on the assumption that the donor level was formed by the s-type wave functions:

$$E_d(T)=E_d(0)-\alpha T,$$

where $E_d(0)=0.057\pm0.005$ eV and $\alpha=(2.0\pm0.2)\times10^{-4}$ eV/K. As already noted, when the crystals with excess As is illuminated by laser radiation, there is a characteristic region with n-type conductivity and an anomalously high mobility (Fig. 4). This state is not observed in crystals with excess In. It is clear from Fig. 4 that the electron mobility in the original samples is not very high because the best InAs crystals, grown by the Czochralski method, had mobilities reaching $\mu_{77}=5\times10^4$ cm/(V·s) at liquid-nitrogen temperatures. Naturally, the greater the concentration of clusters of intrinsic components or impurities, the lower the electron mobility.[8,9] Figure 6 shows the relative volume fraction of lattice distortions as a function of the exposure time. It is clear that the quantity ρ_0 monotonically decreases with exposure time, indicating a reduction in the volume fraction of large-scale inhomogenities in the crystal. This result is in agreement with the measured stoichiometry (spreading of coagulated intrinsic components during exposure leads to a change in state of the atoms in the lattice) and also with the increase in carrier mobility with increasing dose of radiation. We note, however that this mechanism is hardly the dominant one in the unstable phase of n-type conductivity, where for relatively high volume fraction of distortions the mobility at $T=77$ K reaches values that are actually restricted by the theoretical limit for scattering by lattice vibrations under the illumination (Fig. 4, curve *1*). Interestingly, when $N_I\approx n_{77}=2\times10^{16}$ cm^{-3}, the mobility should not exceed $\mu_{77}=7.5\times10^4$ cm^2/(V·s) (when scattering by ionizing impurities and lattice vibrations is taken into account), where N_I is the concentration of ionized impurities. The measured mobility is higher than this value by an order of magnitude.

A possible reason for this behavior of $\mu(T)$ is the ordering of the set of charged scattering centers in the field of the laser radiation, due to Coulomb repulsion and the formation of corrrelated mixed-valence point defects.[10] This ordering of scattering centers requires concentrations of not less than 5×10^{18} cm^{-3}, which is feasible in compensated semiconductors with low point-defect formation energies, e.g., III-V compounds. We note again that this situation occurs only in the case of laser-stimulated inversion from p- to n-type conductivity, followed by a transition to the stable n-type.

The carrier mobility in crystals with stable n-type conductivity is somewhat lower than the mobility observed in samples with excess In after exposure to laser radiation. This suggests a higher concentration of scattering centers in samples with excess As.

Moreover, it is clear from Fig. 4 that, as the power density increases, the initial rise in the electron concentration is accompanied by a reduction in mobility. However, the character of the temperature dependence remains nearly the

same. It is important to emphasize the change in the mobility $\mu(T)$ throughout the temperature range when the laser radiation with power density reduced by an order magnitude and weak electric field are applied together (Fig. 4, curve *5*). In this case the mobility increases with temperature, then reaches a maximum, and finally falls. This shows that there is a change in the scattering mechanism not only at low temperatures $T<130$ K, but also at higher temperatures $130<T<400$ K. The function $\mu(T)$ is largely determined for $T<130$ K by scattering by ionized impurities that are generated under the simultaneous application of the laser radiation and the external field. This contribution increases with increasing radiation dose, in good agreement with the dose dependence of the carrier concentration in the same interval. It follows from the analysis of $R_H(T)$ and the intensities of quasi-forbidden reflections that these centers probably include As atoms in the interstices of their planes.

4. CONCLUSION

We conclude that the effect of laser radiation, with $\hbar\omega<E_g$ and power density much less than the threshold value necessary for thermal damage to the crystal, can be used to vary the electrical and structural properties of InAs as a result of the redistribution of electrically neutral intrinsic components in the field of the laser wave.

[1] P. K. Kashkarov, V. I. Petrov, and D. V. Ptitsyn, Fiz. Tekh. Poluprovodn. **23**, 2080 (1989) [Sov. Phys. Semicond. **23**, 1287 (1989)].

[2] F. F. Sizov and S. V. Plyatsko, J. Cryst. Growth **92**, 571 (1988).

[3] I. Fujimoto, Jpn. J. Appl. Phys. **23**, 287 (1984).

[4] V. V. Lider, F. N. Chukhovskii, and V. N. Rozhanskii, Fiz. Tekh. Poluprovodn. **, 19**, 1231 (1977) [Sov. Phys. Semicond. **19**, 816 (1985)].

[5] D. L. Rode, Phys. Rev. B **3**, 3287 (1971).

[6] Yu. S. Gromovoj, S. V. Plyatsko, F. F. Sizov, and L. A. Korovina, J. Phys. Condens. Matter, **2** 10391 (1990).

[7] V. P. Klad'ko and S. V. Plyatsko, Pis'ma Zh. Teor. Fiz. **22**, 32 (1975) [JETP Lett. **22**, 14 (1975)].

[8] A. N. Baranov, T. I. Voronina, A. A. Gorelenok, T. S. Lagunova, A. M. Litvak, M. A. Sipovskaya, S.£. Starosel'tseva, V. A. Tikhomirova, and V. V. Sherstnev, Fiz. Tekh. Poluprovodn. **26**, 1623 (1992) [*sic.*]

[9] A. N. Baranov, T. I. Voronina, T. S. Lagunova, M. A. Sipovskaya, V. V. Sherstnev, and Yu. P. Yakovlev, Fiz. Tekh. Poluprovodn. **27**, 421 (1993) [Semiconductors **27**, 236 (1993)].

[10] I. M. Tsidil'kovskii, Usp. Fiz. Nauk **162**, 63 (1992) [Sov. Phys. Usp. **162**, 85 (1992)].

Translated by S. Chomet

Effect of superstoichiometric components on the spectral and kinetic characteristics of the luminescence of ZnSe crystals with isovalent impurities

O. V. Vakulenko, V. N. Kravchenko, V. D. Ryzhikov, V. I. Silin, and N. G. Starzhinskii

Physics Department, Taras Shevchenko Kiev University, 252127 Kiev, Ukraine
(Submitted April 22 1996; accepted March 20 1997)
Fiz. Tekh. Poluprovodn. **31**, 1211–1215 (October 1997)

The spectral and kinetic parameters of the X-ray luminescence of ZnSe crystals doped with Zn, Se, and Te were investigated during the growth process at temperatures in the range 80–500 K, and also after annealing in Zn vapor. ZnSe crystals grown from a stoichiometric mixture, or mixture containing chalcogenide impurities, typically produce the minimum level of afterglow and a rapid rise of X-ray luminescence, as well as a shift of its peak from the infrared region toward shorter wavelengths after annealing in zinc. ZnSe crystals grown from material with excess of Zn have a relatively low X-ray luminescence yield and a substantial level of afterglow. It is assumed that the growth of Te-activated crystals is accompanied by the development of thermally stable complexes of the form $V_{Zn}Te_{Se}$ that act as radiative recombination centers. The introduction of excess Zn into the initial mixture produces a reduction in the concentration of V_{Zn} and, hence, in the concentration of radiative recombination centers. It is shown that, for free-electron concentrations $n<10^{18}$ cm^{-3}, the afterglow time constant τ can be described as a function of n by a model of radiative recombination that involves a single impurity level, whereas for $n>10^{18}$ cm^{-3}, the time constant decreases with increasing n, which cannot be explained in terms of the simple model. It is suggested that radiative recombination centers of a new type are produced as a result of prolonged annealing in Zn vapor. © *1997 American Institute of Physics.* [S1063-7826(97)01610-4]

The optical and electrical properties of zine selenide crystals can in many ways be determined by the type and concentration of intrinsic lattice point defects (IPDs) even in the presence of extraneous impurities.[1,2] Ways of controlling the luminescence properties of zinc selenide by introducing the isovalent Te impurity, which produces mixtures with much better properties that those of traditional phosphors,[6] were discussed from theoretical and experimental points of view.[3–5] Since the ensemble of IPDs has a determining influence on scintiliation processes, it is interesting to investigate the effect of excess intrinsic components (Zn, Se, Te) that are introduced during the synthesis of the original medium from which the crystals are grown, and the mechanism responsible for their luminescence.

1. SAMPLES AND EXPERIMENTAL METHODS

We have investigated ZnSe crystals grown by the Bridgeman-Stockbarger method in argon at a pressure $\leqslant 60$ atm. The same original portion of zince selenide was used in all these experiments. It was subjected to heat treatment in vaccum in order to reduce the concentration of extraneous impurities and components that have not reacted in the system.[7] Excess Zn, Se, and the Te dopant were introduced into the initial mixture with concentrations of 2% by weight. The grown crystals were held in Zn vapor at 1290 K and 1 atm for 24 h, or in liquid zinc at 1000 K for 24–72 h.[8]

The elemental composition of samples was monitored by means of X-ray luminescence and chemical analysis. The concentration of oxygen-containing impurities was $\leqslant 0.1\%$ by weight, the concentration of carbon was 5×10^{-4} % by weight, and the concentration of other extraneous impurities was no more than $10^{-5}\%$ by weight. The concentration of the Te activator in these crystals and also the excess of zinc and selenium, is given in Table I.

The luminescence spectral characteristics were investigated using the KSVU-23 measuring and computing system. The crystals were excited by the REIS-I X-ray source. Luminescence kinetics was investigated with a dedicated measuring and computing system.[9] The RAPAN-160/200 source (tungsten anode, 160–200 kV, 0.1–0.5 mA, $t_{IMP}=2$ sec) was used in measurments of the afterglow level η, and the emission time constant τ was measured under excitation by the MIRA-2D X-ray source ($h\nu\leqslant 200$ kV, $t_{IMP}\leqslant 10$ msec). The afterglow level was determined as the ratio of luminescence intensity $I(T)$ at time $t=10$ msec (after excitation) to its maximum value I_M multiplied by 100%. The afterglow time constant was defined as the time during which the illuminescence intensity fell by a factor of e after the end of excitation.

2. EXPERIMENTAL RESULTS

The basic luminescence parameters measured at 300 K were: the position of the peak in emission spectrum λ_M, the luminescence decay time constant τ, and the afterglow level η due to zinc selenide crystals that had undergone various types of heat treatment (the values are listed in Table I). The impurity introduced into initial material is indicated in parentheses and the annealing atmosphere is indicated after the colon. The notation Zn^0,Se^0, and Te^0 refers to doping with the respective elements and Te^{2-} represents doping with zinc telluride.

TABLE I. Spectral and kinetic parameters of ZnSe crystals containing isovalent impurities at 300 K.

No.	Crystal	λ_M, nm	τ, μs	η,% in 10 ms	I_{XL}, arb. units
$A1$	ZnSe	620	<1	2	1
$A2$	ZnSe:Zn	628	55	17	12
$A3$	ZnSe(Se^0)	870	<1	25	1.4
$A4$	ZnSe(Se^0):Zn	625	90	<0.05	150
$A5$	ZnSe(Zn^0)	617	270	20	0.3
$A6$	ZnSe(Zn^0):Zn	625	220	23	2
$A7$	ZnSe(Te^0)	830	30	5	0.7
$A8$	ZnSe(Te^0):Zn	635	80	<0.05	320
$B1$	ZnSe(Te^{2-})	890	26	12	83
$B2$	ZnSe(Te^{2-}):Zn	640	100	<0.05	980
$B3$	ZnSe(Te^{2-},Zn^0)	620	550	7	45
$B4$	ZnSe(Te^{2-},Zn^0):Zn	630	>5000	31	28
$B5$	ZnSe(Te^{2-},Se^0)	850	70	5	75
$B6$	ZnSe(Te^{2-},Se^0):Zn	640	180	<0.05	610
$B7$	ZnSe(Te^{2-},Te^0)	880	280	21	102
$B8$	ZnSe(Te^{2-},Te^0):Zn	640	140	<0.05	820
$B9$	ZnSe(Te^{2-}):Zn*	595	≤3	<0.05	580

**Note:* The $B9$ crystals were obtained after prolonged heat treatment of $b1$ crystals in zinc.

After annealing in zinc, only three of the eight selected crystals, namely, samples $A1$, $A5$, and $B3$, had an X-ray luminescence spectrum with its maximum in the red. The other five samples ($A3$,$A7$,$B1$,$B5$,$B7$) produced a dominant band with a maximum in the infrared prior to annealing. After annealing this maximum shifts into the red. This is accompanied by a substantial rise in the intensity of the X-ray luminescence (I_{XL}) and a fall in the afterglow level.

Crystals grown from primary mixture containing excess Zn are less sensitive to annealing in Zn. For example, the $A5 \rightarrow A6$ process results in a rise in X-ray luminescence intensity by a factor of 6-7, whereas $A3 \rightarrow A4$ produces an increase in I_{XL} by a factor of more than 100. The reverse result is observed for $B3 \rightarrow B4$, namely, I_{XL} decreases with substantial rise in τ and η.

At $T = 80$ K, the spectra of most of the crystals that were investigated are dominated by a broad band with a peak in the range $\lambda_M = 620-640$ nm. The only exception are the undoped $A1$ crystals and $A2$ samples derived from them (i.e., annealed in Zn). Their spectra are dominated by the band with $\lambda_M = 560$ nm. The exceptional samples also include $B4$ with $\lambda_M \approx 500$ nm (Fig. 1a) which, in addition, has a relatively large afterglow time constant.

Samples $B2$ have a very stable intensity I_{XL} at high temperatures and a single impurity X-ray luminescence band in the entire temperature range $T = 4.2-350$ K, and also a strong near-edge emission (see Fig. 1a). These results are in agreement with Ref. 10. When excess Zn is added to the initial ZnSe+Te mixture (crystals $B3$ and $B4$), the X-ray luminescence bands become very unstable, the near-edge emission is absent, and afterglow kinetics increases markedly.

For $B9$, produced by heat treatment of $B1$ in zinc at

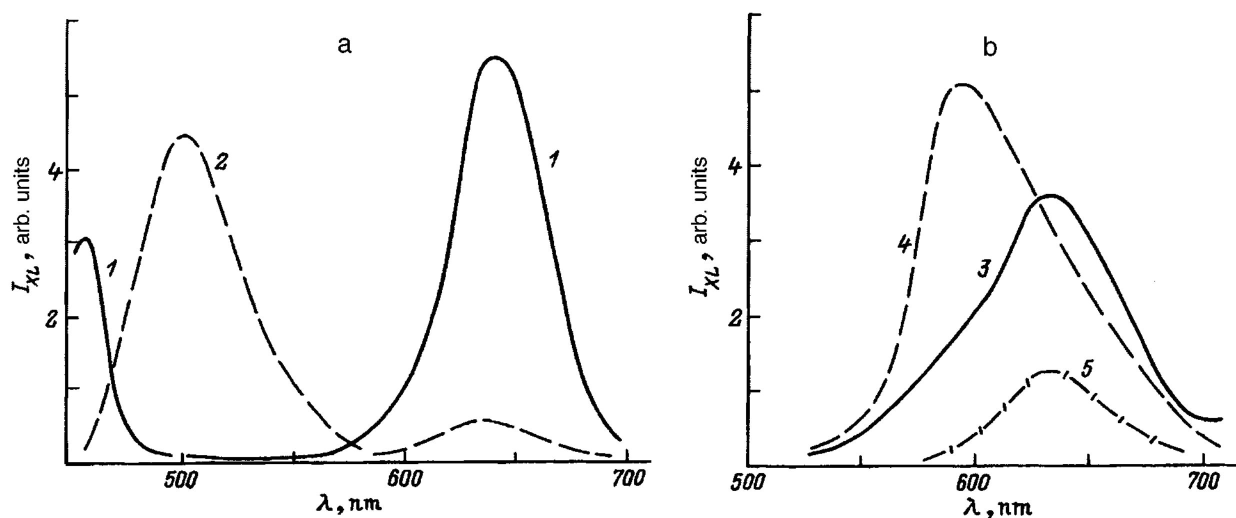

FIG. 1. X-ray luminescence spectra of the following crystals: *1*—$B2$, *2*—$B4$ at $T = 80$ K (a), and the crystal $B9$ at the following temperatures T (in K): *3*—80, *4*—300, *5*—470 (b).

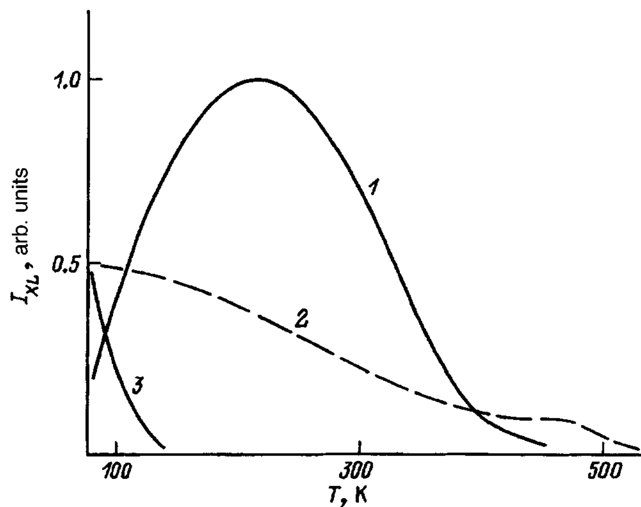

FIG. 2. Temperature dependence of the X-ray luminescence band intensity of crystals $B9$ with the following values of λ_M (in nm): *1*—595, *2*—630, *3*—880.

$T=1000$ K, the characteristic feature that is unusual for the ZnSe(Te) crystal is the stationary X-ray luminescence at 300 K with $\lambda_M=595$ nm (Fig. 1b), fast decay kinetics, and the absence of afterglow and near-edge emission. When the temperature is raised from 80 to 500 K, these crystals show a double inversion of the dominant X-ray luminescence band: in the range 80–100 K, the X-ray luminescence maximum lies in the range 620–630 nm, whereas in the ranges 110–350 K and 400–500 K it lies at 595 nm and again in the region 620–630 nm. Moreover, when $T<130$ K, the X-ray luminescence spectra of samples $B9$ contain an infrared emission band with $\lambda_M \approx 880$ nm. The above temperature-dependent features of the X-ray luminescence spectrum are due to a different temperature dependence of the initial intensity at the maximum of each of these bands (Fig. 2). The intensity of the band with $\lambda_M=630$ nm decreases as the temperature is raised above 80 K, with thermal quenching activation energies $\varepsilon_T=0.05$, 0.12, and 0.6–0.7 eV in the temperature ranges 80–100, 100–400, and 450–550 K, respectively. The intensity of the band with $\lambda_M=595$ nm increases as the temperature is raised from 80 to 220 K, but at higher temperatures it is found to decrease with $\varepsilon_T=0.5$ eV. The intensity of the infrared band decreases monotonically with increasing temperature, and falls to zero at $T\approx 120$ K.

3. DISCUSSION OF THE RESULTS

In terms of their physical, chemical, and optoelectronic properties, the above zinc selenide crystals can be divided into two groups: (1) crystals grown from a mixture with stoichiometric composition or with a chalcogenide impurity and (2) crystals grown from a mixture containing an excess of zinc. After annealing in vapor, the first group displays dominant infrared bands in the X-ray luminescence spectra, an absorption band in the range 500–550 nm, and, after annealing, a sharp rise in the X-ray luminescence intensity, a shift of the maximum of this intensity into the region 630–640 nm, and a minimum level of afterglow. The X-ray luminescence centers are formed in this group of crystals in accordance with the model proposed in Refs. 3 and 4: zinc vacancies V_{Zn} are generated when Te-activated crystals are grown, and the complexes $V_{Zn}Te_{Se}$ are found to be thermodynamically stable even after the subsequent annealing of the ZnSe(Te) crystals in zinc; in addition, they act as centers of selective absorption (in the range 500–550 nm) and of radiative recombination.

The second group of crystals is characterized by selective-absorption bands in the range 470–1500 nm, infrared bands in the X-ray luminescence spectra, a considerable level of afterglow, and a very low luminescence yield, which can be explained as follows. The addition of excess Zn to the initial mixture, ensures that when the crystal is grown at temperatures up to 1900 K and the excess pressure is a few dozen atmospheres, this superstoichiometric component can enter the crystal lattice, fill the vacancies at the sites of the cation sublattice, and prevent the formation of complexes of the form ($V_{Zn}Te_{Se}$); moreover, it can generate vacancies in the anion sublattice V_{Se} (and interstitial Se_I) that gives rise to deep donor levels in the bandgap, with $E_a=0.3$–0.45 eV (Ref. 11).

Such crystals, which usually have high resistivities, should have a distribution of electrical and optical parameters that is highly inhomogeneous and is due to the fluctuation potential of the impurity.[12] The fluctuation potential, as we know,[13] is responsible for the so-called long-term ''frozen'' photoconduction in the semiconductor. This seems to us to be the reason for the extended decay kinetics of X-ray luminescence in samples $B3$ and $B4$.

We have found that samples in the second group have varistor-type nonlinear current-voltage characteristics, which confirms the above picture.

The absence of near-edge emission can also be explained in terms of the influence of the impurity fluctuation potential, which produces the spatial separation of charges in the excited electron-hole pairs[14] which impedes the formation of excitons or direct band-band recombination.

We note the following points in relation to the time parameters of the luminescence emitted by the above samples. We know that in n-type crystals with generally high conductivity, the decay time constant τ is largely due to two main factors, namely, the capture of a hole by a recombination center (τ_p) and the recombination of an electron (free odd donor) with a bound hole (τ_n). When $\tau_p \ll \tau_n$, the intensity decay time constant is $\tau \approx \tau_n$. The time constant τ_n is obviously inversely proportional to the total concentration n of free electrons, which in turn is equal to the sum of two concentrations, namely, the dark concentration n_0 and the nonequilibrium concentration n_1. When n_0 is high enough, we can assume that $n \approx n_0$, so that $\tau \sim (n_0)^{-1}$. Accordingly, $\ln(\tau^{-1})$ is a linear function of $\ln(n_0)$ for $n \leqslant 10^{15}$ cm^{-3} (Fig. 3).

When $n_0 > 10^{15}$ cm^{-3}, the reduction in τ with increasing n_0 is probably limited by τ_p which in turn is determined by the concentration n of capture and recombination centers. It is clear from Fig. 3 that for $10^{15} \leqslant n_0 \leqslant 10^{18}$ cm^{-3}, the time constant τ remains nearly constant, which may be an indica-

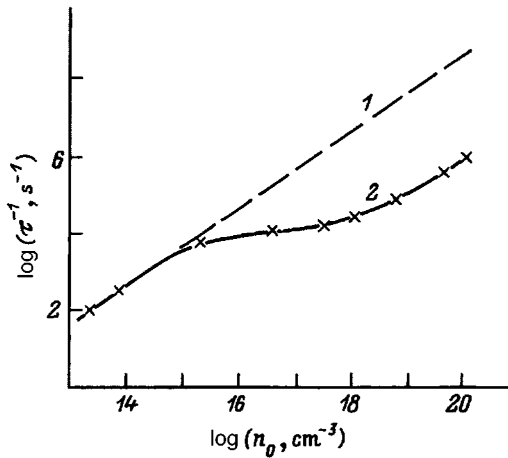

FIG. 3. The temperature decay time constant τ plotted as a function of the free-carrier concentration n_0: *1*—theory, *2*—experiment with ZnSe(Te) crystals.

tion that N remains nearly constant in these samples. The fact that N is independent of N_0 is not unusual because the concentration of majority recombination centers is set, as we have already noted, by the concentration V_{Zn}, and the latter is determined by crystal growth conditions, whereas subsequent annealing of the samples in zinc, which completes the formation of radiative recombination centers, determines n_0, which can vary between broad limits for the same values of the concentration of Zn vacancies.

To obtain a more detailed description of the recombination of nonequilibrium carriers in low-resistivity n-type samples (annealed in zinc), consider the following simple scheme of electron transitions for a single recombination level E_a. The corresponding kinetic equations take the form

$$dp/dt = g - C_p p(N - p_a), \tag{1}$$

$$dp_a/dt = C_p p(N - p_a) - C_n n p_a, \tag{2}$$

where g is the rate of generation of electron-hole pairs as a result of interband excitation, p is the concentration of nonequilibrium free holes in the valence band, p_a is the concentration of nonequilibrium holes localized at recombination centers, and $C_{p,n}$ are coefficients describing the trapping of holes or electrons, respectively, by an impurity center. The remaining notation was described above. The luminescence intensity is given by $I_{XL} = C_n n p_a$.

When $p_a \ll N$, the solution of (1) and (2) gives

$$p_a(t) = \frac{p_\infty}{\tau_p/\tau_n - 1} e^{-t/\tau_p} + \left[(p_a)_\infty - \frac{p_\infty}{\tau_p/\tau_n - 1} \right] e^{-t/\tau_n}, \tag{3}$$

where p_∞ and $(p_\alpha)_\infty$ are the stationary (initial) concentrations of nonequilibrium free and localized holes, respectively, and $\tau_n = 1/nC_n$, $\tau_p = 1/C_p N$.

It is clear from (3) that, in general, the luminescence decay law is not exponential. We shall consider two special cases. When $\tau_p \gg \tau_n$, the first term on the right-hand side of (3) is the dominant term, i.e., the luminescence decay time constant is determined by the concentration of recombination centers. When $\tau_p \ll \tau_n$, we have $p_a(t) \sim \exp(-t/\tau_n)$; i.e., the luminescence kinetics is determined by the concentration of free electrons.

The above electron transition scheme thus provides an explanation of the behavior of τ for $n < 10^{18}$ cm^{-3}. However, when $n > 10^{18}$ cm^{-3}, the luminescence decay time constant is again found to decrease with increasing n. This may mean that a new type of trapping-recombination center is formed in the highly doped crystals, or the shape of the electron track produced by an X-ray photon is altered in some way.

Another possible reason for the reduction in the X-ray emission time constant with increasing dark concentration of electrons may be found in the influence of Auger-type nonradiative transitions in which the energy of the recombining electron is transferred to another free electron (third particle), which thus becomes ''hot''.[13] Auger processes involving free carriers become significant only at high concentrations of the latter, and this was, in fact, the case here. Moreover, the X-ray luminescence intensity of the crystal $B9$ was lower than that of the parent crystal $B2$, so that the contribution due to nonradiative transitions may be significant in the case of $B9$. The Auger mechanism is also supported by the absence of near-edge emission in crystals with the lowest resistivities.

The proposed formation of a new type of recombination center in the case of high free-electron concentrations is also supported by the fact that the crystal $B9$, which had the lowest resistivity, had an anomalous X-ray luminescence spectrum with $\lambda_M = 595$ nm at $T = 300$ K and an anomalous temperature dependence of emission intensity. The band width $\lambda_M = 595$ nm was also seen in the low-resistivity ZnSe:Zn crystals ($n > 10^{19}$ cm^{-3}) after prolonged annealing of stoichiometric samples in liquid zinc.[15] If we start with the above idea that a new type of center is being formed, we can proceed to the tentative consideration of the possible structure of such centers. The most likely scenario is that the new centers are $V_{Zn}^{2-}Te_{Se}(Zn_l^+)_n$, where $n \geqslant 2$. The Te atom, which replaces the Se atom, plays the role of a stabilizer of the vacancies V_{Zn} and prevents the atom Zn from filling an empty site. We thus obtain the complex $V_{Zn}^{2-}Te_{Se}$, which is surrounded by two or more interstitial zinc atoms. This type of center has a repulsive barrier for a hole and low probability of trapping it at low temperatures. The hole trapping probability rises rapidly with increasing temperature and, as a result, the afterglow intensity in the $\lambda_M = 595$-nm band is found to increase.

IV. CONCLUSIONS

The ZnSe crystals grown from the initial stoichiometric mixture or a mixture containing a chalcogenide impurity, and also crystals grown from a mixture containing an excess of zinc, have significantly different spectral and kinetic luminescence parameters, indicating that intrinsic lattice defects play a dominant role in the formation of radiative recombination centers in this material.

The substantial change in the X-ray luminescence parameters of these crystals after prolonged annealing in zinc is probably due to the formation of a new type of combination

center, which is characterized by an anomalous temperature dependence of luminescence intensity.

The measured dependence of the decay time constant on carrier concentration in n-type ZnSe crystals can be interpreted in terms of a recombination model involving a single impurity level, and also a significant contribution of Auger processes at high free-carrier concentrations.

[1] A. N. Georgobiani and M. B. Kotlyarevskii, *The Pysics of* $A^{II}B^{VI}$ *Compounds* [in Russian], Nauka, Moscow, 1986, p. 72.

[2] V. D. Ryzhykov, *Scintillators in the Form of Semiconducting* $A^{II}B^{VI}$ *Compounds: Production, Properties, Applications* [in Russian], NIITEKhIM, Moscow, (1989).

[3] V. D. Ryzhykov and E. F. Chaikovskii, Izv. AN SSSR, Ser. fiz. **43**, 1150 (1979).

[4] V. D. Ryzhykov, *High-efficiency Phodiode-Type Semiconductor Detectors for Monitoring Nuclear Power Stations* [in Russian], NIITEKhIM, Khar'kov, 1984.

[5] V. D. Ryzhikov and N. G. Starzhinskii, Ukr. Fiz. Zh. **33**, 818 (1988).

[6] V. D. Ryzhikov, *Development of Automated Radiation Monotoring for Nuclear Power Stations Using New-generation Phosphor-photodiode Detector Combinations*, VNIIM, Kar'kov, 1990, p. 3.

[7] E. Ya. Mellikov, Ya. V. Khiie, P. L. Kukk, and I. V. Karpenko, Izv. AN SSR, Neorg. Mater. **18**, 363 (1982).

[8] V. I. Silin, N. G. Starzhinskii, and M. Sh. Fainer, Org. Neorg. Mater. No. 26, 7 (1990).

[9] S. M. Ignatov, V. D. Ryzhikov, V. I. Silin, N. G. Starzhinskii, and Yu. A. Yakovlev, Org. Neorg. Mater. No. 26, 14 (1990).

[10] H. L. Oczkowski, Phys. Status Solidi A **68**, 199 (1981).

[11] S. Kishida, K. Matsuura, H. Nagase, H. Mori, F. Takeda, and I. Tsurumi, Phys. Status Solidi A **95**, 155 (1986).

[12] B. I. Shklovskii and A. L. Efros, *Electronic Properties of Doped Semiconductors* [in Russian], Naukov, Moscow, (1979).

[13] J. I. Pankove, *Optical Processes in Semiconductors*, Dover, N.Y., (1975).

[14] V. B. Sandomirskii, A. G. Zhdan, M. A. Messerer, I. B. Gurlyaev, Ya. A. Pyasta, and A. S. Darevski, Solid-State. Electron. **16**, 1097 (1973).

[15] V. D. Ryzhikov, V. I. Silin, and N. G. Starzhinskii, Nucl. Tracks Radiat. Meas., **21**, 53 (1993).

Translated by S. Chomet

Electroluminescence of the unconfined heterostructure *p*-GaInAsSb/*p*-InAs at liquid-helium temperatures

N. L. Bazhenov, G. G. Zegrya, V. I. Ivanov-Omskiĭ, M. P. Mikhaĭlova, M. Yu. Mikhaĭlov, K. D. Moiseev, V. A. Smirnov, and Yu. P. Yakovlev

A. F. Ioffe Physicotechnical Institute, Russian Academy of Sciences, 194021, St. Petersburg, Russia
(Submitted March 26, 1997; accepted for publication April 1, 1997)
Fiz. Tekh. Poluprovodn. **31**, 1216–1219 (October 1997)

The electroluminescence of the single unconfined type-II heterojunction p-GaInAsSb/p-InAs was investigated in the temperature range $T=4.2-77$ K. As the temperature was reduced below $T=77$ K, the luminescence bands with maxima at 311 meV (band A) and 384 meV (band B) were found to shift toward higher energies. At 4.2 K, the short-wave band split into two bands, B_1 and B_2. These results are explained in terms of a model involving recombinations of electrons from the conduction band to an acceptor level of InAs, and also recombinations of electrons and holes localized in self-consistent quantum wells on either side of the heterojunction. © *1997 American Institute of Physics.* [S1063-7826(97)01710-9]

Luminescence from an unconfined type-II single p-GaInAsSb/p-InAs heterojunction at 77 K was recently discovered and investigated,[1] and a qualitative analysis of this phenomenon was carried out. It was shown that the electroluminescence of this $p-p$ heterostructure was due to recombinations of electrons and holes localized in self-consistent quantum wells on either side of the heterojunction. However, the question as to whether the shape of the potential barriers and the self-consistent quantum wells on the heterojunction is determined directly by the fabrication technology, or whether it also depends on the external bias, has not been fully answered. It was therefore desirable to investigate the electroluminescence under pulsed excitation in order to be able to vary the current across the heterojunction in a broad range and to estimate the characteristic time constants of the attendant radiative processes. Radiative recombination in an unconfined type-II $p-p$-heterojunction under pulsed excitation at liquid-nitrogen temperatures was investigated in Ref. 2. It was shown that the luminescence spectra contained two emission bands with maxima at 384 and 311 meV, with half widths of 18–19 meV, and an estimate was made of the time constants of radiative and nonradiative recombinations on the type-II boundary, which were found to be $\tau_R \simeq 2\times10^{-7}$ sec and $\tau_{A2}=(0.5-1.4)\times10^{-7}$ sec, respectively.

The aim of the research reported here was to investigate the electroluminescence of the unconfined heterojunction p-GaInAsSb/p-InAs under pulsed excitation at liquid-helium temperatures. The experiments were performed for different currents and different positions of the measuring pulse relative to the current pulse.

EXPERIMENTAL METHODS AND SAMPLES

The single p-GaInAsSb/p-InAs heterojunctions were produced by liquid-phase epitaxy. The fabrication technology and the measurement techniques were described in detail in an earlier paper.[2,3] The substrate for this structure was Zn doped to a concentration of the order of 5×10^{16} cm^{-3}. The wide-gap epitaxial layer of the solid solution $Ga_{1-x}In_xAs_ySb_{1-y}(x=0.17,y=0.22)$ was also Zn doped to a concentration of $p=10^{18}$ cm^{-3}.

EXPERIMENTAL RESULTS AND DISCUSSION

Figure 1 shows the luminescence spectra of the above junction when a negative potential was applied to the narrow-gap semiconductor p-InAs (reverse bias) at four temperatures between 4.2 and 100 K. At $T=77$ K, the spectra contained two lines with maxima at photon energies of 311 meV (line A) and 384 meV (line B), respectively. As the temperature was reduced to $T=4.2$ K, band A became narrower, but its peak remained practically fixed (at 314 meV). This was accompanied by a change in the structure of band B, which split into two lines with peaks at 371 meV (B_1) and 400 meV (B_2). The position of B_1 was nearly the same as the position of the band B at $T=77$ K. When compared with the spectrum recorded at the intermediate temperature of $T=15$ K, it was clear that an increase in temperature from liquid-helium temperatures produced a rise in the intensity of B_1, but its position remained constant and coincided with that of band B at $T=77$ K, whereas B_2 shifted toward lower photon energies and expanded, eventually absorbing B_1.

The position of the two long-wave bands is thus practically independent of temperature, whereas the short-wave band shifts toward higher energies as the temperature is reduced. The temperature coefficient of the shift is -2.2×10^{-4} eV/K, which is close to the temperature coefficient of the gap width in InAs -2.8×10^{-4} eV/K (Ref. 4).

The current-voltage characteristics of the above structure changes little as the temperature is reduced from 77 K down to 4.2 K. This shows that the current flow is of the tunnelling type. We note that band A is not observed in the case of forward bias, when the positive potential is applied to the

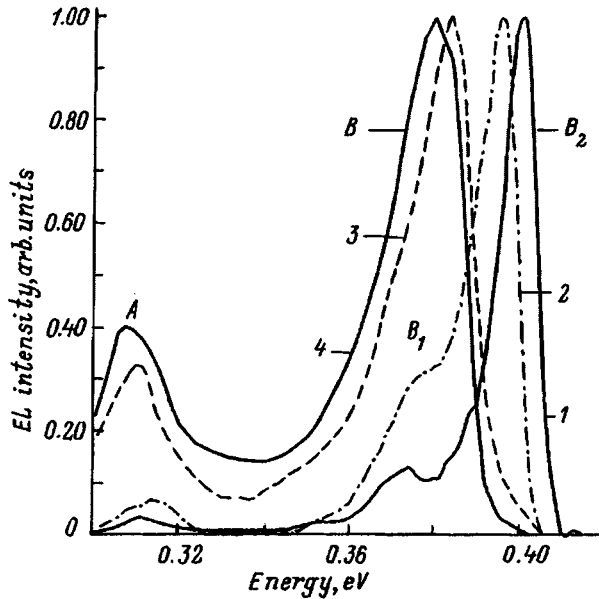

FIG. 1. Electroluminescence spectra at 4.2 K (*1*), 15 K (*2*), 77 K (*3*), and 100 K (*4*).

semiconductor *p*-InAs with the narrower gap.

Figure 2 shows the spectra of B_1 and B_2 for the above structure, both for reverse bias and forward bias. It is clear that the shape of the spectra is similar in the two cases. As the excitation intensity inceases, the emission line intensity rises linearly, but the band positions remain the same.

Band B_2 is symmetric in the case of the forward bias, and has the Gaussian shape. Band B_2 is asymmetric in the case of reverse bias. Its short-wave edge is, as before, described by the Gaussian distribution with the same parameters as in the case of the forward bias, but the long-wave edge is Lorentzian. Nevertheless, it may be concluded that

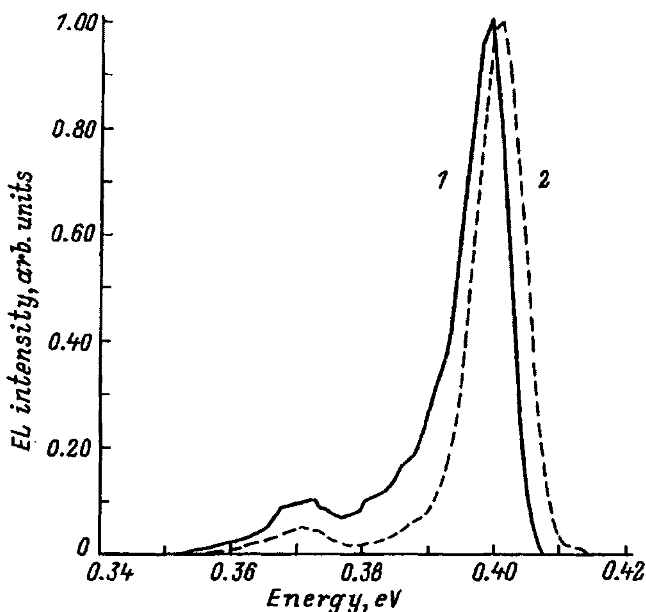

FIG. 2. Electroluminescence spectra at 4.2 K under reverse bias (*1*) and forward bias (*2*).

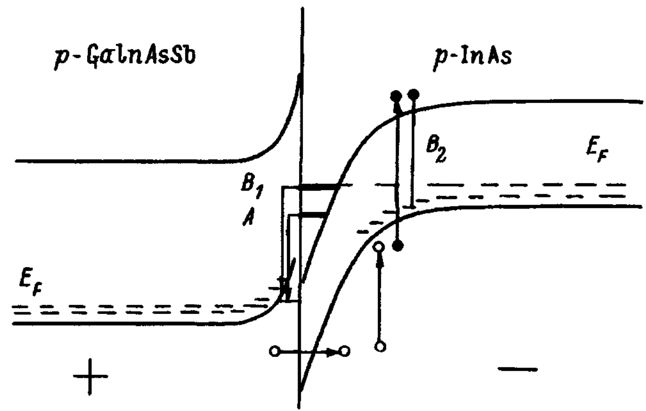

FIG. 3. Band diagram of the heterojunction under reverse bias.

the shape of the spectrum of the above heterostructure depends only slightly on either the degree of excitation or the direction of the current. This suggests that the bound structure is determined largely by the fabrication technology, rather than by the applied bias. Moreover, carrier recombinations occur in the same part of the heterojunction for both bias polarities.

The nature of B_2 can be better understood by considering the band diagram shown in Fig. 3 (E_F is the Fermi level). The heterojunction is reverse-biased in the figure. The effective process in this case is hole tunnelling from the valence band of the solid solution to the valence band of InAs. A hole that has tunnelled through has lost energy by the Auger process, and this is accompanied by the excitation of a nonequilibrium electron from the valence band of InAs to the conduction band, and by the transition of the hole to the top of the valence band. The electron in the conduction band undergoes a radiative recombination to an acceptor level, which leads to the appearance of the band B_2 in the electroluminescence spectrum. Since both substrate and layer are doped with Zn, which produces the 25-meV acceptor level in InAs (Ref. 5), and the gap width of InAs determined from photoluminescence at $T=4.2$ K is 423 meV, it is natural to assume that the recombination of electrons occurs on an acceptor level corresponding to zinc. In the case of forward bias, there is an analogous process, but tunnelling of holes occurs from the valence band of InAs to the valence band of GaInAsSb. Moreover, in the case of forward bias exceeding the contact potential difference (this was so in our experiment), electrons can tunnel from the valence band of GaInAsSb to the conduction band of InAs, and recombination of holes can take place. We note that, since band bending is greater under reverse bias, and since electron recombination occurs precisely in the region where the bands are highly bent, we may expect that the low-wave edge of the electroluminescence band is shallower than that of the short-wave edge because of the contribution due to recombinations accompanied by tunnelling. It is precisely this behavior that we saw in the experiment.

The fact that the position of the electroluminescence band is bias-independent can be explained in our model of the band diagram as follows. A quantum well is present on

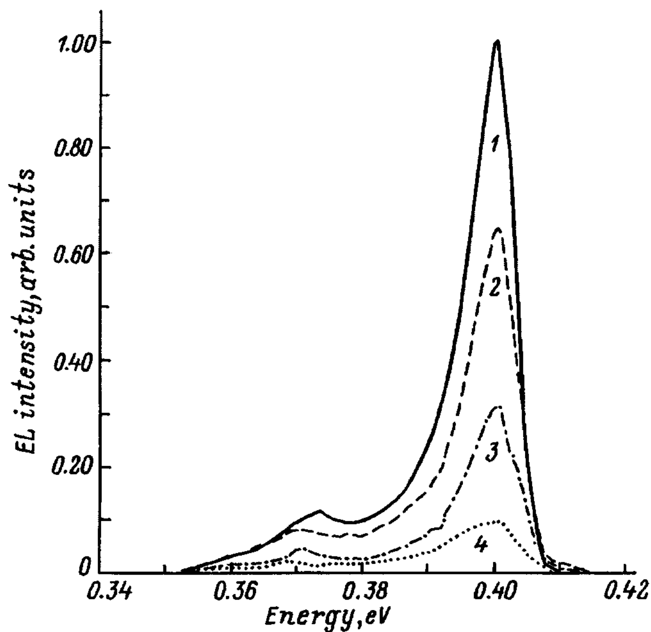

FIG. 4. Electroluminescence spectra recorded under reverse bias at 4.2 K at the following times after the end of the current flowing through the heterojunction (in μ sec): *1* — 0, *2* — 4, *3* — 8, *4* — 12.

the $p-p$-heterojunction, and its shape is virtually independent on the magnitude and polarity of the applied bias. When the bias is applied, the local levels in the well are filled with electrons, and their tunnelling recombination with holes leads to the appearance of the bands A and B_1.

Figure 4 illustrates the electroluminescence decay kinetics after a $10-\mu$sec current pulse across the heterojunction under reverse bias. It is clear that, when the excitation current is turned off, there is a fall in the intensities of B_1 and B_2. A reduction by a factor of e occurs in a time of approximately 8 μsec, which is close to the relaxation time of the integrated luminescence in such structures.[3] On the whole, this confirms the assumption that the energy structure of the heterojunction is essentially independent of the applied voltage. At the same time, the rate of reduction in the band intensity with shifting measuring gate confirms that the two radiative recombination channels have the same source of nonequilibrium electrons.

CONCLUSIONS

We have investigated the electroluminescence spectra of the single heterojunction p-GaInAsSb/p-InAs in pulsed electric fields at $T=4.2-100$ K. The experimental data obtained in this investigation have resulted in an improvement of the radiative recombination model proposed in Refs. 1 and 2. In addition, when applied to the recombination of electrons localized in the self-consistent quantum well on the heterojunction on the side of p-InAs, this model describes radiative transitions of electrons to the acceptor level of p-InAs.

This research was carried out with the partial support of the Russian Fund for Fundamental Research (Grant No. 96-02-17841a) and INTAS (Grant No. 94-0789)

[1] M. P. Mikhailova, G. G. Zegrya, K. D. Moiseev, and Yu. P. Yakovlev, Solid State Electron. **40**, 673 (1996).
[2] N. L. Bazhenov, G. G. Zegrya, M. P. Mikhailova, K. D. Moiseev, V. A. Smirnov, O. Yu. Solov'eva, and Yu. P. Yakovlev, Fiz. Tekh. Poluprovodn. **11**, 658 (1977) [*sic.*]
[3] N. L. Bazhenov, G. G. Zegrya, V. I. Ivanov-Omskii, K. D. Moiseev, M. P. Mikhailova, V. A. Smirnov, and Yu. P. Yakovlev, *23rd International Symp. on Compound Semiconductors*, September 23–27, St. Petersburg, Russia, rep. 11. p2.37.
[4] P. K. Baranskii, V. P. Klochkov, and I. V. Potykevich, *Handbook of Semiconductor Electronics* [in Russian], Nauk. Dumka, Kiev, (1975).
[5] X. Gong, H. Kan, T. Yamagichi, I. Sazuki, M. Aoyama, M. Kumagawa, N. L. Rowell, A. Wang, and R. Rinfret, Jpn. J. Appl. Phys. **33**, 1740 (1994).

Translated by S. Chomet

Effect of deep levels on current excitation in $6H$-SiC diodes

N. I. Kuznetsov

A. F. Ioffe Physicotechnical Insitute, Russian Academy of Sciences, 194021 St. Petersburg, Russia

J. A. Edmond

Cree Research Inc. 2810 Meridian Parkway, Suite 176, Durham, NC 27713, USA

(Submitted January 30, 1997; accepted for publication April 3, 1997)
Fiz. Tekh. Poluprovodn. **31**, 1220–1224 (October 1997)

The results of an experimental study of deep levels in the p-base of $6H$-SiC diodes are presented. A deep level of unknown origin, with ionization energy $E_c-1.45$ eV, acts as an effective recombination center for minority carriers, and controls recombination processes. A level with ionization energy $E_c-0.16$ eV is attributed to a nitrogen donor impurity. Electron capture and thermal activation processes associated with this level substantially extend the duration of current relaxation in the $p-n$ junction. © *1997 American Institute of Physics.*
[S1063-7826(97)01810-3]

INTRODUCTION

Silicon carbide is at present attracting considerable attention as one of the most promising wide-gap semiconductors for fast high-power instrumentation, capable of operating at high temperatures. Traps with energy levels in the bandgap of the semiconductor, as we know, affect adversely the response of such devices. Two types of trap are commonly recognized: recombination levels and attachment levels. According to the interaction with band conduction, attachment levels can be divided into two types, namely, single attachment levels (β-levels) for which the establishment of thermal equilibrium with the band takes much longer than the carrier lifetime and multiple attachment levels (α-levels), for which the time for establishing thermal equilibrium with the band is shorter than the carrier lifetime. The effect of attachment levels on current relaxation in $p-n$ junctions was discussed in Refs. 1 and 2, where it was shown that the β-levels have practically no effect on current relaxation because of the low rate of thermal depletion, whereas the effect of α-levels can be appreciable only at high densities of these levels. The current-relaxation time constant then increases by a factor of $1+N_\alpha/N_{c\alpha}$ as compared with the lifetime of minority carriers, where N_α is the density of α-levels, $N_{c\alpha}=N_c \exp(-E_\alpha/kT)$, E_α is the ionization energy of the α-levels, and N_c is the density of states in the conduction band.

Very little is known at present about the traps in $6H$-SiC that act as centers for the effective recombination of minority carriers.[3–5] The effect of attachment levels on photoconductivity in SiC was described in Refs. 6–8, where it was shown that the α-levels, which are identified with the nitrogen donor impurity, determine the slow component of the photoconductivity decay curve.

The aim of the research reported here was to determine the parameters of recombination and attachment levels by transient and current spectrometry of deep levels and to investigate the effect of traps on current relaxation in $6H$-SiC diodes.

1. SAMPLES

We have investigated $6H$-SiC diodes. The diode structure was grown in a single technological process, using vapor-phase deposition (CVD) (Ref. 9). The substrates were n^+-type $6H$-SiC wafers with impurity concentrations of the order of 10^{18} cm^{-3}, available from Cree Research Inc. (USA). The expitaxial layers were deposited on the (0001) face of the Si substrate. Aluminum and nitrogen were used as the acceptor and donor impurities, respectively. The first step was to grow the n^+-type expitaxial layer, highly doped with nitrogen, and then the Al-doped p-type epitaxial layer. In the final stage, the p^+-layer, highly doped with aluminum, was deposited. The thickness of the p layer was approximately 5 μm. The electrical parameters of the $p-n$-junctions were investigated on mesa-structures with a diameter of 300 μm, using plasma-ion etching.[10] The contacts with the p^+-layer and the n^+-substrate were produced by depositing Al and Ni, respectively, followed by fusing into the medium.

The mesa-structures had the diode-type current-voltage characteristics. The cutoff voltage on the forward I–V characteristic was about 2.7 V. The total voltage drop across the structure was 4.5 V at constant forward current of 1 A. An abrupt breakdown voltage of about 600 V was observed on the reverse I–V characteristic.

The measured capacitance-voltage characteristics were used to determine the concentration profile for the uncompensated acceptor impurity in the p-layer of the diode. Figure 1 shows the typical dependence of N_a-N_d on distance from the $p-n$ junction, measured at room temperature. It is clear from the figure that the difference N_a-N_d increases with increasing distance from the $p-n$ junction, and then reaches a constant level of about 3×10^{16} cm^{-3}. The concentration gradient on the rising segment is 2×10^{20} cm^{-4}. The dependence of the barrier capacitance of such diodes on the applied voltage is $C^{-3}\sim U$, suggesting a continuous $p-n$ junction. The cutoff voltage on the capacitance-voltage characteristic was about 2.6 V. This figure is close to the built-in potential of the $6H$-SiC $p-n$ junction in which the p and n layers are doped with aluminum and nitrogen, respectively.

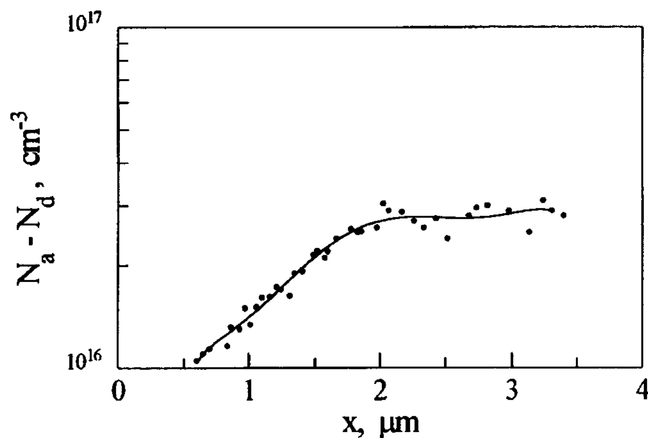

FIG. 1. Typical plot of $N_a - N_d = f(x)$ in the p-layer of the $6H$-SiC diode at room temperature.

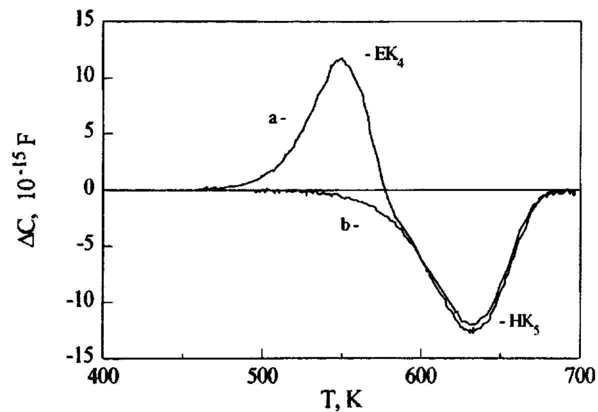

FIG. 2. Fragments of the c-DLTS spectra recorded at $t_1 = 100$ μsec, $t_2 = 200$ μsec. a—spectrum recorded when the reverse bias across the sample was switched over to a forward current of 10 mA. b—spectrum recorded when the reverse bias was abruptly reduced to zero.

The diffusion length of minority carriers (electrons) in the p-layer was determined at room temperature by measuring the current induced by an electron probe. It was found to be $1-1.5$ μm. This corresponds to an electron lifetime of $(2-5) \times 10^{-9}$ sec, which yields an electron mobility of 200 cm^2/(V·s) (Ref. 11).

2. EXPERIMENTAL RESULTS AND DISCUSSION

Deep levels. Deep levels in the bandgap of a semiconductor are commonly investigated by capacitive deep-level transient spectroscopy, known as the c-DLTS method, which was originally proposed by Lang.[12] However, capacitive methods have a limited temperature range when p-type SiC levels are investigated, because the holes are frozen-in when the sample is cooled below 200 K. We have therefore employed current transient spectroscopy—the i-DLTS method[13] — to investigate these levels at low temperatures.

The DLTS measurements were performed in the temperature range between 77 and 700 K. A reverse bias of 5 V was applied to the mesa-structure. The traps were filled with majority carriers (holes) by abruptly reducing the reverse bias to zero. To fill the traps with minority carriers, the reverse bias was abruptly switched to a direct current of 10 mA. The level parameters were determined by recording a family of DLTS spectra for a constant ratio $t_2/t_1 = 2$ and different t_1 in the range between 1 and 500 msec and between 10 μsec and 10 msec, using c-DLTS and i-DLTS, respectively. The quantities t_1 and t_2 are the instants of time at which the capacitance and current-relaxation amplitudes were measured in the c-DLTS and i-DLTS.

Figure 2 shows fragments of the c-DLTS spectrum. It is clear that there are two peaks at temperatures in excess of 400 K, marked HK_5 and EK_4, respectively. Each peak in the DLTS spectrum corresponds to a level in the bandgap. Peaks with a negative sign are due to majority-carrier (holes in this case) charge transfers on the corresponding level, whereas peaks with positive sign are due to minority-carrier (electrons) charge transfers.

Figure 3 shows fragments of the i-DLTS spectrum. It is clear that there are three peaks at temperatures above 200 K, marked HK_1, EK_2, and EK_3. Since the direction of the current passing through the $p-n$ junction is independent of the carrier type (electron or hole) involved in the deep-level charge transfers, the peaks on the i-DLTS spectrum have the same sign.[13] The HK_1 peak is due to majority-carrier (hole) charge transfers on the HK_1 *level*. The peaks EK_2 and EK_3 are due to minority-carrier (electrons) charge transfers on the EK_2 and EK_3 levels.

The parameters of these levels were determined from the Arrhenius relation (Fig. 4), which was constructed from the family of DLTS spectra. The numerical results are summarized in Table I. The capture cross sections were calculated using the following effective masses for electrons and holes: $m_e^* = 0.27 m_0$ (Ref. 14) and $m_h^* = 1.0 m_0$ (Ref. 15).

Since the level EK_4 lies near the midpoint of the bandgap (see Table I) and since it has a relatively high capture cross section for minority carriers (electrons), it can act as a center for the effective recombination of carriers. Actually, the electron lifetime τ_n determined by this level is approximately 10^{-8} sec. The value obtained for τ_n is close to that

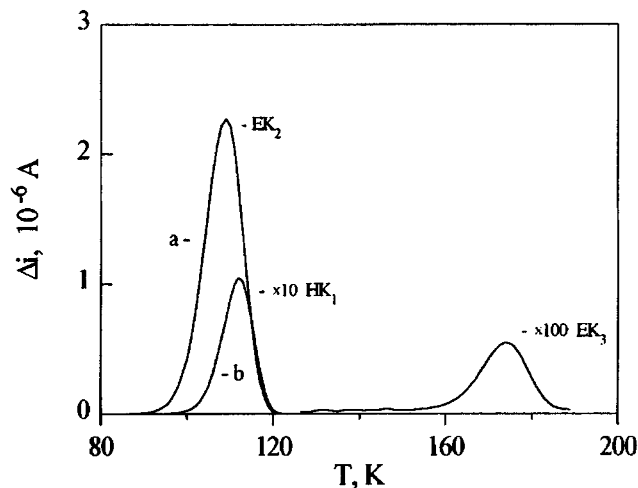

FIG. 3. Fragments of the i-DLTS spectra recorded at $t_1 = 0.1$ μsec, $t_2 = 0.2$ μsec. a—spectrum recorded when the reverse bias across the sample was switched over to a forward current of 10 mA. b—spectrum recorded when the reverse bias was abruptly reduced to zero.

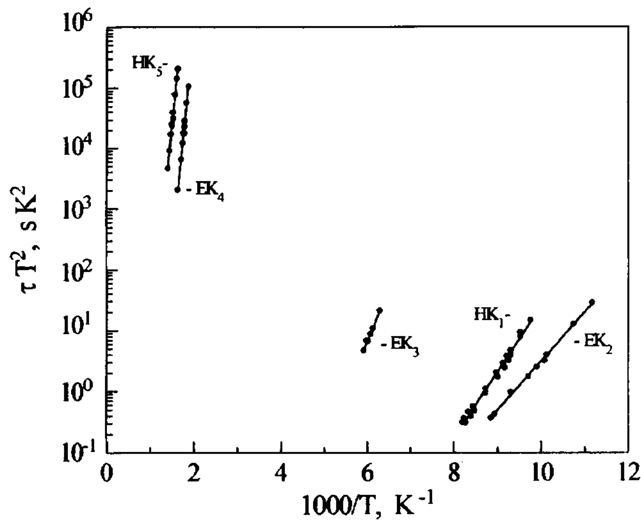

FIG. 4. Arrhenius plot for the new levels.

calculated earlier from the diffusion length. The small discrepancy between the values of τ_n may be due to the presence of an additional channel for recombination on deep energy levels.

Since the ionization energy of HK_1 is close to the ionization energy of the aluminum impurity in $6H$-SiC (Ref. 16 and 17) and since the p- layer was doped with aluminum, we attribute HK_1 to the aluminum impurity. We note, however, that the parameters of HK_1 were determined with allowance for the temperature dependence of the hole capture cross section of the charged center.[18]

Measurements performed on different mesa structures have shown that the EK_2 concentration is relatively high, i.e., $(3-5)\times 10^{17}$ cm^{-3}. It is important to note that this level is concentrated near the $p-n$ junction. The EK_2 ionization energy is close to that of the nitrogen atom that occupies the cubic position in the crystal structure of $6H$-SiC (Refs. 14 and 19). We therefore assign EK_2 to the nitrogen donor impurity. We emphasize that the $N_a - N_d$ concentration profile (Fig. 1) could have been due to the diffusion of nitrogen into the p-layer when the structure was grown. Judging by its interaction with the conduction band, the EK_2 level can be attributed to the α-levels, because the time taken to establish thermal equilibrium between this level and the conduction band, $t_\alpha = 2\times 10^{-10}$ sec, is much shorter than the electron lifetime τ_n. Since EK_2 has a sufficiently high concentration, it may influence the current relaxation across the $p-n$ junction. Actually, as noted in the Introduction, the current relaxation time should increase by the factor $1+N_\alpha/N_{c\alpha}$, i.e., by a factor of 8–12 at room temperature when the EK_2 concentration is taken into account. It follows that when the current kinetics across the $p-n$ junction is investigated, one can expect relaxation with a time constant much greater than the lifetime of minority carriers. On the other hand, attachment processes have no effect on the steady distribution of free carriers in the case of direct current flow. This is so because the capture of nonequilibrium carriers to the attachment levels under steady conditions is balanced by the thermal ejection of carriers from these levels. Hence the current-voltage characteristics of diodes under steady-state conditions are determined by carrier recombination processes and not attachment processes.

Current-voltage characteristics. The forward branches of the current-voltage characteristics have an exponential shape. At low currents ($10^{-6}-10^{-3}$ A/cm^2), the behavior of the current can be described by the classical theory of Shockley, Noyce, and Sah.[20] According to this theory, the flow of current is due to the recombination of carriers within the space charge layer via the recombination level lying near the center of the bandgap the effective carrier lifetime calculated from these current-voltage characteristics was 5×10^{-9} sec. This figure is practically equal to the value of τ_n obtained from the diffusion length. The EK_4 level can take on the role of the recombination level among the deep levels that we have detected. For average currents in the range to $10^{-3}-1$ A/cm^2, the behavior of the current can be described by the generalized Shockley-Noyes-Sah theory.[21] According to this theory, the flow of current is due to carrier recombination via a doubly charged center. Unfortunately, our DLTS measurements have not revealed the presence of this center, but we note that the presence of this doubly charged center could explain the discrepancy between the values of the electron lifetimes deduced from the EK_4 level parameters and from measurements of the diffusion length and current-voltage characteristic. We recall that, in addition to the recombination channel via the EK_4 level, there is a further recombination channel in the form of the doubly charged center mentioned above.

Current kinetics in the $p-n$ junction. The current kinetics in the $p-n$ junction was investigated using equipment with time resolution of the order of 5×10^{-10} sec. The sample used in these measurements was forward-biased, producing a forward current J_f. At time $t=0$, a reverse-bias pulse of $10^{-7}-10^{-6}$ sec was applied. The reverse J_r was produced during this pulse. The shape of the reverse current pulse was observed on a high-frequency oscillograph (Fig. 5). The variation in this current with time can be divided into two phases. In phase 1 ($0<t<t_r$), the reverse current J_r was constant. It was assumed that phase 1 concludes during t_r

TABLE I. Parameters of the new level.

Level	E_t, eV	σ_n, cm^2	σ_p, cm^2	N_t, cm^{-3}	Method
EK_2	$E_c-0.16$	$\sim 10^{-14}$	-	$(3-5)\times 10^{17}$	i-DLTS
EK_3	$E_c-0.34$	8×10^{-13}	-	$\sim 4\times 10^{14}$	i-DLTS
EK_4	$E_c-1.45$	$\sim 10^{-13}$	-	$\sim 10^{14}$	c-DLTS
HK_1	$E_v+0.24$	-	$7.4\times 10^{-13}\ (300/T)^3$	$\sim 10^{16}$	i-DLTS
HK_5	$E_v+1.41$	-	6×10^{-16}	$\sim 10^{14}$	c-DLTS

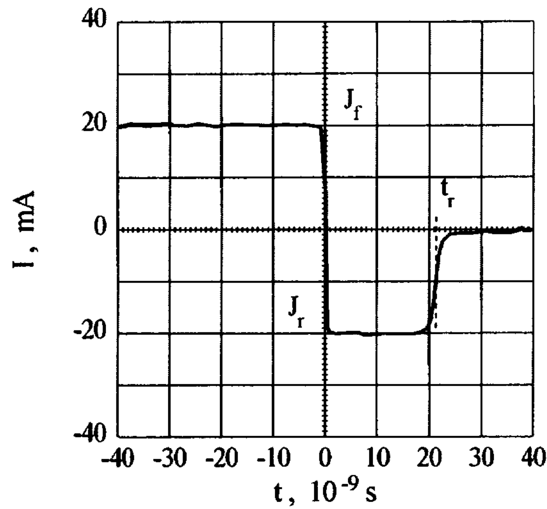

FIG. 5. Oscilloscope trace of a current pulse when the diode is switched from forward to reverse current ($J_f \rightarrow J_r$).

when the density of the injected minority carriers falls to zero. During phase 2 ($t > t_r$), the reverse current J_r falls rapidly to values corresponding to the leakage current. The time t_r depends on the ratio J_r/J_f and the lifetime τ_r of minority carriers. It can be found from the transcendental equation[22]

$$\frac{J_f}{J_f+J_r}=\operatorname{erf}\left(\sqrt{\frac{t_r}{\tau_r}}\right). \tag{1}$$

Measurement of the duration t_r of the reverse-current step (Fig. 5), when the diode is switched from forward to reverse current, is widely used to determine the lifetime of minority carriers. When $J_r/J_f = 1$, the duration of the forward current phase is approximately $0.3\tau_r$ (Ref. 23). Measurements of t_r with $J_r/J_f = 1$ performed on different diodes have shown that t_r lay in the range $(2-5)\times 10^{-8}$ sec. Hence, $\tau_r = (7-17)\times 10^{-8}$ sec, which means that τ_r is much greater than the value of τ_n obtained earlier from the diffusion length and the current-voltage characteristic. This difference between τ_r and τ_n is due to a difference between the conditions under which the measurements were performed. The diffusion length and the current voltage characteristics were measured under steady-state conditions, so that the results obtained were independent of the attachment levels. The current kinetics in the $p-n$ junction, on the other hand, was examined under nonsteady conditions and the results obtained were influenced by the attachment α-levels. Capture and thermal activation of minority carriers associated with the EK_2 level control the length t_r of the reverse current J_r. Actually, a correlation was observed between between the concentration of the EK_2 level and the time t_r. The time t_r increases with the EK_2 level concentration. Hence the step duration t_r does not directly correspond to the electron lifetime in this case.

CONCLUSIONS

We have investigated 6H-SiC diodes, whose structure was grown by CVD in a single process. Aluminum and nitrogen were used as the acceptor and donor impurities, respectively. It was found that a level with ionization energy $E_c - 1.45$ eV was present in the p-layer of the diodes and acted as an effective recombination center for minority carriers. A level with ionization energy of $E_c - 0.16$ eV can be attributed to the donor nitrogen impurity. Electron capture and thermal activation processes associated with this level greatly extend the duration of current relaxation in the $p-n$ junction.

The authors wish to thank V. A. Dmitriev and the staff of Cree Research Inc. for providing them with the $p-n$ structures, and V. A. Solov'ev for carrying out the measurements.

This research was supported, in part, by the U.S. Department of Defense.

[1] F. M. Berkovskii, S. M. Ryvkin, and N. B. Strokan, Fiz. Tekh. Poluprovodn. **3**, 230 (1961) [*sic*].
[2] F. M. Berkovskii, S. M. Ryvkin, and N. B. Strokan, Fiz. Tekh. Poluprovodn. **3**, 3535 (1961) [*sic*].
[3] M. M. Anikin, A. S. Zubrilov, A. A. Lebedev, A. M. Strel'chuk, and V. E. Chelnokov, F. M. Berkovskii, S. M. Ryvkin, and N. B. Strokan, Fiz. Tekh. Poluprovodn. **25**, 479 (1991) [Sov. Phys. Semicond. **25**, 289 (1991)].
[4] N. T. Son, E. Sorman, W. M. Chen, O. Kordina, B. Monemar, and E. Janzen, Appl. Phys. Lett. **65**, 2687 (1994).
[5] St. G. Muller, D. Hoffmann, A. Winnacker, E. N. Mokhov, and Yu. A. Vodakov, Inst. Phys. Conf. Ser. **142**, 361 (1996).
[6] G. F. Goluyanov, Fiz. Tekh. Poluprovodn. **4**, 3170 (1993) [Semiconductors **27**, 925 (1993)].
[7] A. I. Veinger and K. P. Fiz. Tekh. Poluprovodn. **2**, 294 (1968) [Sov. Phys. Semicond. **2**, 247 (1968)].
[8] G. Borda, E. E. Violin, G. N. Violina, and Yu. M. Tairov, Fiz. Tekh. Poluprovodn. **11**, 2551 (1969) [*sic*].
[9] H. S. Kong, J. T. Glass, R. F. Glass, and R. F. Davis, J. Appl. Phys. **64**, 2672 (1988).
[10] J. W. Palmour, R. F. Davis, T. M. Wallett, and K. B. Bhasin, J. Vac. Sci. Technol. A **4**, 590 (1990).
[11] T. Tachibana, H. S. Kong, Y. C. Wang, and R. F. Davis, J. Appl. Phys. **67**, 6375 (1990).
[12] D. V. Lang, J. Appl. Phys. **45**, 3023 (1974).
[13] N. I. Kuznetsov, Fiz. Tekh. Poluprovodn. **27**, 1674 (1993) [Semiconductors **27**, 925 (1993)].
[14] W. Suttrop, G. Pensl, W. J. Chyke, R. Stein. S. Leibenzeder, J, Appl. Phys. **72**, 3708 (1992).
[15] H. J. van Daal, W. F. Knippenbery, J. D. Wasscher, J. Phys. Chem. Solids **24**, 109 (1963).
[16] M. Ikeda, H. Matsunami, and T. Tanaka, Phys. Rev. B **22**, 2842 (1980).
[17] N. I. Kuznetsov, A. P. Dmitriev, and A. S. Furman, Fiz. Tekh. Poluprovodn. **28**, 1010 (1994) [Semiconductors **28**, 584 (1994)].
[18] V. N. Abakumov, V. I. Perel', I. N. Yassievich, Fiz. Tekh. Poluprovodn. **12**, 3 (1978) [Sov. Phys. Semicond. **12**, 1 (1978)].
[19] O. V. Vakulenko and O. A. Guseva, Fiz. Tekh. Poluprovodn. **15**, 1528 (1981) [Sov. Phys. Semicond. **15**, 886 (1981)].
[20] C. T. Sah, R. N. Noyce, and W. Shockley, Proc. IRE **45**, 1228 (1957).
[21] V. V. Evstropov, K. V. Kiselev, I. L. Petrovich, and B. V. Tsarenkov, Fiz. Tekh. Poluprovodn. **18**, 1852 (1984) [Sov. Phys. Semicond. **18**, 1156 (1984)].
[22] Yu. R. Nosov, *Physical Principles of the Semiconductor Diode Operating in the Pulse Mode*, Nauka, 1968.
[23] S. M. Sze, *Physics of Semiconductor Devices*, Wiley, N.Y. (1981).

Translated by S. Chomet

Effect of the electric field in the space-charge layer on the efficiency of short-wave photoelectric conversion in GaAs Schottky diodes

T. V. Blank, Yu. A. Gol'dberg, O. V. Konstantinov, O. I. Obolenskiĭ, and E. A. Posse

A. F. Ioffe Physicotechnical Institute, Russian Academy of Sciences, 194021 St. Petersburg, Russia
(Submitted March 17, 1997; accepted for publication April 17, 1997)
Fiz. Tekh. Poluprovodn. **31**, 1225–1229 (October 1997)

A study is reported of the quantum efficiency of the short-wave photoelectric effect as function of the reverse bias applied to GaAs Schottky diodes when the light absorption length is much shorter than the width of the space charge region. The quantum efficiency of photoelectric conversion is found to depend strongly on the contact electric field and the photon energy. The field independence of the quantum efficiency is interpreted in terms of a fluctuational trap model. The model can also be used to determine the loss factor for hot photocarriers, which is found to increase in a stepwise manner with increasing photon energy. This effect is explained in terms of the formation of excitons in X- and L-valleys of the semiconductor.
© *1997 American Institute of Physics.* [S1063-7826(97)01910-8]

1. INTRODUCTION

The research reported here is the continuation of previous studies[1,2] of the short-wave photoelectric effect in Schottky diodes based on III–V semiconductors. In an earlier paper we reported strong temperature dependence of photoelectric conversion (PEC) in the surface-barrier structures (Schottky diodes) Ni–GaAs (Ref. 1) and Au-GaP (Ref. 2). Classical models of PEC do not involve the mechanism responsible for the strong temperature dependence of PEC quantum efficiency. To explain fully the observed relationships, we proposed in Ref. 1 a model involving a special form of traps in the space-charge region (SCR). When an electric field is present, such traps arise from fluctuations in the bottom profile of the conduction band and the ceiling of the valence band (Fig. 1). Such traps are capable of holding both photoelectrons and photoholes by localizing them in neighboring regions. The idea of traps for photocarriers in SCR constitutes a modification of the usual picture of the photoelectric conversion process. It is usually considered that the contact electric field separates all the photocarriers that have cooled down in the SCR. The presence of traps in the SCR offers a further mechanism for recombination loss that was disregarded earlier. This mechanism is very temperature sensitive. It facilitates the thermal dissociation of occupied energy levels in traps, which leads to a exponential rise in the PEC quantum efficiency. The localization (activation) energy determined in Ref. 1 from the temperature dependence of the photocurrent was found to be of the order of 20 meV.

In this paper, we report that the proposed fluctuational traps in the SCR can receive additional experimental confirmation by the observed rise in the photocurrent with increasing electric field in the SCR. It is clear from Fig. 1 that the trap potential well is triangular: the application of a reverse bias, i. e., the increase in the field, compresses the well, so that, for a fixed temperature, the increase in the electric field is accompanied by a reduction in the number of photocarriers localized in traps in the SCR, which means that there is a reduction in the recombination loss, and this is responsible for the rise in the photocurrent. The effect of the electric field was found to be very large: when this field is increased from $\mathscr{E}=1.5\times10^4$ to 4.5×10^4 V/cm, the photocurrent rises by a factor of more than 2. By using the simple triangular potential well model we are able to provide an entirely satisfactory qualitative explanation of the field dependence of the PEC quantum efficiency. This is clear from Fig. 2.

We note that previous work[3–5] was largely confined to other mechanisms for the effect of the applied voltage on PEC quantum efficiency. A rapid rise in the PEC quantum efficiency was observed in Ref. 3 in highly doped structures and was attributed to collisional ionization. The increase in PEC quantum efficiency observed in Refs. 4 and 5 was due to an increase in the width of the space charge region when a reverse bias was applied. This mechanism operates when the SCR is sufficiently narrow and its width W is less than the light absorption length l. In our case, the latter condition was not only violated in short-wave PEC, but it was also found that $l \ll W$ for $h\nu > 2$ eV. Moreover, collisional ionization was impossible when the contact field amounted to a few tens of kV/cm. It follows that traditional mechanisms for the field dependence of the PEC quantum efficiency are not valid in the case of the short-wave photoelectric effect.

We also note that, in the research reported here, we do not use the concept of internal quantum yield in order to avoid confusion in terminology. We assume that each photon is absorbed in the semiconductor with the creation of one electron-hole pair. In this sense, the internal quantum yield is assumed to be equal to unity. However, this concept often incorporates various types of loss as well. In our case, the internal quantum yield is a function of temperature and of the applied bias as well of the wavelength of the incident light. We therefore prefer to assign an individual coefficient to each type of loss and avoid using the phrase *internal quantum yield*.

2. FORMULATION OF EXPERIMENT AND RESULTS

We have investigated Ni–GaAs surface-barrier structures—a highly doped substrate n-type GaAs with elec-

 1063-7826/97/101053-04$10.00 © 1997 American Institute of Physics

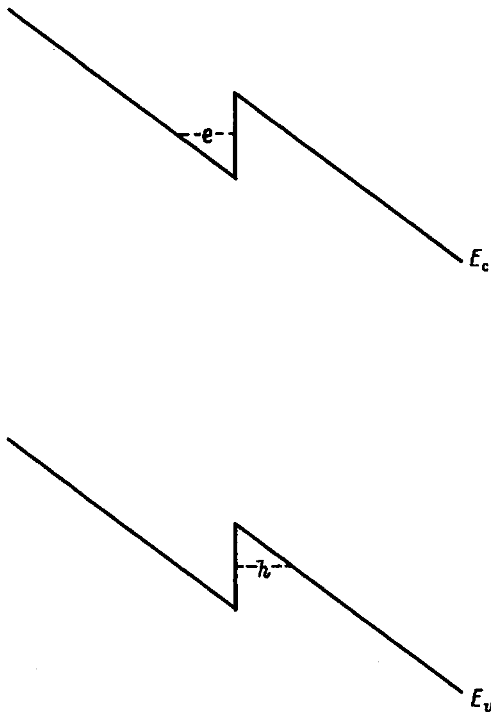

FIG. 1. Traps for electrons (e) and holes (h) produced by fluctuations in the bottom profile of the conduction band (E_c) and the top of the valence band (E_v) in the presence of the contact electric field.

tron concentration $n=10^{17}$ cm^{-3} at 300 K. A weakly doped n-type GaAs expitaxial layer ($n=10^{15}$ cm^{-3} at 300 K), 10 μm thick, was grown on one side of the substrate. A semitransparent nickel barrier contact[6] was then deposited chemically on the expitaxial layer and an ohmic contact was placed on the substrate by fusing indium to it. The total thickness of the structure was of the order of 200 μm and the illuminated surface area was about 0.06 cm^2.

We investigated the short-wave PEC quantum efficiency as a function of the reverse bias in the range 0–6 V. The photocurrent spectra were recorded at 300 K, using the DMR-4 monochromator in the photon energy range 1.8–5.2 eV. The structures under investigation were examined in the short-circuit photocurrent regime.

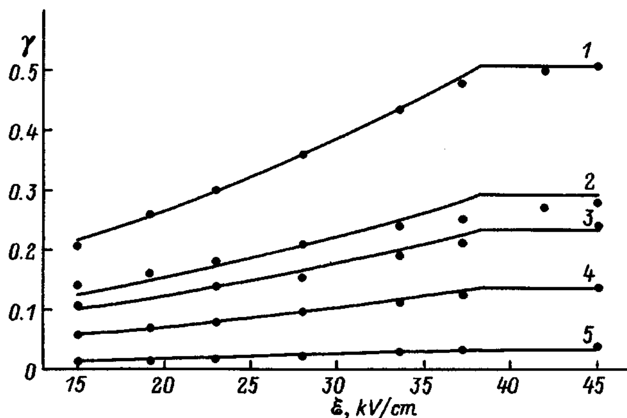

FIG. 2. External quantum yield γ as a function of maximum electric field strength in the SCR at 300 K. Points represent the measured values of γ. The increments in the electric field correspond to increments in the reverse bias between 0 and ~6 eV. The values of $h\nu$ are (in eV): *1*—2.25, *2*—2.7, *3*—3.1, *4*—4.13, *5*—5.1.

The PEC quantum efficiency (external quantum yield) was determined from the standard formula

$$\gamma=\frac{1}{eP}h\nu, \tag{1}$$

where I is the photocurrent, P is the incident photon power, and $h\nu$ is the photon energy.

Figure 2 shows the measured PEC quantum efficiency as a function of the field.

3. MECHANISM OF THE FIELD DEPENDENCE OF PEC QUANTUM EFFICIENCY

It is clear from Fig. 2 that the PEC quantum efficiency depends strongly on the applied bias. As noted above, a similar phenomenon was explained earlier[4,5] in terms of an expansion of the space charge region with increasing applied reverse bias and the corresponding increase in the fraction of electron-hole pairs separated by the contact electric field. However, this picture is valid only for photon energies just greater than the band gap, when the light absorption lengths exceeds the SCR thickness. In our case, the opposite condition, namely, $l \ll W$ was satisfied, so that the increase in the SCR width should in no way influence the PEC quantum efficiency. The increase in quantum efficiency with increasing electric field could be related to the increase in the height of the potential barrier experienced by photoelectrons entering the metal, i. e., a reduction in the loss of photoelectrons. However, simple estimates show that this phenomenon could not have such a strong influence on the PEC quantum yield as was revealed experimentally. Another possible mechanism for the dependence of the PEC quantum efficiency on the applied bias is a change in the thickness of the dead layer on the surface of the semiconductor from which all the electrons are extracted into the metal by image forces. However, the width for this layer amounts to a few tens of an angstrom and does not depend strongly on the reverse bias. This means that the change in this width for photon absorption lengths of the order of a few hundred angstroms can in no way explain the substantial change in the observed PEC quantum efficiency.

We consider that the large increase in the PEC quantum efficiency with increasing electric field can be explained in terms of the model proposed in Ref. 1 for the description of the temperature dependence of PEC quantum efficiency. This model assumes the presence of fluctuations in the bottom profile of the conduction band and the ceiling of the valence band (Fig. 1). In the contact electric field, this kind of fluctuation becomes a trap for electrons and for holes. Carriers of different sign become localized in closed spatial regions, which may give rise to their recombination.

The PEC quantum efficiency is essentially the probability that a photon will be absorbed in the semiconductor with the creation of an electron-hole pair which is then separated by the contact electric field and which contributes to the

photocurrent. The following formula, reproduced in Ref. 1, gives this probability as the product of the probabilities of three successive events:

$$\gamma=(1-R)(1-\delta_{\text{hot}})(1-\delta_{\text{therm}}), \tag{2}$$

where $1-R$ is the probability that the photon will not be reflected by the surface and will be absorbed by the semiconductor (R is light reflection coefficient), $1-\delta_{\text{hot}}$ is the probability that the electron-hole pair produced by a photon will cool down in the SCR, i. e., it will be influenced by the contact field (δ_{hot} is the coefficient representing the loss of hot carriers, which depends on the photon energy in the properties of the semiconductor), and $1-\delta_{\text{therm}}$ is the probability that the cooling electron-hole pair will be separated by the contact field and will contribute to the photocurrent (δ_{therm} is the coefficient representing the loss of thermalized carriers; it is determined by the recombination of carriers captured by the traps and depends on both the temperature and the electric field in the SCR).

We note that recombination losses on the surface were neglected because they are small in this particular series of samples.

The concentration of thermalized free carriers increases with increasing temperature because of the thermal dissociation of electron-hole pairs captured by the traps. Consequently, the PEC quantum efficiency increases with increasing temperature. The temperature dependence of the quantum efficiency was used in Ref. 1 to determine the carrier localization energy in the absence of bias across the structure. This was the starting point for the calculation of the field dependence of the PEC quantum efficiency.

The proposed mechanism for the dependence of the PEC quantum efficiency on the applied reverse bias may be described as follows. As the reverse bias increases, i.e., the contact electric field increases, the band slope in the SCR is found to increase, which in turn leads to a reduction in the localization energy of the electron-hole pair in the trap. For a given temperature, this reduction in the localization energy leads to an increase in the concentration of thermalized free carriers and, consequently, an increase in the PEC quantum efficiency.

In the case of the Boltzmann statistics

$$1-\delta_{\text{therm}}=e^{-\Delta E(\mathscr{E})/kT}, \tag{3}$$

where ΔE is the localization energy of the electron-hole pair, $\mathscr{E}$ is the electric field in the SCR, k is Boltzmann's constant, and T is the temperature. The quantum efficiency given by (2) then takes the form

$$\gamma=(1-R)(1-\delta_{\text{hot}})e^{-\Delta E(\mathscr{E})/kT}. \tag{4}$$

The dependence of the localization energy on the contact electric field is given by

$$\Delta E(\mathscr{E})=\Delta E_0-[\varepsilon(\mathscr{E})-\varepsilon(\mathscr{E}_0)], \tag{5}$$

where $\Delta E_0=22$ meV is the localization energy in the absence of the reverse bias when the electric field $\mathscr{E}$ in the SCR is $\mathscr{E}_0=15$ kV/cm, and $\varepsilon(\mathscr{E})$ is the level energy measured from the bottom of the well. Using the triangular potential well with infinite walls as the initial coarse approximation, we obtain

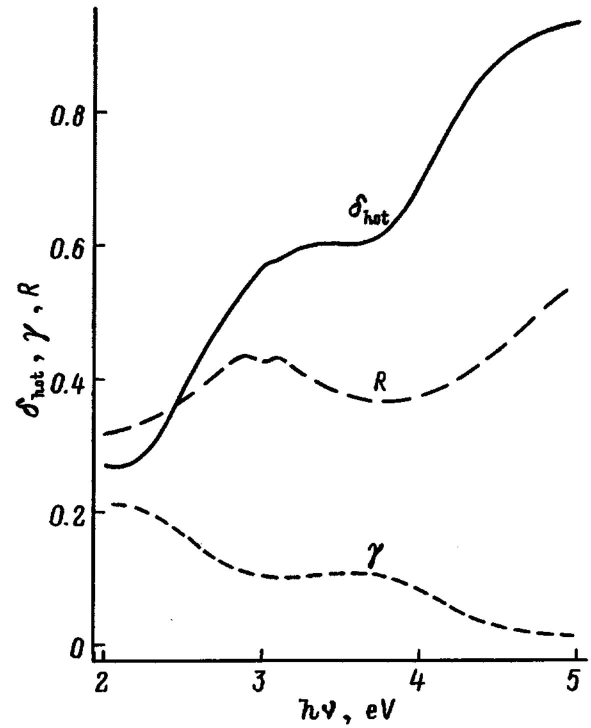

FIG. 3. Hot-carrier loss coefficient δ_{hot}, PEC quantum efficiency γ, and reflection coefficient R as a functions of photon energy.

$$\varepsilon(\mathscr{E})=\xi_1\left(\frac{\hbar^2e^2}{2m}\mathscr{E}^2\right)^{1/3}. \tag{6}$$

where $\xi_1\simeq2.34$ is the first root of the Airy function, $\hbar$ is Planck's constant, and e and m are the charge and effective mass of the electron.

It is clear from (5) and (6) that the localization energy decreases rapidly with increasing contact electric field in the SCR, which it turn leads to an increase in the PEC quantum efficiency. When the contact field is so strong that the localization energy is zero, the PEC quantum efficiency ceases to depend on the electric field. The triangular-well model with infinite walls is, of course, too approximate and disregards several factors, e. g., tunnelling through the potential barrier. This is why the theoretical curves show the 'knee' as they enter the saturation regime (Fig. 2).

4. EXCITONIC MECHANISM FOR SHORT-WAVE DECREASE OF THE PHOTOELECTRIC CONVERSION QUANTUM EFFICIENCY

If we know the dependence of the PEC quantum efficiency on photon energy we can construct the spectral dependence of the hot-carrier loss coefficient (Fig. 3). We have found that δ_{hot} is a stepped function of the photon energy, with two rapidly rising segments. The first of them is located near the photon energy $h\nu\simeq2.8$ eV and the second at $h\nu\simeq4.5$ eV. This behavior can be explained in terms of the properties of the GaAS band structure illustrated in Fig. 4.

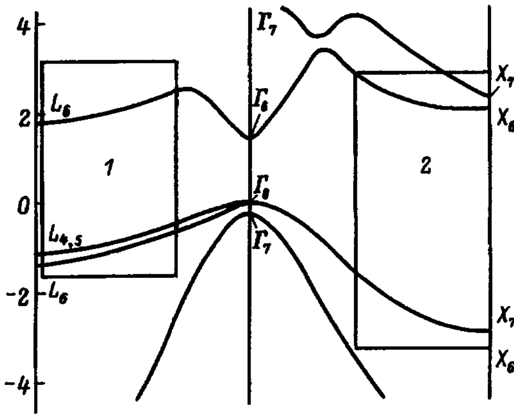

FIG. 4. Band structure of GaAs according to Ref. 7. Rectangles marked *1* and *2* represent the Brillouin zones in which there is absorption of photons with energies $h\nu \simeq 2.8$ eV (1) and 4.5 eV (2). We assume that electrons and holes produced in these regions form a tightly bound exciton and do not contribute to the photocurrent.

This figure shows segments of the Brillouin zone in which the conduction and valence bands run almost parallel to one another. These segments provide a major contribution to the absorption of photons. Region 1 corresponds to interband transitions in the L-valley with energy of the order of 2.8 eV, whereas region 2 corresponds to interband transitions in the X-valley with energy of the order of 4.5 eV.

Since in the neighborhood of the X- and L-points on the Brillouin zone the bottom of the conduction band runs almost parallel to the top of the valence band, the photoelectron and photohole velocities point in the same direction and are also close in absolute value. The Coulomb interaction then ensures that an electron and a hole can form a hot exciton. This exciton should tightly bind the electron to the hole, and should not allow their separation by the contact field in the SCR.

The formation of a hot exciton in direct transitions in the X- and L-valleys was examined in Ref. 8, where it was shown that the reciprocal of the effective mass m is given by

$$\frac{1}{m^*} = 2\frac{d^2}{d(\hbar k)^2}[E_c(k) - E_v(k)]|_{k=k_m}. \tag{7}$$

Here k_m is the point of local minimum separation between conduction and valence bands.

It is clear from Fig. 4 that the curvature of the dispersion relations is small in the neighborhood of the X- and L-points, which leads to greater effective reduced mass of the exciton, i.e., greater binding energy. This type of exciton is not readily dissociated by the contact electric field. Moreover, because of its small radius, the exciton has a weak interaction with optical phonons, i. e., a large mean free path.

Studies of the properties of such hot X- and L-excitions constitute a separate topic because of the large number of interesting physical effects, e. g., re-emission.

It seems possible, therefore, that excitons can pass through the entire SCR, reach the metal or the quasi-neutral portion of the semiconductor, and recombine there. The generation of photocarriers in the neighborhood of X- and L-points does not, therefore, contribute to the photocurrent. In our view, this is the reason for the rapid fall in the PEC quantum efficiency with increasing photon energy.

5. CONCLUSIONS

We have carried out an experimental investigation of the quantum efficiency of the photoelectric effect in the shortwave part of the spectrum as a function of the applied reverse bias in GaAs Schottky diodes, in which the light absorption length is much smaller than the width of the SCR. The field dependence of the PEC quantum efficiency was found to be very strong. It was explained in terms of a model involving fluctuational traps in SCR, used earlier to describe the temperature dependence of quantum efficiency. It was established that this model was also suitable for the description of the field dependence of the PEC quantum efficiency.

A mechanism has also been proposed for the loss of photocarriers due to the formation of excitons in the X- and L-valleys of the semiconductor. The dependence of the coefficient representing the loss of hot photocarriers on the photon energy was deduced by investigating the spectral dependence of the PEC quantum efficiency. It fits satisfactorily into the above physical picture of the ongoing processes.

[1] Yu. A. Gol'dberg, O. V. Konstantinov, O. I. Obolenskii, E. A. Posse, B. V. Tsarenkov, Fiz. Tekh. Poluprovodn. **31**, 563 (1997) [Semiconductors **31**, 473 (1997)].
[2] Yu. A. Gol'dberg, O. V. Konstantinov, E. A. Posse, B. V. Tsarenkov, Fiz. Tekh. Poluprovodn. **29**, 421 (1995) [Semiconductors **29**, 215 (1995)].
[3] A. A. Gutkin, M. V. Dmitriev, O. V. Mironova, and D. N. Nasledov, Fiz. Tekh. Poluprovodn. **5**, 385 (1971) [Semiconductors **5**, 339 (1971)].
[4] L. N. Dmitruk and O. Yu. Borkovskaya, Mikroelektronika **8**, 68 (1979).
[5] B. L. Smith and M. Abbott, Solid-State Electron. **15**, 361 (1972).
[6] Yu. A. Gol'dberg, T. V. L'vova, and B. V. Tsarenkov, Prib. Tekh. Eksper. No. 4, 212 (1976).
[7] Landolt-Burnstein, *Numerical Data and Functional Relationship in Science and Technology*, Springer-Verlag, Berlin/Heidelberg/New York, Vol. 17 (*Semiconductors*), subvolume a (*Physics of Group IV Elements and II–V Compounds*).
[8] R. F. Kazarinov and O. V. Konstantinov, Zh. Éksp. Teor. Fiz. **40**, 936 (1961) [Sov. Phys. JETP **40**, 654 (1961)].

Translated by S. Chomet

A RHEED study of the transition from two-dimensional to three-dimensional growth in the InAs/GaAs system

G. É. Tsyrlin, N. P. Korneeva, V. N. Demidov, N. K. Polyakov, V. N. Petrov, and N. N. Ledentsov[a)]

Analytic Instrumentation Institute, Russian Academy of Sciences, 198103 St. Petersburg, Russia
(Submitted April 18, 1997; accepted for publication April 23, 1997)
Fiz. Tekh. Poluprovodn. **31**, 1230–1232 (October 1997)

A specially developed detection system and an analysis of RHEED diffraction patterns were used to investigate the dynamics of transition from two-dimensional to three-dimensional growth mechanism in the heteroepitaxial InAs/GaAs system. An analysis of the dynamics of the diffraction patterns was used for the first time to investigate the dynamics of formation of quantum dots. A time shift in the dynamic behavior of the diffracted intensity for diffraction patterns recorded at different angles was found. This shift is explained in terms of the size differences in the three-dimensional islands at the initial stage of decay of the pseudomorphic layer. InAs/GaAs quantum dots grown under certain conditions produce reflections at 45° relative to the principal reflections. This is evidence for the ordering of islands in the [001] and [010] crystallographic directions. © *1997 American Institute of Physics.*
[S1063-7826(97)02010-3]

1. INTRODUCTION

There is now considerable interest in fabricating semiconductor nanostructures by direct molecular beam epitaxy (MBE).[1–3] One of the most promising ways of producing quantum dots as objects that limit the motion of charges in all three directions is heteroexpitaxial growth in mismatched systems, e. g. , in InAs/GaAs systems.[4–10] In this case, quantum dots are produced by using the spontaneous decay of a pseudomorphic layer onto a set of coherent nanoislands at the interface between semiconductors of different composition and with severe enough lattice mismatch. There is now a relatively extensive literature on the geometric properties of an ensemble of quantum dots in which these properties are investigated by transmission electron microscopy (TEM), scanning tunneling microscopy (STM), atomic force microscopy (AFM), and other methods. However, none of these methods provide a way of studying surfaces *in situ*. TEM images are very sensitive to the stress field and the data obtained by STM and AFM represent the structure of the surface after the hardening of the sample. In the case of MBE, reflective high energy electron diffraction (RHEED) is the most widely used *in situ* diagnostic technique for monitoring the state of the surface and its variation dynamics. In this paper, we report an investigation by RHEED of the dynamics of transition from the two-dimensional to the three-dimensional mechanism of heteroepitaxial growth in the InAs/GaAs system for different modifications of MBE technology.

2. EXPERIMENTAL METHODS

For the RHEED investigation, we have constructed a system for the detection and analysis of RHEED patterns. It operates in real time in steps of 40 nsec (Ref. 11) and incorporates a sensitive video camera connected via an interface to a computer and a video recorder. The software used with the system enables us to analyze any point on the diffraction image, and also the variation in intensity on the diffraction pattern in a chosen direction.

The growth experiments were performed with the EP1203 MBO equipment. After the GaAs buffer layer was grown with (2×4) surface reconstruction, and to exlude the desorption of In atoms, the surface temperature was reduced until the (2×2) superstructure was seen to appear. The growth conditions were identical in all these experiments: the rate of growth of InAs was 0.1 monolayer per second, the As/In flux ratio was of the order of 10, and the temperature of the substrate for the indium arsenide layers was 470 °C. We used two modifications of MBE, namely, submonolayer MBE (SMBE)[12] and submonolayer migration-stimulated epitaxy (SMSE).[13] In the SMBE method, the shutter of the As source is always open, whereas the shutter of the In source opens periodically. In the case of SMSE, the two shutters are open alternately. In both cases, each In deposition cycle accounts for 0.5 monolayer. The state of the surface was monitored visually on a TV monitor with simultaneous recording on the videotape.

3. EXPERIMENTAL RESULTS AND DISCUSSION

Analysis of the diffraction patterns showed that volume reflections corresponding to the transition from the two-dimensional to the three-dimensional growth mechanism appear for a larger amount of deposited InAs in the SMBE method as compared with the SMSE under identical growth conditions. This is so because the accumulated stress (due to the mismatch between the lattice constants of GaAs and InAs) occurs more rapidly in SMSE because of the more metal-stabilized growth conditions (3×1) and (1×1) surface reconstructions in SMSE and SMBE, respectively.[14]

Intensity measurements on the diffraction patterns along the principal reflections showed that the transition from the two-dimensional to the three-dimensional growth mechanism

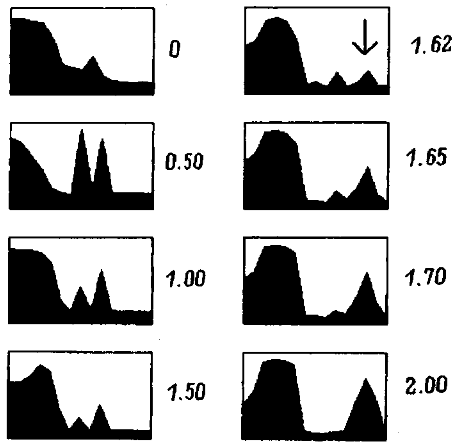

FIG. 1. Variation in the intensity of the (01) reflection during submonolayer molecular-beam epitaxy. Numbers next to the drawings represent the thickness of the InAs layer in terms of the number of monolayers. Arrow shows the appearance of volume reflections.

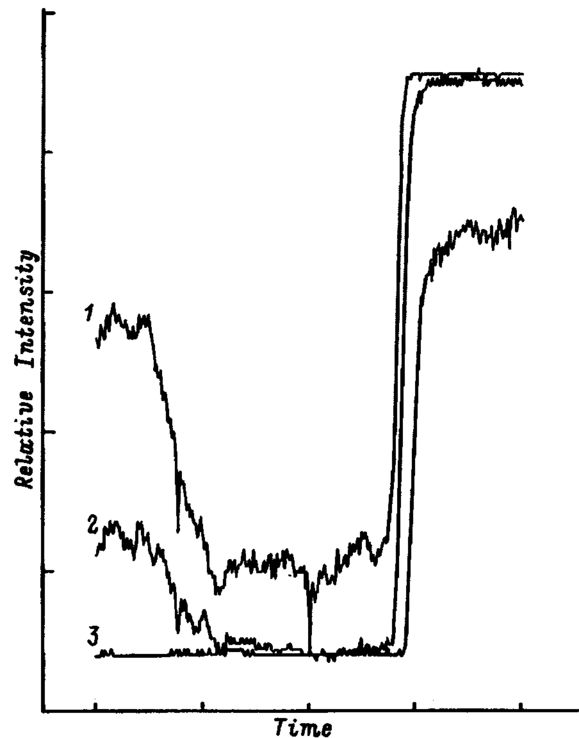

FIG. 2. Time dependence of the diffracted intensities at 4°(*1*),5°(*2*), and 8°(*3*) during submonolayer molecular-beam epitaxy.

in the decay of the pseudomorphic InAs layer onto ensemble of islands is governed by a relatively complex mechanism. In SMBE, the RHEE pattern becomes somewhat diffuse after the deposition of 0.2 monolayers of InAs, and the volume component of the diffraction spots begins to appear in the range 10-15 monolayers. This growth stage is characterized by a corrugated surface structure.[15] When the thickness of the InAs layer reaches its critical value of the order of 16-18 monolayers, the diffraction pattern transforms rapidly to pure volume reflections and shows no changes for up to dozens of monolayers of InAs. The overall picture remains the same in the case of SMSE, but the transition from diffuse reflections to the pure volume reflections occurs more rapidly. The separation between the volume reflections corresponds to the InAs lattice constant for both growth modes. Figure 1 illustrates the dynamics of the intensity variation in the case of the 0.1 reflection in SMSE. The onset of islands on the surface, estimated from the RHEED data, occurs when 1.6 monolayers are deposited within accuracy of 0.02 monolayer.

Our investigation of the kinetics of the transition from two-dimensional to three-dimensional growth mechanism has shown that there is an interval during which three-dimensional islands are formed on the surface. Figure 2 shows the time dependence of the RHEED intensity recorded at different reflection angles. We see that there are different instants of time at which the reflection intensity begins to rise rapidly. The onset of intensity saturation is also found to occur at different times for different reflection angles. The intensy minimum corresponds to the beginning of the transition of the two-dimensional to three-dimensional growth mechanism, whereas saturation occurs when the island sizes assume steady values. In our view, the observed shift can be associated with different island dimensions (height and perimeter) at the intial stage of decay of the pseudomorphic layer. Once saturation has been reached, the island dimensions become ordered and only their surface density increases. This is confirmed by STM data and optical studies of such structures[16] where an increase in the amount of InAs deposited on GaAs from two to three monolayers was found to lead to a rise in the density of quantum dots on the surface, whereas their lateral dimensions remained the same as before. According to the data reported in Refs. 17 and 18, the transition from two-dimensional to three-dimensional growth mechanism in InAs/GaAs passes through an intermediate formation of quasi-three-dimensional clusters (height 2×4 monolayers), and the appearance of InAs islands on the surface occurs via a stage with a large spread in the geometric dimensions. Further deposition of InAs results in the stabilization of the island dimensions. Recent data on the optical properties of the InAs/GaAs ensemble on the whole confirm this model of heteroepitaxial growth, and are in agreement with the dynamics of RHEED patterns on the initial stage of decay of the pseudomorphic layer.

The growth experiments revealed changes in the RHEED patterns consisting of the appearance of reflections at 45° relative to the principal reflections when the critical thickness of the InAs layer was exceeded. These changes suggest that the islands become ordered in the [001] and [010] directions. In accordance with the conclusions reported in Ref. 19, the surface energy minimum corresponds to the spatial distribution of islands in the form of a two-dimensional square lattice with axes along the [001] and [010] directions. The theoretical results given in Ref. 19 are thus seen to provide a qualitative explanation of the dynamics of the RHEED patterns. The data obtained for such structures by TEM and STM methods have also confirmed that the islands are distributed in the form of a two-dimensional periodic lattice.[5,16]

4. CONCLUSIONS

The above results thus constitute evidence for the fact that RHEED studies can be used as a precise means of *in situ* monitoring the onset of the transition from the two-dimensional to the three-dimensional growth mechanism, e. g., during heteroepitaxial growth in the InAs/GaAs system. Studies of the dynamics of RHEED patterns confirm that the growth kinetics has a substantial effect on the evolution of surface morphology during the initial stages of growth.

This research was carried out with the partial support of the Russian Fund for Fundamental Research (Grant No. 95-02-05084-A), the INTAS Fund (Grant No. 94-1028), and the Physics of Solid State Nanostructures Program.

[a]A.F. Ioffe Physicotechnical Institute, Russian Academy of Sciences, 194021 St. Petersburg, Russia

[1]Y.-W. Mo, B. S. Swartzentruber, R. Kariotis, M. B. Webb, and M. G. Lagally, Phys. Rev. Lett. **63**, 2393 (1989).
[2]R. Nötzel, N. N. Ledentsov, L. Däweritz, M. Hohenstein, and K. Ploog, Phys. Rev. Lett. **67**, 3812 (1991).
[3]J. Tersov and R. M. Tromp, Phys. Rev. Lett. **70**, 2782 (1993).
[4]L. Goldstein, F. Glas, J. Y. Marzin, M. N. Charasse, and G. Le Roux, Appl. Phys. Lett. **47**, 1099 (1985).
[5]M. Grundman, J. Christen, N. N. Ledentsov, J. Böhrer, D. Bimberg, S. S. Ruvimov, P. Werner, U. Richter, U. Gösele, J. Heydenreich, V. M. Ustinov, A. Yu.Egorov, A. E. Zhukov, P. S. Kop'ev, and Zh. I. Alferov, Phys. Rev. Lett. **74**, 4043 (1995).
[6]R. Leon, S. Fafard, D. Leonard, J. I. Merz, and P. M. Petroff, Phys. Rev. B **50**, 11687 (1994).
[7]N. Kirstaedter, N. N. Ledentsov, M. Grundmann, D. Bimberg, V. M. Ustinov, S. S. Ruvimov, M. V. Maximov, P. S. Kop'ev, Zh. I. Alferov, U. Richter, P. Werner, U. Gösele, and J. Heydenreich, Electron. Lett. **30**, 1416 (1994).
[8]D. S. I. Mui, D. Leonard, L. A. Coldren, nd P. M. Petroff, Appl. Phys. Lett. **66**, 1620 (1995).
[9]G. E. Cirlin, G. M. Guryanov, A. O. Golubok, S. Ya. Tipissev, N. N. Ledentsov, P. S. Kop'ev, M. Grundmann, and D. Bimberg, Appl. Phys. Lett. **67**, 97 (1995).
[10]G. M. Guryanov, G. E. Cirlin, V. N. Petrov,N. K. Polyakov, A. O. Golubok, S. Ya. Tipissev, E. P. Misikhina, V. B. Gubanov, Yu. B. Samsonenko, and N. N. Ledentsov, Surf. Sci. **331-333**, 414 (1995).
[11]V. B. Gubanov, G. M. Gur'yanov, V. N. Demidov, V. G. Dubrovskii, N. P. Korneeva, V. N. Petrov, N. K. Polyakov, Yu. B. Samsonenko, and G. E. Cirlin, Nauch. Priborostroenie **6**, 3 (1996).
[12]P. D. Wang, N. N. Ledentsov, C. M. Sotomayor Torres, M. Grundmann, and V. M. Ustinov, Appl. Phys. Lett. **64**, 1526 (1994).
[13]G. E. Tsirlin, A. O. Golubok, S. Ya. Tipisev, N. N. Ledentsov, and G. M. Gur'yanov, Fiz. Tekh. Poluprovodn., **29**, 1697 (1995) [Semiconductors **29**, 884 (1995)].
[14]G. M. Gur'yanov, G. E. Cirlin, V. N. Petrov, N. K. Polyakov, A. O. Golubok, S. Ya. Tipissev, V. B. Gubanov, B. Samsonenko, N. N. Ledentsov, V. A. Shchukin, M. Grundmann, D. Bimberg, and Zh. I. Alferov, Surf. Sci. **352-354**, 651 (1996).
[15]G. M. Gur'yanov, G. E. Cirlin, A. O. Golubok, S. Ya. Tipissev, N. N. Ledentsov, V. A. Shchukin, M. Grundmann, D. Bimberg, and Zh. I. Alferov, Surf. Sci. **352-354**, 646 (1996).
[16]G. E. Cirlin, V. N. Petrov, N. K. Polyakov, V. N. Demidov, N. P. Korneeva, A. O. Golubok, S. Ya. Tipissev, V. G. Dubrovskii, G. M. Gur'yanov, M. V. Maximov, N. N. Ledentsov, and D. Bimberg, *Abstracts of International Symp. on Nanostructures: Physics and Technology 96*, St. Petersburg, Russia, 1996, p. 375.
[17]N. P. Kobayashi, T. R. Ramachandran, P. Chen, and A. Madhukar, Appl. Phys. Lett. **68**, 3299 (1996).
[18]T. R. Ramachandran, R. Heitz, P. Chen, and A. Madhukar, Appl. Phys. Lett. **70**, 640 (1997).
[19]V. A. Shchukin, N. N. Ledentsov, M. Grundmann, P. S. Kop'ev, and D. Bimberg, Surf. Sci. **352-354**, 117 (1996).

Translated by S. Chomet

High-temperature irradiation of gallium arsenide

V. V. Peshev and S. V. Smorodinov

V. D. Kuznetsov Siberian Technical Insititute, 63405 Tomsk, Russia
(Submitted March 26, 1997; accepted for publication April 29, 1997)
Fiz. Tekh. Poluprovodn. **31**, 1234–1235 (October 1997)

Deep level transient spectrocopy was used to investigate the introduction of P2 and P3 centers into n-type epitaxial layers of GaAs as a result of exposure to 4-MeV electrons in the temperature range 380−550 °C. It is shown that the rate at which the centers are introduced into the layers is independent of temperature in this range. The P2 center concentration is proportional to $D^{0.7}$, whereas for the $P3$ center this function is $D^{0.5}$, where D is the electron dose. © *1997 American Institute of Physics.* [S1063-7826(97)02110-8]

Only a few papers dealing with high-temperature irradiation of GaAs have been published. Deep electron traps were reported in Ref. 1 after exposure to radiation at 300 °C. It is shown in Ref. 2 that the dominant center in n-type GaAs irradiated at 400 °C is the $P3$ center. However, the temperature range in which defects introduced at high temperatures are stable is not known; not known either is the kinetics of their acquisition by the layer. In this paper we report a study of the dose dependence of the concentration of the radiation-induced defects in GaAs in the temperature range 380−550 °C.

We investigated Schottky-barrier diodes produced by the deposition of Ti on n-type epitaxial GaAs layers with electron concentration $n \approx 3\times 10^{15}$ cm^{-3}. The layers were exposed to 4-MeV electron pulses with mean current density of 0.8 μA/cm^2, with the temperature maintained by a heater. The deep level parameters were measured by c-DLTS.

Figure 1 shows the high-temperature part of the spectrum of a Schottky diode exposed at 380 °C to an integral electron flux $D = 2.4\times 10^{15}$ cm^{-2}. Comparison of the diode spectra recorded at 380 °C with the spectra of diodes irradiated at room temperature and annealed at 380 °C has shown that the center introduced at high temperatures corresponds to centers formed during the annealing process. Measurements of the emission activation energy E_{na} and of the effective capture cross section σ_{na} for electrons trapped by the dominant center (Fig. 1) yielded $E_{na} = 0.74$ eV and $\sigma_{na} = 10^{-13}$ cm^2, which is close to the corresponding parameters for the $P3$ center.[3] Unfortunately, the peaks are not well resolved, so that reliable identification of the $P2$ peak (Fig. 1) was not possible. Our data ($E_{na} = 0.6$ eV, $\sigma_{na} = 10^{-14}$ cm^2) are inconsistent with the data reported in Ref. 3, but are close to those obtained in Ref. 4 for the $P2$ center.

Figure 2 shows the concentration N_{P3} of $P3$ defects as a function of the irradiation dose, obtained at different temperatures, giving $N_{P3} \sim D^{0.5}$. We note that this type of dose dependence corresponds to a care in which a defect that is complementary to the $P3$ center is mobile at the 'irradiation temperature' and vanishes at unsaturated sinks[5] – possibly dislocations. Moreover, it follows from Fig. 2 that the rate at

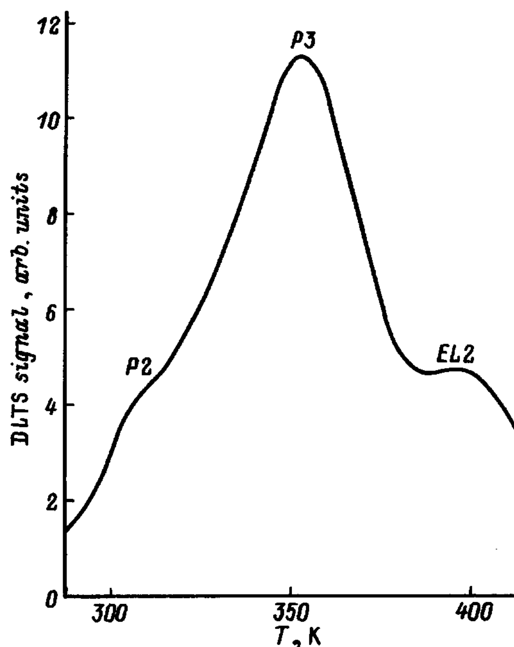

FIG. 1. High-temperature branch of the Schottky barrier diode, measured by c-DLTS. The diode was exposed to an electron beam at $T = 380$ °C, $\tau = 5\times 10^{-3}$ sec.

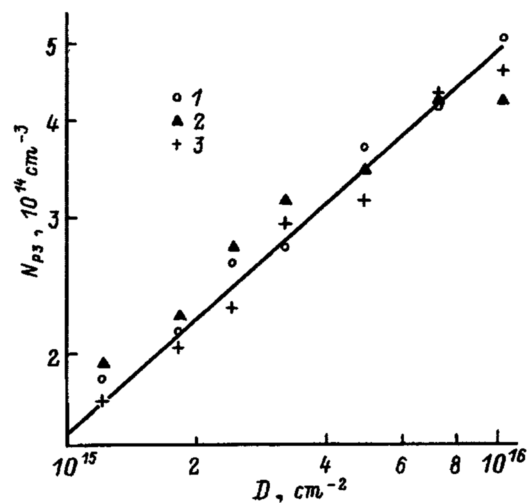

FIG. 2. Concentration of P3 centers plotted as a function of the electron-beam flux density at the following temperatures (in °C): 380 (*1*), 480 (*2*), 550 (*3*).

 1063-7826/97/101060-02$10.00 © 1997 American Institute of Physics

which the $P3$ defects are introduced is independent of the irradiation temperature in the range 380–550 °C. We have shown that the concentration of $P2$ centers is also a nonlinear function of the dose and is described by $N_{P2} \sim D^{0.7}$. It has not yet been established unambiguously whether the $P3$ centers in samples irradiated at room temperature are produced as a result of the modification of defects during subsequent annealing ($T \geqslant 300$ °C) or whether they are defects which are acquired during irradiation at at room temperature, but which are masked by peaks due to the well-known centers $E4$ and $E5$. In the former case, N_{P3} should be a linear function of the dose because it is known that the $E4$ and $E5$ acquisition kinetics is linear. If, on the other hand, $N_{P3} \sim D^{0.5}$ for the same samples, then it may be concluded that we have the second case and defects that are complementary to the $P3$ centers should be mobile at room temperature. Further research should yield the function $N_{P3} = f(D)$ for samples annealed at $T \geqslant 300$ °C after irradiation at room temperature.

We have thus shown that the concentration of the $P2$ and $P3$ centers is proportional to $D^{0.7}$ and $D^{0.5}$, respectively, and that the rate at which these centers are acquired is independent of temperature in the range 380–550 °C.

[1] D. Stievenard and J. C. Bourgoin, J. Appl. Phys. **59**, 743 (1986).
[2] V. N. Brudnyi and V. V. Peshev, Phys. Status Solidi (A) **105**, K57 (1988).
[3] D. Pons and J. C. Bourgoin, J. Phys. C: Sol. St. Phys. **18**, 3839 (1985).
[4] V. A. Ivanyukovich, V. I. Karas', and V. M. Lomako, Fiz. Tekh. Poluprovodn. **24**, 1427 (1990) [Sov. Fiz. Semicond. **24**, 893 (1990)] .
[5] M. W. Thompson, *Defects and Radiation Damage in Metals*, Cambridge University Press, Cambridge, (1969).

Translated by S. Chomet

The role of defects in the formation of local states induced by atoms adsorbed on a semiconductor surface

S. Yu. Davydov

A. F. Ioffe Physicotechnical Institute, Russian Academy of Sciences, 194021 St. Petersburg, Russia
(Submitted November 11, 1996; accepted for publication February 18, 1997)
Fiz. Tekh. Poluprovodn. **31**, 1236–1241 (October 1997)

The generalized Anderson-Haldane band model of a semiconductor is used to consider the influence of quasi-localized electron states in the band gap on states induced by metal atoms adsorbed on the semiconductor surface. The formation of the Schottky barrier is discussed for low degrees of metal cover. Numerical calculations were performed for the metal-p-GaAs (110) system. © *1997 American Institute of Physics.* [S1063-7826(97)02210-2]

The problem of the formation of the Schottky barrier on a metal-semiconductor boundary has a long history, but still awaits an unambiguous solution.[1,2] At present, there ar two popular models of the contact, namely, the unified model of a defect, originating in the work of Spicer *et al.*[3] and the model in which states are induced in the band gap by the metal. The latter is based on an idea reported by Heine.[4] The defect model provides a satisfactory explanation of the Fermi level pinning and, consequently, of the weak dependence of the Schottky barrier height Φ under different metallic components of the contact with the semiconductor. Conversely, the induced-states model is capable of describing the significant changes in Φ as one passes from one metal coating on the semiconductor to another. Both tendencies are observed experimentally. In addition, both weak and strong variations in the Schottky barrier height have been observed in the same system (see, for example, Refs. 5 and 6, which report a study of the metal–silicon carbide contact, which is probably due the technology used to produce the contact).

At present, the popular approach to Schottky barrier theory is borrowed from the physics of adsorption.[1] This approach has also been used to formulate the defect model[7] and the model of induced states.[8,9] It is therefore interesting to consider a unified model of the metal-semiconductor contact. In this paper, we shall consider the influence of surface defects on the position and population of local and quasi-local levels of an isolated adatom, which will model the early stage of contact formation.

1. THE MODEL

We shall consider the adsorption of a one-electron atom on the surface of a semiconductor. The Hamiltonian of the system in the spinless approximation can be written in the form

$$H=\sum_k \varepsilon_k c_k^+ c_k + E_a a^+ a + \sum_k V_k(c_k^+ a + \text{H.c.}), \tag{1}$$

where the first term represents the semiconductor, ε_k describes the electronic structure of the semiconductor and e^+ is the operator representing the creation of an electron in the state $|k\rangle$ (the band index is omitted); the second term describes an atom with single-electron energy level E_a, a^+ is the operator describing the creation of an electron in the state $|a\rangle$; and the third term describes the hybridization of the semiconductor and atomic states.

The Green's function G corresponding to the Hamiltonian (1) is

$$G^{-1}(\omega)=\omega-E_a-\Lambda(\omega)+i\Gamma(\omega), \tag{2}$$

where

$$\Gamma(\omega)=\pi\sum_k |V_k|^2\delta(\omega-\varepsilon_k), \tag{3}$$

$$\Lambda(\omega)=P\,\frac{1}{\pi}\int_{-\infty}^{\infty}\frac{\Gamma(\omega')}{\omega-\omega'}\,d\omega'. \tag{4}$$

Here ω is the energy variable, $\delta(x)$ is the Dirac δ-function, P denotes the principal value of the integral, and $\Gamma(\omega)$ is a function which is proportional to the semiconductor density of states $\rho_k=\Sigma_k\delta(\omega-\varepsilon_k)$ and which determines the half-width of the atomic quasi-level.

We shall write the density of states $\Gamma(\omega)$ in the form (see Fig. 1)

$$\Gamma(\omega)=\begin{cases}\Gamma, & \text{if } |\omega|>\Delta/2;\\ \gamma, & \text{if } |\omega|<\delta/2;\\ 0 & \text{in other cases.}\end{cases} \tag{5}$$

Here $\Gamma=\pi V_b^2\rho_b$, and $\gamma=\pi V_i^2\rho_i$, where $V_{b(i)}$ is the matrix element describing the hybridization of the atomic state $|a\rangle$ with the defect band states, and $\rho_{b(i)}$ is the density of the defect band states. We thus have two semi-infinite bands (conduction and valence) with density of states $\rho_b=\text{const}$, separated by a gap of Δ. A band of impurity states (the i-band) lies at the center of the gap. It has a width δ and constant density ρ_i. When $\gamma=0$, this model becomes identical with the well-known Haldene–Anderson model.[10] We note that although we have placed the i-band at the center of the gap merely for simplicity, this is probably in approximate agreement with the experimental situation.[1,2]

Substituting (5) in (4), we obtain

$$\Lambda(\omega)=\frac{\Gamma}{\pi}\ln\left|\frac{\omega-\Delta/2}{\omega+\Delta/2}\right|-\frac{\gamma}{\pi}\ln\left|\frac{\omega-\delta/2}{\omega+\delta/2}\right|. \tag{6}$$

The shift function $\Lambda(\omega)$ is shown in Fig. 1. The position of the adatom levels ω^* (both local and quasi-local) is given by

 1063-7826/97/101062-05$10.00 © 1997 American Institute of Physics

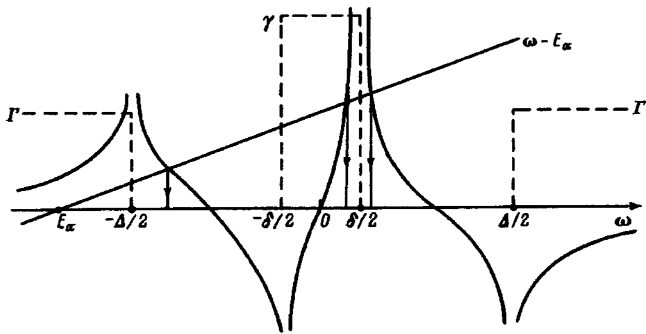

FIG. 1. Different branches of the solution of (7) are marked 1, 2, 3. Atomic level broadening $\Gamma(\omega)$ (dashed) and shift $\Lambda(\omega)$ (solid). The top of the valence band is $E_V=-\Delta/2$ and the bottom of the conduction band is $E_C=\Delta/2$. The impurity band lies between $-\delta/2$ and $\delta/2$. The arrows at the crossing points of the line $\omega-E_a$ with the profile $\Lambda(\omega)$ show the solutions of (7) corresponding to two local and one quasi-local levels.

$$\omega-E_a-\Lambda(\omega)=0. \quad (7)$$

In what follows, we shall confine our attention to solutions of (7) that lie in the region of the gap, $-\Delta/2<\omega^*<\Delta/2$. A graphical method of finding these solutions is shown in Fig. 1. It is clear from this figure that the minimum number of roots of (7) is three. Two of them lie in the gaps $(-\Delta/2<\omega^*<-\delta/2)$ and $(\delta/2<\omega^*<\Delta/2)$ and correspond to local levels of the adatom, and one overlaps the i-band and is a quasi-local level. However, if the atomic level with energy E_a lies near the center of the i-band, it can be shown that when the inequality

$$C\equiv\frac{4}{\pi}\left(\frac{\gamma}{\delta}-\frac{\Gamma}{\Delta}\right)<1 \quad (8)$$

is satisfied, two additional quasi-levels appear in the second gap and the total number of solutions of (7) is five.

We note, however, that the local solutions ω^* corresponding to regions that are very close to the top of the valence band and the lower and upper edges of the i-band, and also the quasi-local solution in the region of the top i-band, may be fictitious. The point is that, because of the stepwise shape of the band edges, the function $\Lambda(\omega)$ has discontinuities at $\omega=\pm\Delta/,\pm\delta/2$. When a better approximation for the density of states is adopted for the semiconductor, the function $\Lambda(\omega)$ does not show these discontinuities. The result is that some of these solutions will be absent near the points $(\pm\Delta/2)$ and $(\pm\delta/2)$. However, these possibly fictious solutions have little effect on the charge of the adatom (see below).

2. ADATOM LEVELS AND THEIR POPULATIONS

It follows from Fig. 1 that, as E_a increases from $-\infty$ to $+\infty$, the local energy level ω^* shifts from the top of the valence band to the bottom of conduction band. It can be shown that this shift increases more rapidly as Γ decreases. For given E_a, smaller Γ corresponds to local levels which lie closer to the gap edges.

When the defect i-band is present [we shall refer to this model as the 'defect model' and will distinguish it from the 'defect-free model' corresponding to $\gamma=0$ in (5)], the function $\omega^*(E_a)$ is as shown in Fig. 2. The conditions for the inequality given by (8) are satisfied for the case shown in Fig. 2a. This is precisely why in the case of atomic levels E_a which lie near the center of the gap, Eq. (7) has five solutions, three of which correspond to the quasi-local levels that overlap the i-band. It can be shown that it is necessary and sufficient for the realization of the five solutions for the atomic level energy E_a to satisfy the inequality

$$-\tilde{E}_a\leq E_a\leq\tilde{E}_a, \quad (9)$$

where

$$\tilde{E}_a=(2/3)\tilde{\omega}(1-C),$$

$$\tilde{\omega}=\frac{\sqrt{\pi}}{4}\sqrt{\frac{1-C}{(\gamma/\delta^3)-(\Gamma-\Delta^3)}}. \quad (10)$$

As the ratio γ/Γ increases (other parameters being constant), the inequality given by (8) ceases to be valid. It can be shown that, as γ increases, the adatom level in the upper gap 2 shifts toward the bottom of the conduction band (for the

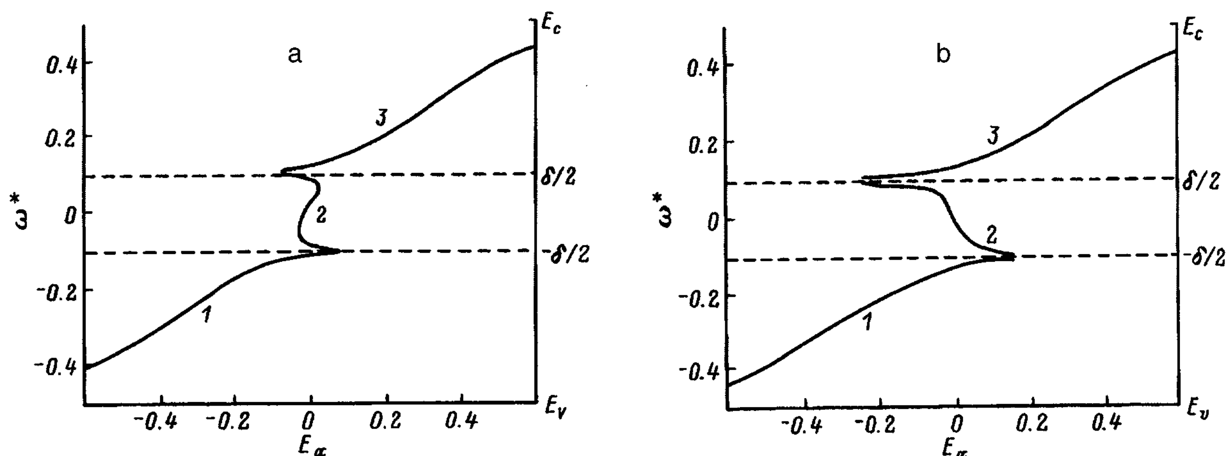

FIG. 2. Local energy level ω^* of an adatom as a function of E_a in the presence of the i-band. The unit of energy is the gap Δ and $\delta=0.2$, $\Gamma=0.25$. $\gamma/\Gamma=0.5$ (a) and $\gamma/\Gamma=1$ (b).

lower gap 1, it shifts toward the top of the valence band). We note that the greatest shift is displayed by levels lying near the top of the i-band.

We must now consider the population of the adatom. Its population is

$$n_a=\frac{1}{\pi}\,\mathrm{Im}\int_{-\infty}^{E_F}G(\omega)d\omega. \tag{11}$$

We shall write n_a in the form of the sum

$$n_a=Z_b+Z_1+Z_i+Z_2, \tag{12}$$

where Z_b represents the contribution due to the hybridization between the state $|a\rangle$ and occupied states in the valence band:

$$Z_b=\frac{1}{\pi}\int_{-\infty}^{E_V}\frac{\Gamma}{[\omega-E_a-\Lambda(\omega)]^2+\Gamma^2}\,d\omega. \tag{13}$$

The quantity Z_i represents the contribution of the i-band:

$$Z_i=\frac{1}{\pi}\int_{-\delta/2}^{E_F}\frac{\gamma}{[\omega-E_a-\Lambda(\omega)]^2+\gamma^2}\,d\omega. \tag{14}$$

Naturally, this expression is valid only for $\delta/2\geqslant E_F\geqslant-\delta/2$. When $E_F<-\delta/2$, we have $Z_i=0$.

The population of the local levels in the lower (Z_1) and upper (Z_2) gaps can be determined from the formula[10]

$$Z_{1,2}=\left|1-\frac{d\Lambda(\omega)}{d\omega}\right|^{-1}_{\omega^*_{1,2}}, \tag{15}$$

which in our case leads to

$$Z_{1,2}=\left\{1+\frac{1}{\pi}\left[\frac{\Gamma\Delta}{(\Delta/2)^2-\omega^2}+\frac{\gamma\delta}{\omega^2-(\delta/2)^2}\right]\right\}^{-1}_{\omega^*_{1,2}}. \tag{16}$$

Naturally, these contributions are also realized only when the local level lies below the Fermi level.

The integral given by (13) can be evaluated approximately. We shall begin with the case $\gamma=0$ (defect-free model). It can be shown that, approximately,

$$Z_b(\gamma=0)=\frac{1}{\pi}\,\mathrm{arctg}\,\frac{\Delta/2+\tilde{E}_a}{\Gamma}, \tag{17}$$

where

$$\tilde{E}_a=E_a+\frac{\Gamma}{\pi}\ln\frac{1+R}{1-R},\quad R=\sqrt{1+(4\Gamma/\pi\Delta)}. \tag{18}$$

The formula given by (17) provides a qualitative description of the dependence of Z_b on the parameters of the problem, e.g., on the position of the level E_a (see Fig. 3 in Ref. 10), which constitutes an upper bound, i.e., it tends to overestimate Z_b. We recall that the sum of all the contributions to the adatom population n_a [see (12)] must not exceed unity.

If we now turn to the defect model, we must take into account the fact that, for energies corresponding to the valence band, the quantity $\delta/2|\omega|$ is a small parameter. It can then be shown that allowance for the i-band leads in the first approximation simply to a shift of the level E_a:

$$E_a\rightarrow E_a-2(\gamma\delta/\pi\Delta). \tag{19}$$

It is readily seen that the shift of an adatom level toward negative energies gives rise to an increase in its population.

If we now look upon the ratio δ/Δ as a small parameter, we can show that

$$Z_i=\frac{1}{\pi A}\left\{\mathrm{arctg}\left(\frac{E_FA-E_a}{\gamma}\right)+\mathrm{arctg}\left[\frac{(\delta A/2)+E_a}{\gamma}\right]\right\}, \tag{20}$$

where $A=1-C$. We know that, whatever the sign of A, the quantity Z_i is always positive. The function $Z_i(E_a)$ has a maximum $Z_{i\,\max}$ for the following relationship between the two diameters:

$$E_a=\frac{1}{2}\left(E_F-\frac{\delta}{2}\right)A,\quad |E_F|\leqslant\frac{\delta}{2}, \tag{21}$$

We then have

$$Z_{i\;\max}=\frac{2}{\pi A}\,\mathrm{arctg}\left[\frac{A(E_F+\delta/2)}{2\gamma}\right]. \tag{22}$$

We note that the dependence of Z_i on the Fermi energy E_F (for standard values of the parameters of the problem) is nearly linear.

The function $Z_{1,2}$ peaks at

$$E^*_{a1,2}=\omega^*-\Lambda(\omega^*),$$

where

$$\omega^*=\pm\frac{1}{2}\sqrt{\frac{\Delta^2r+\delta^2}{1+r}},\quad r=\sqrt{\gamma\delta/\Gamma\Delta}. \tag{23}$$

Here $Z_{1\,\max}=Z_{2\,\max}=Z_{2\,\max}=Z_{\max}$ and

$$Z_{\max}=\left[1+\frac{4(1+r)^2}{\pi}\frac{\Gamma\Delta}{\Delta^2-\delta^2}\right]^{-1}. \tag{24}$$

The functions $Z_1(E_a)$ and $Z_2(E_a)$ are mirror reflections of one another relative to the center of the i-band.

The total population n_a of the adatom is shown in Fig. 3 as a function of the position of the Fermi level. For simplicity, the function $Z_i(E_F)$ is approximated by straight lines in all cases. Figure 3 shows the results for the defect-free (dashed) and defect (solid) models. It is clear from the figure that the maximum difference between the population numbers n_a in the two models occurs when E_a and E_F lie close to the center of the i-band. However, if the energy level of the atom is shifted toward the edges of the bands (valence and conduction), the difference between the population numbers n_a for the two models becomes appreciable only for small values of $|E_F|$.

3. ADSORPTION OF METAL ATOMS ON *p*-type SEMICONDUCTOR AND FORMATION OF THE SCHOTTKY BARRIER

At present, the formation of a Schottky barrier during the adsorption of metal atoms on p-type semiconductors without surface defects is commonly described as follows (we are concerned here with low substrate temperatures when metal islands cannot be formed).[1,7,11] States induced by adsorbed metal atoms fall into the band gap of the semiconductor. For p-type doping, electrons from localized states leave for the interior, creating a positive charge on the surface and a nega-

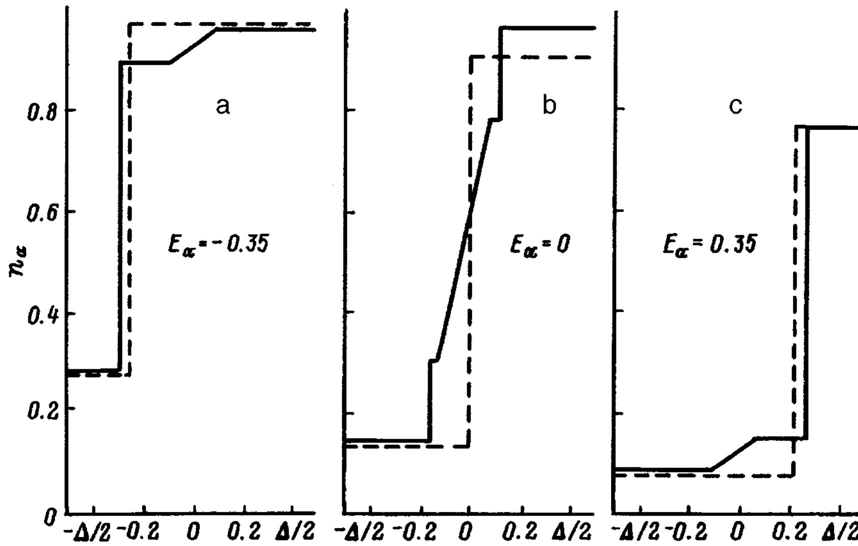

FIG. 3. Adatom populations n_a in the defect-free case (dashed) and in the presence of the i-band (solid) as functions of of the position of the Fermi level; $\Delta=1$, $\delta=2$, $\Gamma=0.25$, $\gamma/\Gamma=0.5$. The calculations were performed for $E_a=-0.35\Delta$ (a), $E_a=0$ (b), and $E_a=-0.35\Delta$.

tive charge in the interior, which leads to the upward band bending near the contact. This bending depends on the surface concentration of the adatoms (degree of cover). The band bending continues until the Fermi level on the surface crosses (coincides with) the adatom level. For the most extensively investigated metal-GaAs (110) system with acceptor concentration 10^{19} cm^{-3}, this occurs when the degree of cover is of the order of 0.01 monolayers (Ref. 11). It is clear that, for this type of cover, the adatoms can be regarded as isolated. Consequently, we are entitled to use our model in calculations involving the Schottky barrier.

Let us consider the adsorption of metal atoms (M=Na, K, Rb, Cs, Cu, Ag, Au, Al, Ga, In) on the (110) surface of p-type GaAs. We assume a band gap $\Delta=1.52$ eV (Ref. 12) and electron affinity $\chi=4.05$ eV (Ref. 1). The midpoint of the gap from which the energy is measured lies below the vacuum level at the distance $\chi+\Delta/2$. The atomic level energy relative to the midpoint is

$$E_a=-1+\chi+\Delta/2, \tag{25}$$

where I is the ionization potential of the adsorbed atom.

The parameter $\Gamma=\pi\rho_b V_b^2$ can be estimated in two ways. First, we can consider the interaction between the $|sp^3\rangle$ orbital of the semiconductor and the $|s\rangle_a$ orbitals of the metal atoms (in the case of the alkali metals and Cu group metals) or $|p\rangle_a$ orbitals (in the case of Al, Ga, and In). We can then set V_b equal to the universal Harrison matrix element V_2 (Refs. 13 and 14). We then find that $V_b=-14.4/d^2$ and $V_b=-20.06/d^2$ for the $|sp^3\rangle-|s\rangle_a$ and $|sp^3\rangle-|p\rangle_a$, respectively (d is measured in Å and V_b in eV). The adsorption bond length is $b=r_a+r_s$ where r_a and r_s are the atomic radii of the adsorbed atom and semiconductor atom to which the adatom is directly coupled. The density of states ρ_b is estimated by analogy with the Friedel model:[15]

$$\rho_b=4/W_V, \tag{26}$$

where W_V is the width of the valence band of the semiconductor that contains four electrons per atom (for GaAs, $W_V=12.5$ eV; Ref. 13). Table I lists the calculated E_a and Γ (see variant *1*). The ionization potentials and atomic radii are taken from Ref. 16. We considered adsorption on the Ga atom.

The second method of determining Γ is as follows. As is done in quantum chemistry and in the theory of alloys, we assume that the matrix element is $V_b=(t_a t_s)^{1/2}$, where t_a and t_s are the interatomic matrix elements of the adsorbate and adsorbent, respectively. On the other hand, in the tight-binding theory the width of the valence band of the semiconductor is $W_V=2n_s t_s$, where n_s is the number of nearest neighbors. If we again use the Friedel model for the density of states ρ_b, we obtain

$$\Gamma=\frac{\pi}{2}t_a. \tag{27}$$

Table I lists the values of Γ calculated from (27) (variant 2). Figure 4 plots the calculated ω^*-E_V as a function of the ionization potential I of the metal atoms. It is clear from the figure that, in variant *2*, ω^*-E_V is an almost linear function of I (with the exception of Au), whereas in variant 1, the fall in ω^*-E_V slows down with increasing I. The experimental data are shown in Fig. 5 (Refs. 1 and 8). Comparison of the

TABLE I. Model parameters used to calculated the Schottky barrier formed by metal atoms adsorbed on p-type GaAs (110).

Quantity	Calculation variants	Na	K	Rb	Cs	Cu	Ag	Au	Al	Ga	In
$-E_a/\Delta$		0.22	−0.31	−0.41	−0.61	1.68	1.82	2.91	0.77	0.78	0.64
Γ/Δ	*1*	1.23	0.69	0.61	0.53	2.70	2.14	2.14	4.21	4.46	3.08
Γ/Δ	*2*	0.78	0.57	0.44	0.38	1.59	1.24	1.25	214	2.93	1.65

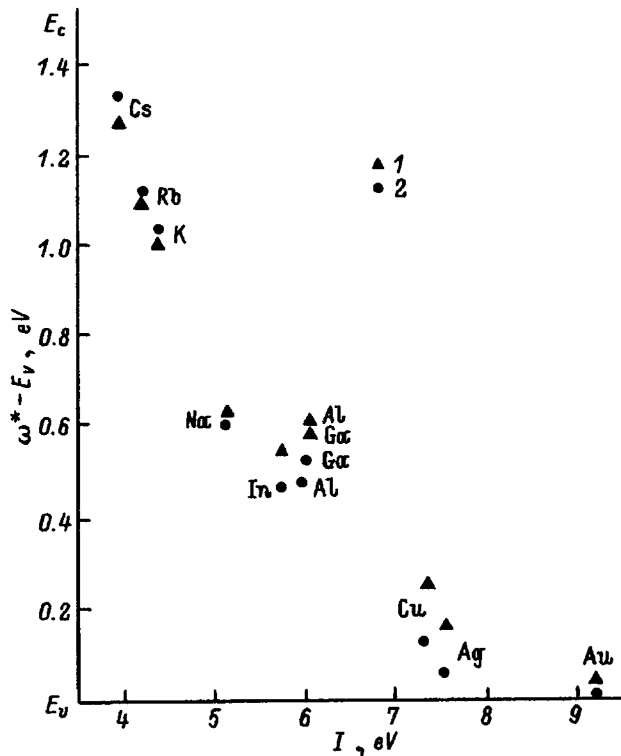

FIG. 4. Position of local levels of the metal atoms (relative to the top of the valence band) adsorbed on the GaAs surface as functions of their ionization potentials I. The digits *1* and *2* refer to the two variants in Table I.

theory with experimental data shows that the overall tendency of these data is better described by variant 2, whereas the difference $\omega^* - e_V$ is better described by variant 1, especially for metals with high ionization potentials (Eu, Ag, and Au).

We now consider the defect model for $\gamma = 0$. Differentiating (7) with respect to the ionization potential, we obtain

$$\frac{\partial \omega_{1,2}^*}{\partial I} = -Z_{1,2}, \tag{28}$$

where $Z_{1,2}$ is given by (16). It is readily seen that the function $\omega_{1,2}^*(I)$ tends to a linear relationship as the term in square brackets decreases. In the region under consideration $(|\omega^*| > \delta/2)$, the quantity $|\partial \omega^*/\partial I|$ for the defect model is smaller than for the defect-free model because the expression in the square brackets in (16) acquires an additional positive term. Moreover, when the i-band appears, the local levels are closer, as compared with the defect free model, to the edges of the corresponding bands $(\pm \Delta/2, \pm \delta/2)$, so that there is a reduction in the derivative $|\partial \omega^*/\partial I|$. These conclusions are in qualitative agreement with results reported in Ref. 7. On

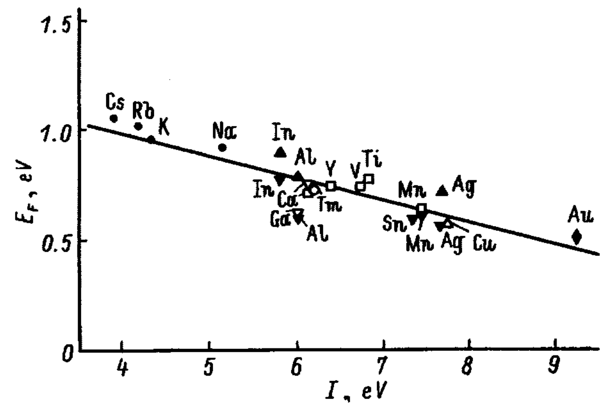

FIG. 5. Experimentally determined positions of the Fermi level relative to the top of the valence band (height of Schottky barrier) for the metal–p-GaAs (110) contact, based of Refs. 1 and 8.

the other hand, quantitative results are difficult to obtain because we do not have the values of the parameters γ and δ, since the nature of the defects produced on the contact is unknown.[1]

We have thus been able to use a single model to provide a qualitative (and, in the absence of defects, a quantitative) explanation of the experimentally observed tendencies accompanying the formation of the Schottky barrier on the metal–p-GaAs (110) contact.

[1] W. Mönch, Rep. Prog. Phys. **53**, 221 (1990).
[2] F. Bechstedt and R. Enderlein, *Semiconductor Surfaces and Interfaces*, Akademie-Verlag, Berlin (1988).
[3] W. E. Spicer, I. Lindau, P. Skeath, C. Y. Su, and P. Chye, Phys. Rev. Lett. **44**, 420 (1980).
[4] V. Heine, Phys. Rev. **138** A1689 (1965).
[5] J. R. Waldrop, Appl. Phys. **75**, 4558 (1994).
[6] A. N. Andreev, A. A. Lebedev, M. G. Rastegaeva, F. M. Snegov, A. L. Syrkin, V. E. Chelnokov, and L. N. Shestopalov, Fiz. Tekh. Poluprovodn. **29**, 1828 (1995) [Semiconductors **29**, 955 (1995)].
[7] R. Lideke, Phys. Rev. B **40**, 1947 (1989).
[8] W. Mönch, Europhys. Lett. **7**, 275 (1988).
[9] S. Yu. Davydov and S. K. Tikhonov, Fiz. Tekh. Tela **37**, 2749 (1995) [Phys. of Solid State **37**, 1514 (1995)].
[10] F. D. M. Haldane and P. W. Anderson, Phys. Rev. B **13**, 2553 (1976).
[11] J. E. Klepeis and W. A. Harrison, Phys. Rev. B **40**, 5810 (1989).
[12] V. I. Gavrilenko, A. M. Grekhov, D. B. Korbutik, and V. G. Litovchenko, *A Handbook of the Optical Properties of Semiconductors* [in Russian], Nauk. Dumka, Kiev (1978).
[13] W. A. Harrison, *Electronic Structure and the Properties of Solids*, Freeman, San Francisco, 1980 [Russian trans., Mir. Moscow, 1983] Vol. 1.
[14] W. A. Harrison, Phys. Rev. B **27**, 3592 (1983).
[15] W. A. Harrison, *Electronic Structure and the Properties of Solids*, Freeman, San Franscisco, 1980 [Russian trans., Mir. Moscow, 1983] Vol. 2.
[16] I. S. Grigor'ev and E. Z. Meilikhov (Eds.), *Handbook of Physical Quantities* [in Russian], Energoatomizdat, Moscow, 1991.

Translated by S. Chomet

Characteristics of the formation of (Al, Ga)Sb/InAs heterointerfaces in molecular-beam epitaxy

P. V. Neklyudov, S. V. Ivanov, B. Ya. Mel'tser, and P. S. Kop'ev

A. F. Ioffe Physicotechnical Institute, Russian Academy of Sciences, 194021 St. Petersburg, Russia
(Submitted February 25, 1997; accepted for publication March 5, 1997)
Fiz. Tekh. Poluprovodn. **31**, 1242–1245 (October 1997)

A thermodynamic model is given for the molecular-beam epitaxy formation of InSb, GaAs, and AlAs heterointerfaces in (Al, Ga)Sb/InAs heterostructures. The maximum critical temperature of formation of a planar InSb-type heterointerface on an (Al, Ga)Sb layer, $T \approx 390$ °C, is determined from a comparison of the pressure of Sb_4 molecules in the external flux with their equilibrium value above a stressed monolayer on a heterointerface and is found to be in good agreement with existing experimental data. In contrast, the critical temperature of formation of a heterointerface of the AlAs (GaAs) type, corresponding to the onset of rapid reevaporation of As, is much higher than the growth temperatures normally used in molecular-beam epitaxy (350–550 °C). © *1997 American Institute of Physics.* [S1063-7826(97)02310-7]

INTRODUCTION

In addition to the usual technological factors underlying the production of high-quality layers in the development of molecular-beam epitaxy (MBE) technology for the growth of efficient radiation sources using (Al, Ga, In)(As, Sb) heterostructures with a quantum well and short-period superlattices, the type of chemical bond at the (Al, Ga)Sb/InAs heterointerface in the quantum well and the existence of stressed, short-period superlattices must also be taken into consideration. The problem is that the transition through such a heterointerface is accompanied by a simultaneous change of the atomic species in both the cationic and the anionic sublattices, and the atoms arrange themselves in two possible configurations at the heterointerface: An ''InSb-like'' heterointerface is formed when the InAs layer terminates in In atoms, while the Al(Ga)Sb layer begins with Sb atoms. In the second case As atoms from the InAs layer and Al or Ga atoms from the Al(Ga)Sb layer create an ''Al(Ga)As-like'' heterointerface, on which Al–As or Ga–As bonds form.[1]

It has been shown earlier that each type of heterointerface can be deliberately created in MBE growth by properly sequencing the operation of the individual shutters for the Al(Ga), Sb, In, and As molecular beams.[1] The type of heterointerface has also been observed to have a significant influence on the electrical and optical characteristics of the quantum well,[2] with considerable preference for heterointerfaces of the InSb type. Further detailed Raman scattering studies of heterointerfaces have revealed major difficulties in preparing heterointerfaces of the AlAs type at growth temperatures $T_s > 350$ °C (Ref. 3), as well as an explicit growth-temperature dependence of the intensity of the peak created in the Raman spectrum by a heterointerface of the InSb type; this dependence was interpreted as an increase in the roughness of the formative InSb-type heterointerface as the growth temperature is increased.[4]

THERMODYNAMIC ANALYSIS

In the thermodynamic context the formation of heterointerfaces of the type Al(Sb–In)As, Sb(Al–As)In, Ga(Sb–In)As, and Sb(Ga–As)In can be portrayed as the initial stage of pseudomorphic growth, i.e., growth on a substrate strongly mismatched with the epitaxial layer in terms of their lattice parameters; this stage has been investigated previously for the MBE growth of GaSb on a GaAs substrate[5] and of InSb on GaAs (Ref. 6). By analogy we assume that the elastic stress generated in the formation of the transition monolayer on the heterointerface produces a marked increase in the partial pressure of the group V element above this monolayer. As a result, an equilibrium pressure of this kind, which increases as a function of the temperature, can exceed the value customarily used in MBE for the pressure of group-V molecules in the external flux (10^{-5}–10^{-6} Torr). This phenomenon can deplete group-V atoms from the surface of the monolayer formed on the heterointerface and, as a result, make it impossible to form a perfect heterointerface of the type required. In this case the two-phase gas-⟨solid phase⟩ equilibrium is replaced by three-phase gas-⟨liquid phase⟩-⟨solid phase⟩ equilibrium. In the given situation, therefore, it is necessary to investigate the equilibrium pressures of molecules of group-V elements (As_2, Sb_4) above the corresponding liquidus of group-III elements for each binary compound capable of forming at the heterointerface in the presence of high elastic stress.

The reaction of formation of III-V compounds (which we denote by AB from now on, A standing for In or Ga, and B for Sb or As) in MBE (evaporation) and the corresponding effective-mass equation have the form

$$\mathrm{A}_{\mathrm{gas}} + \frac{1}{n}(\mathrm{B}_n)_{\mathrm{gas}} = \mathrm{AB}_{\mathrm{sol}}, \tag{1}$$

$$K_{\mathrm{AB}}^{-1}(T) = P_{\mathrm{A}}(P_{\mathrm{B}})^{1/n}, \tag{2}$$

where $\mathrm{A}_{\mathrm{gas}}$ and $(\mathrm{B}_n)_{\mathrm{gas}}$ are the molecules in the gaseous phase, $\mathrm{AB}_{\mathrm{sol}}$ is the compound AB in the solid phase, n is the number of atoms in a group V molecule $n=2$ for As (Ref. 7) and $n=4$ for Sb (Ref. 5) in the range of growth temperatures T_s of interest], $K_{\mathrm{AB}}(T)$ is the equilibrium constant of the reaction (2), and P_{A} and P_{B} are the equilibrium partial pressures above the surface of AB. The minimum pressure of

group-V molecules in the external flux P_B^0 for the AB layer to grow without the formation on the growth surface of droplets enriched with group-III element, at a given growth rate, i.e., for given values of P_A^0 and T_s, can be written as

$$P_{B,\min}^0=\frac{1}{n}\sqrt{m_B/m_A}(P_A^0-P_A^{A-L})+P_B^{A-L}, \quad (3)$$

where m_A/m_B is the ratio of the molar masses, P_A^{A-L} and P_B^{A-L} are the equilibrium partial pressures of group-III and group-V molecules, respectively, above the liquidus of the A–AB phase diagram for the compound AB, according to Eq. (1). Also, the equilibrium partial pressures of group-III atoms above the A–AB liquidus can be written in the form

$$P_A^{A-L}=P_A^L[A_L]\gamma_A, \quad [A_L]+[B_L]=1, \quad (4)$$

where P_A^L, γ_A, and $[A_L]$ are the equilibrium pressure of group-III atoms above the pure melt, the activity coefficient of the element in the liquid phase, and the concentration of component A in the liquid phase (in mol.%), respectively; and $[B_L]$ is the concentration of the component B in the liquid phase. The activity coefficient is the quantity

$$\gamma_A=\exp[\alpha(T)[B_L]^2/kT], \quad (5)$$

where $\alpha(T)$ is the interaction parameter in the liquid phase, and k is the Boltzmann constant. The resultant expression for the equilibrium partial pressure P_B^{A-L} in the growth of compounds with matched lattice parameters can be obtained from (1) and (4):

$$(P_B^{A-L})^{1/n}=K_{AB}^{-1}P_A^{A-L}. \quad (6)$$

For the pseudomorphic, heteroepitaxial growth of a monolayer at a heterointerface we must take into account the stress-induced additional Gibbs free energy ΔG_{str} with the corresponding change of enthalpy[8]

$$\Delta H_{str}=2G[(1+\nu)/(1-\nu)]V_m[(a-a_0)/a_0]^2, \quad (7)$$

where $\nu=C_{12}/(C_{11}+C_{12})$ is the Poisson ratio, V_m is the molar volume of the buffer layer (in m^3/mol), $G=\frac{1}{2}C_{44}$ [for the (100) surface], and C_{11}, C_{12}, C_{44}, and a are the elastic constants and lattice constant of the unstressed binary compound formed on the heterointerface. Since P_A^{A-L}, which is the pressure above the A–AB liquidus, does not change in the presence of stress, it is the only variable parameter in Eq. (1) due to the variation ΔG_{str}. If it is valid to assume that the crystal order is invariant in pseudomorphic growth of a monolayer on a buffer layer, the reaction entropy S remains constant, i.e., $\Delta S_{str}=0$. Consequently, using the appropriate constants from Table I and the temperature dependences from Table II, we can write the equilibrium partial pressures of group-V molecules above the A–AB liquidus as follows for the pseudomorphic formation of a monolayer at a heterointerface:

a) InSb-type heterointerface on an AlSb buffer ($\Delta H_{str}=6.34\times10^{-2}$ eV)

$$(P_{Sb_4}^{In-L})_{str}=3.09\times10^{15}\exp(-3.39/kT)\times\gamma_{In}^{-4}(1-[Sb_L])^{-4}, \quad (8)$$

TABLE I. Lattice constant a_0 and elastic constants C_{11}, C_{12}, C_{44} for III–V compounds.

Compound	a_0, Å ($T=300$ K)	C_{11}	C_{12} 10^{11}dyn/cm^2	C_{44}
GaAs	5.6533	12.10	5.42	6.04
AlAs	5.6605	12.50	5.34	5.42
InAs	6.0584	8.32	4.50	3.95
GaSb	6.0959	8.83	4.10	4.44
AlSb	6.1355	8.70	4.30	4.07
InSb	6.4794	6.10	3.00	2.90

b) InSb-type heterointerface on a GaSb buffer ($\Delta H_{str}=7.84\times10^{-2}$ eV)

$$(P_{Sb_4}^{In-L})_{str}=3.09\times10^{15}\exp(-3.33/kT)\times\gamma_{In}^{-4}(1-[Sb_L])^{-4}, \quad (9)$$

c) GaAs-type heterointerface on a GaSb buffer ($\Delta H_{str}=2.07\times10^{-1}$ eV)

$$(P_{As_2}^{Ga-L})_{str}=8.98\times10^{11}\exp(-3.54/kT), \quad (10)$$

d) AlAs-type heterointerface on an AlSb buffer ($\Delta H_{str}=2.11\times10^{-1}$ eV)

$$(P_{As_2}^{Al-L})_{str}=3.97\times10^{8}\exp(-4.02/kT)\times\gamma_{Al}^{-2}(1-[As_L])^{-2}. \quad (11)$$

Here the activation energies are given in eV, and the pressure in atm.

RESULTS AND DISCUSSION

Figure 1 shows the above-calculated temperature curves of the equilibrium partial pressures of As and Sb over the corresponding stressed compounds of the heterointerface monolayers and, for comparison, the equilibrium pressure of antimony $P_{Sb_4}^{In-L}$ (curve *1*), calculated according to Eq. (6) for the homoepitaxial growth of InSb/InSb. The dotted curves represent the minimum required pressures in the external fluxes of antimony and arsenic molecules [see (3)] for the growth surface to be enriched with a group-V element in the growth of pseudomorphic InSb and GaAs layers on the surface of AlSb and GaSb buffer layers at various growth rates. It is evident from the figure that the formation of an InSb–type heterointerface on AlSb or on GaSb causes the partial pressure of Sb above the In–InSb liquidus to increase significantly (by more than two orders of magnitude), to pressures normally used in the growth of (Al, Ga)Sb, at critical temperatures $T_C\approx390$ °C and $T_C\approx380$ °C for AlSb and GaSb buffer layers, respectively. A further increase in the increment of the growth temperature T_s above T_C could lead to the rapid reevaporation of Sb from the surface, preventing the formation of a homogeneous, planar monolayer of InSb on the heterointerface. The results of our thermodynamic analysis are in good agreement with the experimental results of Seta et al.,[13] who have shown that the deliberate implantation of an InSb monolayer on an InAb/AlSb heterointerface at $T_s>400$ °C tends to suppress the oscillations of the dif-

TABLE II. Reaction equilibrium constants K_{AB}^{-1}, pressures P_A^L of group-III atoms above the pure melt, activity coefficients α, and concentrations $[B_L]$ in the liquid phase for III–V compounds.

Parameter	InSb	GaAs	AlAs
K_{AB}^{-1}	$7.68\times10^{11}\exp(-3.31/kT)$	$2.73\times10^{11}\exp(-4.72/kT)$	$1.63\times10^{11}\exp(-5.39/kT)$
P_A^L, atm	$1.03\times10^{5}\exp(-2.4/kT)$ (Ref. 6)	$2.73\times10^{11}\exp(-4.72/kT)$ (Ref. 10)	$8.18\times10^{5}\exp(-3.17/kT)$ (Ref. 9)
$[B_L]$, mol%	$47\exp(-0.33/kT)$ (Ref. 11)	≈ 0 (Ref. 11)	$26.6\exp(-1.08/kT)$ (Ref. 12)
$\alpha(T)$, eV (Ref. 11)	$(0.147-5.2)\times10^{-4}T$	$(0.223-3.93)\times10^{-4}T$	$(-0.276-2.38)\times10^{-4}T$

Note: The numbers in brackets give the literature references for the values of the parameters.

fraction of high-energy reflected electrons. Sela *et al.*[4] have observed that the intensity of the In–Sb mode in the Raman spectrum of InAs/AlSb structures grown at various temperatures increases systematically as T_s is increased. This behavior was attributed to an increase in the number of In–Sb bonds at the heterointerface, i.e., an increase in the roughness of the heterointerface. The slope of the intensity–temperature curve increased abruptly at $T_s=440-450$ °C; this event can be identified with the start of rapid reevaporation of Sb from the surface of the monolayer.

In contradistinction to the formation of an InSb-type heterointerface, it is evident from Fig. 1 that the maximum temperatures of formation of GaAs or AlAs monolayers on an (Al,Ga)Sb/InAs heterointerface with a quantum well are much higher than the temperatures used in the MBE of these heterostructures (350–550 °C), despite the greater mismatch with the GaSb or AlSb buffer layer in terms of their lattice parameters. This result suggests that the difficulties previously encountered in the preparation of heterointerfaces of the AlAs and GaAs type[3,14,15] are mostly likely attributable to the temperature dependence of As–Sb exchange reactions at the heterointerface or to breakdown of the structure of the AlAs monolayer formed on AlSb when the critical thickness is less than one monolayer,[16] and not to stress-induced As depletion of the surface.

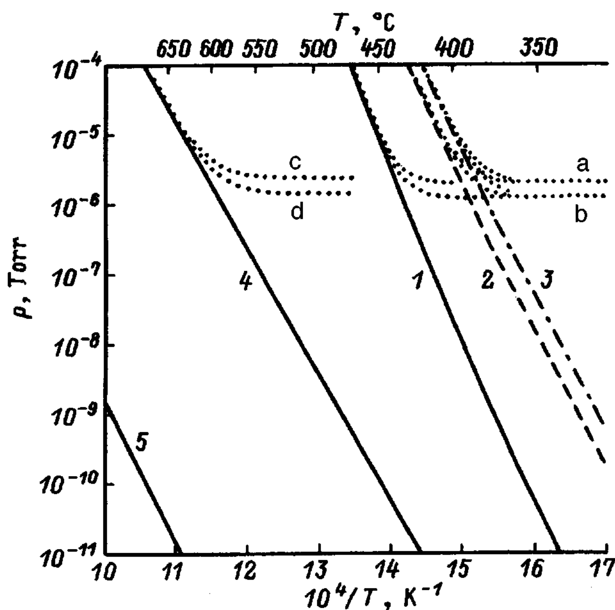

FIG. 1. Calculated temperature dependence of the equilibrium partial pressures. *1–3*) Sb_4 molecules: *1*) above the In–InSb liquidus without lattice mismatch; *2, 3*) with mismatch for the formation of an InSb–type heterointerface on buffer layers of: *2*) Sb [see Eq. (8)]; *3*) GaSb [Eq. (9)]; *4, 5*) As_2 molecules with lattice mismatch above the liquidus of: *4*) Ga–GaAs [Eq. (10)]; *5*) Al–AlAs [Eq. (11)]. The dotted curves represent the minimum pressures of different molecules in the external flux [see (5)] at various growth rates. a) Sb_4 molecules, 1 μm/h; b) Sb_4, 0.6 μm/h; c) As_2, 1 μm/h; d) As_2, 0.6 μm/h.

It therefore follows from the submitted thermodynamic model of the formation of an (Al, Ga)Sb/InAs heterointerface with a quantum well that the large stress-induced increase in the equilibrium partial pressure of group-V element above the formed monolayer can inhibit the formation of the desired type of heterointerface at growth temperatures such that the given pressure exceeds the pressure in the external flux. This behavior can be manifested as an appreciable increase in the roughness of the heterointerface due to the depletion of group-V atoms from the monolayer. The maximum temperatures corresponding to the formation of a homogeneous, planar heterointerface of the InSb type are $T_C\approx390$ °C and $T_C\approx380$ °C for AlSb and GaSb buffer layers, respectively. The given values of the critical temperatures are in good agreement with experimental data. In the thermodynamic model planar heterointerfaces of the type AlAs and GaAs can form over the entire temperature range 300–550 °C.

Based on the foregoing analysis, a technology has been developed for the formation of InSb interfaces on an (Al, Ga)Sb/InAs interface, completely devoid of bonds of the Ga–As type. The objects used as test samples were quantum-well AlSb/InAs/AlSb structures with a two-dimensional electron channel, in which the carrier mobility depends critically on the type of interface.[17] The attainable electron mobilities [above 200 000 $cm^2/(V\cdot s)$ at $T=4.2$ K] and the presence of only the peaks in the Raman spectra, which correspond to the In–Sb mode, are conclusive evidence that heterointerfaces of the type InSb are indeed formed.

This study has received support from the International Association for the Promotion of Cooperation with Scientists from the Independent States of the Former Soviet Union (INTAS Grant 94-1172) and the Russian Fund for Fundamental Research in conjunction with Deutsches Forschungsgemeinschaft (Grant RFFI-DFG-96-02-0023G).

[1] G. Tuttle, H. Kroemer, and J. H. English, J. Appl. Phys. **67**, 3032 (1990).
[2] B. Brar, J. Ibbetson, H. Kroemer, and J. H. English, Appl. Phys. Lett. **64**, 3392 (1994).
[3] J. Wagner, J. Schmitz, D. Behr, J. D. Ralston, and P. Koidl, Appl. Phys. Lett. **65**, 1293 (1994).

[4] I. Sela, C. R. Bolognesi, L. A. Samoska, and H. Kroemer, Appl. Phys. Lett. **60**, 3283 (1992).
[5] S. V. Ivanov, P. D. Altukhov, T. S. Argunova, A. A. Bakun, A. A. Boudza, V. V. Chaldyshev, Yu. A. Kovalenko, P. S. Kop′ev, R. N. Kutt, B. Ya. Meltser, S. S. Ruvimov, L. M. Sorokin, S. V. Shaposhnikov, and V. M. Ustinov, Semicond. Sci. Technol. **8**, 347 (1993).
[6] S. V. Ivanov, A. A. Boudza, R. N. Kutt, N. N. Ledentsov, B. Ya. Meltser, S. S. Ruvimov, S. V. Shaposhnikov, and P. S. Kop′ev, J. Cryst. Growth **156**, 191 (1995).
[7] P. S. Kop′ev and N. N. Ledentsov, Fiz. Tekh. Poluprovodn. **22**, 1729 (1988) [Sov. Phys. Semicond. **22**, 1093 (1988)].
[8] R. E. Nahory, M. A. Pollack, E. D. Beebe, and J. C. DeWinter, J. Electrochem. Soc. **125**, 1053 (1978).
[9] O. Madelung, M. Schulz, and H. Weiss, *Numerical Data and Functional Relationships in Science and Technology*, Vol. 17A (Springer-Verlag, Berlin, 1982).
[10] S. V. Ivanov, P. S. Kop′ev, and N. N. Ledentsov, J. Cryst. Growth **104**, 345 (1990).
[11] M. B. Panich and H. Ilegems, in *Progress in Solid State Chemistry*, edited by J. Reiss and J. D. McCaldin, Vol. 7 (Pergamon, New York, 1972), p. 39.
[12] S. Yu. Karpov, Yu. V. Kovalchuk, V. E. Myachin, and Yu. V. Pogorelskii, J. Cryst. Growth **129**, 563 (1993).
[13] M. Seta, H. Asahi, S. G. Kim, K. Asami, and S.-I. Gonda, J. Appl. Phys. **74**, 5033 (1993).
[14] J. Spitzer, H. D. Fuchs, P. Etchegoin, M. Ilg, and M. Cardona, Appl. Phys. Lett. **62**, 2274 (1993).
[15] B. R. Bennett, B. V. Shanabrook, R. J. Wagner, J. L. Davis, and J. R. Waterman, Appl. Phys. Lett. **63**, 949 (1993).
[16] M. Yano, M. Okuizumi, Y. Iwai, and M. Inoue, J. Appl. Phys. **74**, 7472 (1993).
[17] P. D. Wang, N. N. Ledentsov, C. M. Sotomayor-Torres, S. V. Ivanov, B. Ya. Meltser, and P. S. Kop′ev, Solid State Commun. **9**, 361 (1994).

Translated by James S. Wood

Influence of the quality of the heterointerface on the cyclotron resonance spectra of InAs/(AlGa)Sb heterostructures

Yu. B. Vasil'ev, S. D. Suchalkin, S. V. Ivanov, B. Ya. Mel'tser, A. F. Tsatsul'nikov, P. V. Neklyudov, and P. S. Kop'ev

A. F. Ioffe Physicotechnical Institute, Russian Academy of Sciences, 194021 St. Petersburg, Russia
(Submitted April 15, 1997; accepted for publication April 22, 1997)
Fiz. Tekh. Poluprovodn. **31**, 1246–1248 (October 1997)

Cyclotron resonance is measured in solitary type-II InAs–AlGaSb quantum wells grown by molecular-beam epitaxy under various growth conditions. Quantum oscillations observed in the cyclotron resonance spectra in InAs–GaSb samples are attributed to scattering by a short-range potential due to roughness of the heterointerface. A new method based on measurement of the cyclotron resonance spectra is proposed for assessing the quality of the heterointerface.
© *1997 American Institute of Physics.* [S1063-7826(97)02410-1]

1. INTRODUCTION

The properties of heterostructures are known to be determined largely by the surface quality of the heterointerfaces. In AlGaAs/GaAs heterostructures with quantum wells, for example, the quality of a heterointerface formed by the deposition of GaAs on the surface of AlGaAs is far inferior to that obtained when AlGaAs is grown on a GaAs surface; this condition leads, for example, to poor transport characteristics of a two-dimensional electron gas in modulated structures with a quantum well or with superlattices by comparison with solitary heterojunctions. Since the presence of a heterointerface creates an additional mechanism of carrier scattering by roughness of its surface, the quality of the interface can be assessed by measuring the carrier mobility in the quantum well (see, e.g., Ref. 1).

Here we propose a new method for evaluating the surface quality of heterointerfaces by analyzing the cyclotron resonance spectra. In contrast with other methods, it can be used to estimate the longitudinal dimensions of irregularities on a heterointerface and to determine the main type of scatterers in a structure, features that are extremely useful wherever luminescence characterization is difficult, as, for example, in type-II InAs/GaSb structures with a discontinuous band gap at the heterointerface. It is well known that the cyclotron resonance lineshape has distinctive characteristics in the form of quantum oscillations in the case of short-range scatterers.[2] These oscillations have been observed previously in the system of a two-dimensional electron gas on a Si surface,[3] but the observation of such a cyclotron resonance lineshape in other materials has not been reported. We have observed quantum oscillations in a study of submillimeter absorption in a solitary GaSb–InAs–GaSb quantum well. We have carried out investigations that enable us to relate the cyclotron resonance lineshape to the presence of small-scale roughness on the surface of a heterointerface.

The object chosen for the investigation was the system InAs/AlGaSb, in which different types of bonds can be formed at the heterointerface [In–Sb or (Al)Ga–As], depending on the technique and conditions of its formation.

2. EXPERIMENTAL PROCEDURE

The samples were structures with solitary GaSb–InAs–GaSb and AlSb–InAs–AlSb quantum wells grown by molecular beam epitaxy on GaAs(001) substrates. The procedure used to grow a thick ($\sim 2\ \mu$m) GaSb/Al(Ga)Sb buffer structure is described in detail in Ref. 4. All the structures were grown at a substrate temperature of 500 °C, which makes it very difficult to form a solitary heterointerface of the In–Sb type, almost regardless of the barrier material, because of the strong reevaporation of Sb from the strained InSb boundary monolayer.[5] Heterointerfaces were formed in the InAs/GaSb structure by switching the fluxes of group-V elements onto the GaSb surface with a minimum holding time (3 s) under the As flux before turning on the In flux. In all other structures with InAs/AlSb a single InSb monolayer was specially grown on the AlSb surface with a more than sixfold excess flux of Sb atoms above the flux of In atoms, after which the Sb and As fluxes were switched simultaneously.

Cyclotron resonance was measured at a fixed laser emission wavelength ($\lambda = 119\ \mu$m) by sweeping a magnetic field oriented perpendicular to the sample surface. All the samples were ground off to a wedge configuration to avoid interference in the substrate. As a rule, the samples were additionally furnished with electrical contacts for measurements of magnetoresistance oscillations.

The density and mobility of electrons in the two-dimensional InAs channel were measured by means of the Hall effect in the temperature range 4.2–300 K.

3. RESULTS AND DISCUSSION

Figure 1 shows cyclotron resonance spectra obtained for two solitary InAs quantum wells with differently configured heterointerfaces. The upper curve corresponds to measurements for a structure with GaSb barriers, and the lower curve corresponds to measurements for a structure with AlSb barriers. The two wells have essentially the same width (approximately 20 nm) and similar values of the surface carrier density in the two-dimensional InAs channel (approximately 3×10^{12} cm^{-2}) and the mobility at 300 K [$\sim 2.5 \times 10^4$ cm^2/(V·s)]. However, the values of the low-

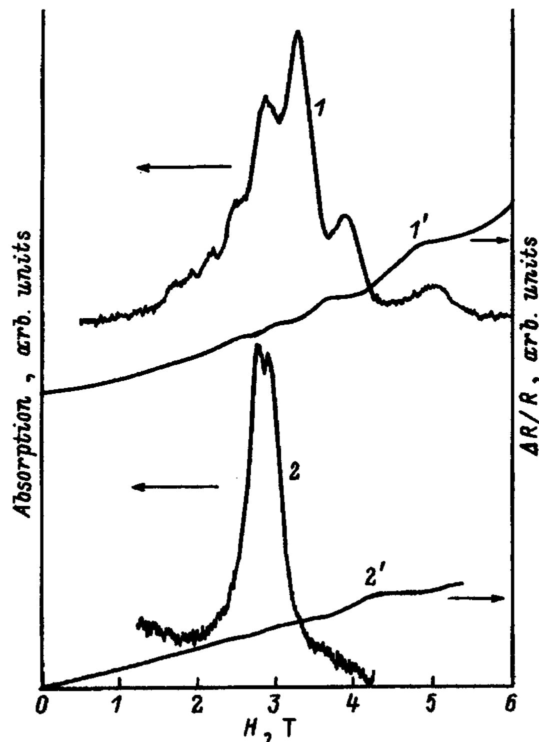

FIG. 1. Cyclotron resonance spectra (*1, 2*) at $\lambda = 119$ μm and dependence of the magnetoresistance $\Delta R/R$ on the magnetic field H (*1'*, *2'*) for quantum wells. *1*, *1'*) GaSb–InAs–GaSb; *2*, *2'*) AlSb–InAs–AlSb.

temperature carrier mobility in the InAs/AlSb structure (2×10^5 cm^2/(V$\cdot$s), Ref. 6) are more than three times the values in the InAs/GaSb structure, probably because of a higher-quality heterointerface. Significant differences, not only in the width, but also in the shape of the cyclotron resonance line are observed in the cyclotron resonance spectra.

The upper curve in the figure corresponds to a characteristic lineshape clearly indicative of quantum oscillations. The prominent features of the cyclotron resonance line correspond to magnetic fields at which the Fermi level coincides with one of the Landau levels in accordance with the theoretical predictions of Ando.[2] This statement is further corroborated by measurements of the magnetoresistance oscillations using a two-contact procedure, conducted simultaneously with absorption measurements. It is evident that the oscillations on the cyclotron resonance line correlate with the magnetoresistance oscillations. Control measurements in oblique magnetic fields have shown that the quantum oscillations in the absorption shift identically with the magnetoresistance oscillations and, in accordance with the expected behavior of the two-dimensional electron gas, according to the law of the cosine of the angle of inclination.

Conversely, for a structure with a quantum well of the type InAs/AlSb quantum oscillations are not visible on the cyclotron resonance line, and the linewidth is much smaller than for the upper curve. The splitting of the peak (lower curve in Fig. 1) is not associated with the kind of filling of the Landau levels; its nature is discussed in another paper.[7]

We now discuss the cause of the quantum oscillations in greater detail. Normally, in strong magnetic fields the properties of the system depend on the distribution of carriers among the Landau levels. Additionally, the characteristic space scale of the scattering potential plays an important role in the investigation of cyclotron resonance. As mentioned in one survey,[2] this influence is strongest for the case $d \ll l$, where d is a characteristic length of the scatterers, and $l = (\hbar c/eH)^{1/2}$ is the magnetic length. When a set of conditions is satisfied such that the Fermi level crosses the Landau levels several times within the limits of the cyclotron resonance line, the cyclotron resonance spectrum can acquire an oscillatory structure. The onset of oscillations is a consequence of the dependence of the absorption coefficient of the two-dimensional electron gas on the density of states at the Fermi level. As in the case of ordinary magnetoresistance oscillations, these oscillations are determined by the carrier density and have a characteristic period $1/H$ along the axis. In accordance with theoretical predictions,[2] in the range of lower magnetic fields $\omega_c < \omega_0$ (ω_0 is the frequency of the sensing radiation, and ω_c is the cyclotron frequency) the absorption maxima coincide with the magnetoresistance maxima, whereas at the edge of the absorption line, corresponding to high magnetic fields ($\omega_c > \omega_0$), the magnetoresistance maxima correspond to absorption minima. It has been shown[2] that the presence of quantum oscillations is a sign that the main type of electron scattering in the given system is scattering by a short-range potential. The prime candidate for the source of such a scattering potential is roughness of the heterointerface with a characteristic length shorter than the magnetic length. We can approximately estimate the characteristic dimensions of this roughness from the fact that for the given magnetic fields $H \sim 3$ T the magnetic length $l = 15$ nm. This estimate gives a length of the order of several tens of angstroms. It is obvious that more precise estimation of the dimensions of the irregularities will require additional measurements over a broad range of magnetic fields. The observation of quantum oscillations in the absorption in the system InAs/GaSb is for the most part abetted by a sufficiently high electron density in the quantum well (more than 10^{12} cm^{-2}), for which small-scale roughness plays an especially major role.[8]

Such a significant difference in the cyclotron resonance spectra of the two structures, which is consistent with the results of low-temperature Hall measurements, can be attributed to a departure from planarity and probably to a local variation in the type of bond at the InAs/GaSb heterointerface as a result of the substitution of As atoms for Sb atoms, a reaction that is greatly accelerated at high temperatures,[9] whereas in the InAs/AlSb structure the type of bond at the heterointerface is predominantly In–Sb (Ref. 6) in the presence of substantially better planarity.

In addition to scattering by surface roughness elements, another possible cause of the onset of quantum oscillations in InAs–GaSb structures could be the presence of a nearby layer of holes in the valence band of GaSb. Indeed, the screened hole gas has the properties of a short-range scatterer, which in principle is capable of leading to quantum oscillations in the absorption. Additional experiments have been performed on a series of InAs/AlSb/GaSb samples, in

which the width of the barrier between electrons in InAs and holes in GaSb was varied from 2 nm to 30 nm, and the InAs/AlSb heterointerface was formed by growing a single monolayer of InSb at a high excess Sb pressure. However, quantum oscillations were not observed in any of these samples, ruling out the hole layer as a cause of absorption oscillations. We note that absorption oscillations have been observed previously at GaSb/InAs heterointerfaces.[10] The authors in this case interpreted their cause as intersubvalley transitions between Landau levels located in the conduction band of InAs and Landau levels in the valence band of GaSb.

It is important to note that the absence of quantum oscillations in structures with an AlSb barrier might be attributed, not to improvement of the quality of the heterointerface, but to a lower probability of scattering by roughness due to the greater height of the AlSb barriers. It follows from our estimates, however, that the height of the barriers does not have an appreciable influence on the probability of scattering by roughness of the heterointerface in contrast with, for example, the width of the well.

We have thus observed for the first time quantum oscillations in the cyclotron resonance spectrum in a solitary quantum well in InAs/GaSb. We have proposed a new method for investigating the surface quality of a heterointerface by measuring the cyclotron resonance spectra. We have obtained preliminary data that can be used to estimate the longitudinal dimensions of scatterers at the interface. More detailed studies in different magnetic fields will be required to improve the accuracy of such estimates.

This work has received support from the Japan Society for the Promotion of Science, the International Association for the Promotion of Cooperation with Scientists from the Independent States of the Former Soviet Union (INTAS, Grant 94-1172), the Russian Fund for Fundamental Research (RFFI, Grants 97-02-18355 and 97-02-18175), and jointly from the latter and Deutsches Forschungsgemeinschaft (RFFI-DFG, Grant 96-02-00223G).

[1] W. C. Mitchel, G. J. Brown, I. Lo, S. Elharmi, M. Ahoujja, K. Ravindran, R. S. Newrock, M. Razeghi, and Kh. He, Appl. Phys. Lett. **65**, 1578 (1994).
[2] T. Ando, J. Phys. Soc. Jpn. **38**, 989 (1975).
[3] G. Abstreiter, J. P. Kotthaus, J. F. Koch, and G. Dorda, Phys. Rev. B **14**, 2480 (1976).
[4] S. V. Ivanov, P. D. Altukhov, T. S. Argunova, A. A. Bakun, A. A. Boudza, V. V. Chaldyshev, Yu. A. Kovalenko, P. S. Kop'ev, R. N. Kutt, B. Ya. Meltser, S. S. Ruvimov, S. V. Shaposhnikov, L. M. Sorokin, and V. M. Ustinov, Semicond. Sci. Technol. **8**, 347 (1993).
[5] P. V. Neklyudov, S. V. Ivanov, B. Ya. Mel'tser, and P. S. Kop'ev, Fiz. Tekh. Poluprovodn. **31**, 2157 (1997) [Semiconductors **31**, (1997)].
[6] P. D. Wang, N. N. Ledentsov, C. M. Sotomayor-Torres, S. V. Ivanov, B. Ya. Meltser, and P. S. Kop'ev, Solid State Commun. **9**, 361 (1994).
[7] Yu. Vasilyev, H. Kobori, T. Ohyama, S. Suchalkin, S. Ivanov, P. Kop'ev, and B. Meltser, Phys. Rev. B (to be published).
[8] T. Ando, A. B. Fowler, and F. Stern, Rev. Mod. Phys. **54**, 437 (1982) [*Electronic Properties of Two-Dimensional Systems* (Russian trans., Mir, Moscow, 1985)].
[9] D. H. Chow, R. H. Miles, J. R. Soderstrom, and T. C. McGill, J. Vac. Sci. Technol. B **8**, 710 (1990).
[10] Y. Guldner, J. P. Vieren, P. Voisin, M. Voos, J. C. Maan, L. L. Chang, and L. Esaki, Solid State Commun. **41**, 755 (1982).

Translated by James S. Wood

Deep-level transient spectroscopy in InAs/GaAs laser structures with vertically coupled quantum dots

M. M. Sobolev, A. R. Kovsh, V. M. Ustinov, A. Yu. Egorov, A. E. Zhukov,
M. V. Maksimov, and N. N. Ledentsov

A. F. Ioffe Physicotechnical Institute, Russian Academy of Sciences, 194021 St. Petersburg, Russia
(Submitted March 6, 1997; accepted for publication March 19, 1997)
Fiz. Tekh. Poluprovodn. **31**, 1249–1255 (October 1997)

Indium arsenide/gallium arsenide structures with vertically coupled quantum dots imbedded in the active zone of a laser diode are investigated by deep-level transient spectroscopy (DLTS), and the capacitance-voltage characteristics are analyzed. The DLTS spectrum was found to undergo significant changes, depending on the temperature of preliminary isochronous annealing of the sample, $T_a < T_{ac} = 245$ K or $T_a > T_{ac}$, and on the cooling conditions, with a bias voltage $V_b = 0$ or with an applied carrier pulse $V_f > 0$. The changes are attributed to the onset of Coulomb interaction of carriers trapped in a quantum dot with point defects localized in the nearest neighborhoods of the quantum dots and also to the formation of a dipole when $T_a < T_{ac}$ and cooling takes place with $V_f > 0$, or to the absence of a dipole when $T_a > T_{ac}$ and $V_b = 0$. It is discovered that the tunneling of carriers from the deeper states of defects to the shallower states of quantum dots takes place in the dipole, and the carriers are subsequently emitted from the dots into bands. © *1997 American Institute of Physics.*
[S1063-7826(97)02610-0]

1. INTRODUCTION

Research on heterostructures with spatial confinement of the carriers in three dimensions has attracted growing interest in recent times.[1] Structures of this kind are of major importance from the viewpoint of their fundamental properties and hold considerable promise for applications in optoelectronics. Arakawa and Yariv[1] have predicted theoretically the position of the threshold laser current density and a significant increase in its temperature stability. We have now succeeded in generating radiation through the ground state of quantum dots up to room temperature in injection heterolasers with an active zone utilizing vertically coupled (In, Ga)As/GaAs quantum dots. This type of laser has an unprecedented room-temperature threshold current density of 100 A/cm^2 (Ref. 2). On the other hand, the specific conditions under which the quantum dots are grown, above all the low growth temperature of the GaAs layer covering the dots, are conducive to the formation of point defects in the vicinity of a quantum dot, which act as centers for the trapping and nonradiative recombination of nonequilibrium carriers. At near-room temperatures the thermal emission of carriers from the dots and their retrapping by defects can only lower the quantum efficiency of radiative recombination. Further optimization of the active zone of quantum dot lasers requires investigation of the parameters of the quantum states of such structures, the presence of defects and impurities with deep levels, the interaction of charged defects with carriers localized in the quantum dots, and the tunneling of carriers between deep states and quantum states.

Deep-level transient spectroscopy (DLTS) is the most effective method for the spectroscopy of deep-level defects and impurities.[3] This method has been very successful in application to the study of quantum wells.[4,5] Its potential for the investigation of quantum dots was first demonstrated in Ref. 6. Another method with a successful record in the characterization of quantum dots and the determination of a number of electrical parameters is capacitance-voltage (C–V) spectroscopy.[7]

In the present article we report the results of an experimental study of heterolaser structures with an active zone based on an array of vertically coupled InAs/GaAs quantum dots, using the C–V and DLTS methods. We have found that the DLTS spectra contain peaks associated with deep states of known defects and impurities and also with quantum dot states. We have observed for the first time the Coulomb interaction of carriers localized in quantum dots and in deep impurity and defect states. We have disclosed carrier tunneling effects between states in a vertically coupled array of quantum dots and deep impurity and defect states.

2. SAMPLES AND METHODS OF INVESTIGATION

The laser heterostructures were grown on n^+-GaAs(100) substrates. The active zone, which consists of an array of vertically coupled quantum dots, was placed in the middle of a p^0-GaAs layer of thickness 0.12 μm bounded on both sides by AlAs(20 Å)GaAs(20 Å)×15 short-period superlattices. The quantum dot array was formed by the sixfold deposition of InAs layers of thickness 5 Å separated by a GaAs spacer layer of thickness 50 Å. The dots had a square base with sides oriented along the [001] and [010] directions and formed a primitive square lattice in the horizontal plane. The laser structures were grown in standard geometry (with separate confinement of the electron and light beams). The geometry of the laser structure is similar to that described in Ref. 2. At room temperature a strong line at $h\nu = 1.1$ eV is observed in the photoluminescence spectra of such a structure,[2] because of the ground state of electrons and holes in the tunnel-coupled dots. The quantum states of the dots,

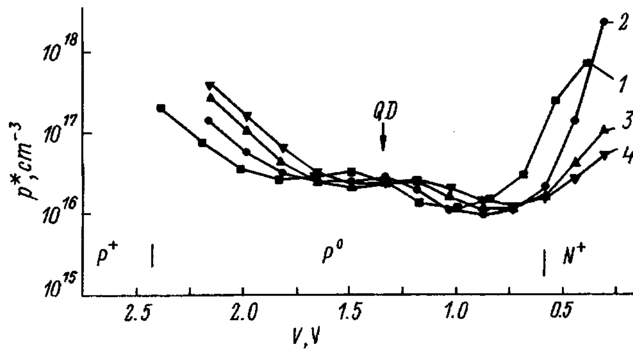

FIG. 1. Profile of the distribution of the effective carrier density p^* for laser structure with six rows of InAs/GaAs quantum dots plotted as a function of the thickness of the space-charge layer $x \sim y$ at various temperatures. *1*) $T=86$ K; *2*) 122 K; *3*) 170 K; *4*) 200 K. The vertical bars indicate the boundaries of the waveguide and the emitter; the position of the quantum dots is labeled QD.

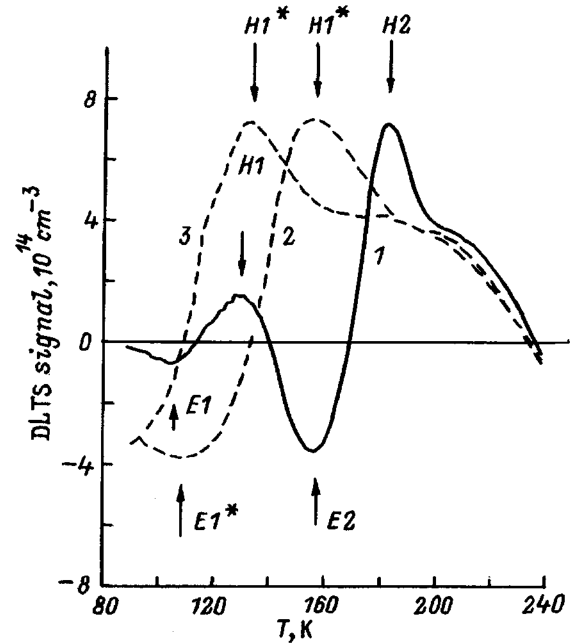

FIG. 2. DLTS spectra of a laser structure with six rows of InAs/GaAs quantum dots for various isochronous annealing temperatures, $V_b=1.06$ V, $V_f=1.71$ V. *1*) $T_a=250$ K; *2*) 245 K; *3*) 240 K.

the deep levels of defects and impurities, and the profiles of the carrier distribution in the laser heterostructures were investigated by DLTS and $C-V$ spectroscopy using a BIO-RAD DL4600 spectrometer operating in the dual-gate integrating mode. A Boonton-72B bridge operating at a frequency of 1 MHz was used for the capacitance measurements. This device has a sensitivity $\Delta C/C_0 \approx 10^{-4}$.

3. RESULTS

The carrier-density profiles were determined from the $C-V$ characteristics measured at various temperatures in the range 80–300 K. Figure 1 shows the profiles of the effective hole-density distribution $p^*(x)$ determined from the $C-V$ characteristics. At $V=0$ the space-charge layer takes up almost the entire waveguide, including the active zone consisting of six rows of quantum dot arrays and a wetting layer. As the reverse bias voltage is increased, the space-charge layer broadens in the direction of the p^+-emitter. To determine the profile of the effective hole density in the active zone and waveguide, the $C-V$ characteristics were measured by applying a forward bias voltage V_f to the structure. Samples were specially selected with a high cutoff voltage on the curve $1/C^2=f(V)$, making it possible to determine the $p^*(x)$ profiles in these regions. It follows from Fig. 1 that a peak (labeled QD in Fig. 1) associated with carrier accumulation is observed at the center of the GaAs waveguide, where the active zones with the quantum dots and the wetting layer should reside. The position of the maximum of this peak depends on the temperature at which the $C-V$ characteristics are measured. Since the regions of interest to us appeared only after the application of a forward bias voltage, it was necessary to modify the DLTS method for the determination of spectra associated with carrier emission from the quantum dots and deep-level traps. In accordance with the results of the $C-V$ measurements, the carrier pulse was transmitted in the forward direction and varied in the interval $V_f=(1.7-0.95)$V. This pulse had a duration of 5 μs. Also sent in the forward direction was a voltage pulse, at the level of which the DLTS signal was recorded. This voltage was varied in the interval $V_b=(0.9-1.6)$V and was always lower than V_f. Special measurements of the forward current were not performed. For the DLTS measurements in the temperature range (80–260) K the total capacitance of the sample was easily compensated. The DLTS spectrum was also unaffected by switching of the measurement range of the capacitance bridge and the connection of a resistance in series with the sample. This fact is indirect evidence that the forward current was insignificant and did not produce an appreciable change in the capacitance of the sample, and that the condition $RC\omega > 1$ was satisfied. Moreover, if not mentioned specifically, all the measurements were performed in darkness. Prior to each measurement the sample was subjected to isochronous annealing for 1 min at a fixed temperature. The annealing temperature was varied in the interval (240–300) K. The sample was then cooled to $T=80$ K with a forward bias V_f or with $V_b=0$. Then the DLTS measurement procedure was initiated with the sample heated to 300 K. It was established that the DLTS spectrum depends on the isochronous annealing temperature T_a (Fig. 2). The critical temperature of transition from one type of spectrum to another was $T_{ac}=245$ K (Fig. 2, curve *2*). The DLTS spectrum represented by curve *1* in Fig. 2 was observed at $T_a>245$ K, and the spectrum represented by curve *3* was observed at $T_a<245$ K. Also, the DLTS spectra measured at $T_a<245$ K depended on whether the sample was cooled with V_b or at $V_f>0$ and also on the value of T_a. The thermal activation energies E_a and the capture cross sections $\sigma_{n,p}$ of the levels observed in the spectra were determined from the Arrhenius relations for these levels (Table I). The corresponding carrier emission rate was determined from the relation

$$e_{n,p}=A\sigma_{n,p}T^{3/2}\exp(-E_a/kT), \tag{1}$$

where A is a constant independent of T, and k is the Boltzmann constant.

TABLE I.

Level symbol	Energy E_a, meV	Capture cross section σ, cm^2	Level identification
		$T_a > T_{ac}$	
$E1$	111	1.7×10^{-17}	
$E2$	235	1.3×10^{-14}	$EL14$ (Refs. 10 and 11)
$E3$	426	4.2×10^{-16}	Ni_{Ga} (Ref. 12)
$H1$	194	2.5×10^{-16}	
$H2$	390	1.8×10^{-13}	$HL5$ (Ref. 8)
$H3$	420	1.6×10^{-14}	$HL4$ (Ref. 8)
		$T_a < T_{ac}$	
$E1^*$	110	5.2×10^{-16}	
$H1^*$	194	2.5×10^{-18}	
$H2^*$	420	1.6×10^{-14}	$HL4$ (Ref. 8)

Note: The parameters of the $H1$ and $H1^*$ states are determined for $V_b = 1.07$ V and $V_f = 1.60$ V. In the last column the numbers in brackets indicate the corresponding references.

To determine the spatial localization of the levels observed in the DLTS spectra in the cases of isochronous annealing at $T_a > 245$ K and $T_a < 245$ K, the spectra were measured while V_b and V_f were varied (Figs. 3a, 3b, 4a, and 4b). Unusual properties are exhibited by the level $H1$ ($T_a > 240$ K) as V_b is varied (Fig. 3a) and by the level $H1^*$ as V_f is varied (Fig. 4b). As V_b is increased, the $H1$ peak in the spectra shifts toward lower temperatures with scarcely any change in the amplitude and shape of the pulse. It appears at $V_b = 1.0$ V and disappears at $V_b = 1.3$ V. It is evident from the results in Table II that at $V_b = 1.07$ V the thermal activation energy is equal to 194 meV, and as V_b is increased, E_a drops abruptly to 132 meV and then slowly increases. An increase in V_b corresponds to a decrease in the electric field in our case. As V_f is varied, a peak appears at $V_f > 1.4$ V and goes to saturation at $V_f = 1.7$ V. These changes correspond to localization of the peak and the profile of the carrier distribution $p^*(x)$ (Fig. 1). As V_b is increased, the $H2$ and $H3$ peaks of the DLTS spectrum disappear, and an $E3$ peak appears, providing further evidence of their spatial localization. The amplitudes of the $H2$ and $H3$ peaks do not depend on the amplitude of the carrier pulse. In isochronous annealing at $T_a < 245$ K (Fig. 4) the $E1, H1$, and $H2$ levels vanish, and the $E1^*$ and $H1^*$ levels appear. The position of the $H1^*$ peak in the DLTS spectra depends on the amplitude of the carrier pulse and shifts toward higher temperatures as V_f is increased. The thermal activation energy of the $H1^*$ level varies from 194 meV to 89 meV as V_f is increased from 1.2 V to 1.6 V (Table II). The amplitudes of the corresponding peaks remained essentially constant at all (Fig. 4b). Another prominent feature of the $H1^*$ peak is the fact that it has considerable width and on the high-temperature side makes a smooth transition to the $H2^*$ peak (Fig. 4). The $H1^*$ and $H3^*$ peaks decrease with increasing value of V_b and vanish at $V_b = 1.3$ V. This behavior further confirms their spatial localization. The variation of V_b is accompanied by a change in the amplitudes of the $H1^*$ and $H3^*$ peaks. The concentration of these centers decreases considerably for $V_b > 1.3$ V. The activation energies of the $E1$ and $E1^*$ levels are very close to each other, with a value

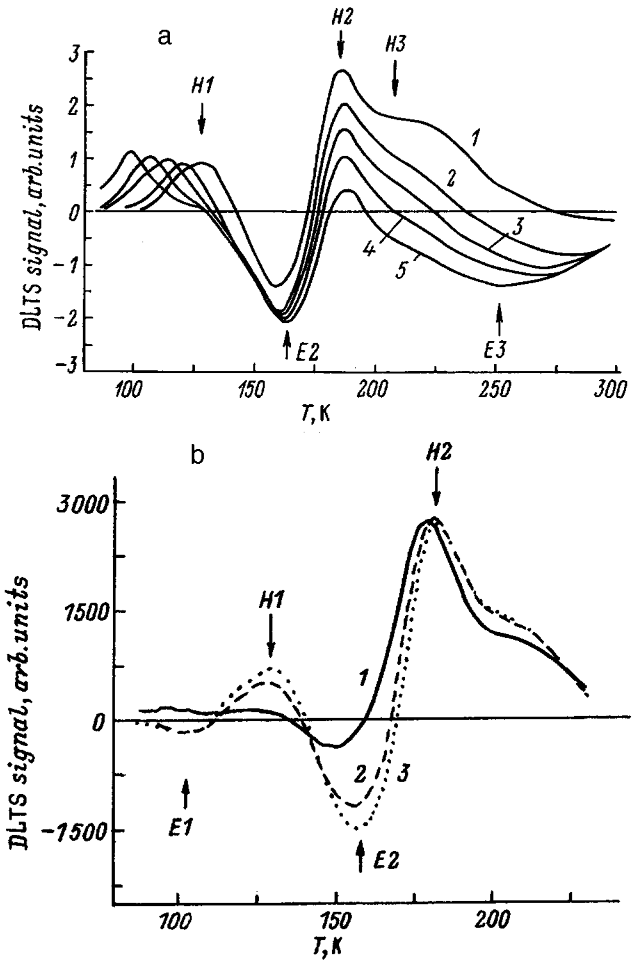

FIG. 3. DLTS spectra of a laser structure with six rows of InAs/GaAs quantum dots after isochronous annealing at $T_a > 245$ K and precooling at zero bias ($V_b = 0$). a) Measured at $V_f = 1.64$ V with various biases V_b: *1)* 1.07 V; *2)* 1.15 V; *3)* 1.20 V; *4)* 1.25 V; *5)* 1.30 V. b) Measured at $V_b = 1.07$ V for various carrier pulse amplitudes V_f: *1)* 1.40 V; *2)* 1.59 V; *3)* 1.69 V.

$E_a = 110$ meV. The DLTS peak of the $E1^*$ level, unlike $E1$ and like $H1^*$, is broad.

4. DISCUSSION OF THE RESULTS

The deep-level parameters determined from the Arrhenius relations (Table I) and the observed trends in the variation of the DLTS spectra (Figs. 2–4) provide a basis for identifying the $H2, H3, H3^*, E2$, and $E3$ peaks with well-known levels from previous papers.[8–12] The parameters of the $H2$ level are close to those of the $HL5$ level first ob-

TABLE II. Dependence of the thermal activation energies of the $H1$ and $H1^*$ levels on V_b and V_f.

$T_a < 245$ K, $V_b = 0.9$ V		$T_a > 245$ K, $V_f = 1.64$ V	
V_fV	E_a meV	V_bV	E_a meV
1.2	89	1.07	194
1.4	103	1.15	132
1.5	132	1.20	156
1.6	194	1.25	163
		1.30	184

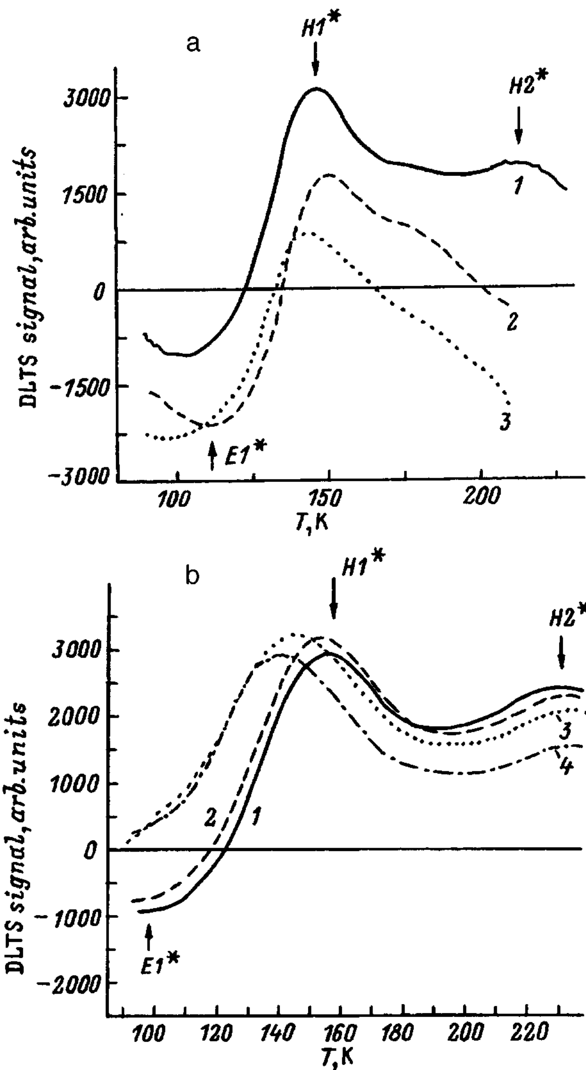

FIG. 4. DLTS spectra of a laser structure with six rows of InAs/GaAs quantum dots after isochronous annealing at $T_a < 245$ V and precooling with $V_f > 0$. a) Measured at $V_f = 1.64$ V with various biases V_b: 1) 1.0 V; 2) 1.15 V; 3) 1.30 V. b) Measured at $V_b = 0.9$ V for various carrier pulse amplitudes V_f: 1) 1.6 V; 2) 1.5 V; 3) 1.4 V; 4) 1.2 V.

served in GaAs grown by liquid-phase epitaxy.[8] The corresponding center comprises a complex of native defects, whose composition includes an arsenic vacancy V_{As} (Ref. 9), and it is formed in the presence of a Ga excess in the solution melt. In our case a defect including V_{As} can appear as the result of a local deviation from stoichiometry during the growth of a heteroepitaxial GaAs layer and the formation of quantum dots. The maximum density of $H2$-type centers in our samples was $N_t = 8.5 \times 10^{14}$ cm^{-3}. Both the $H3$ peak and the $H3^*$ peak have been identified as the $HL4$ level, which is associated with a Cu impurity.[8] This state, like the center with the $H2$ level, is localized in neighborhoods of the quantum dot on the side of the p^+-emitter. The $E2$ and $E3$ levels have also been identified with known levels. The center with energy $E2$ is identified with the $EL14$ level first observed in Ref. 10, and its appearance has previously[11] been linked to the presence of Ni. This defect is fairly uniformly distributed in the neighborhoods of the quantum dot. The $E3$ level is found to have parameters close to those of a level observed in Ref. 12 and has been attributed to a substitutional Ni impurity in the Ga lattice. This defect is localized in the neighborhood of the quantum dot on the side of the n^+-emitter. The formation of defects associated with Cu and Ni impurities is probably attributable to the presence of residual contaminants in the epitaxial growth sources.

As for the $H1$ and $H1^*$ levels, their behavior as a function of the isochronous annealing conditions, temperature, and variations of V_b and V_f (Figs. 3 and 4) defy interpretation if they are linked to any kind of defect, including the bistable variety.[13] The position of the $H1^*$ peak in the DLTS spectra depends on the annealing temperature (Fig. 2) and on the cooling conditions ($V_f > 0$ or $V_b = 0$) and changes in optical illumination. This phenomenon is usually observed for configuration-bistable defects, but it is not characteristic of a metastable defect for the position of the maximum of a DLTS peak to change as V_f is varied.[13] In studies of heterostructures by the total-conductivity method[14,15] the effective energy of the band discontinuity has been found to decrease with decreasing temperature or the frequency f at which the conductivity and capacitance measurements are performed. Similar variations in the thermal activation energy of carriers in level-to-band emission have also been observed for a quantum well.[4,5,16] In Ref. 16 the variation of the band discontinuity has been attributed to the presence of an ''interface dipole'' formed by donors ionized in a thin layer (≤ 50 Å) and to in-plane acceptors at a distance of several tens of angstroms from the heterointerface. The authors postulate that the electrostatic potential of this dipole is subtracted or added to the dipole potential of the band discontinuity at the heterointerface. Since the distance between the contaminated planes are of the same order or smaller than the de Broglie wavelength of the carriers, upon crossing the heterointerface they ''see'' a new band discontinuity. The energy $E_a = 194$ meV determined by us for the $H1^*$ level at $V_b = 1.07$ V and $V_f = 1.64$ V is much higher than for the wetting layer if it is regarded as a quantum well. Grundmann *et al.*[17] have observed a photoluminescence peak from the wetting layer at an energy of 1.43 eV ($T = 8$ K); the width of the band gap of GaAs at this temperature is $E_g = 1.51$ eV. Consequently, the energy of the ground state of the quantum well cannot exceed 80 meV. It can therefore be assumed that the $H1^*$ level is not associated with the quantum well of the wetting layer, but is a hole state of the quantum dot. The variations observed by us in the DLTS spectra with changes in the isochronous annealing temperature and the cooling conditions ($V_f > 0$ or $V_b = 0$) most likely tie in with the fact that in cooling with $V_f > 0$ the allowed bands contain carriers that become trapped in quantum states in the quantum dots, thereby contaminating them. On the other hand, we have already determined that the DLTS spectrum of deep-level defects in the immediate vicinity of a quantum dot is similar to the spectrum customarily observed for GaAs prepared by liquid-phase epitaxy with an excess of Ga in the solution melt. Also characteristic of GaAs prepared by this technique is the presence of a Ga_{As} defect, which is a double acceptor with energy levels of 77 meV and 230 meV (Ref. 18). These levels are not usually detected in the temperature range of our investigation. For $V_b > 1.30$ V we have observed only the

''tail'' of a level with a thermal activation energy of 230 meV. Consequently, since the thermal activation energy of the levels of the Ga_{As} defect in the immediate vicinity of a quantum dot is lower than for the quantum state $H1^*$, it is possible to have a temperature interval in which deep acceptors still do not trap holes, are ionized, and have a negative charge. The surface densities of Ga_{As} and $H2$ defects and holes p_d trapped in a quantum dot (Fig. 2), determined from the relation[6]

$$\Delta C/C = p_d L(2N_A W^2)$$

(L is the depth of the quantum dot layer, W is the width of the space-charge region, and N_A is the density of acceptors in the GaAs layer), coincide and $\approx 10^{11}$ cm^{-2}. The parameters determined from the C-V characteristics (Fig. 1) and DLTS measurements (Fig. 2), including the values $\Delta C/C \approx 2.5\times10^{-2}$ and $N_A \approx 1.5\times10^{16}$ cm^{-3}, are used in estimating p_d. The Coulomb interaction of holes localized in a quantum dot with oppositely charged defects and impurities in its neighborhoods must lead to the formation of a charged dipole. The dot-to-band thermal activation energy of carriers changes, possibly in connection with, among other factors, a change in the transmissivity of the barrier for carrier tunneling. To be recaptured in the quantum dot, the barrier must also be surmounted. By varying T_a and V_f we alter the population of the quantum dot and the height of the thermal barrier for carrier emission into a band. In cooling with $V_b=0$ carriers are not present in the bands, and a dipole is not formed. The electron level $E1^*$ observed under these conditions is probably an electronic quantum state of the same dot. If the sum of the energies of the $E1^*$ and $H1^*$ levels is subtracted from the width of the GaAs band gap, a quantity of the order of 110 meV is obtained, fully consistent with photoluminescence data.[2,17]

We have also observed characteristic variations in the thermal activation energy for the $H1$ level observed in the DLTS spectra at $T_a>245$ K (Table II). Likewise they can be explained from the standpoint of carrier emission from quantum dots as long as the formation of a dipole between the quantum dot and the defect does not take place at $T_a>245$ K. At these isochronous annealing temperatures a dipole is not formed, and the DLTS spectrum no longer depends on the preliminary cooling conditions ($V_b=0$ or $V_f>0$). In our investigated structures the size of the quantum dots in each successive row of the array of vertically coupled dots is greater than in the preceding row as a result of the conditions attending the formation of these dots. Consequently, at $V_b=1.07$ V we observe emission from the largest quantum dot, for which the levels are deeper. Holes from quantum dots that are smaller in size and therefore have shallower energy levels will tunnel into the largest quantum dot, which has the deepest quantum level, and it then becomes the source from which the thermal emission of holes takes place. Increasing V_b to 1.15 V causes the thickness of the space-charge layer to decrease by approximately 90 Å, which corresponds to the size of two quantum dots. Increasing V_b, therefore, we keep the largest quantum dots with the highest activation energies outside the limits of the space-charge layer. As V_b is further increased, the activation energy increases rather slowly in connection with the tunneling of holes from the quantum dots, which depends on the electric field of the p-n junction. The shape of the DLTS peak for this level remains unchanged for all values of V_b. This fact doubtless indicates that emission takes place only from one quantum dot having the deepest state, to which carriers tunnel from shallower states out of smaller quantum dots. The populations of the quantum dot states for a given V_f do not change.

Consequently, two different DLTS spectra containing peaks associated with quantum dots can be observed, depending on the isochronous annealing temperature, $T_a<T_{ac}=245$ K or $T_a>245$ K. Moreover, the DLTS spectra obtained for $T_a<245$ K does not contain any of the peaks that exist in the spectra obtained for $T_a>245$ K. The peak of the $E1^*$ level broadens, and the $H1^*$ peak makes a smooth transition on the high-temperature side to a broad band. In several investigated samples prepared from the same plate we have observed that the DLTS spectrum measured for $V_b=0$ and $T_a<T_{ac}$ changes its form to one in which the $E1^*$ and $H1^*$ levels vanish and the $E1, E2, H1$, and $H2$ levels appear. We believe, therefore, that the $E1$ and $E1^*$ levels and the $H1$ and $H1^*$ levels belong to the same quantum dot. In the first, case, with annealing at $T_a>T_{ac}$ and cooling with $V_b=0$, the quantum dot is not populated, Coulomb interaction with charged impurities and defects in the neighborhoods of the quantum dot does not take place, and a dipole is not formed. Being situated sufficiently far from the quantum dot, impurities and defects are not attracted to it. In the case of annealing at $T_a<T_{ac}$ and cooling at V_f quantum dot is populated with carriers, the Coulomb interaction of carriers localized in the quantum dots with charged defects and impurities surrounding the quantum dots takes place, and a dipole is formed, becoming frozen at temperatures $T_a<T_{ac}$. In this dipole the wave functions of the impurities and defects overlap with the quantum states of the dots. It becomes possible for carriers to tunnel from the deeper states of these impurities and defects to the shallower states of the quantum dots and to subsequently undergo thermal emission into bands. This phenomenon is most likely responsible for the broadening of the $E1^*$ and $H1^*$ levels, the disappearance of the $E2$ and $H2$ levels from the DLTS spectra, and the appearance of a broad band.

5. CONCLUSIONS

We now summarize the results of our DLTS investigations of laser structures with an active zone in the form of six rows of arrays of InGa/GaAs quantum dots.

1. We have established that the low-temperature deposition and growth of quantum dots in GaAs epitaxial layers is accompanied by the generation of point defects in the nearest neighborhoods of the quantum dots as a result of local nonstoichiometry. The surface densities of these defects and quantum dots are close to one another and approximately equal to 10^{11} cm^{-2}.

2. We have discovered that the DLTS spectrum exhibits significant changes, depending on whether the sample is subjected to preliminary isochronous annealing at $T_a<T_{ac}=245$ K or $T_a>T_{ac}$ and on the cooling conditions at

$V_f>0$ or $V_b=0$. The changes are associated with: the onset of Coulomb interaction between carriers trapped and localized in quantum dots, on the one hand, and ionized defects and impurities, on the other; the formation of a dipole when $T_a<T_{ac}$ and cooling takes place with $V_f>0$; or the absence of such a dipole for $T_a>T_{ac}$ and cooling at $V_b=0$.

3. We have observed that overlap of the impurity and defect wave functions with quantum states of the quantum dots takes place in the dipole. Carriers tunnel from the deeper states of defects to the shallower states of quantum dots.

4. We have established that one phenomenon determined from DLTS measurements with preliminary isochronous annealing of the sample at $T_a<T_{ac}$ and subsequent cooling with $V_f>0$ — the lowering of the thermal activation energy of transition of carriers from quantum dots into an allowed band from 194 meV to 89 meV as the amplitude of the carrier pulse V_f is increased — is attributable to a change in the transmissivity of the barrier for carrier tunneling as the population of quantum states in the quantum dots increases. When the investigated sample is isochronously annealed at $V_b=0$, the thermal activation energy of holes from a quantum dot varies between the limits (132–194) meV in connection with the onset of tunneling of holes from quantum dots, which depends on the electric field of the $p-n$ junction.

The authors gratefully acknowledge P. S. Kop'ev and S. G. Konnikov for their assistance with the study and for valuable discussions.

[1] Y. Arakawa and A. Yariv, IEEE J. Quantum Electron. **QE-22**, 1887 (1986).

[2] V. M. Ustinov, A. Yu. Egorov, A. R. Kovsh, A. E. Zhukov, M. V. Maximov, A. F. Tsatsul'nikov, N. Yu. Gordeev, S. V. Zaitsev, Yu. M. Shernyakov, N. A. Bert, P. S. Kop'ev, Zh. I. Alferov, N. N. Ledentsov, J. Böhrer, D. Bimberg, A. O. Kosogov, P. Werner, and U. Gösele, J. Cryst. Growth **175** (1997) (in press).

[3] D. V. Lang, J. Appl. Phys. **45**, 3023 (1974).

[4] T. Matsumoto, Y. Ito, and T. Ishida, Jpn. J. Appl. Phys. **28**, 1541 (1989).

[5] K. L. Jiao and W. A. Anderson, J. Appl. Phys. **73**, 271 (1993).

[6] S. Anand, N. Carlsson, M.-E. Pistol, L. Samuelson, and W. Seifert, Appl. Phys. Lett. **67**, 3016 (1995).

[7] P. N. Brunkov, S. G. Konnikov, V. M. Ustinov, A. E. Zhukov, A. Yu. Egorov, M. V. Maksimov, N. N. Ledentsov, and P. S. Kop'ev, Fiz. Tekh. Poluprovodn. **30**, 924 (1996) [Semiconductors **30**, 492 (1996)].

[8] A. Mitonneau, G. M. Martin, and A. Mircca, Electron. Lett. **13**, 666 (1977).

[9] P. N. Brunkov, S. Gaĭbullaev, S. G. Konnikov, V. G. Nikitin, M. I. Papentsev, and M. M. Sobolev, Fiz. Tekh. Poluprovodn. **25**, 338 (1991) [Sov. Phys. Semicond. **25**, 205 (1991)].

[10] G. M. Martin, A. Mitonneau, and A. Mircca, Electron. Lett. **13**, 191 (1977).

[11] L. Samuelson, P. Omling, and H. G. Grimmeis, J. Cryst. Growth **55**, 164 (1981).

[12] D. L. Partin, J. W. Chen, A. G. Milnes, and L. F. Vassamillet, J. Appl. Phys. **50**, 6845 (1979).

[13] M. M. Sobolev, I. V. Kochnev, M. I. Papentsev, and V. S. Kalinovsky, Semicond. Sci. Technol. **11**, 1692 (1996).

[14] S. R. Forrest and O. K. Kim, J. Appl. Phys. **53**, 5738 (1982).

[15] K. Kazmierski, P. Philippe, P. Poulain, and B. de Cremoux, J. Appl. Phys. **61**, 1941 (1987).

[16] F. Capasso and F. Beltram, Mater. Soc. Symp. Proc. **104**, 47 (1988).

[17] M. Grundmann, N. N. Ledentsov, O. Stier, D. Bimberg, V. M. Ustinov, P. S. Kop'ev, and Zh. I. Alferov, Appl. Phys. Lett. **68**, 979 (1996).

[18] P. W. Yu, W. C. Mitchel, M. G. Mier, S. S. Li, and W. L. Wang, Appl. Phys. Lett. **41**, 532 (1982).

Translated by James S. Wood

Arrays of strained InAs quantum dots in an (In Ga)As matrix, grown on InP substrates by molecular-beam epitaxy

V. M. Ustinov, A. E. Zhukov, A. F. Tsatsul'nikov, A. Yu. Egorov, A. R. Kovsh,
M. V. Maksimov, A. A. Suvorova, N. A. Bert, and P. S. Kop'ev

A. F. Ioffe Physicotechnical Institute, Russian Academy of Sciences, 194021 St. Petersburg, Russia
(Submitted March 11, 1997; accepted for publication March 19, 1997)
Fiz. Tekh. Poluprovodn. **31**, 1256–1260 (October 1997)

Arrays of strained InAs islands in an (In, Ga)As matrix on an InP(100) substrate are synthesized by molecular-beam epitaxy, and their structural and optical properties are investigated. According to transmission electron microscope and high-energy electron diffraction data, the critical thickness corresponding to the onset of island growth is 3 monolayers. The resulting InAs islands are coherently strained, and their base diameter varies from 20 nm to 90 nm. The formation of islands produces in the photoluminescence spectra a dominant long-wavelength line, which shifts toward lower energies as the effective thickness of the InAs increases. The radiation emitted by the InAs islands spans a wavelength range of 1.65–2 μm. © *1997 American Institute of Physics.* [S1063-7826(97)02710-5]

Arrays of semiconductor quantum dots have an auspicious outlook for applications in injection lasers. In particular, a major reduction of the threshold current density and abatement of its temperature dependence have been predicted.[1] One of the most promising techniques for the formation of quantum dot arrays is a method based on self-organization effects observed in deposition by molecular-beam epitaxy (MBE). The structural and optical properties of (In, Ga)As quantum dot arrays situated in an (Al, Ga)As matrix[2,3] and injection lasers utilizing such arrays have been well studied.[4,5] Their application as the active zone of an injection laser has resulted in the attainment of continuous lasing through the ground state of quantum dots up to room temperature at an output power of approximately 1 W with a threshold current density below 100 A/cm^2 (Refs. 5 and 6).

The majority of (In, Ga)As quantum dot lasers have been investigated in the wavelength range 0.9–1.1 μm. The investigations have shown that the emission wavelength of quantum dots prepared on GaAs substrates is limited at the long-wavelength end to 1.27–1.3 μm (Refs. 7 and 8). The problem of extending the emission range attainable in structures containing quantum dots to 2 μm is timely in regard to applications in fiber-optic communication and environmental monitoring systems.

It will be shown below that advances into the targeted wavelength range can be made by using arrays of InAs quantum islands situated in an (In, Ga)As matrix grown on an InP(100) substrate. Structures of this kind are also important from the standpoint of fundamental research on the spontaneous formation of objects with lowered dimensionality, complementing studies in the system of materials (In, Ga)As/(Al, Ga)As. In addition, controlled variation of the degree of matching of the matrix and substrate provides a means for investigating the influence of residual stress on the process of three-dimensional nucleation. Here we report the first MBE synthesis and investigation of the structural and optical properties of arrays of InAs quantum islands formed in an (In, Ga)As matrix with the lattice parameter matched to an InP substrate.

The investigated structures were grown by MBE using a solid-state As_4 source in a Riber-32P apparatus on semiinsulating InP(100) substrates. The investigated InAs layer (island array) was imbedded in the middle of an (In, Ga)As layer of thickness 0.15 μm grown on a buffer layer of thickness 0.2 μm and bounded on the substrate and top sides by InAlAs(2 nm)-InGaAs(2 nm) short-period superlattices. The effective quantity Q_{InAs} of deposited InAs in the active zone was varied from one sample to another in the range 0–13 monolayers (ML). The deposition temperature was 500 °C, and the growth rate was approximately 10 nm/min for the InGa(Al)As layers and 15 nm/min for the deposition of InAs in the active zone. The layers were grown in an arsenic-rich environment.

The degree of matching of the lattice constants of the matrix and InP substrate materials was determined by dual-crystal x-ray diffraction on test layers of thickness 1 μm. The mismatch was less than 10^{-3}, which suffices to guarantee the pseudomorphic growth of InGa(Al)As layers to a thickness of 1 μm (Ref. 9). A photoluminescence study was performed at 10–150 K using a He–Ne laser (exciting photon energy 1.954 eV) for excitation and a cooled InSb photodiode for recording. The excitation power was 20 W/cm^2. Transmission electron microscope (TEM) examinations were performed on a Philips EM 420 microscope with an accelerating voltage of 100 kV. The TEM samples were prepared by conventional mechanical polishing and subsequent sputtering with Ar^+ ions and were investigated in a planar geometry and in the cross section.

The transition from the two-dimensional to the three-dimensional InAs growth regime was determined from a change in the observed high-energy electron diffraction (HEED) pattern in reflection. The formation of three-dimensional nucleation centers produces a striated diffraction pattern, whereas in the case of an atomically smooth surface the observed pattern consists of a system of fringes (''strands'') running perpendicular to the substrate surface. According to our data, this transition takes place at $Q_{\mathrm{InAs}} \simeq 3.0-3.3$ ML, in good agreement with earlier results[10]

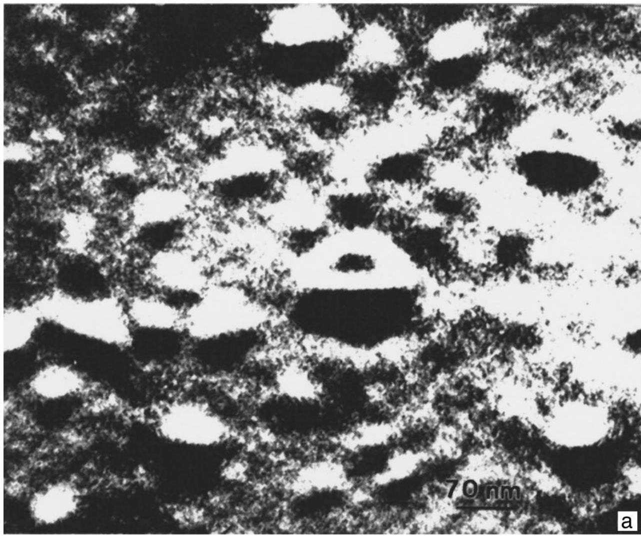

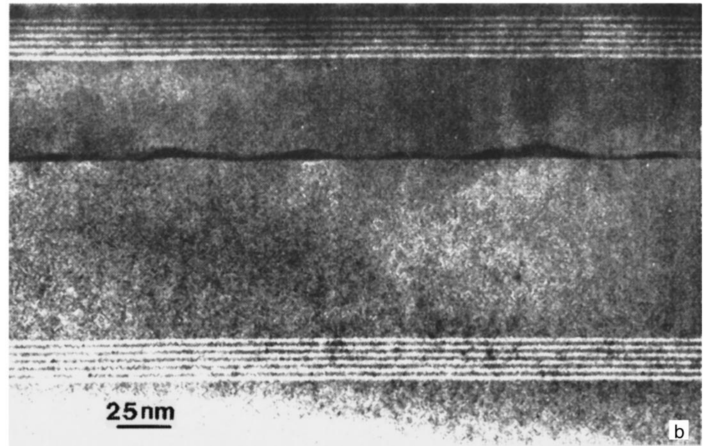

FIG. 1. Images of a structure prepared by the deposition of six InAs monolayers in an (In, Ga)As matrix. a) Viewed in the plane of the structure; b) cross section. The data have been obtained by means of a transmission electron microscope.

for the deposition of InAs in an (In, Al)As/InP matrix and with observations[2,11] for the system $In_{0.5}Ga_{0.5}As$ on GaAs, which is characterized by approximately the same mismatch between the strained layer and the matrix. It should be noted, however, that the striated contrast of the HEED pattern is not as pronounced in our situation as for the system of materials $In_{0.5}Ga_{0.5}As$/GaAs. In our opinion, this departure indicates that three-dimensional InAs islands formed on an InGaAs/InP surface are characterized by a lower height-to-base ratio, because the striated contrast results from the electron beam passing through microscopic relief on the surface.

Figure 1a shows a TEM micrograph (in planar geometry) of the structure formed by the deposition of six InAs monolayers. The picture was taken along the [001] direction in the reflection $g=200$. A dense array of islands is clearly visible in the micrograph. The characteristic contrast is attributable to the coherent stress of the InAs islands. The average base diameter of the islands, according to the TEM data (Fig. 1a), is approximately 50 nm, which greatly exceeds the corresponding dimension of strained (In, Ga)As islands in a GaAs matrix, which can vary from 8 nm to 20 nm, depending on the deposition conditions.[12] It is important to note that the island dimensions determined by diffraction TEM in the present study may be slightly higher as a result of the stress fields propagating into the matrix.

Figure 1b shows an image of a transverse section of the sample ($g=200$). The regions of dark contrast correspond to InAs. The InAs islands, which have a roughly triangular shape in the cross section, lie on a thin wetting layer of InAs. As the island array is overgrown by an InGaAs layer, the planar growth surface is restored, as evinced by the absence of bending of the interfaces in the InGaAs/InAlAs superlattice (upper part of Fig. 1b). The islands have a typical height of approximately 4–5 nm. According to HEED data, the islands are characterized by a low height-to-base ratio (1:10).

The TEM data therefore corroborate the formation of three-dimensional strained islands in the active zone of samples having an effective thickness of the deposited InAs layer greater than 3 ML. A detailed investigation of the structural properties of such structures by TEM methods, including high-resolution techniques, will be reported in a separate paper.

Figure 2 shows the photoluminescence spectra of structures with different effective thicknesses of the deposited InAs, measured at 77 K. The radiation emitted from a bulk (In, Ga)As matrix for a sample with $Q_{InAs}=0$ has a maximum at an energy of 799 meV, where the width of the peak is 17 meV. The spectra of samples containing an island array ($Q_{InAs}\geqslant 3$ ML) exhibit a strong band shifted far into the long-wavelength region relative to emission from the

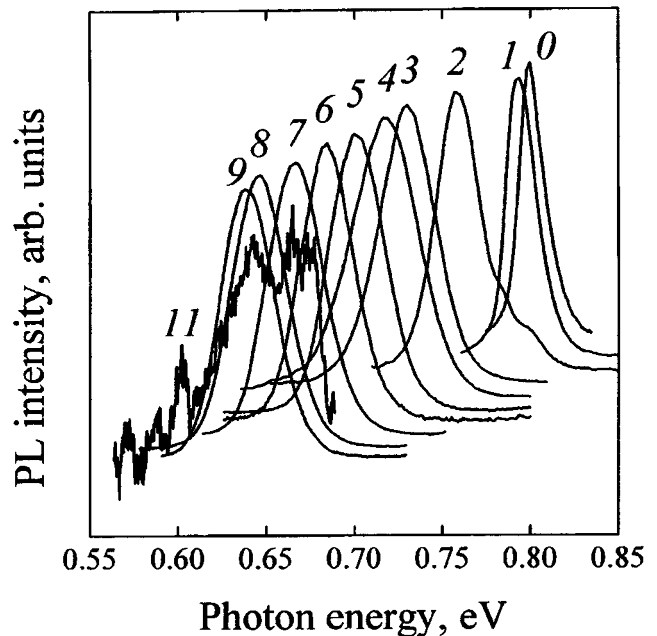

FIG. 2. Photoluminescence spectra (77 K) of (In, Ga)As/InAs/(In, Ga)As heterostructures. The numbers at the top of each curve indicate the quantity of deposited indium arsenide Q_{InAs}, measured in the number of monolayers.

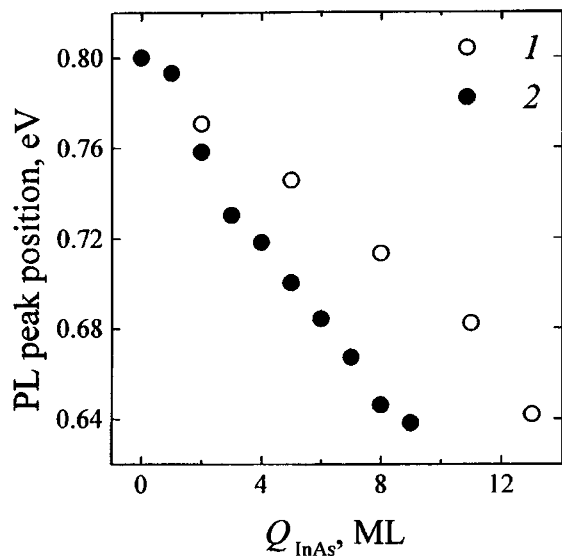

FIG. 3. Spectral position of the maximum of the photoluminescence line (77 K) vs quantity of deposited indium arsenide Q_{InAs} measured in the number of monolayers. *1)* Two-dimensional distribution of InAs according to data in Ref. 13; *2)* island distribution of InAs from data of the present study.

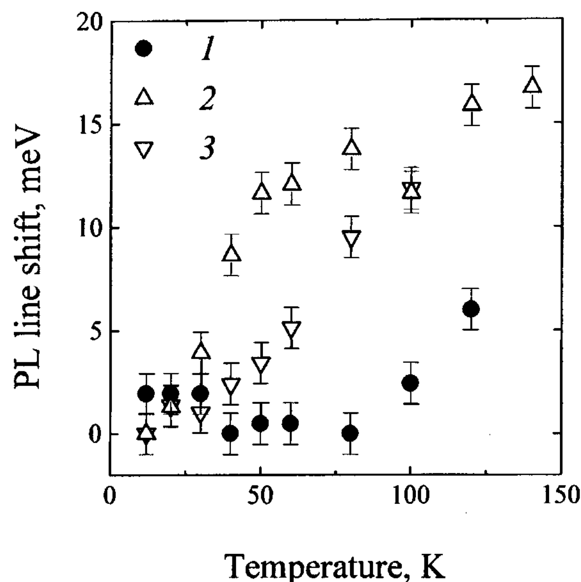

FIG. 4. Shift of the maximum of the photoluminescence line vs temperature T in structures with different quantities of deposited indium arsenide. *1)* $Q_{InAs}=2$ ML; *2)* 6 ML; *3)* 9 ML.

(In, Ga)As matrix. This line has a typical width of 35–37 meV. The total photoluminescence intensity remains approximately constant up to $Q_{InAs}=9$ ML, after which the intensity is observed to drop abruptly (by more than two orders of magnitude at 11 ML). For a sample with $Q_{InAs}=13$ ML no luminescence signal was recorded by the detection system used in the work.

Increasing the quantity of deposited InAs causes the photoluminescence maximum shift systematically toward longer wavelengths. Figure 3 shows the energy position of the maximum of the photoluminescence line at 77 K as a function Q_{InAs}. The experimental data are compared with the results of an investigation,[13] in which special technological procedures were used to suppress the formation of islands in the deposition of InAs on a (In, Ga)As surface [(In, Ga)As/InAs/(In, Ga)As quantum well]. It is clearly perceived that as soon as three-dimensional InAs islands are formed, the energy of the peak becomes much lower than the quantum-well values. The energy difference attains 65 meV for 9-ML islands. The data show that the emission from strained InAs islands in an (In, Ga)As matrix spans the wavelength interval 1.65–2.0 μm at 77 K. The longest emission wavelength attained in our work (77 K, $Q_{InAs}=9$ ML) is 1.944 μm.

In our opinion, the data describing the dependence of the spectral position and the total intensity of the photoluminescence line in the investigated structures with InAs island arrays on the quantity of material deposited can be explained satisfactorily within the framework of the following model. Redistribution of the deposited InAs leads to the formation of an array of three-dimensional islands in the active zone and thus causes the carrier localization energy to rise sharply as a result of the increased effective size of the active zone in the direction perpendicular to the interface by comparison with the case of a two-dimensional distribution of the same quantity of deposited material. This effect accounts for the long-wavelength shift of the photoluminescence line relative to emission from an (In, Ga)As/InAs quantum well. When the effective thickness of the deposited indium arsenide increases, as in the case of InAs islands in a GaAs matrix,[2,7] the average size of the islands increases, causing the luminescence line to shift further toward lower energies. On the other hand, the pseudomorphic growth of strained islands can be maintained up to a critical size, above which misfit dislocations begin to form. A further increase in the quantity of deposited InAs leads to an ever-greater fraction of islands that exceed the critical size and do not participate in radiative recombination, owing to the large number of defects.[7] A decrease in the total luminescence intensity is observed as a result. We can therefore conclude that a significant fraction of the InAs islands attain the critical size when the effective thickness of the deposited material is of the order of 11–13 ML.

Figure 4 shows the temperature dependence of the shift of the maximum of the photoluminescence band. It is evident from this figure that structures with effective InAs thicknesses of 6 ML and 9 ML exhibit in the temperature range 10–80 K a more rapid shift of the photoluminescence maximum toward lower photon energies than for a sample with 2 ML of InAs, in which quantum dots do not form, and the shift of the photoluminescence line reflects a change in the width of the (In, Ga)As band gap. A similar large shift of the photoluminescence band has also been observed for InAs quantum dots in a GaAs matrix[14] and was attributed to the different localization energies for quantum dots of different sizes. An increase in the temperature raises the probability of thermal ejection of nonequilibrium electrons and holes from small quantum dots, for which the localization energy is not very high. This effect reduces the intensity of the short-wavelength part of the line by virtue of recombination through such quantum dots, thereby producing a long-wavelength shift of the photoluminescence band. Since quantum dots have smaller dimensions in a structure with

3 ML of InAs (which corresponds to the onset of the island-formation stage) than in the deposition of 6-Ml and 9-ML InAs layers, carrier ejection and, hence, shifting of the maximum of the photoluminescence band begin at lower temperatures.

In summary, arrays of strained InAs islands in an (In, Ga)As matrix have been synthesized by MBE using self-organization effects, and a preliminary study of their structural and optical properties has been carried out. The transition to island growth of InAs, according to HEED and TEM data, takes place when the thickness attains 3 ML. The newly formed InAs islands lie on a thin wetting layer, are coherently strained, and have a base diameter in the interval 20–90 nm with a height of 4–5 nm. An increase in the effective thickness of the deposited InAs produces more rapid long-wavelength shifting of the luminescence maximum than in the case of a two-dimensional distribution of the same quantity of material.

We close with the observation that structures containing strained InAs islands in an (In, Ga)As/InP matrix are capable of extending the wavelength range to 2 μm and, at the same time, possess the potential capabilities of zero-dimensional systems.

This work has received support from the Russian Fund for Fundamental Research (Project 96-02-17824) and the ''Physics of Solid State Nanostructures'' program of the Ministry of Science of the Russian Federation (Project 2-001).

[1] Y. Arakawa and H. Sakaki, Appl. Phys. Lett. **40**, 939 (1982).

[2] P. M. Petroff and S. P. DenBaars, Superlattices Microstruct. **15**, 15 (1994).

[3] J. M. Moison, F. Houzay, F. Barthe, L. Leprince, E. Andre, and O. Vatel, Appl. Phys. Lett. **64**, 196 (1994).

[4] S. V. Zaitsev, N. Yu. Gordeev, Yu. M. Sherniakov, V. M. Ustinov, A. E. Zhukov, A. Yu. Egorov, M. V. Maximov, P. S. Kop'ev, Zh. I. Alferov, N. N. Ledentsov, N. Kirstaedter, and D. Bimberg, in *Proceedings of the Ninth International Conference on Superlattices, Microstructures, and Microdevices* (Liege, Belgium, 1996).

[5] V. M. Ustinov, A. Yu. Egorov, A. R. Kovsh, A. E. Zhukov, N. N. Ledentsov, M. V. Maksimov, A. F. Tsatsul'nikov, N. Yu. Gordeev, S. V. Zaitsev, Yu. M. Shernyakov, N. A. Bert, P. S. Kop'ev, Zh. I. Alferov, N. N. Ledentsov, J. Bohrer, D. Bimberg, A. O. Kosogov, P. Werner, and U. Gosele, J. Cryst. Growth **175** (1997) (in press).

[6] Yu. M. Shernyakov, A. Yu. Egorov, A. E. Zhukov, S. V. Zaĭtsev, A. R. Kovsh, I. L. Krestnikov, A. V. Lunev, N. N. Ledentsov, M. V. Maksimov, A. V. Sakharov, V. M. Ustinov, Chzhao Czhén', P. S. Kop'ev, Zh. I. Alferov, and D. Bimberg, JETP Lett. (in press).

[7] A. Yu. Egorov, A. E. Zhukov, P. S. Kop'ev, N. N. Ledentsov, M. V. Maksimov, V. M. Ustinov, A. F. Tsatsul'nikov, Zh. I. Alferov, D. L. Fedorov, and D. Bimberg, Fiz. Tekh. Poluprovodn. **30**, 1345 (1996) [Semiconductors **30**, 879 (1996)].

[8] R. P. Mirin, J. P. Ibbetson, K. Nishi, A. C. Gossard, and J. E. Bowers, Appl. Phys. Lett. **67**, 3795 (1995).

[9] A. E. Zhukov, A. Yu. Egorov, V. M. Ustinov, A. F. Tsatsul'nikov, M. V. Maksimov, N. N. Faleev, and P. S. Kop'ev, Fiz. Tekh. Poluprovodn. **31**, 19 (1997) [Semiconductors **31**, 15 (1997)].

[10] S. Fafard, Z. Wasilewski, J. McCaffrey, S. Raymond, and S. Charbonneau, Appl. Phys. Lett. **68**, 991 (1996).

[11] A. Yu. Egorov, A. E. Zhukov, P. S. Kop'ev, N. N. Ledentsov, M. V. Maksimov, and V. M. Ustinov, Fiz. Tekh. Poluprovodn. **28**, 1439 (1994) [Semiconductors **28**, 809 (1994)].

[12] S. Ruvimov, P. Werner, K. Scheerschmidt, U. Richter, U. Gosele, J. Heydenreich, N. N. Ledentsov, M. Grundmann, D. Bimberg, V. M. Ustinov, A. Yu. Egorov, P. S. Kop'ev, and Zh. I. Alferov, Inst. Phys. Conf. Ser., No. 146, 31 (1995).

[13] E. Tounic, O. Brandt, and K. Ploog, Semicond. Sci. Technol. **8**, S236 (1993).

[14] A. F. Tsatsul'nikov, N. N. Ledentsov, M. V. Maksimov, A. Yu. Egorov, A. E. Zhukov, S. S.Ruvimov, V. M. Ustinov, V. V. Komin, I. V. Kochnev, P. S. Kop'ev, Zh. I. Alferov, Fiz. Tekh. Poluprovodn. **30**, 1793 (1996) [Semiconductors **30**, 938 (1996)].

Translated by James S. Wood

Structure and properties of porous silicon obtained by photoanodization

E. V. Astrova,[a] V. V. Ratnikov, R. F. Vitman, A. A. Lebedev, A. D. Remenyuk, and Yu. V. Rud'

A. F. Ioffe Physicotechnical Institute, Russian Academy of Sciences 194021 St. Petersburg, Russia
(Submitted December 24, 1996; accepted for publication April 3, 1997)
Fiz. Tekh. Poluprovodn. **31**, 1261–1268 (October 1997)

The results of an investigation of layers of porous silicon (PS), which was obtained by electrochemical etching of *p*-Si under different illumination conditions — natural light, incandescent light, and light from a mercury lamp with and without a filter — are reported. The structure of the layers was studied by double-crystal x-ray diffractometry, the composition was monitored by means of the IR absorption spectra, and the radiative properties were monitored according to the photoluminescence (PL) spectra. It was established that electrochemical etching under illumination produces PS with a higher porosity and more intense PL whose maximum is shifted into the short-wavelength region. These changes are accompanied by a large disordering of the structure and an increase in the oxygen content in the layer. It is concluded that illumination accelerates the chemical interaction of PS with the electrolyte due to oxidation. High-porosity porous silicon stored in air exhibits quenching of PL. Conversely, PL is excited in layers with a lower porosity. Aging of PS is characterized by an increase in the microdeformation of the layers, a decrease in the crystallite sizes with a partial loss of coherence between the crystallites and the substrate, and an increase in the fraction of the amorphous phase. © *1997 American Institute of Physics.* [S1063-7826(97)03010-X]

1. INTRODUCTION

Despite the well-known progress made in the understanding of the nature of visible-range luminescence of porous silicon (PS), after its discovery by L. T. Canham in 1990,[1] this problem has still not been completely clarified. It is known that PS is an unstable material, subject to aging and degradation, making investigation and practical application of PS difficult.[2] However, until now not enough attention has been directed to the correlation between the microstructure and photoluminescence (PL) properties of PS in the course of aging for periods of several months.[3]

In the present work we made an attempt to relate the light-emitting properties of PS with its structural features by studying the aging process in samples of different porosity. Photoanodization of *p*-Si under different illumination conditions[4–6] was used to control the porosity and x-ray diffractometry was used to obtain data on the structure of PS.

2. EXPERIMENT

Polished boron-doped single-crystal silicon wafers served as the starting material for the experimental samples. The resistivity of Si was equal to 1 $\Omega \cdot$cm and the orientation was (111). Anodization was conducted in the electrolyte HF:C_2H_5OH=1:1, to which five drops of a 1-M solution of $NaNO_2$ for 15 ml of etchant were added. The current density was equal 20 mA/cm^2 and the etch time was equal to 10 min. After the process was completed, the samples were washed with deionized water and dried in air. The surface of the silicon was illuminated uniformly. A comparative estimate of the intensity E of the illumination was made with a luxmeter with a selenium F-102 photocell. Illumination was performed by four methods:

I — natural light ($E=15$ lx);

II — 20-W tungsten incandescent lamp 15 cm from the surface of the wafer ($E=70$ lx);

III — DRK-120 mercury lamp with a 3-mm-thick UFS-6 filter placed 15 cm from the sample ($E=70$ lx); the transmission region of the filter was $303<\lambda<405$ nm ;

IV — same mercury lamp without a filter ($E=120$ lx).

The gravimetric porosity and the average thickness of the layers were determined according to the formulas in Ref. 7 . The measurements of the photoluminescence spectra were performed at room temperature with a 20-mW He–Cd laser with $\lambda=440$ nm. The photoluminescence intensity is indicated in relative units, but in all cases the PL was measured under the identical excitation and detection conditions, which made it possible to compare the PL intensities. The infrared (IR) spectra were obtained by measuring the optical transmission of the samples on a Specord-IR 75 spectrometer in a two-beam arrangement.

The x-ray (XR) diffraction measurements were performed on a DRON-2.0 double-crystal diffractometer (DCD) with Cu$K\alpha_1$ radiation. Two variants of a dispersion-free symmetric Bragg diffraction arrangement $(n,-n)$ for $hkl=111$ and 333 were used: integral (i-DCD) — with a counter and no slit and differential (d-DCD) — with a narrow slit in front of the counter giving a resolution of $\sim$50 angular seconds. The latter variant of the DCD made it possible not only to improve the resolution of the reflection curve, but also to determine the angular width of the reflection at detected intensity $i=0.5i_{\max}$ in directions parallel ($w_{\parallel}$) and perpendicular ($w_{\perp}$) to the reciprocal lattice vector **H**. Accordingly, the counter with the narrow slit was placed in the exact position of the reflection from the substrate or the PS and then displaced into a fixed position $\pm\Delta(2\Theta)$ and a reflection curve was recorded in each position with rotation of the sample (ω — scanning along the normal to **H**; Fig. 1).

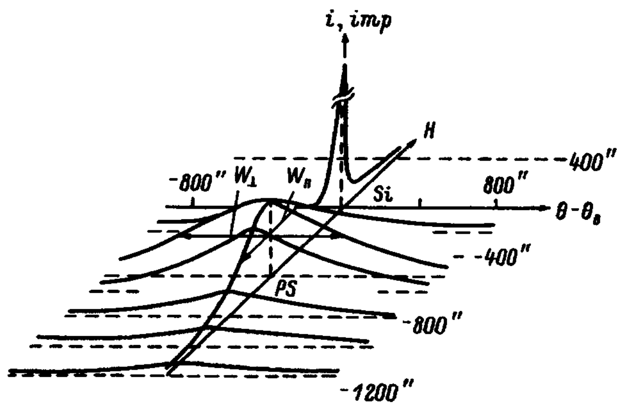

FIG. 1. Measurement of the distribution of the diffracted intensity by the d-DCD method for sample 3*A* 3.5 months after preparation. Cu$K\alpha_1$, (111). The angular positions of the counter are shown to the right of the ω curves.

The envelope of the maxima of the ω curves gives the so-called half-integral curve. In Ref. 8 it is shown that the curve obtained in this manner gives a much better resolution and the diffraction pattern can be analyzed in detail by recording a series of ω curves. The radius R of curvature of the samples was determined according to the angular displacement of the peak of the substrate under the PS with stepped scanning of the sample in the XR beam. The sensitivity of the method made it possible to measure $R \leqslant 200$ m.

3. EXPERIMENTAL RESULTS

Photoluminescence and porosity. The PL spectra of freshly prepared samples (on the day after the PS was obtained) are shown in Fig. 2. The values of the porosity p and the thickness t of the layer, the wavelength $\lambda_{\max}$ corresponding to the maximum of the PL, and the intensity of the PL at the maximum (I_{mp} — freshly prepared and I_{ms} — after storage) for samples 1*A*, 2*A*, 3*A*, and 5*A* are tabulated in Table I. It is seen from the table that sample 5*A* with highest porosity is obtained with the strongest illumination with radiation in a wide spectral range (Hg lamp with no filter). This sample exhibits the strongest PL and the position of the PL maximum is located at the shortest wavelength. Storing the samples changed their PL (see Fig. 2b and Table I). The changes were smallest for sample 1*A*: The intensity of luminescence and the position of its maximum for this sample remained almost constant. In all other samples the intensity decreased and there was a small short-wavelength shift of λ_m. The strongest quenching of PL, as compared with freshly prepared samples, occurred in sample 5*A* (a factor of 5).

IR absorption. The IR absorption spectra of the samples immediately after preparation of the PS layers were found to be very close to one another for samples 1*A*, 2*A*, and 3*A* and substantially different for sample 5*A*. All spectra contain distinct Si–H lines (915, 2000, and 2120 cm^{-1}), as well as small peaks, due to O–Si–H bonds (840, 2200, 2260 cm^{-1}), and absorption due to longitudinal Si–O–Si vibrations (near 1100 cm^{-1}). The absorption due to the presence of oxygen is strongest in the spectrum of sample 5*A*, prepared with the highest illumination intensity.

Figures 3a and 3b show sections of the spectra where changes are observed during storage of the samples in the ambient atmosphere. During the initial stages of storage (first three days) substantial changes occurred only in the spectrum of sample 5*A* as a result of an increase of absorption in the bands associated with oxygen-containing centers. Longer-term storage for 3 months gave rise to appreciable changes in the spectra of all samples, mainly as a result of the weakening of the Si–H bands and intensification of absorption by oxygen-containing groups. These changes are not very large and are close to one another for samples 1*A*, 2*A*, and 3*A* and appreciably larger for sample 5*A*. Quenching of absorption at frequencies corresponding to Si–H bonds occurs as a result of a transformation of these bonds into Si–O–H. The 915, 2090, and 2120-cm^{-1} bands shift to

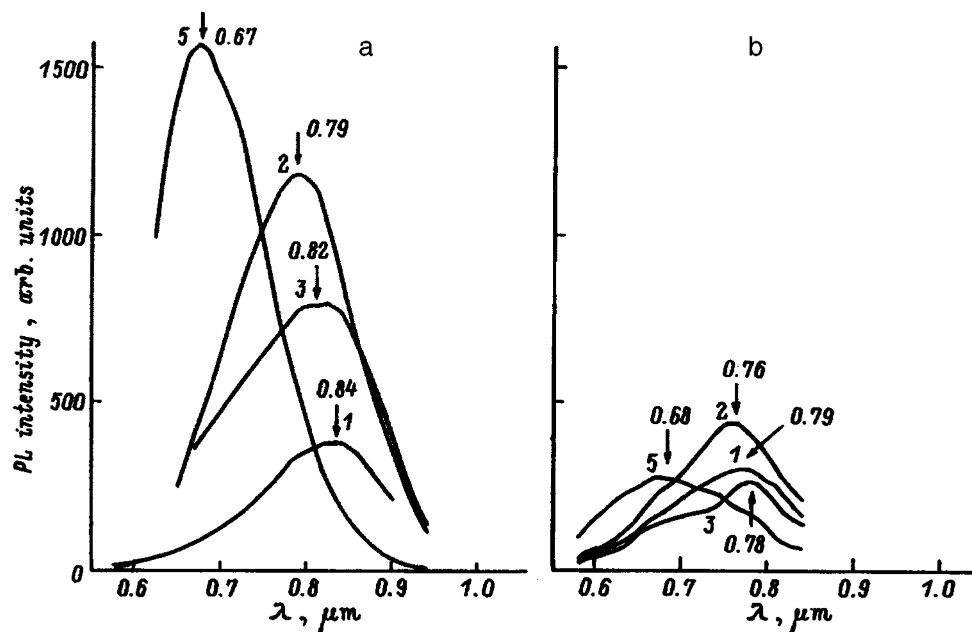

FIG. 2. PL spectra for PS layers obtained by photoanodization under different conditions of illumination: for sample 1*A* — natural illumination, 2*A* — tungsten lamp, 3*A* — Hg lamp with a filter, 5*A* — Hg lamp without a filter; a — next day after preparation, b — 3 months after storage in air. The spectra were measured under identical conditions of excitation; $T = 300$ K.

TABLE I. Preparation conditions and luminescence characteristics of PS layers.

No.		Illumination conditions	p, %	t, μ	After 1 day		After 3 months		
					λ_m, μ	I_{mp}	λ_m, μ	I_{ms}	I_{ms}/I_{mp}
1A	I	natural light	67	10.3	0.84	10.7	0.79	10.5	0.98
2A	II	W incandescent lamp	73	9.4	0.79	40.0	0.76	15.8	0.40
3A	III	Hg lamp with filter	70	9.9	0.82	24.0	0.78	10.4	0.43
5A	IV	Hg lamp without filter	83	10.3	0.67	57.0	0.68	12.0	0.21

840, 2200, and 2260 cm^{-1}, respectively. The absorption due to Si–O–Si bands at 1080 and 1150 cm^{-1} increases with storage time, the relative contribution of the 1150-cm^{-1} band increasing and becoming comparable in intensity to the 1080- cm^{-1} band. Of the other changes in the spectrum, we call attention to the strong decrease in the intensity of the Si–Si–H bands at 660 and 630 cm^{-1} and the appearance of a distinct triplet near 2930 cm^{-1}, characteristic of C–H bands. The appearance of this latter band can be explained by the formation, during storage in air, of an oxide contaminated by elements from the surrounding medium, including carbon; this has been shown in Ref. 9 by means of secondary-ion mass spectrometry.

X-Ray diffractometry. Measurement of the radius of curvature for samples from batch A showed the absence of curvature for all samples — both starting and stored in air. A substantial transformation of the i-DCD reflection curves is observed in the case of the samples stored in air for up to 3.5 months. Of the two narrow peaks for PS and Si, after 3.5 months only a narrow substrate peak remains in all reflection curves of samples stored for 1 week (Fig. 4a). The PS peak transforms into an incoherent signal, distributed in a wide angular interval near the substrate peak (± 1000 angular seconds and more).

All experimental structures can be divided into three groups according to the form and parameters of the i-DCD reflection curves:

Group I (samples 1A, 2A, and 3A after one week) is characterized by narrow PS and Si peaks against a weak incoherent background. The ratio of the intensities of the peaks at the maximum is $i_{os}^{\max} \approx 0.1 i_{\text{Si}}^{\max}$, the half-widths $w_{ps} \approx w_{\text{Si}}$, and the angular spacing of the peaks $\Delta\Theta'' = 130$ angular seconds.

In group II (samples 5A after one month and 1A, 2A, and 3A after 2.5 months) the PS peak changes form, its intensity decreases $i_{os}^{\max} \approx 0.01 i_{\text{Si}}^{\max}$, and its widths increase $w_{ps} \approx (5-7) w_{\text{Si}}$. The spacing $\Delta\Theta''$ increases by 20%.

Group III (samples 1A, 2A, and 3A after 3.5 months and 5A after 2.5 months) is characterized by degeneration of the PS peak into a very weak incoherent signal near the substrate peak $i_{ps}^{\max} \approx 0.003 i_{\text{Si}}^{\max}$.

The i-DCD reflection curves from the PS layers 1 week and 2.5 months, respectively, after the layers were obtained

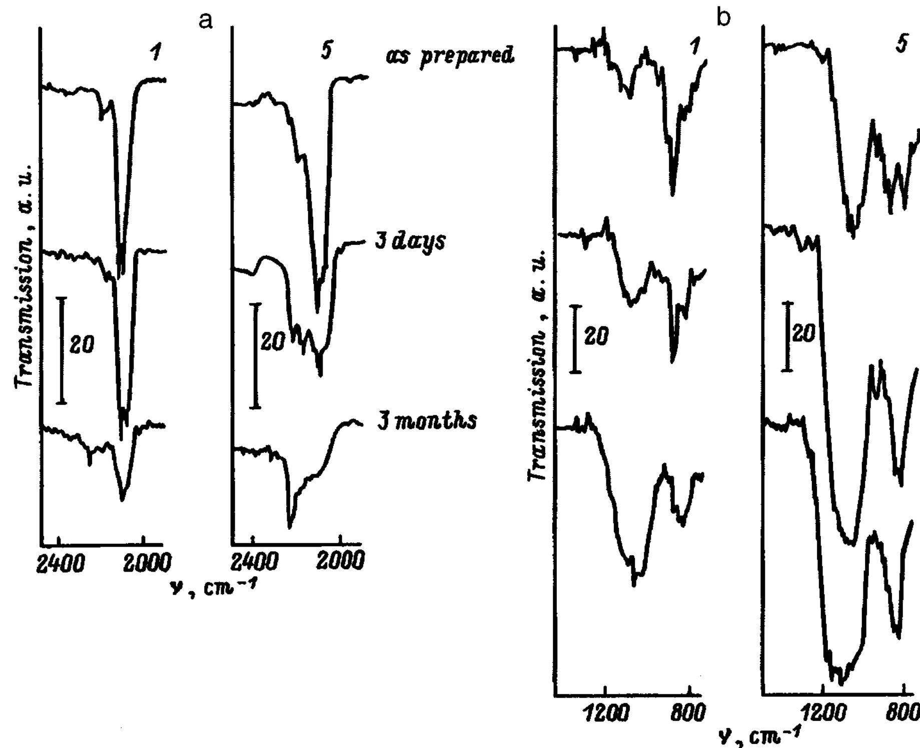

FIG. 3. Transformation of the IR absorption spectra of samples 1A and 5A: a — near $\nu = 2000$ cm^{-1}, b — near $\nu = 800-1150$ cm^{-1} ($T = 300$ K).

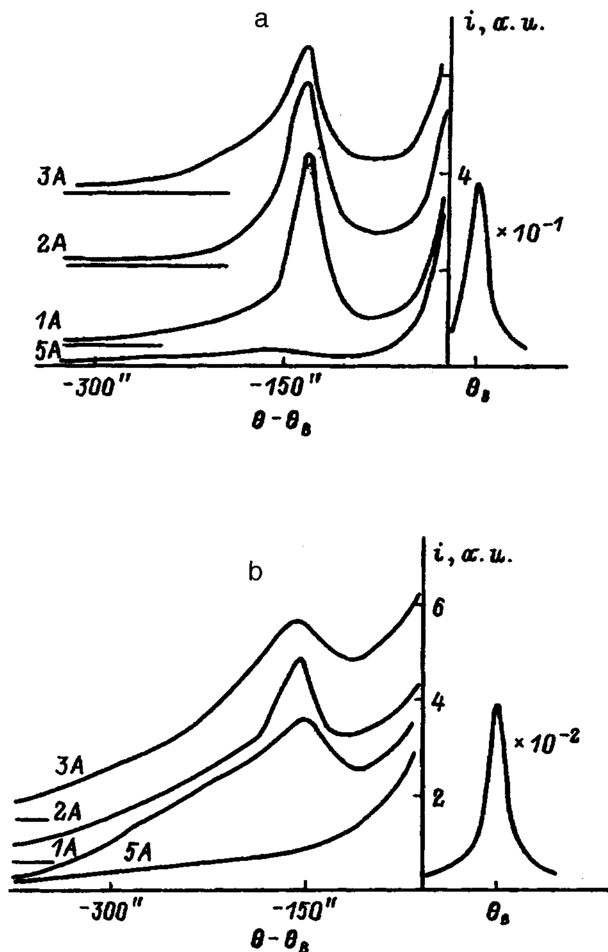

FIG. 4. i-DCD x-ray reflection curves for the samples $1A$, $2A$, $3A$, and $5A$ 1 week (a) and 2.5 months (b) after preparation. The curves are shifted along the vertical axis. Right side — reflection peak from the (111) planes of the substrate, Cu$K\alpha_1$ radiation.

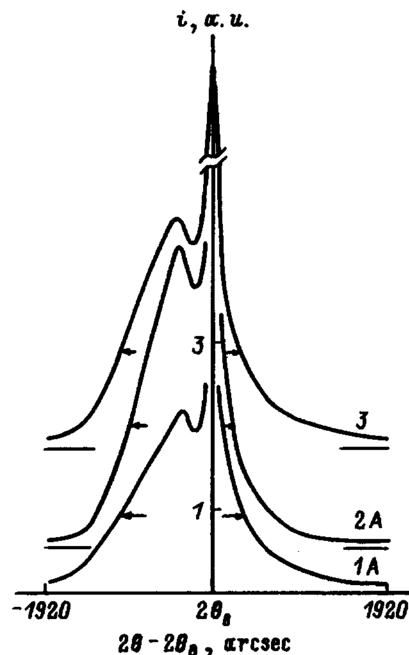

FIG. 5. Intensity distribution in the direction of the reciprocal lattice vector **H** for samples $1A$, $2A$, and $3A$ 3.5 months after preparation. The curves are shifted along the vertical axis. The arrows mark the $0.5i_{\max}$ level. Cu$K\alpha_1$, (111).

are shown in Figs. 4a and 4b. Figure 5 shows the distribution of the reflection intensity, obtained from the d-DCD measurements, along **H**. The results of an analysis of the curves in Figs. 4 and 5 are presented in Table II. The relative changes $(\Delta d/d)_\perp$ in the lattice parameter of PS in a direction perpendicular to the Si surface were obtained from the angular spacing $\Delta\Theta''$ of the PS reflection peaks from the Si substrate. Aside from the half-width w of the i-DCD curve, the half-widths $w_\perp$ and $w_\parallel$ obtained in directions perpendicular and parallel to the vector **H** from the d-DCD measurements and the dimensions $L_\perp$ and $L_\parallel$ of the region of coherent scattering in directions perpendicular and parallel to the surface of the sample are presented. For samples $1A$, $2A$, and $3A$ (1 week) d-DCD measurements were not performed because of the inadequate resolution of the d-DCD method in this case. The values obtained for $w_\perp$ and $w_\parallel$ in the reflection $hkl=333$ were measured in order to analyze the angular dependence of the components of the half-width of the signal from PS.

4. DISCUSSION

Illumination of the sample accelerates the chemical interaction of the PS layer with the solution. This is indicated by the increasing porosity of the layer, which is highest for sample $5A$, with the thickness of the layer remaining nearly constant. The spectral composition of the illumination does not play an appreciable role, since the PS sample $2A$, obtained with predominantly long-wavelength light from the tungsten lamp ($\lambda \approx 1$ μm), and the PS sample $3A$, prepared using the short-wavelength filtered light from the Hg lamp (0.3–0.4 μm), do not exhibit any substantial differences. Storage leads to a virtually identical decrease in the brightness of their PL (Table I), the IR absorption spectra remain practically identical throughout the entire storage time of the samples, and the structural differences are also small in most cases (see Table II).

The IR absorption spectra demonstrate an increase in the number of oxygen bonds in the samples prepared under illumination. In Refs. 10 and 11 , the PS exposed to light in an electrolyte after anodization was investigated in a high vacuum without intermediate contact with air. It was shown by photoemission spectroscopy that illumination results in strong oxidation of the PS surface even in solution. Furthermore, previously we observed an increase in the oxygen-containing bonds when an oxidizer was introduced into the electrolyte.[12] Thus, photoinduced oxidation and accelerated dissolution of PS occur under illumination. The crystallites become smaller, their disorientation increases, and their lattice parameter increases. As a result, the coherent Bragg reflection peak in the diffraction pattern separates from the substrate peak, the intensity at the maximum of the reflection becomes more diffuse (the half-width increases) and decreases, and the incoherent background increases substantially (Fig. 4b). The initial stages of oxidation in the electrolyte and in air result in a higher PL intensity, despite

TABLE II. Results of x-ray diffraction measurements on PS layers.

Storage	Sample No.	$\Delta\Theta''$, ang. sec.	$(\Delta d/d)_\perp$, 10^{-3}	w, ang. sec.	$w_\perp$, ang. sec.	$L_\perp$, Å	$w_\parallel$, ang. sec.	$L_\parallel$, Å
1 week	1*A*	132	2.53	24				
1 week	2*A*	131	2.52	30				
1 week	5*A*	133	2.54	43				
1 week	5*A*	159	3.05	174	160	4070	80	2050
2.5 months	1*A*	152	2.92	160	155	4270	75	2180
2.5 months	2*A*	158	3.03	159	220	2960	120	1370
2.5 months	3*A**	160	3.07	156	150[100]	4350	80[100]	2050
2.5 months	5*A*	280	5.38	390	350	1860	90	1820
3.5 months	1*A*	240	4.61		690	950	190	860
3.5 months	2*A*	210	4.03		700	890	190	860
3.5 months	3*A**	240	4.61		760[720]	870	186[360]	880

Note. *The numbers in square brackets are the values for $hkl=333$, Cu$K\alpha_1$.

disordering effects, whereas the later stages of oxidation result in degradation of the PL intensity (Fig. 2b). It should be noted that as long as the number of silicon–hydrogen and oxygen–silicon–hydrogen bonds with vibrational frequencies near 2000 cm^{-1} is large, the PL remains stable. Degradation of the PL in sample 5*A* after $\sim$3 months is accompanied by a large decrease in the total number of Si–H bonds (see Fig. 3a) and a decrease in the concentration of the Si–O vibrational groups at $\nu\approx 1100$ cm^{-1} (Fig. 3b). We observed a similar picture in the dose dependence of the effect of γ-irradiation on the PL,[13] where in the dose range $\leq 10^{19}$ cm^{-2} the PL increased simultaneously with oxidation of the Si–H group without a decrease in the total concentration of these bonds. For doses $\geq 10^{19}$ cm^{-2} the degradation of the PL and destruction of the Si–H and O–Si–H groups proceeded in parallel.

Photoanodization makes it possible to obtain PS with smaller crystallites, whose surface is nevertheless well passivated. This results in a low rate of nonradiative recombination of charge carriers on the surface of the crystallites, which can explain the intensification of PL on the basis of the quantum-well model.[1] It is known that thermal oxidation can intensify PL.[12,14] However, if the crystallites and the voids between them are small, then oxidation can break the narrow bridges in the Si framework, strongly change the lattice constant of PS, and introduce substantial microstresses. At some moment, as a result of these processes, the crystallites crack and decrease in size, down to amorphization.[15] In the process the passivation by hydrogen and oxygen is destroyed, as is indicated by the decrease in the intensity of the Si–H and Si–O IR bands and the degradation of PL (Fig. 2b). At the same time, any judgments about the correlation between the structural characteristics of PS (average size of the crystallites, the lattice constant in the crystallites, disorientation and microstresses) and the parameters of PL can only be indirect. The reason is that the low transmission of the DRON-2.0 diffractometer made it possible to measure the diffraction of x-rays only from relatively large crystallites ($d>500$ Å), which do not play a determining role in the PL.

All experimental samples were characterized by the absence of macrocurvature of the PS/Si compositions at all stages of storage. For this reason, the possible residual macrostresses in the PS/Si system $\sigma<1.5\times 10^7$ N/m^2 (as estimated according to Ref. 16). This gave us the grounds to assume that the PS lattice was relaxed and obtain from the angular spacing $\Delta\Theta''$ the value $(\Delta d/d)_\perp\approx(\Delta a/a)_0$, where a is the lattice parameter of the relaxed PS lattice. It is evident from Table II that the relative change in the lattice parameter gradually increases with storage time of PS in air. One reason why the PS lattice parameter increases is thought to be the presence of a hydrogen[17] or oxide[18] layer on the surface of the crystallites. The oxidation process in the air gives rise to a deformation of the Si framework of the PS and destroys the PS when the macrocrystallites of the initial PS transform into micro- and nanocrystallites followed by complete amorphization. The difference in $(\Delta d/d)_\perp$ after 1 week correlates well with the porosity values of these layers. The increase in the lattice parameter of PS during storage is likewise apparently due to the size reduction of the fragments of its Si framework.

It can be asserted on the basis of the shape and parameters of the i-DCD reflection curves for PS samples 1*A*, 2*A*, and 3*A*, measured 1 week after the PS was obtained (Fig. 4a, Table II) that the main element of the structure of PS at this stage are macrocrystallites with dimensions in the direction of the normal to the surface of the samples $L_\perp\geq 4$ μm (for $hkl=111$ and Cu$K\alpha_1$, the extinction length $\Lambda=4.65$ μm).

It should be noted that at all stages of storage of PS a large fraction of the PS crystallites retained coherence, i.e. the reflecting planes of the PS and the substrate were parallel. This can be judged from the fact that the maxima of the series of ω curves obtained by the d-DCD method remain on the **H** axis (Fig. 1). However, the degree of coherence drops sharply with aging, reflecting the on-going process of destruction of the PS framework. The d-DCD curves show that the scattering in group-II and -III samples is always asymmetric ($w_\perp>w_\parallel$), with the exception of the reflection (333) for PS sample 3*A* (3.5 months).

In the classical block model of an imperfect crystal[19] the x-ray lines are broadened as a result of the finite dimensions of the regions of coherent scattering (crystallites) in directions parallel and perpendicular to the surface $w_1\sim 1/(L_\parallel\cos\Theta_B)$ and $w_2\sim 1/(L_\perp\sin\Theta_B)$, respectively, the relative disorientation of the crystallites $w(\varphi)\neq f(\Theta_B)$, and the microdeformation of the individual crystallites $w[(\Delta d/d)_\perp]\sim\tan\Theta_B$, i.e., $w_\parallel=w_1+w[(\Delta d/d)_\perp]$ and $w_\perp=w_2+w(\varphi)$.

To analyze the structure of the PS in the values that we

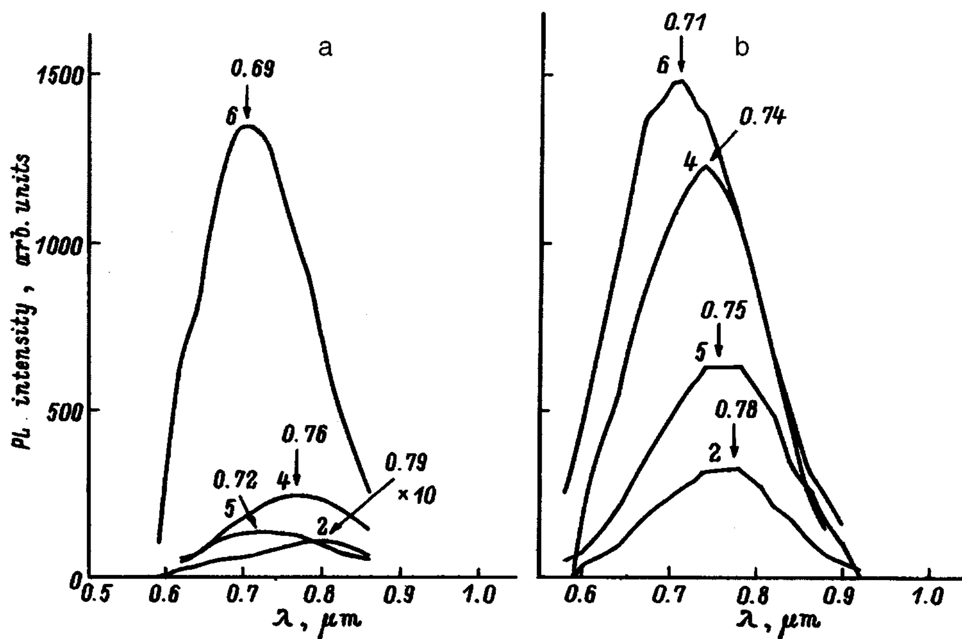

FIG. 6. PL spectra of samples from batch B after preparation (a) and after storage for 6 months in air (b). Porosity of the samples: 57% — $2B$, 58% — $4B$, 65% — $5B$, and 73% — $6B$.

obtained for $w_\parallel$ and $w_\perp$, it is necessary to determine complexes of these quantities. This is done for the example of the PS sample $3A$ (2.5 and 3.5 months) according to the dependence of the components on the diffraction angle Θ_B for the reflections 111 and 333. Performing these measurements, we obtained for the group-II PS $w_\perp(111)/w_\perp(333)\simeq 1.5$. This is close to the computed value of the ratio $w_2(111)/w_2(333)$, i.e. in this case the broadening of the (111) reflections is determined mainly by the size effect, $w_\perp \simeq w_2$, and gives the size $L_\perp$ of the crystallites in a direction normal to the surface. The ratio $w_\parallel(111)/w_\parallel(333)\simeq 1.25$ was found to be less than the computed value of $w_1(111)/w_1(333)$, making the estimate of the contributions of w_1 and $w[(\Delta d/d)_\perp]$ to $w_\parallel$ less certain. For this reason, the values of $L_\parallel$, presented in Table II for the PS samples $5A$ (1 week) and $1A$, $2A$, and $3A$ (2.5 months), are approximate and give the minimum possible lateral size of the crystallites. Therefore, the scattering for group-II PS is determined mainly by crystallites with dimensions $L_\perp \geqslant 0.4$ μm and $L_\parallel \geqslant 0.2$ μm.

A similar analysis for group-III PS shows that the large increase in $w_\perp$ and $w_\parallel$ in this case is due to further destruction of the Si framework. In addition, now, the disorientation of the microcrystallites $w_\perp \approx w(\varphi)$ makes the main contribution to $w_\perp$, since $w_\perp(111)\approx w_\perp(333)$. As before, less certain judgments can be made about the contribution of different components to $w_\parallel$. For this reason, the values of $L_\perp$ and $L_\parallel$ presented in Table II should be viewed as lower limits. In addition, their ratio $L_\perp/L_\parallel \approx 1$ indicates that the shape of the crystallites becomes more isotropic. This is apparently due to the destruction of the bridges in the thinnest regions of fragments of the columnar structure of PS as a result of an increase in the mechanical stresses as a result of oxidation.

The observed pattern of almost complete and for the 5-A layer (3.5 months) complete vanishing of the diffraction peak from PS, also observed by other authors,[20,21] reflects the process of destruction of the Si framework and size reduction of its fragments during storage in air. The degradation of the structure of the PS sample $5A$ (3.5 months) has advanced so far that probably a substantial fraction of this sample consists of amorphous SiO_2 or SiO_x ($x<2$) specked with n-Si nanocrystals. The sample $5A$ shows the advance in the kinetics of aging even after 3.5 months of storage: According to our phase analysis data, it contains ~ 2 times more amorphous phase than the $1A$ (3.5 months) layer. However, the small dimensions and small total volume of n-Si in PS, as well as the strong distortion of the crystal lattice in them, make the measurement of the diffraction from nanocrystallites in PS a difficult technical problem.

5. CONCLUSIONS

The experiments performed show that the disordering and size reduction of the structural elements of PS occur as a result of illumination during anodization and as a result of storage. Both processes are characterized by an increase in the oxygen concentration. However, this disordering is accompanied by an increase in the PL intensity in the first case (during photoanodization) and by quenching in the second case (during aging). We call attention to the fact that the quenching observed here as a result of storage in air does not always happen. We observed excitation of PL in the batch of samples B with a lower porosity (see Fig. 6). Hence it follows that the brightness of the PL can change during storage in air in one or another direction, depending on the initial porosity of the PS. It follows from the data obtained in this study that the layers with $p\approx 70\%$ demonstrate a higher stability of PL. Less porous samples, upon oxidation, exhibit an increase in the brightness of the luminescence and the more porous samples, upon amorphization, exhibit quenching.

Let us now briefly summarize:

1. Illumination during anodization intensifies the PL and shifts it to shorter wavelengths, increases the porosity and oxygen content, and intensifies the disordering in the PS layer.

2. Illumination initiates in the electrolyte an oxidation process that accelerates the chemical dissolution of the porous layer.

3. Storage of high-porosity layers in air results in quenching of the PL.

4. During storage the structure of the PS degrades from a structure consisting mainly of macrocrystallites with sizes $\geqslant 4\ \mu$m into a structure consisting of smaller crystallites, which lose the substrate orientation and which are more isotropic with respect to size. The lattice constant increases ($\Delta a/a \approx 5 \times 10^{-3}$).

5. The aging of PS is attributable to oxidation, which results in a mechanical destruction of the crystallites, to disruption of the passivation of their surface, and to amorphization.

We thank L. V. Belyakov and V. Kh. Kudoyarova for a helpful discussion.

This work was supported by Russian Fund for Fundamental Research (No. 96-02-16907a) and a program of the Ministry of Science FTNS 96-1012.

[a]e-mail: ast@power.ioffe.rssi.ru

[1] L. T. Canham, Appl. Phys. Lett. **57**, 1046 (1990).
[2] F. Yan, Phys. Status Solidi A **142**, K 1–4.
[3] H. Yoon and M. S. Goorsky, Mater. Res. Soc. Symp. Proc. **378**, 893 (1995).
[4] T. Assano, K. Higa, S. Aoki, M. Tonouchi, and T. Miyasano, Jpn. J. Appl. Phys. **31**, L373 (1992).
[5] N. Koshida and H. Koyama, Jpn. J. Appl. Phys. **30**, L1221 (1991).
[6] L. V. Belyakov, D. N. Goryachev, O. M. Sreseli, and I. D. Yaroshetskiĭ, Fiz. Tekh. Poluprovodn. **27**, 1961 (1993) [Semiconductors **27**, 1078 (1993)].
[7] A. Halimaoui in *Porous Silicon Science and Technology. Winter School,* edited by J.-C. Vial and J. Derrien, Springer-Verlag, N. Y., 1995, Les Editions de Physique Les Ulis.
[8] R. N. Kyutt, Fiz. Tverd. Tela (Leningrad) **31**, 270 (1989) [Sov. Phys. Solid State **31**, 1432 (1989)].
[9] L. T. Canham, M. R. Houlton, W. Y. Leong, C. Pickering, and J. M. Keen, J. Appl. Phys. **70**, 422 (1991).
[10] H. Koyama, T. Nakagawa, T. Ozaki, and N. Koshida, Appl. Phys. Lett. **65**, 1656 (1994).
[11] J. Suda, T. Ban, T. Koizumi, H. Koyama, J. Tezuka, Sh. Shin, and N. Koshida, Jpn. J. Appl. Phys. **33**, 581 (1994).
[12] E. V. Astrova, V. V. Emtsev, A. A. Lebedev, D. S. Poloskin, A. D. Remenyuk, Yu. V. Rud, and R. F. Vitman, Mater. Res. Soc. Symp. Proc. **405**, 185 (1996).
[13] E. V. Astrova, V. V. Emtsev, A. A. Lebedev, R. F. Vitman, D. S. Poloskin, A. D. Remenyuk, and Yu. V. Rud', Fiz. Tekh. Poluprovodn. **30**, 507 (1996) [Semiconductors **30**, 279 (1996)].
[14] V. Petrova-Koch, T. Mucschnik, A. Kux, B. K. Meyer, F. Koch, and V. Lemann, Appl. Phys. Lett. **61**, 943 (1992).
[15] R. R. Kunz, P. M. Nitishin, H. R. Clark, and M. Rotschild, Appl. Phys. Lett., **67** 1761 (1995).
[16] F. K. Reinhart and R. A. Logan, J. Appl. Phys. **44**, 3171 (1973).
[17] T. Ito, H. Kiyama, T. Yasumatsu, H. Watabe, and A. Hiraki, Physica B **170**, 535 (1991).
[18] T. Ito, T. Jasumatsu, H. Watabe, and A. Hiraki, Jpn. J. Appl. Phys. **29**, L201 (1990).
[19] K. P. Ryaboshapka, Zavod. lab. **47**, 26 (1981).
[20] D. Bellet, S. Billat, G. Dolino, M. Ligeon, C. Meyer, and F. Muller, Solid State Commun. **86**, 51 (1993).
[21] O. Belmont, D. Bellet, and J. Brechet, J. Appl. Phys. **79**, 7586 (1996).

Translated by M. E. Alferieff

Optimization of the operating conditions of thermocouples allowing for nonlinearity of the temperature distribution

S. V. Ordin

A. F. Ioffe Physicotechnical Institute, Russian Academy of Sciences, 194021 St. Petersburg, Russia
(Submitted December 24, 1996; accepted for publication January 17, 1997)
Fiz. Tekh. Poluprovodn. **31**, 1269–1271 (October 1997)

It is shown that the Peltier heat, previously regarded as a purely contact characteristic, must be included in the equation describing the heat-flux balance in the volume of a sample (simplified Ioffe–Stil'bans equation). Analytical expressions for the temperature distribution in a loaded thermocouple, which describe the main deviations from the linear distribution, are derived by a self-consistent calculation allowing for a temperature dependence of the Peltier heat. Equations which extend the Ioffe relations to the case of large temperature differentials and large heat fluxes are obtained for the efficiency of a thermocouple. © *1997 American Institute of Physics.* [S1063-7826(97)03110-4]

1. INTRODUCTION. PHENOMENOLOGICAL ANALYSIS OF THERMOELECTRIC PROCESSES

Active research in the field of thermoelectricity and subsequent extensive use of thermoelectric converters started with the theoretical estimates obtained by A. F. Ioffe in 1950 for the efficiency of a thermocouple[1] and determination of the parameter Z characterizing the thermoelectric figure of merit of materials

$$Z=\frac{\alpha^2\sigma}{\kappa}, \tag{1}$$

where α is the thermoelectric power, and σ and κ are, respectively, the electrical and thermal conductivities of the material. In Ref. 1, Ioffe based his analysis of heat fluxes in a thermocouple on the accepted idea that the Peltier heat π is of a contact character. This corresponds to the assumption that the temperature distribution in the thermocouple is linear. Attempts have been made to describe the deviation of the temperature distribution from linearity in a simple case of temperature-independent thermoelectric parameters, taking into account the volume heat evolution due to the Thompson and Joule–Lenz effects.[2] An attempt was made on the basis of this approach to obtain more accurate expressions for the efficiency.[3] However, the corrections obtained in Ref. 3 to the Ioffe formulas were found to be negligible and the question of refining the equations for the efficiency of a thermocouple was considered to be closed. The solution of thermophysical problems, taking into account thermoelectric effects in cases where they are not small (refrigeration and heat-pump regimes), was based on a model proposed in Ref. 2 . This procedure was reflected in nearly all monographs on thermoelectricity.[4–7]

On the other hand, thermoelectric effects are described by generalized kinetic equations.[8–10] If the kinetic coefficients are expressed in terms of the thermoelectric parameters, then the following system of equations is obtained for the current density $\mathbf{j}$ and the heat flux density $\mathbf{q}$ in an isotropic medium in the absence of a magnetic field:

$$\mathbf{j}=\sigma\mathbf{E}+\alpha\sigma(-\nabla T),$$

$$\mathbf{q}=\pi\mathbf{j}+\kappa(-\nabla T), \tag{2}$$

where T is the temperature, $\mathbf{E}$ is the electric field intensity, and $\pi=\alpha T$. The coefficients in Eqs. (2) are characteristics of macroscopic regions in the material. Since, in general, there are no grounds for assuming that the cross terms are zero, the Peltier heat π and the thermoelectric power α must also be included, just as σ and κ, in order to find the temperature distribution in the volume of the thermocouple. The use in Ref. 2 of the Thompson heat τ and the Joule heat σ, previously considered to be volume terms, constituted the introduction of π and α in an implicit form into the equation for the heat flux density.[2] Indeed, the Thompson and Joule heating are components of $\nabla\cdot(\pi\mathbf{j})$, and their use in the heat-flux balance equation[2,3] is an approximate reconstruction of the heat flux $\pi\mathbf{j}$ from $\nabla\cdot(\pi\mathbf{j})$.

The volume nature of the Peltier heat also follows from its statistically macroscopic definition as the heat transferred in the volume of the sample by a single electron.[10] Contact effects can be substantial for both α and β, as well as σ and $\varkappa$, but they must be taken into account phenomenologically in an analysis of the boundary conditions. Cases in which the influence of a boundary (contact) cannot be ignored in the entire volume of the thermocouple are the only exceptions. A phenomenological analysis shows that to solve the thermophysical problems with allowance for the thermoelectric effects the volume nature of the Peltier heat must be taken into account using the equations of nonequilibrium thermodynamics (2).

 1063-7826/97/101091-03$10.00 © 1997 American Institute of Physics

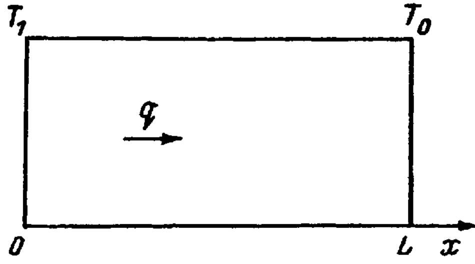

FIG. 1. Schematic diagram of a thermocouple and the direction of propagation of a heat flux q in it.

2. THERMOELECTRIC CONVERSION EFFICIENCY WITH ALLOWANCE FOR THE TEMPERATURE DISTRIBUTION IN A THERMOCOUPLE

Let us consider the temperature distribution in a thermocouple with thermally insulated sides, unit cross section, and length L operating in the generator mode with heat flux q and current j flowing along it (Fig. 1). We shall use the same simplification as in Ref. 2 — the thermoelectric parameters α, σ, and $\varkappa$ are assumed to be temperature-independent. Since materials for thermocouples must have a high efficiency in the entire working temperature interval, this assumption does not greatly decrease the range of applicability of the desired solutions, but it enables us to obtain solutions in an analytic form. For prescribed conditions the temperature in the thermocouple will depend only on the coordinate x, running parallel to the axis of the thermocouple, and the heat-flux balance equation is an equation for the heat flux (2) rewritten in the scalar form

$$q=\alpha jT-\kappa\frac{dT}{dx}. \tag{3}$$

Thus, we must solve a first-order differential equation with constants in order to find the temperature distribution in the thermocouple. Since, ordinarily, in generator mode the temperature of the cold end of the thermocouple is stabilized, we give the first boundary condition $T(L)=T_0$ and obtain the following expression for the temperature distribution $T(x)$:

$$T(x)=T_0\exp\left[-\frac{\alpha j}{\kappa}(L-x)\right]+\frac{q}{\alpha j}\left\{1-\exp\left[\frac{\alpha j}{\kappa}(L-x)\right]\right\}. \tag{4}$$

The explicitly nonlinear form of the function $T(x)$ is attributable to the fact that when a current flows in the generator regime, the electrons flowing from the hot into the cold region scatter, lowering the Peltier heat and thereby increasing the heat load (gradient) on the term determined by the thermal conductivity κ. Thus, the scattering of the electrons results in a redistribution of the thermal energy in the volume of the thermocouple between electronic and phonon subsystems; this determines the parameter π in each macroscopic local region in the material.

A thermocouple can operate in the generator mode either in a regime with a constant heat flux q flowing through it or in a regime with a fixed temperature drop across it. These conditions fix the second boundary condition required to obtain the solution of Eq. (3).

In the fixed-flux regime $q=q^*=\text{const}$ the temperature distribution $T(x)$ is given by Eq. (4), where q is replaced by q^*. Using the expression obtained for $T(x)$, we can express the temperature drop across the thermocouple as

$$(-\Delta T)=T(0)-T(L)=\left(\frac{q^*}{\alpha j}-T_0\right)\left[1-\exp\left(-\frac{\alpha j}{\kappa}L\right)\right]. \tag{5}$$

Using the equation for the current (2), we find another equation relating j and ΔT

$$j=\frac{\alpha\sigma(-\Delta T)}{(1+m)L}, \tag{6}$$

where the parameter m equals the ratio of the load resistance R_l to the internal resistance $R_i=L/\sigma$ of the thermocouple.

Substituting into Eq. (6) the expression for $(-\Delta T)$, we obtain an equation for the current

$$j=F(j), \tag{7}$$

which determines the current as a function of the prescribed parameters q^*, R_l, α, σ, and κ. Equation (7) for the current can be approximately solved graphically, approximating the functional $F(j)$ by a straight line passing through the point

$$\left[\frac{\alpha\sigma q^*}{\kappa(1+m)},0\right]\quad\text{and}\quad\left[0,\frac{q^*}{\alpha T_0}\right].$$

Finding the intersection point of the chosen approximation with the quantity j, we obtain an expression for the current

$$j=\frac{q^*}{\alpha T_0}\frac{ZT_0}{(1+m+ZT_0)}. \tag{8}$$

This expression for the current can also be obtained by expanding the exponential in the expression (5) in a series and retaining the linear term. Substituting the expression found for the current (8) into the relation for the efficiency η in the fixed heat flux regime

$$\eta=\frac{j^2R_l}{q^*}, \tag{9}$$

we obtain the efficiency of the thermocouple under an arbitrary load

$$\eta=\frac{q^*R_T}{T_0}\frac{mZT_0}{(1+m+ZT_0)^2}, \tag{10}$$

where $R_T=L/\kappa$ is the thermal resistance of the thermocouple. Differentiating the expression obtained with respect to m, we find the condition under which η has maximum, $m=1+ZT_0$, and an expression for $\eta_{\max}$ which corresponds to the optimal load

$$\eta_{\max}=\frac{1}{4}\frac{q^*R_T}{T_0}\frac{ZT_0}{(1+ZT_0)}. \tag{11}$$

As one can see from the expression obtained for $\eta_{\max}$, the efficiency $\eta_{\max}$ increases with increasing thermal resistance R_T. In addition, the parameter determining the thermoelectric figure of merit of the material $\alpha^2\sigma/\kappa^2$ is differerent from Z. However, a natural constraint for the operating re-

gime under consideration is the maximum admissable temperature drop, for which the maximum efficiency is reached in accordance with the Carnot cycle. For this reason, we shall also consider the operating regime of a thermocouple with a fixed temperature differential. We fix such a regime on the thermocouple by a boundary condition applied at the hot end of the thermocouple, fixing its temperature, $T(0)=T_1=$ const. The expression for the temperature distribution (4) becomes

$$T(x)=T_0+(-\Delta T)\frac{1-\exp[-(\alpha j/\kappa)(L-x)]}{1-\exp(-\alpha jL/\kappa)}. \tag{12}$$

The temperature distribution (12) is clearly nonlinear. The derivation of the relation (12) employed an expression for the heat flux q obtained from the boundary condition at the hot end of the thermocouple

$$q=\alpha j\left[T_0+\frac{(-\Delta T)}{1-\exp(-\alpha jL/\kappa)}\right], \tag{13}$$

which, because of the continuity of the flux, should be the same in any section of the thermocouple. Substituting the expression for $T(x)$ [Eq. (12)] into the initial equation (3), it is easy to show that $q(x)=$ const. Since the temperature differential is fixed in this operating regime, we can write, using directly the expression for the current (6) and the expression obtained for the total flux (13), a formula for the efficiency of the thermocouple with an arbitrary load

$$\eta=\frac{(-\Delta T)}{T_1}\frac{1-\exp[z(-\Delta T)/(1+m)]}{1-(T_0/T_1)\exp[z(-\Delta T)/(1+m)]}\frac{m}{(m+1)}. \tag{14}$$

For small values of the parameter $Z(-\Delta T)/(1+m)$, which is satisfied quite strictly under real operating conditions, the expression (14) simplifies and becomes

$$\eta=\frac{(-\Delta T)}{T_1}\frac{ZT_1}{(1+m+ZT_0)}\frac{m}{(m+1)}. \tag{15}$$

In Ioffe's formula,[1] put into a similar form, the denominator contains instead of the term ZT_0 the term $ZT_0+(-\Delta T)[1-1/2(1+m)]$, which appears because of the replacement of the nonlinearity of the temperature distribution by the qualitative assumption that the Joule heat is uniformly distributed between the hot and cold ends of the thermocouple. Differentiating expression (15) with respect to m, we obtain the condition for a maximum of η:

$$m=(1+ZT_0)^{1/2},$$

and the expression itself for $\eta_{\max}$ with the corresponding optimal load in the fixed temperature differential regime

$$\eta_{\max}=\frac{(-\Delta T)}{T_1}\frac{ZT_1}{(1+\sqrt{1+ZT_0})^2}. \tag{16}$$

The expressions (11) and (16) for $\eta_{\max}$ were obtained strictly in the first approximation and can be used for heat flux densities and temperature differentials, which are employed in real situations, while Ioffe's formulas, which represent the zeroth approximation, are valid for extremely weak heat fluxes and small temperature differentials. The modern level of programming makes it possible, in principle, both to employ for the purpose of optimizing the operating conditions of thermocouples the exact expression for the efficiency (14) and to find with prescribed accuracy a solution of the equation for the current (7). Furthermore, the starting equation (3) can be solved numerically, given the real temperature dependences of the thermoelectric parameters.

I am deeply grateful to A. Yu. Zyuzin, M. I. Fedorov, and T. A. Polyanskaya for helpful discussions and for valuable remarks.

[1] A. F. Ioffe, *Semiconductor Thermocouples* [in Russian], Soviet Academy of Sciences Press, Leningrad (1960).

[2] A. F. Ioffe, L. S. Stil'bans, E. K. Iordanishvili, and T. S. Stavitskaya, *Thermoelectric Cooling* [in Russian], Soviet Academy of Sciences Press, Moscow (1956).

[3] A. I. Burshteĭn, *Physical Principles of the Calculation of Semiconductor Thermoelectric Devices* [in Russian], Fizmatgiz, Moscow (1962).

[4] A. S. Okhotin, A. A. Efremov, V. S. Okhotin, and A. S. Pushkarskiĭ, *Thermoelectric Generators* [in Russian], Atomizdat, Moscow (1971), p. 147.

[5] L. N. Anatychuk, *Thermocouples and Thermoelectric Devices* [in Russian], Naukova dumka, Kiev (1979), p. 79.

[6] A. A. Sarkisov, V. A. Yakimov, and E. P. Kaplar, *Thermoelectric Generators with Nuclear Heat Sources* [in Russian], Énergoatomizdat, Moscow (1987), p. 11.

[7] D. M. Rowe [Ed.], *CRC Handbook of Thermoelectrics*, CRC Press, N. Y. (1995).

[8] A. C. Beer, *Galvanomagnetic Effects in Semiconductors*, Academic Press, N. Y. (1963).

[9] B. M. Askerov, *Electronic Transport Phenomena in Semiconductors* [in Russian], Nauka, Moscow (1985).

[10] J. Ziman, *Principles of the Theory of Solids*, Cambridge University Press, N. Y. (1972), 2nd edition [Russian translation, Mir, Moscow (1974), pp. 262–272].

Translated by M. E. Alferieff

Effect of an external bias voltage on the photoelectric properties of silicon MIS/IL structures

Ya. S. Budzhak, V. Yu. Erokhov, and I. I. Mel'nik

State University "L'vov Polytechnology" 290013 L'vov, Ukraine
(Submitted July 17, 1996; accepted for publication January 28, 1997)
Fiz. Tekh. Poluprovodn. **31**, 1273–1277 (October 1997)

The mechanism by which an external bias voltage influences the photoelectric properties of Al/tunneling-thin SiO_2/*p*-Si structures with an induced inversion layer is investigated theoretically. A characteristic feature of the structure studied is the presence of a special inversion grid. Between this grid and the substrate a positive voltage is applied. Relations expressing the functional dependence on the bias voltage of the structure parameters and the output electrical characteristics of photocells, which are based on it, are obtained. The results of numerical calculations illustrating the effectiveness of using a bias voltage to increase the efficiency of photocells based on Al/SiO_2/*p*-Si structures with an induced inversion layer are presented.
© *1997 American Institute of Physics.* [S1063-7826(97)03210-9]

1. INTRODUCTION

A number of scientists have been conducting,[1–4] for a long time now, investigations of Al/tunneling-thin SiO_2/*p*-Si structures with an induced inversion layer (MIS/IL). The distinguishing feature of these structures is the presence of a shallow ($\sim 0.1\ \mu$m) *n–p* junction which arises at the surface of the semiconductor under the action of a fixed positive charge in the insulator layer (Fig. 1a). The simplicity of the technological implementation of MIS/IL structures and the absence of high-temperature diffusion processes and diffusion defects of the crystal lattice open up unique possibilities for producing the structures on the basis of highly efficient and solar photocells (PCs).[5–7] However, the practical achievement of the theoretically predicted high efficiency of MIS/IL solar cells (SCs) has turned out to be problematic because of large losses of the generated power in the high-resistance inversion layer (IL). The attempts[8–10] made to decrease the resistivity of the IL by increasing the built-in charge density have inevitably complicated the technology for fabrication of MIS/IL structures and have increased the cost of PCs based on them.

The most noteworthy method in this connection was that of Ref. 11, where it was suggested that, together with a positive charge built into the insulator layer, the difference between the electronic work functions of the semiconductor and thin strips of metal inversion grids be used to invert the type of conductivity in the surface region of the semiconductor substrate. An inversion grid based on a metal with a low work function was formed on top of an insulator layer of tunneling thickness between the strips of the current-collecting grid (Fig. 1b). The thickness of the grid was chosen so as to minimize the optical losses. Despite the fact that this method is acceptable from the technological standpoint, it should be noted that it has a substantial drawback in that the materials for the inversion grid are limited to metals with a work function less than 4 eV. This circumstance alone makes this method unsuitable as means for increasing substantially the efficiency of MIS/IL-based photocells.

2. MECHANISM OF THE EFFECT OF A BIAS VOLTAGE ON THE PARAMETERS OF A MIS/IL STRUCTURE

Our objective in the present paper is to give a theoretical justification for the efficacy of the method that we propose for improving the photoelectric properties of silicon MIS/IL structures. This method is based on the use of external factors together with internal factors (built-in charge, low density of surface states, difference in the work functions), specifically, reverse bias voltage, in structures with an induced inversion layer.[12] While retaining all advantages of the MIS/IL structure shown in Fig. 1b, it is suggested that its parameters be influenced by applying a positive voltage (relative to the substrate) to the inversion grid. In this case, the condition of electrical neutrality of the reverse-biased MIS/IL structure in a state of thermodynamic equilibrium is determined, by analogy with Ref. 13, by the equation

$$Q_i - Q_{sc} + Q_{ox} + Q_{td} - Q_{ts} = 0, \tag{1}$$

where Q_i, Q_{sc}, Q_{ox}, Q_{td}, and Q_{ts} are, respectively, the charges per unit area on the metal inversion grid, in the surface region of the semiconductor, in the insulator layer, and in the donor and acceptor surface states, respectively. Representing Q_{sc} as in Ref. 14 , we determine from Gauss's law the applied voltage drop across the Si–SiO_2 interface

$$\Delta = -\frac{d}{\varepsilon_{ox}} Q_i = -\frac{d}{\varepsilon_{ox}} \left(qN_{ox} + Q_{td} - Q_{ta} - \sqrt{2kT\varepsilon_s N_a} F\left(\beta\psi_s, \frac{n_i}{N_a} \right) \right), \tag{2}$$

where d and ε_{ox} are, respectively, the thickness and permittivity of the oxide layer, and N_{ox} is the density of the positive charge fixed in it;

$$F\left(\beta\psi_s, \frac{n_i}{N_A} \right) = \left\{ [\exp(-\beta\psi_s) + \beta\psi_s - 1] + \left(\frac{n_i}{N_A} \right)^2 (\exp\beta\psi_s - \beta\psi_s - 1) \right\}^{1/2}, \tag{3}$$

 1063-7826/97/101094-05$10.00 © 1997 American Institute of Physics

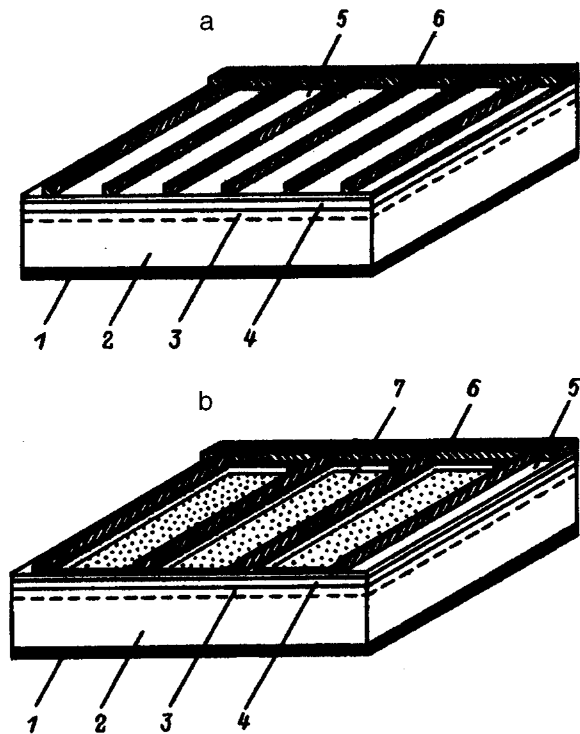

FIG. 1. Schematic diagram of solar cells with a MIS/IL structure: a — Standard structure, b — structure with an inversion grid. *1* — Backside contact, *2* — *p*-type silicon substrate, *3* — space charge region, *4* — inversion layer, *5* — SiO_2 film, *6* — current-collecting grid, *7* — inversion grid.

ψ_s is the surface electrostatic potential, $\beta = q/kT$; and all other notation is standard.

Another expression for Δ can be obtained, as shown in Ref. 3 , by analyzing the band diagram of a MIS/IL structure in the reverse-bias regime (Fig. 2b). In this case

$$\Delta = -\left[\frac{E_g}{q} + \chi - \Phi_m - \psi_s - V_p + V\right], \tag{4}$$

where E_g and χ are, respectively, the band gap and the electron affinity of the semiconductor, Φ_m is the electronic work function of the metal of the inversion grid, V_p is the depth of the Fermi level with respect to the valence band top, and V is the magnitude of the external voltage applied to the inversion grid.

Combining relations (3) and (4) and taking into account the dependence of the degree of filling of the acceptor and donor surface traps on the magnitude of the surface potential,[13] we obtain

$$F\left(\beta\psi_s, \frac{n_i}{N_A}\right) + \frac{q^2 D_{it}(\psi_s + V_p)}{\sqrt{2kT\varepsilon_s N_A}} = \frac{\frac{E_s}{q} + \chi - \Phi_m - \psi_s - V_p + V}{\frac{d}{\varepsilon_{ox}}\sqrt{2kT\varepsilon_s N_A}} + \frac{qN_{ox} + qD_{it}[E_c - q(\psi_s + V_p)]}{\sqrt{2kT\varepsilon_s N_A}}, \tag{5}$$

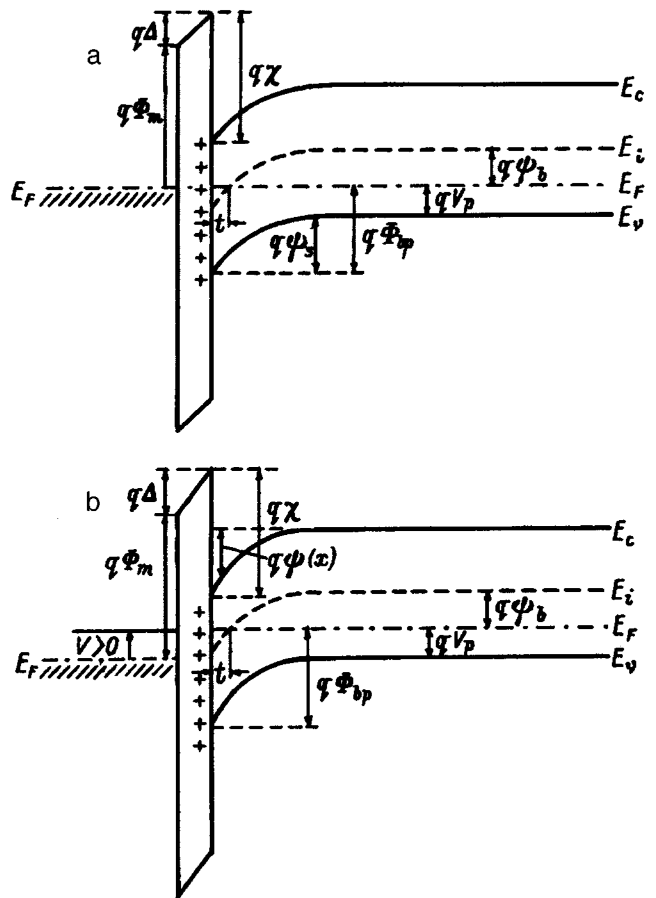

FIG. 2. Energy diagram of a metal/tunneling-thin SiO_2/*p*-Si structure: a — no external bias, b — with reverse bias.

where D_{it} is the energy density of the surface traps, and E_c is the energy position of the conduction band bottom with respect to the valence band top.

The relation (5) obtained above makes it possible to calculate the dependence of the surface potential ψ_s on the magnitude of the external voltage applied to the inversion grid in the reverse-bias regime (Fig. 3).

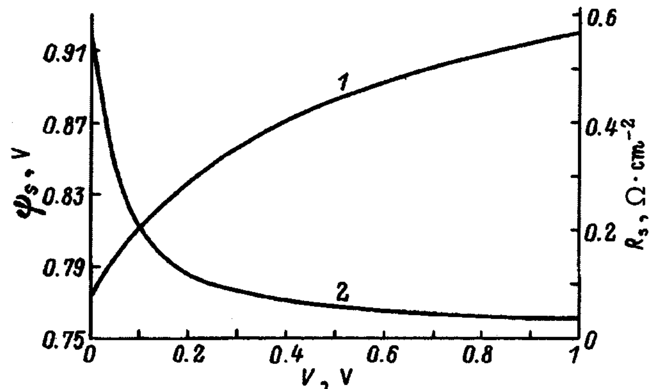

FIG. 3. Surface potential ψ_s (*1*) and serial resistance R_s of a MIS/IL-based solar cell (*2*) versus the external bias voltage V. Computational parameters: a — $D_{it} = 5\times10^{11}$ $cm^{-2}\cdot eV^{-1}$, $N_A = 5\times10^{15}$ cm^{-3}, $N_{ox} = 10^{11}$ cm^{-2}, $d = 30$ Å; b — $T = 300$ K, $A^{**} = 110$ $A/K^2\cdot cm^2$, $N_v = 1.04\times10^{19}$ cm^{-3}.

Since the purpose of the method examined above is primarily to decrease the ohmic power losses during the operation of a MIS/IL-based PC, we shall determine the degree to which the external bias influences the serial resistance R_s. On the basis of Ref. 15 and keeping in mind the analogy between MIS/IL in SCs and PCs with a n^+-p junction, we shall express the resistivity of the IL in terms of its surface resistance R_i and the width d_1 of the inversion grid

$$R_{\text{inv}}=R_i\frac{d_1^2}{12}. \tag{6}$$

According to Ref. 7, the surface resistance of the IL is determined by the relation

$$R_i=\frac{1}{\mu_n\sqrt{2kT\varepsilon_sN_A}\{[\beta\psi_s+(n_i/N_A)^2e^{\beta\psi_s}]^{1/2}-(\beta\psi_s)^{1/2}\}}, \tag{7}$$

where μ_n is the electron mobility in the IL. Since the low resistances of the contacts and conductors in a MIS/IL-based PC device can be disregarded in contrast with R_{inv},[11] combining Eqs. (6) and (7) and expressing the resistivity R_{sc} of the semiconductor, according to Ref. 11, in terms of the surface resistance R_{ss}, we obtain the expression for R_s

$$R_s=R_{sc}+R_{\text{inv}}=\frac{R_{ss}\left[2d_0^2+3d_1\left(d_0+\frac{d_1}{2}\right)\right]}{6}$$
$$+\frac{d_1^2}{12\mu_n\sqrt{2kT\varepsilon_sN_A}\{[\beta\psi_s+(n_i/N_A)^2\exp\beta\psi_s]^{1/2}-(\beta\psi_s)^{1/2}\}}, \tag{8}$$

where d_0 is the distance between the current-collecting and inversion grids. Since in a MIS/IL structure odinarily $R_{\text{inv}}\simeq 10^{-1}\ \Omega$ and $R_{\text{sc}}\simeq 10^{-2}\ \Omega$, analysis of Eq. (8) gives grounds for assuming that, to a high degree of accuracy, the serial resistance R_s of a structure of this type is a function of the surface potential and, in accordance with Eq. (5), a function of the applied external voltage (Fig. 3).

Since the height Φ_{bp} of the potential barrier of the MIS/IL structure is a sum of the bending of the energy bands at the surface of the semiconductor and the depth V_p of the Fermi level (Fig. 2)

$$\Phi_{bp}=\psi_s+V_p=\psi_s+\frac{kT}{q}\ln\left(\frac{N_v}{N_A}\right) \tag{9}$$

(here N_v is the effective density of states in the valence band), it is obvious that a reverse bias will increase Φ_{bp}. The potential barrier, in turn, is related to the saturation current density J_s of the structure by an inverse exponential function[14]

$$J_s=A^{**}T^2\exp\left(-\frac{q\Phi_{bp}}{kT}\right)\exp[-(q\Phi_T)^{1/2}d], \tag{10}$$

where A^{**} is the effective Richardson constant, and Φ_T is the average barrier height an insulator layer of thickness d. Substituting the expression (9) into Eq. (10) and making

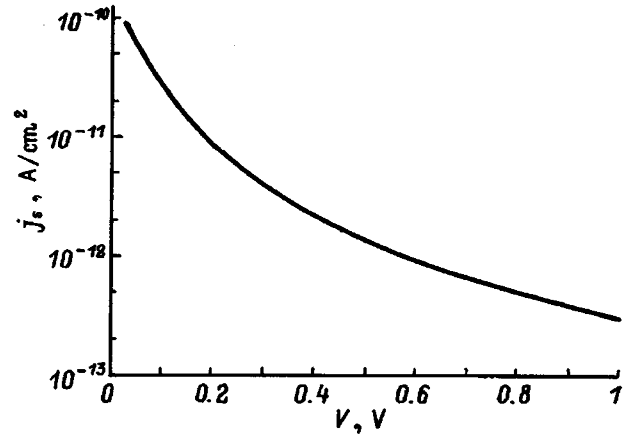

FIG. 4. Saturation current density J_s in a MIS/IL structure plotted as a function of the reverse bias V.

some simple transformations, we obtain a relation expressing the dependence of the saturation current I_s on the surface potential

$$I_s=AA^{**}T^2\exp\left\{-\left[\beta\psi_s+\ln\left(\frac{N_v}{N_A}\right)\right]\right\}$$
$$\times\exp[-d(q\Phi_T)^{1/2}], \tag{11}$$

where A is the area of the induced $n-p$ junction which, because of the small fluctuation of the junction surface, we can assume to be equal to the area of the PC. Thus, if the dependence of J_s on the bias voltage V is known, then the degree to which an external voltage can affect the saturation current density of a MIS/IL structure can be calculated (Fig. 4).

We also note that as the surface potential of the MIS/IL structure in the reverse-bias regime increases, the thickness of the induced IL will increase.[16] Using the equation presented in Ref. 7 for the electrostatic potential ψ as a function of the coordinate x at the surface of the semiconductor, determining the IL thickness t by finding the point of intersection of $\psi(x)$ and the Fermi level (Fig. 2), and, correspondingly, using ψ_b as the lower limit of the integral in Eq. (12), we obtain

$$t=\left(\frac{\varepsilon_s}{2kTN_A}\right)^{1/2}\int_{\psi_b}^{\psi_s}\left[\beta\psi+\left(\frac{n_i}{N_A}\right)^2\exp\beta\psi\right]^{-1/2}d\psi. \tag{12}$$

3. EFFECT OF AN EXTERNAL BIAS ON THE OUTPUT CHARACTERISTICS OF A MIS/IL-BASED PC

Since, according to the relations presented in Ref. 7 , the IL thickness together with other structural parameters determine the photocurrent density generated in a MIS/IL-based SC, it is not difficult to calculate the functional dependence of the photocurrent on the external voltage applied to the inversion grid. Accordingly, we represent the photocurrent in the PC as a sum of the hole current and electron current generated by a light flux F in the depleted region and in the induced IL:

$$J_L = qF(1-R) \times \left[\frac{L_1 \nu_n \exp \nu_n t + L_2 \nu_n \exp(-\nu_n t) - \alpha \exp(-\alpha t)}{1 - \nu_n^2/\alpha^2} + \frac{K_1 \nu_p \exp \nu_p t + K_2 \nu_p \exp(-\nu_p t) - \alpha \exp(-\alpha t)}{1 - \nu_p^2/\alpha^2} \right], \quad (13)$$

where

$$L_1 = \frac{e^{-(l+\nu_n t)} - e^{-(t+\nu_n l)}}{2\sinh(\nu_n l - \nu_n t)}, \quad L_2 = \frac{e^{-(\alpha l+\nu_n t)} - e^{-(\alpha t+\nu_n l)}}{2\sinh(\nu_n l - \nu_n t)},$$

$$K_1 = \frac{(\alpha+h)e^{-\nu_p t} - (\nu_p + h)e^{-\alpha t}}{(\nu_p+h)e^{\nu_p t} - (\nu_p - h)e^{\nu_p t}},$$

$$K_2 = \frac{(\alpha+h)e^{\nu_p t} + (\nu_p - h)e^{-\alpha t}}{(\nu_p+h)e^{\nu_p t} - (\nu_p - h)e^{-\nu_p t}};$$

ν_n and ν_p are the reciprocals of the electron and hole diffusion lengths, respectively, and $h = S/D_p$; here S is the surface recombination rate on the front surface of the PC, and D_p is the hole diffusion coefficient. The coefficient R takes into account the part of the photon current reflected from the surface of the semiconductor substrate with thickness l and optical absorption coefficient α. The effect of the electric field produced by the positive charge built into the insulator and the voltage applied to the inversion grid on the diffusion length of the minority carriers photogenerated in the IL must be also be taken into account in the expression (13). The quantity ν_p is therefore introduced in the second term of this relation as a function of the electric field, which in turn depends on the external bias.

Since the photocurrent I_L, together with the saturation current I_s, determine the open circuit voltage V_{oc} of the solar cell

$$V_{oc} = \frac{nkT}{q} \ln\left(\frac{I_L}{I_s} + 1\right), \quad (14)$$

it can be asserted that V_{oc} is also a function of the external bias voltage. To obtain an analytic expression for the function $V_{oc}(\psi_s)$ we substitute the expression (11) into Eq. (14) and transform the function in the argument of the logarithm:

$$V_{oc} = \frac{nkT}{q} \left[\ln\left(\frac{I_L}{AA^{**}T^2}\right) + \beta\psi_s + \ln\left(\frac{N_v}{N_A}\right) + d(q\Phi_T)^{1/2} + 1 \right], \quad (15)$$

where n is a diode figure of merit.

Having determined in this manner the kinetics of the effect of an external bias on the structural parameters and output energy characteristics of a PC, we can now directly investigate the dependence of the photogeneration efficiency in a SC of this type on the positive voltage applied to the inversion grid. We thus represent the PC efficiency as a function of the serial resistance R_s, the saturation current I_s, the photocurrent I_L, and the power P_{in} of the incident light flux:[16]

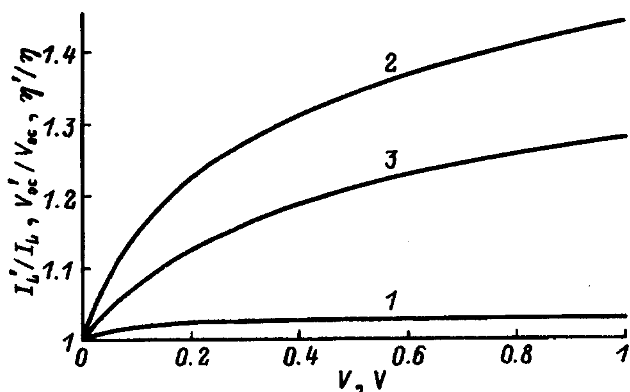

FIG. 5. *1* — $I_L'(V)/I_L$, *2* — $V_{oc}'(V)/V_{oc}$, *3* — $\eta'(V)/\eta$, where I_L, V_{oc}, and η are the output characteristics of a MIS/IL photocell without an external bias; I_L', V_{oc}', η' — same in the reverse-bias regime.

$$\eta = \left[\left(\frac{nkT}{q}\right) I_L(1-\gamma) \ln\left(\gamma \frac{I_L}{I_s}\right) - R_s I_L^2 (1-\gamma)^2 \right] / P_{in}, \quad (16)$$

where

$$\gamma = \left[1 + \frac{1}{1 + 2R_s I_L \gamma \left(\frac{q}{nkT}\right)} \ln\left(\gamma \frac{I_L}{I_s}\right) \right]^{-1}.$$

Analysis of this relation shows that an external voltage applied to the inversion grid will change substantially the SC efficiency, which is entirely a function of the external, bias-dependent, structural parameters and output electrical characteristics (Fig. 5).

4. CONCLUSIONS

A detailed analysis of the computational relations obtained for the structural parameters, output energy characteristics, and efficiency of a MIS/IL-based PC as a function of the reverse bias shows that an external positive voltage ranging from 0 to 0.6 V is most effective. Since the open-circuit voltage of a PC reaches the upper limit of this interval, it is best to use an additional MIS/IL-based SC as a source of external voltage. This implies the development of a solar module (SM) in which the output voltage of the auxiliary SC is applied in the reverse direction on the inversion grids of several basic SCs. Since under the influence of an external voltage bias the leakage current through the inversion grid decreases to 10^{-13} A/cm^2 (Fig. 4), and since the losses of applied voltage which are due to this current are very small, the number of basic PCs in the proposed SM could be large. Calculations show that even with only two basic SCs the operating efficiency of such a SM will be higher than that of a solar module of standard design in which three SCs with a MIS/IL structure are connected in series or in parallel.

In summary, it can be concluded that the proposed method for improving the photoelectric properties of $AlSiO_2/p$-Si structures is an effective method for increasing

the operational efficiency of MIS/IL-based PCs while remaining sufficiently simple for practical implementation.

This work was supported, in part, by the International Soros Program for supporting education in the exact sciences (ISSEP), Grant No. PSU 062066.

[1] A. M. Cowley and S. M. Sze, J. Appl. Phys. **36**, 3212 (1965).
[2] D. L. Pulfrey, IEEE Trans. Electron. Dev. **ED-23**, 587 (1976).
[3] A. N. Daw and P. Chattopadhyay, Solid-State Electron. **27**, 1057 (1984).
[4] M. Y. Doghish and F. D. Ho, IEEE Trans. Electron. Dev. **ED-40**, 1446 (1993).
[5] P. van Halen, R. P. Mertens, R. J. van Overstraeten, R. E. Thomas, and J. van Meerbergen, IEEE Trans. Electron. Dev. **ED-25**, 507 (1978).
[6] M. A. Green, R. B. Godfrey, M. R. Willison, and A. W. Blakers, in *Proceedings 14th IEEE Photovoltaic Spec. Conference*, New York, 1980, p. 684.
[7] G. S. Salter and R. E. Thomas, Solid-State Electron. **20**, 95 (1977).
[8] R. Hezel, Solid-State Electron. **24**, 863 (1981).
[9] R. Schorner and R. Hezel, IEEE Trans. Electron Dev. **12**, 1466 (1981).
[10] R. Hezel and K. Jaeger, J. Electrochem. Soc. **36**, 518 (1989).
[11] P. Chattopadhyay, Solid-State Electron. **31**, 1641 (1988).
[12] V. Yu. Erohov, I. I. Melnyk, and I. M. Rarenko, in *Proceedings 1st International Conference Mater. Sci. Chalcogenide and Diamond-Structure Semiconductors*, Chernivtsi (1994), Vol. 2, p. 211.
[13] V. N. Osyuk, *Electronic Processes in Semiconductors with Space Charge Regions* [in Russian], Novosibirsk (1984).
[14] S. M. Sze, *Physics of Semiconductor Devices*, Wiley, N. Y., 1981, 2nd edition [Russian translation, Mir, Moscow, 1984].
[15] R. N. Hall, Solid-State Electron. **24**, 595 (1981).
[16] A. Fahrenbruch and R. Bube, *Fundamentals of Solar Cells*, Academic Press, N. Y., 1983 [Russian translation, Mir, Moscow, 1987].

Translated by M. E. Alferieff

ERRATA

Erratum: Structure and electrical conductivity of polycrystalline silicon films grown by molecular-beam deposition accompanied by low-energy ion bombardment of the growth surface [Semiconductors 31, 237–240 (March 1997)]

D. A. Pavlov, A. F. Khokhlov, D. V. Shungurov, and V. G. Shengurov

Fiz. Tekh. Poluprovodn. **31** (October 1997)
[S1063-7826(97)03310-3]

The spelling of the name of the third author of this article should read as follows: D. V. Shengurov.

 1063-7826/97/101099-01$10.00 © 1997 American Institute of Physics

Thermodynamic analysis of the molecular-beam epitaxial growth of quaternary III-V compounds: $Ga_xIn_{1-x}P_yAs_{1-y}$

A. Yu. Egorov, A. R. Kovsh, A. E. Zhukov, V. M. Ustinov, and P. S. Kop'ev

A. F. Ioffe Physicotechnical Institute, Russian Academy of Sciences, 194021 St. Petersburg, Russia

(Submitted February 3, 1997; accepted for publication February 10, 1997)
Fiz. Tekh. Poluprovodn. **31**, 1153–1157 (October 1997)

A thermodynamic description of the molecular-beam epitaxial growth of quaternary III-V compounds with two group-V elements is proposed. A thermodynamic analysis of the growth of the compounds $Ga_xIn_{1-x}P_yAs_{1-y}$ and GaP_yAs_{1-y} is carried out on the basis of the proposed method. © *1997 American Institute of Physics.* [S1063-7826(97)00110-5]

1. INTRODUCTION

Molecular-beam epitaxy (MBE) is presently the most efficient epitaxial technology, which permits the fabrication of semiconductor heterostructures of ternary III-V compounds with one group-V element and is distinguished by the high accuracy of the composition profiles. At the same time, in the MBE of ternary compounds with two group-V elements and especially of quaternary compounds, controlling the composition of the growing layer becomes a very complex task and requires a large number of growth experiments together with postgrowth testing. For this reason, the creation of an adequate theoretical model of the MBE growth of multicomponent compounds is still of great interest. In 1985, Heckingbottom showed that MBE can be regarded as a quasinonequilibrium process, and that it can be described within a thermodynamic model.[1] This approach was developed further in Ref. 2, which describes a method for calculating the conditions that control the growth process and presents the results of a thermodynamic analysis for the growth of binary and ternary III-V compounds.

In this paper we describe a calculation method for the growth of ternary compounds with two group-V components and present the results of a thermodynamic analysis of the growth of ternary and quaternary compounds in the In–Ga–P–As system of materials.

2. THERMODYNAMIC MODEL OF THE GROWTH OF THE QUATERNARY COMPOUNDS $Ga_xIn_{1-x}P_yAs_{1-y}$

The thermodynamic analysis of the MBE growth of quaternary solutions is based on the following basic approximations. Molecular-beam epitaxy is regarded as a quasiequilibrium process, in which equilibrium between the gas and solid phases is established on the surface of the growing layer.[1] The substrate temperature is taken as the temperature of the system. The pressures corresponding to the fluxes of atoms and molecules from the substrate surface are taken as the equilibrium partial pressures. The thermodynamic properties of the quaternary systems are approximated by a regular-solution model.[3]

Assuming for definiteness that the group-III elements reach the growth surface in atomic form and that the group-V elements reach it in the form of dimers, we consider the reaction between the principal components during MBE of a quaternary compound having the formula $Ga_xIn_{1-x}P_yAs_{1-y}$:

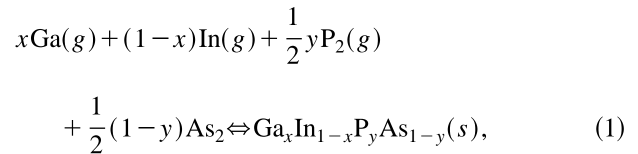

$$x\mathrm{Ga}(g)+(1-x)\mathrm{In}(g)+\frac{1}{2}y\mathrm{P}_2(g)+\frac{1}{2}(1-y)\mathrm{As}_2\Leftrightarrow \mathrm{Ga}_x\mathrm{In}_{1-x}\mathrm{P}_y\mathrm{As}_{1-y}(s), \quad (1)$$

where g refers to substances in the gas phase, and s refers to substances in the solid phase.

The solid solution $Ga_xIn_{1-x}P_yAs_{1-y}$ is regarded as a homogeneous mixture of four binary compounds with corresponding activity coefficients. The activity coefficients characterize the degree of deviation of the properties of each binary component in a real solution from its properties in an ideal solution. Then, according to the law of mass action, the reaction indicated will conform to the system of equations

$$\frac{P_{\mathrm{Ga}}P_{\mathrm{As}_2}^{1/2}}{a_{\mathrm{GaAs}}}=K_{\mathrm{GaAs}},\quad \frac{P_{\mathrm{Ga}}P_{\mathrm{P}_2}^{1/2}}{a_{\mathrm{GaP}}}=K_{\mathrm{GaP}},$$
$$\frac{P_{\mathrm{In}}P_{\mathrm{As}_2}^{1/2}}{a_{\mathrm{InAs}}}=K_{\mathrm{InAs}},\quad \frac{P_{\mathrm{In}}P_{\mathrm{P}_2}^{1/2}}{a_{\mathrm{InP}}}=K_{\mathrm{InP}}, \quad (2)$$

where the K_i is the equilibrium constant of the formation reaction of the respective binary compound, P is the equilibrium partial pressure of the respective element at the substrate surface, and a_i is the activity of the respective binary compound in the quaternary solid solution.

The activities of the binary compounds in the quaternary solid solution can be expressed in terms of the interaction parameters of the binary compounds in ternary solid solutions[3] and are given by the expressions

$$kT\ \ln a_{\mathrm{InAs}}=kT\ \ln[(1-x)(1-y)]+[ya_1+(1-y)a_2]x^2+[xa_3+(1-x)a_4]y^2-[a_c-(1-x)(a_2-a_1)-(1-y)(a_4-a_3)]xy, \quad (3.1)$$

$$kT\ \ln a_{\mathrm{GaP}}=kT\ \ln xy[ya_1+(1-y)a_2](1-x)^2+[xa_3+(1-x)a_4](1-y)^2-[a_c+x(a_2-a_1)+y(a_4-a_3)](1-x)(1-y), \quad (3.2)$$

$$kT\ \ln a_{\mathrm{InP}}=kT\ \ln[(1-x)y]+[ya_1+(1-y)a_2]x^2+[xa_3+(1-x)a_4](1-y)^2+[a_c-(1-x)(a_2-a_1)+y(a_4-a_3)]x(1-y), \quad (3.3)$$

$$kT\ \ln a_{\mathrm{GaAs}}=kT\ \ln[x(1-y)]+[ya_1+(1-y)a_2](1-x)^2+[xa_3+(1-x)a_4]y^2+[a_c+x(a_2-a_1)-(1-y)(a_4-a_3)](1-x)y, \quad (3.4)$$

where a_1 is the interaction parameter between GaP and InP in a ternary GaAsP solution; and a_2, a_3, and a_4 are the interaction parameters in GaAs–InAs, GaAs–GaP, and InAs–InP, respectively. Of the four equations (3.1)–(3.4), only three are linearly independent, since a restriction is imposed on the system of equations in the form of the relationship between the chemical potentials μ of the binary components in the solid phase

$$\mu_{\mathrm{GaAs}}+\mu_{\mathrm{InP}}=\mu_{\mathrm{GaP}}+\mu_{\mathrm{InAs}}, \quad (4)$$

which specifies the parameter a_c. Equation (4) is actually the condition for equilibrium in the solid-phase exchange reaction

$$\mathrm{GaAs}+\mathrm{InP}\Leftrightarrow\mathrm{GaP}+\mathrm{InAs}. \quad (5)$$

Then, using the system of equations (2) and (3), we can express a_c in terms of the equilibrium constants of the formation reactions of the binary compounds

$$a_c=-kT\ \ln\frac{a_{\mathrm{GaP}}a_{\mathrm{InAs}}}{a_{\mathrm{GaAs}}a_{\mathrm{InP}}}=-kT\ \ln\frac{K_{\mathrm{GaAs}}K_{\mathrm{InP}}}{K_{\mathrm{InAs}}K_{\mathrm{GaP}}}. \quad (6)$$

In the case of the growth of the stoichiometric compound, the fluxes of the group-III and group-V atoms utilized for growth are equal. According to the mass conservation law, we can write the expression

$$F^0_{\mathrm{Ga}}-F_{\mathrm{Ga}}+F^0_{\mathrm{In}}-F_{\mathrm{In}}=2(F^0_{\mathrm{As}_2}-F_{\mathrm{As}_2}+F^0_{\mathrm{P}_2}-F_{\mathrm{P}_2}), \quad (7)$$

where the F^0_i are the incident fluxes of atoms or molecules onto the growth surface (the external fluxes), and the F_i are the re-evaporated fluxes that create the equilibrium partial pressures of the elements over the growth surface.

The ratio between the mole fractions x and y of the components of the quaternary solution is also determined by the ratio between the fluxes utilized for growth:

$$\frac{x}{1-x}=\frac{F^0_{\mathrm{Ga}}-F_{\mathrm{Ga}}}{F^0_{\mathrm{In}}-F_{\mathrm{In}}}, \quad (8)$$

$$\frac{y}{1-y}=\frac{F^0_{\mathrm{P}_2}-F_{\mathrm{P}_2}}{F^0_{\mathrm{As}_2}-F_{\mathrm{As}_2}}. \quad (9)$$

Using Eqs. (8) and (9), we can write (7) in terms of the In and P fluxes alone:

$$\frac{F^0_{\mathrm{Ga}}-F_{\mathrm{Ga}}}{x}=2\frac{F^0_{\mathrm{P}_2}-F_{\mathrm{P}_2}}{y}. \quad (10)$$

Expressing the flux in terms of the pressure according to the formula

$$F_i=\frac{P_i}{(2\pi m_i kT)^{1/2}}, \quad (11)$$

where P_i is the pressure corresponding to the flux, and m_i is the molecular weight, and using (2), we obtain

$$\left[F^0_{\mathrm{Ga}}-\frac{a_{\mathrm{GaP}}K_{\mathrm{GaP}}}{(P_{\mathrm{P}_2})^{1/2}(2\pi m_{\mathrm{Ga}}kT)^{1/2}}\right]\frac{1}{x}=2\left[F^0_{\mathrm{P}_2}-\frac{P_{\mathrm{P}_2}}{(2\pi m_{\mathrm{P}_2}kT)^{1/2}}\right]\frac{1}{y}. \quad (12)$$

Now, assigning the incident Ga and P fluxes, i.e., F^0_{Ga} and $F^0_{\mathrm{P}_2}$, as well as the composition of the quaternary compound, i.e., the values of x and y, we can find the solution of this equation relative to P_{P_2}. Substituting the values found for P_{P_2} into system of equations (2), we find all the pressures corresponding to the re-evaporated fluxes, i.e, P_{Ga}, P_{In}, and P_{As_2}, and then utilizing (11), we find the re-evaporated fluxes themselves. Finally, using Eqs. (8) and (9), we find the required incident In and As fluxes: F^0_{In} and $F^0_{\mathrm{As}_2}$.

Thus, all the external fluxes of the group-III and group-V elements needed to obtain a quaternary solid solution $\mathrm{Ga}_x\mathrm{In}_{1-x}\mathrm{P}_y\mathrm{As}_{1-y}$ of definite composition, as well as the re-evaporated fluxes of the elements, have been established.

In the case of the growth of a ternary compound with two group-V elements, for example, $\mathrm{GaP}_y\mathrm{As}_{1-y}$ (i.e., when $x=1$), Eq. (12) transforms into

$$F^0_{\mathrm{Ga}}-\frac{a_{\mathrm{GaP}}K_{\mathrm{GaP}}}{(P_{\mathrm{P}_2})^{1/2}(2\pi m_{\mathrm{Ga}}kT)^{1/2}}=2\left[F^0_{\mathrm{P}_2}-\frac{P_{\mathrm{P}_2}}{(2\pi m_{\mathrm{P}_2}kT)^{1/2}}\right]\frac{1}{y}, \quad (13)$$

and the expressions for the activities take on the form

$$kT\ \ln a_{\mathrm{GaP}}=kT\ \ln y+a_3(1-y)^2, \quad (14.1)$$

$$kT\ \ln a_{\mathrm{GaAs}}=kT\ \ln(1-y)+a_3y^2. \quad (14.2)$$

3. CALCULATION RESULTS AND DISCUSSION

The equilibrium constants of the formation reactions of the binary compounds used in the calculations were taken from Ref. 4, and the interaction parameters of the binary compounds in the ternary solid solutions were borrowed from Ref. 5.

The results of the calculations in the case of the growth of $\mathrm{GaP}_y\mathrm{As}_{1-y}$ on a GaAs substrate are presented in Figs. 1 and 2. The calculations were performed under the assumption that an elastically stressed layer of $\mathrm{GaP}_y\mathrm{As}_{1-y}$ forms on the GaAs surface and that its crystal lattice constant in the

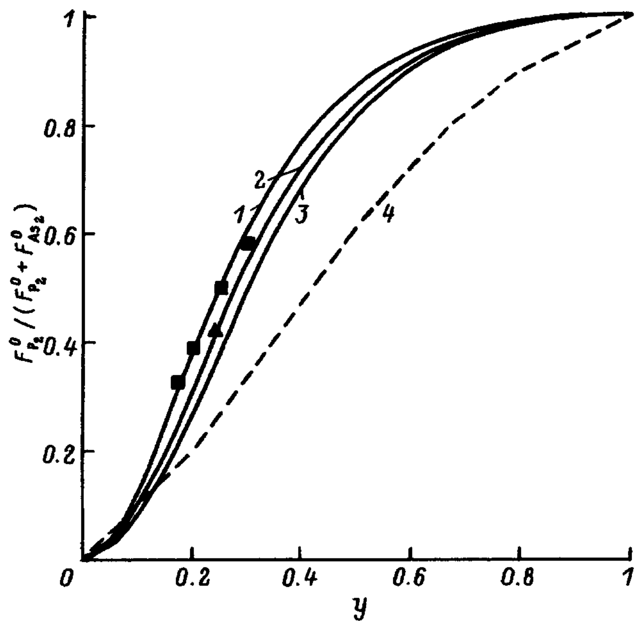

FIG. 1. Relationship between the fraction of the external phosphorus flux in the total external flux of group-V elements and the composition of the compound GaP_yAs_{1-y} grown $[F^0_{Ga}=10^{14}\ (cm^2\cdot s)^{-1}$, $F^0_{As_2}=3\times10^{14}\ (cm^2\cdot s)^{-1}]$ for various substrate temperatures T, °C: *1* — 400, *2* — 500, *3* — 600. The dashed line is a plot of the calculation results from Ref. 2. The points are experimental data from Ref. 6.

growth plane is determined by the lattice constant of GaAs. The influence of the variation of the Gibbs free energy of formation of the binary compounds in the case of elastically stressed growth on the equilibrium constants of the reactions was taken into account in these calculations according to Ref. 7.

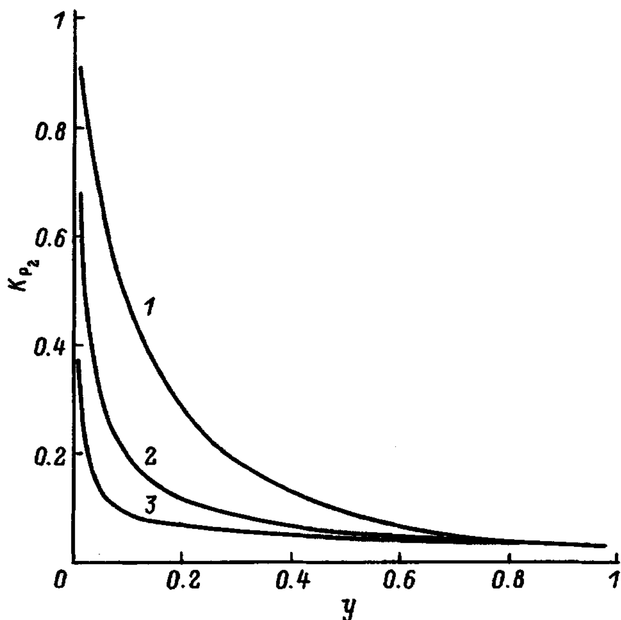

FIG. 2. Dependence of the incorporation coefficient of phosphorus on the composition of the compound GaP_yAs_{1-y} grown $[F^0_{Ga}=10^{14}\ (cm^2\cdot s)^{-1}$, $T=520$ °C] for various values of the external arsenic flux $F^0_{As_2}$,$(cm^2\cdot s)^{-1}$: *1* — 10^{14}, *2* — 3×10^{14}, *3* — 10^{15}.

Figure 1 shows the relationship between the fraction of the external P flux in the total flux of group-V elements and the mole fraction of P in the ternary solution grown for fixed external fluxes of As_2 and Ga and various growth temperatures. For comparison, the figure also presents experimental data taken from Ref. 6 and calculation results from Ref. 2, in which the influence of the elastic stresses on the Gibbs free energy of formation of the binary compounds was disregarded. It is seen from Fig. 1 that allowance for the influence of the elastic stresses leads to better agreement between the theoretical and experimental data.

Figure 2 presents the dependence of the incorporation coefficient of phosphorus K_{P_2}, which is defined as the ratio of the part of the incident P flux that is incorporated into the growing layer to the total incident P flux, on the composition of the layer grown at a fixed flux $F^0_{Ga}=10^{14}(cm^2\cdot s)^{-1}$ for various values of $F^0_{As_2}$ under the condition of enrichment with respect to the group-V elements

$$2(F^0_{As_2}+F^0_{P_2})>F^0_{Ga}.$$

The incorporation coefficient of phosphorous is given by the following expression at $T<620$ °C:

$$K_{P_2}=(F^0_{P_2}-F_{P_2})/F^0_{P_2}=y\frac{1}{2}(F^0_{Ga}-F_{Ga})/F^0_{P_2}$$

$$\approx y\frac{1}{2}F^0_{Ga}/F^0_{P_2}. \qquad (15)$$

As $F^0_{P_2}$ approaches the value of $yF^0_{Ga}/2$ in the region of compositions with a small mole fraction of P, the incorporation coefficient becomes equal to unity, i.e., nearly all of the incident P is incorporated. The decrease in the incorporation coefficient as the mole fraction of P increases is associated, as is seen from Fig. 1, with an increase in the external P_2 flux, which is needed to obtain a compound of definite composition at a fixed incident As_2 flux, while the Ga flux remains unchanged. Similar arguments also account for the decrease in K_{P_2} as $F^0_{As_2}$ increases.

Plots of the ratios between fluxes of group-III and group-V elements as functions of the mole fractions of the components (x and y) in the quaternary solid solution in the case of the growth of $Ga_xIn_{1-x}P_yAs_{1-y}$ that is lattice-matched to GaAs at various growth temperatures in the range 500–600 °C under the conditions of enrichment with respect to the group-V elements are shown in Figs. 3 and 4.

The relationship between the fraction of the external phosphorus flux $F^0_{P_2}$ in the total external group-V flux and the mole fraction of P in the compound $Ga_xIn_{1-x}P_yAs_{1-y}$ grown is presented in Fig. 3. In the temperature range indicated this relationship is virtually independent of the growth temperature. The difference between curves *1* and *2* in the range of compositions with a low P content is attributed to variation of the incorporation coefficient of P, as in the case of the ternary solutions.

Figure 4 presents the relationship between the fraction of the external indium flux F^0_{In} in the total external group-III flux $F^0_{In}+F^0_{Ga}$ and the mole fraction of Ga in the compound grown. It is seen from the figure that at a growth temperature

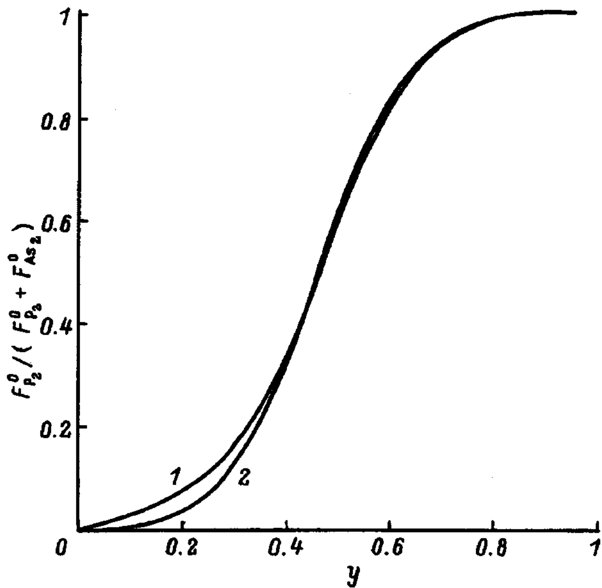

FIG. 3. Relationship between the fraction of the external phosphorus flux in the total external flux of group-V elements and the mole fraction of phosphorus in the compound $Ga_xIn_{1-x}P_yAs_{1-y}$ grown under the conditions of enrichment with respect to the group-V elements $[F^0_{Ga}=10^{14}\ (cm^2\cdot s)^{-1}]$ for substrate temperatures in the range 500–600 °C and various values of the external arsenic flux $F^0_{As_2}$,$(cm^2\cdot s)^{-1}$: *1* — 2×10^{14}, *2* — 2×10^{15}.

of 500 °C the ratio of the external indium flux to the total external group-III flux $F^0_{In}/(F^0_{In}+F^0_{Ga})$ is a linear function of the mole fraction of Ga. This result is a consequence of the fact that at the growth temperature cited the re-evaporated In and Ga fluxes are negligibly small compared with the external fluxes of the respective elements; i.e., the sticking coefficients of Ga and In are close to unity. However, when the growth temperature is increased, the re-evaporated In flux increases significantly, as is reflected in Fig. 5, which shows the dependence of the re-evaporated In flux on the composition of the growing layer for three different growth temperatures. At the same time, the re-evaporated Ga flux remains negligibly small and does not exceed $2\times10^{11}(cm^2\cdot s)^{-1}$ at 600 °C. As a result, the dependence of $F^0_{In}/(F^0_{In}+F^0_{Ga})$ becomes nonlinear at high growth temperatures in the range 500–600 °C. An increase in the total group-V flux $F^0_{P_2}+F^0_{As_2}$ leads to a decrease in the re-evaporated In flux (Fig. 5, curve *3′*). As a result, a smaller external In flux is required to grow a compound of identical composition at high substrate temperatures. The dependence of $F^0_{In}/(F^0_{In}+F^0_{Ga})$ at an increased value of $F^0_{P_2}+F^0_{As_2}$ is shown in Fig. 4. The calculations were performed for an external Ga flux $F^0_{Ga}=10^{14}\ (cm^2\cdot s)^{-1}$, which corresponds to a gallium arsenide growth rate $V_{GaAs}=1$ Å/s. The dependence of the growth rate of a compound on its composition in the case of the growth of a quaternary solid solution for the dependences in this figure is specified by the expression $V_{GaAs}/(1-x)$.

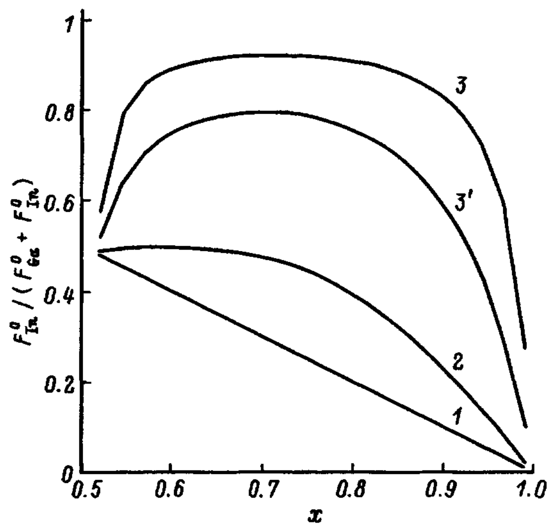

FIG. 4. Relationship between the fraction of the external In flux in the total external flux of group-III elements and the mole fraction of Ga $[F^0_{Ga}=10^{14}\ (cm^2\cdot s)^{-1}]$ in the compound $Ga_xIn_{1-x}P_yAs_{1-y}$ grown for growth under the conditions of enrichment with respect to the group-V elements and various values of the substrate temperature *T*, °C, and the external arsenic flux $F^0_{As_2}$,$(cm^2\cdot s)^{-1}$: *1* — 500 and 2×10^{14}, *2* — 550 and 2×10^{14}, *3* — 600 and 2×10^{14}, *3′* — 600 and 2×10^{15}.

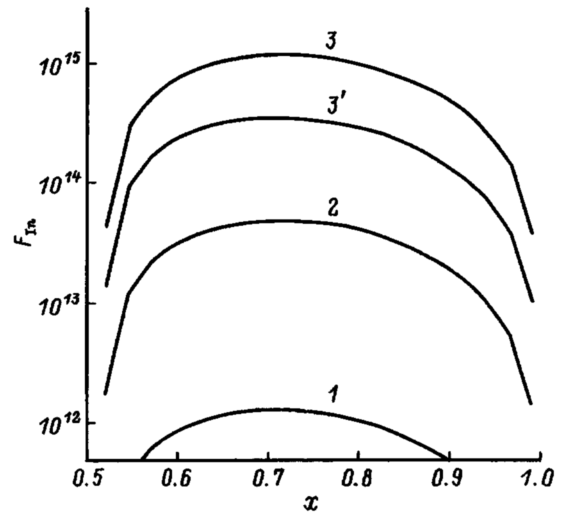

FIG. 5. Re-evaporated In flux from the growth surface of $Ga_xIn_{1-x}P_yAs_{1-y}$ as a function of the mole fraction of Ga $[F^0_{Ga}=10^{14}\ (cm^2\cdot s)^{-1}]$ in the compound for various values of the substrate temperature *T*,°C, and the external arsenic flux $F^0_{As_2}$,$(cm^2\cdot s)^{-1}$: *1* — 500 and 2×10^{14}, *2* — 550 and 2×10^{14}, *3* — 600 and 2×10^{14}, *3′* — 600 and 2×10^{15}.

4. CONCLUSIONS

Thus, a method for obtaining a thermodynamic description of the MBE growth of quaternary solid solutions with two volatile components has been proposed in this paper; a thermodynamic analysis of the growth of the compounds GaP_yAs_{1-y} and $Ga_xIn_{1-x}P_yAs_{1-y}$ has been performed. It has been shown that allowance for the influence of the elastic stresses appearing in the case of the pseudomorphic growth of GaP_yAs_{1-y} on GaAs on the equilibrium constants of the formation reactions of the binary compounds leads to better agreement between the experimental and theoretical data.

We thank S. V. Ivanov and N. N. Ledtsov for some helpful discussions.

This work was performed with the support of a NATO ISEP Linkage Grant.

[1] R. Heckingbottom, in: *NATO Advanced Study Institute on Molecular Beam Epitaxy (MBE) and Heterostructures, Erice, Italy, 1983: Molecular Beam Epitaxy and Heterostructures*, L. L. Chang and K. Ploog (eds.), M. Nijhoff, Dordrecht–Boston (1985) [Russian translation, Mir, Moscow (1989)], p. 65.
[2] H. Seki and A. Koukitu, J. Cryst. Growth **78**, 342 (1986).
[3] A. S. Jordan and M. Ilegems, J. Phys. Chem. Solids **36**, 329 (1975).
[4] P. S. Kop'ev and N. N. Ledentsov, Fiz. Tekh. Poluprovodn. **22**, 1729 (1988) [Sov. Phys. Semicond. **22**, 1093 (1988)].
[5] M. B. Panish and M. Ilegems, Prog. Solid State Chem. **7**, 39 (1972).
[6] B. W. Liang and C. W. Tu, J. Appl. Phys. **74**, 255 (1993).
[7] S. V. Ivanov, P. D. Altukhov, T. S. Argunova, A. A. Bakun, A. A. Budza, V. V. Chaldyshev, Yu. A. Kovalenko, P. S. Kop'ev, R. N. Kutt, B. Ya. Meltser, S. S. Ruvimov, S. V. Shaposhnikov, L. M. Sorokin, and V. M. Ustinov, Semicond. Sci. Technol. **8**, 347 (1993).

Translated by P. Shelnitz

Application of elastic mid-infrared light scattering to the investigation of internal gettering in Czochralski-grown silicon

V. P. Kalinushkin, A. N. Buzynin, D. I. Murin, V. A. Yuryev, and O. V. Astaf'ev

Institute of General Physics, Russian Academy of Sciences, 117942 Moscow, Russia
(Submitted December 27, 1996; accepted for publication February 25, 1997)
Fiz. Tekh. Poluprovodn. **31**, 1158–1163 (October 1997)

The influence of the internal gettering process on the large-scale defects in Czochralski-grown boron-doped single-crystal silicon is investigated by low-angle mid-infrared light scattering. The large-scale defects in the as-grown material and crystals subjected to the internal gettering procedure are classified. The applicability of low-angle light scattering in laboratory investigations and in the industrial inspection of the operations in an internal gettering production cycle is demonstrated. © *1997 American Institute of Physics.*
[S1063-7826(97)00210-X]

1. INTRODUCTION

Internal gettering has become one of the most important technological operations in the production of microelectronics devices based on Czochralski-grown silicon. Nevertheless, a nondestructive method that would permit direct investigations of the variation of the defect composition of a material during gettering and direct inspection of the operations in its production cycle has not been proposed. The purpose of this paper is to propose such a method, which was developed on the basis of low-angle mid-infrared light scattering.[1] This method has been successfully applied to the investigation of large-scale clusters of electrically active defects in semiconductor materials (see, for example, Ref. 2 and the bibliography cited there).

Low-angle mid-infrared light scattering was first applied in Ref. 3 to the investigation of the influence of abrasive and internal gettering in Czochralski-grown boron-doped crystals of standard commercial silicon. The main conclusions drawn in that study are that abrasive gettering leads to significant lowering of the impurity concentration in the large-scale impurity clusters found in the bulk of the crystals, and that internal gettering leads to the appearance of new defects in the substrate bulk, whose contribution to mid-infrared light scattering becomes dominant. Unfortunately, the basic parameters of these defects were not established in Ref. 3.

In the present study we investigate these defects in greater detail, establish their relationship to the defects revealed in the as-grown material in Refs. 4 and 5, and determine their basic parameters.

In addition to standard low-angle light scattering, in the present work we employed low-angle light scattering with the bulk photoexcitation of nonequilibrium charge carriers, which, like electron-beam-induced current (EBIC) measurements, makes it possible to investigate large-scale recombination-active defects.[1,6] This method was used to establish some laws governing the alteration of large-scale recombination-active defects as a result of internal gettering.

In addition, we measured the temperature dependence of the scattering intensity, which made it possible to estimate the activation energies of the point centers appearing in large-scale clusters of electrically active defects.

In addition to low-angle light scattering, the changes in the defect composition of the material were investigated by EBIC and selective etching, making it possible to obtain estimates of the defect concentrations, which are needed to calculate the activation energies of the point centers appearing in their composition from temperature dependences of low-angle light scattering.

2. EXPERIMENTAL METHOD AND SAMPLES

In the low-angle light scattering method used in the present work a continuous-wave CO_2 laser was employed as a source of probing radiation (the wavelength $\lambda = 10.6\ \mu$m). The details of this method were thoroughly described in Refs. 1 and 2. Here we would like to recall only that such parameters of large-scale clusters of electrically active defects as their effective dimensions, the product of their concentration (C), and the square of the deviation of the free carrier concentration (n_{ac}) [or the square of the deviation of the dielectric constant (ε_{ac})] within them $C(\Delta n_{ac})^2$ [or $C(\Delta \varepsilon_{ac})^2$] can be calculated from the angular scattering diagrams measured in low-angle light scattering. An investigation of the influence of the sample temperature on the scattering of infrared light by it makes it possible to estimate the thermal activation energy (ΔE) of the impurities and defects appearing in large-scale clusters of electrically active defects: the scattering intensity of the large-scale clusters of electrically active defects $I_{sc} \sim (\Delta n_{ac})^2$, Refs. 2 and 7–10.

The experiments on the influence of the photoexcitation of nonequilibrium charge carriers in the bulk of a material on the scattering of infrared light can be described as follows. If a crystal contains large-scale recombination centers (for example, precipitates and precipitate colonies, packing defects, etc.) in its bulk, regions with a reduced carrier concentration (depleted regions) form around these centers when nonequilibrium charge carriers are excited. These regions scatter light as ordinary inhomogeneities. The scattering of light by the depleted regions can be detected by employing amplitude-modulated photoexcitation and isolating the corresponding component of the scattered light, which pulsates at the photoexcitation frequency. Then, employing the usual procedure used in low-angle light scattering to measure and

 © 1997 American Institute of Physics

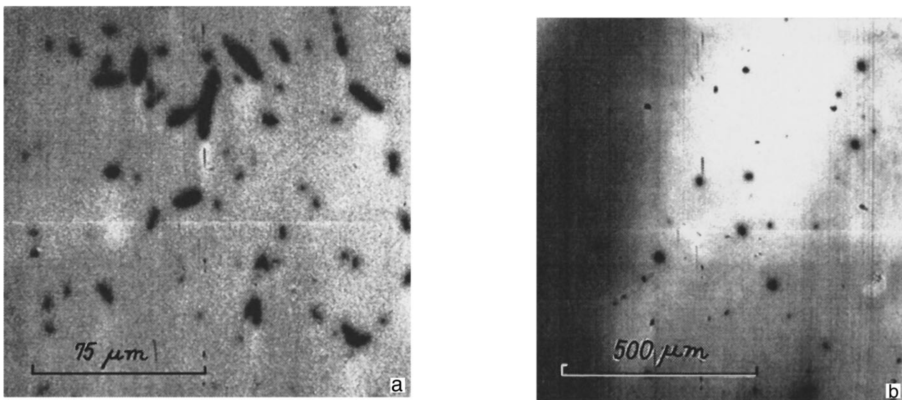

FIG. 1. Typical EBIC photomicrographs of detects: a — as-grown sample, b — after internal gettering. $T=300$ K.

treat the angular scattering diagrams, we can estimate the characteristic dimensions of the depleted regions around the large-scale recombination centers.[1,6] In the present work a YAG:Nd^{3+} laser which generates pulses with a duration of 40 ns, a power of 1 W at a wavelength of 1.06 μm, and a frequency of 1 kHz was employed to excite nonequilibrium charge carriers. The use of this wavelength for photoexcitation permitted nearly uniform pumping of the entire volume of the test sample, since the absorption at this wavelength is not excessively strong, but is perfectly adequate to ensure the efficient generation of electron-hole pairs. The layout of the experimental apparatus for low-angle light scattering with the photoexcitation of nonequilibrium carriers in the sample was described in detail in Refs. 1 and 6.

Besides low-angle light scattering, in the present work we used EBIC and selective etching to expose defects. The samples for EBIC were prepared using a special procedure involving plasma etching of the samples in a special regime before deposition of the Schottky barrier. This procedure significantly increases the sensitivity of EBIC toward large-scale recombination-active defects in the silicon bulk.[11]

A total of 40 wafers of dislocation-free silicon were investigated in this study. The crystals were grown by the Czochralski method and doped with boron to a resistivity of $1-40\ \Omega\cdot$cm. We used material which was produced by three different manufacturers and subjected to the internal gettering procedure in five different plants. In this paper we generalize the data on the influence of different gettering regimes on the defect composition of the samples.

The following two experimental schemes were used in the low-angle light scattering measurements. In one of them the as-grown samples were investigated preliminarily, and then they were subjected to treatment involving an internal gettering cycle and investigated by low-angle light scattering. In the other scheme the wafers were cut into several samples. Some of them were subjected to the internal gettering procedure, while the others served as control samples.

The EBIC and selective etching experiments were carried out only according to the second scheme.

3. EXPERIMENTAL RESULTS

A. As-grown samples

The as-grown samples investigated by us contain the standard set of large-scale clusters of electrically active defects for Czochralski-grown, boron-doped, single-crystal silicon.[4,5,11,12] So-called ''cylindrical defects'' with lengths from 15 to 40 μm and diameters from 5 to 10 μm were discovered in them and can be seen on the EBIC photomicrographs (Fig. 1a). The concentration of these defects varied from 10^6 to 10^7 cm^{-3}. These defects correspond to the portions of the scattering diagrams at the angles $\theta<7°$ (Fig. 2, curve *1*). So-called ''spherical defects,'' whose concentration did not exceed 10^5 cm^{-3}, were also observed in the as-grown samples (Fig. 1a). They correspond to the portions of the scattering diagrams at $\theta>7°$. The diameters of these defects vary from 5 to 20 μm (Fig. 2, curve *1*).

According to estimates based on the temperature dependence of the scattering intensity (Fig. 3), the activation energies of the point centers, which determine the scattering of light by the cylindrical and spherical defects, amount to $40-60$ meV and $120-160$ meV, respectively.[4,5]

The depleted regions around the large-scale recombination-active defects measured less than 4 μm in the as-grown samples and were manifested as a ''plateau'' on the scattering diagrams recorded with the photoexcitation of nonequilibrium carriers (Fig. 4, curve *1*, $\theta>5°$). Sometimes spherical defects were also manifested on the scattering diagrams (Fig. 4, curve *1*, $\theta<5°$).

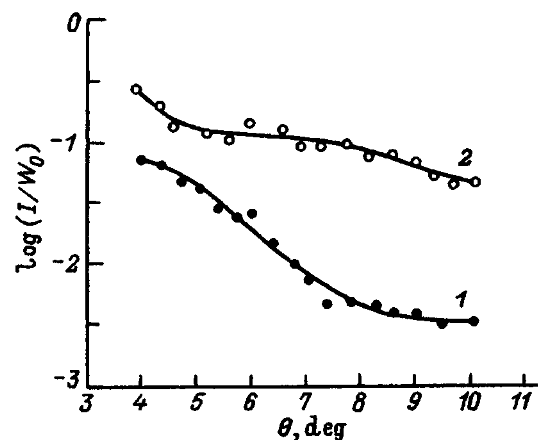

FIG. 2. Typical scattering diagrams of silicon single crystals recorded without photoexcitation: *1* — as-grown sample, *2* — after internal gettering. $T=300$ K.

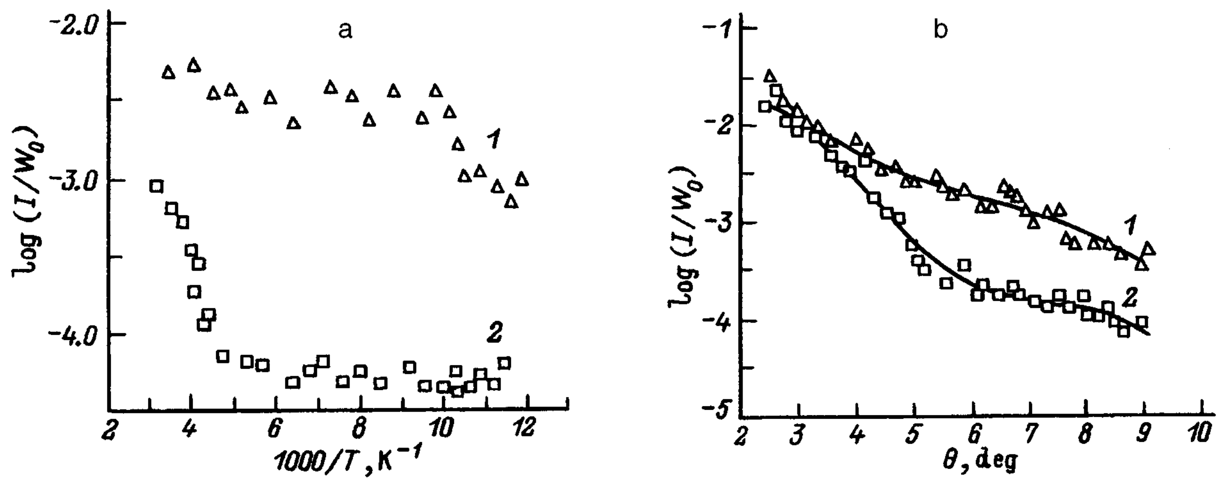

FIG. 3. a — Temperature dependence of the intensity of light scattered by as-grown silicon samples: *1* — cylindrical defects, *2* — spherical defects. b — Characteristic scattering diagrams; T, K: *1* — 300, *2* — 110.

B. Samples subjected to the internal gettering procedure

The main results obtained for the samples which underwent the internal gettering procedure are as follows.

1. As a result of internal gettering, the spherical large-scale recombination-active defects with diameters from 10 to 30 μm become the dominant type of defect (Fig. 1b), the intensity of the light scattered by them increasing by approximately two orders of magnitude in comparison with the light scattering caused by defects of this type in the as-grown samples (Fig. 2, curve *2*). The intensity of the light scattered by the cylindrical defects increases only slightly. As a result, the light scattered by the spherical defects begins to dominate the scattering diagrams for the samples which underwent the internal gettering procedure. It can thus be concluded that the concentration of the spherical defects increases significantly as a result of internal gettering (Fig. 1b). Increases in the scattering intensity and the concentration of the spherical defects were observed in all the samples which underwent the internal gettering procedure and did not depend on the gettering regime. The increase in the intensity of the light scattered by the spherical defects correlated with the appearance of the gettering defects exposed by selective etching, but there was no direct proportionality between the etch pit density and the scattering intensity.

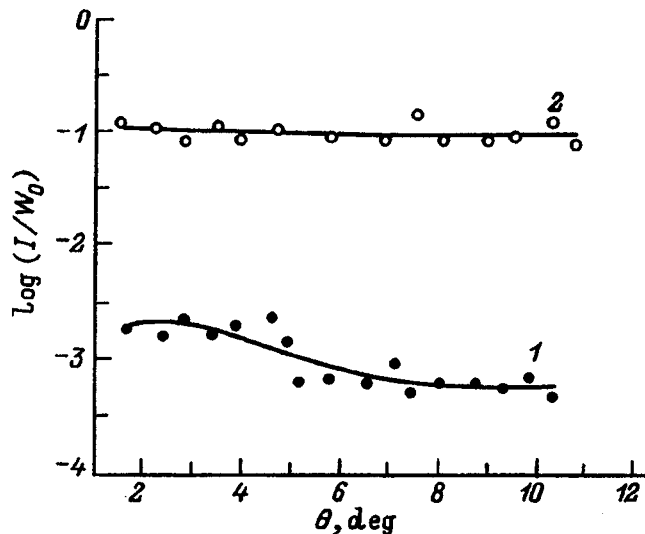

FIG. 4. Typical scattering diagrams of silicon single crystals recorded with photoexcitation: *1* — as-grown sample, *2* — after internal gettering. $T=300$ K.

2. In the low-angle light scattering experiments with the photoexcitation of nonequilibrium charge carriers in the samples it was found that the intensity of the light scattered by the depleted regions around large-scale recombination-active defects increases sharply following internal gettering (Fig. 4, curve *2*). A strong correlation between the scattering intensity and the density of the defects exposed by selective etching was discovered.

3. The activation energies of the dominant centers in the spherical defects are determined, in all likelihood, by the growth conditions and by the thermal history of the samples. As an example, Fig. 5 presents plots of the temperature dependence of the scattering intensity measured on two samples, which were grown by different manufacturers and which underwent the internal gettering procedure. It is seen that the plots of the temperature dependence of the scattering intensity and the activation energies ΔE of the centers, which determine the scattering of light by the spherical large-scale recombination-active defects at room temperature in these samples, differ: $\Delta E=130-170$ meV for sample *1* and $\Delta E=60-90$ meV for sample *2*; i.e., different point centers appear in the spherical defects in these samples following internal gettering. At present, we cannot confidently say which of the following factors determines the composition of the spherical defects after internal gettering: the original content of uncontrolled impurities in the samples or the features of the gettering cycle. In our opinion, the first factor should be more significant.

4. DISCUSSION OF RESULTS AND PROPOSED METHOD

Generalizing the foregoing material, we can conclude that the large-scale recombination-active defects detected in

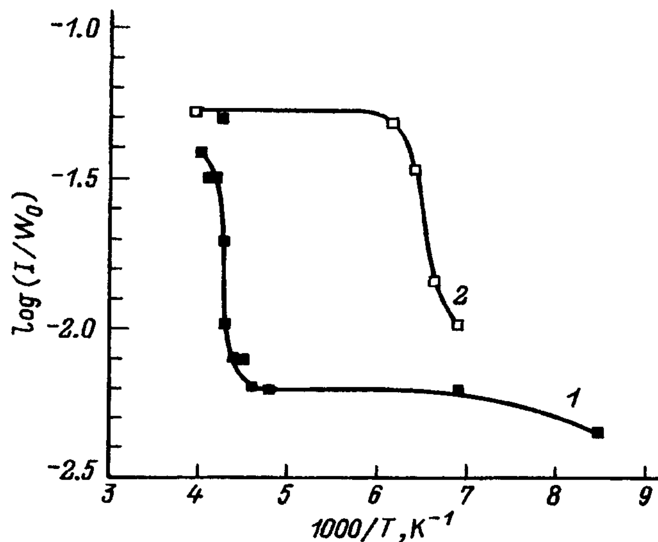

FIG. 5. Temperature dependence of the intensity of light scattered by spherical large-scale clusters of electrically active defects in two silicon single crystals grown which were by different manufacturers and underwent the internal gettering procedure; *1*, *2* — sample numbers.

the bulk of the crystals which underwent the internal gettering procedure are structural defects (most likely, precipitates and precipitate colonies), which appear during the formation of the getter and which serve as gettering defects. As for the spherical defects, in our opinion, they are the atmospheres formed around the gettering defects by impurity atoms draining toward them.[1)] The conclusions drawn are confirmed by the correlation between the intensity of the light scattered by the depleted regions around large-scale recombination-active defects and the etch pit density and by the increase in the intensity of the light scattered by spherical defects following the appearance of a large number of defects exposed by selective etching.

The intensity of the light scattered by inhomogeneities of any type is proportional to the product $C(\Delta\varepsilon)^2$, where C is their concentration and $\Delta\varepsilon$ is the deviation of the dielectric constant in them. In the case of the large-scale recombination-active defects detected by low-angle light scattering with the photoexcitation of nonequilibrium charge carriers, $\Delta\varepsilon$ is determined primarily by the concentration of the nonequilibrium carriers generated. At a constant photoexcitation level (concentration of nonequilibrium carriers) the intensity of the light scattered by the depleted regions around large-scale recombination-active defects is directly proportional to the concentration of the large-scale recombination-active defects in the crystals; therefore, the intensity of the light scattered by the depleted regions in the low-angle light scattering experiments with the photoexcitation of nonequilibrium charge carriers is a direct measure of the concentration of large-scale recombination-active defects in the crystals.

In the case of large-scale clusters of electrically active defects the situation is significantly more complex. The value of $\Delta\varepsilon$ in them is determined by many factors: the mean impurity concentration, the ratio between the number of dissolved impurity atoms and the number of precipitated impurity atoms, the degree of compensation, etc. The gettering process can alter the concentration C of the large-scale recombination-active defects themselves, as well as any of the parameters just cited and consequently, $\Delta\varepsilon$, and should thus lead to apparent destruction of the direct proportionality between the scattering intensity and the measured defect concentration. Therefore, in the case of the spherical defects we are forced to count on only a qualitative correlation between the scattering intensity and the experimentally determined etch pit density.[2)]

On the basis of the foregoing material we propose a method for investigating the internal gettering process in silicon substrates, which consists of the following steps: the presence of gettering defects in the bulk of the crystals is monitored by measuring the light scattering caused by the large-scale recombination-active defects (low-angle light scattering with the photoexcitation of nonequilibrium charge carriers); the presence of the impurity atmospheres around the gettering defects is monitored, and their parameters, i.e., the efficiency of the gettering operation, are determined by measuring the light scattering caused by the spherical large-scale clusters of electrically active defects (standard low-angle light scattering).

We note that an important advantage of the proposed method is its applicability for the initial and in-process inspection of the entire gettering production cycle. It makes it possible to investigate the effectiveness and stability of the getter after any high-temperature operation. The equipment employed for low-angle light scattering measurements can easily be incorporated into a production process, and it already makes it possible to quickly (within $1-2$ min) test substrates of practically any diameter.

Finally, by investigating the temperature dependence of the scattering intensity we can analyze the composition of the impurity atmospheres, i.e., determine which impurities are collected from the depleted zone by the gettering defects. In this case we should refer only to spot checking or laboratory testing.

5. CONCLUSIONS

In conclusion, we would like to focus the reader's attention on one more possibility of using infrared scattering, which is extremely promising in our opinion.

It can be used to perform nondestructive initial or in-process inspection of the presence of large-scale recombination-active defects not only in the bulk of wafers, but also directly in their near-surface regions. The proposed method is similar to the method for revealing large-scale recombination-active defects in the bulk of substrates, but instead of the ''bulk'' photoexcitation of electron-hole pairs, it calls for the use of ''surface'' photoexcitation (by, for example, pulses of the second harmonic of a neodymium laser, $\lambda = 0.53$ μm). In this case the nonequilibrium charge carriers penetrate the near-surface silicon layer to a depth of $20-30$ μm during a measurement, and just this layer is analyzed to determine the presence of recombination-active structural defects and impurity precipitates in it (in principle, the thickness of the layer investigated can be varied by varying the pulse length and the detection time). The main diffi-

culty in such a method is the low scattering intensity; however, preliminary experiments have shown that layers with a concentration of large-scale recombination-active defects not exceeding 10^4-10^5 cm^{-3} can be already by analyzed by this method.[20,21] This method is undoubtedly extremely promising, since it permits the investigation of the degree of purity of the depleted zone (on the basis of the lifetime of the minority carriers as well), rather than processes occurring in the bulk of the substrates. The proposed method could be used to observe, for example, the ''growth'' of precipitates in the depleted zone during the entire production cycle.

We also note that this method is applicable not only for solving problems associated with gettering, but also for investigating any epitaxial and boundary layers.

This work was partially supported by the Russian Fund for Fundamental Research (Grant No. 96-02-19540). We thank this Foundation for its support.

[1)]It should be noted that, according to the proposed model, the spherical defects consist of at least two components: a) dissolved impurities and point defects (and free charge carriers) and b) structural defects, such as precipitates. In standard low-angle light scattering, i.e., without photoexcitation, which is sensitive to regions with an altered concentration of free charge carriers, only the first component is observed. The other component, being recombination-active, is manifested in low-angle light scattering with the photoexcitation of nonequilibrium charge carriers.

[2)]A new method of scanning laser microscopy in the mid-infrared range has recently been developed. It permits the visualization of defects and more exact estimation of their parameters, primarily their concentration C.[13–18] This method seems to us to be extremely promising for investigating internal gettering.[19]

[1] V. P. Kalinushkin, in *Proceedings of the Institute of General Physics, Academy of Sciences of the USSR, Vol. 4, Laser Methods of Defect Investigations in Semiconductors and Dielectrics*, Nova, New York (1988), p. 1.

[2] V. P. Kalinushkin, V. A. Yuryev, and O. V. Astafiev, in *Proceedings of the 1st International Conference on Materials for Microelectronics,* Barcelona, 1994 [Mater. Sci. Technol. (in press)].

[3] E. N. Gulidov, V. P. Kalinushkin, D. I. Murin, M. G. Ploppa, A. M. Prokhorov, M. V. Shvedenko, and B. L. Éĭdel'man, Mikroelektronika **14**, 130 (1985).

[4] O. V. Astaf'ev, A. N. Buzynin, A. I. Buval'tsev, D. I. Murin, V. P. Kalinushkin, and M. G. Ploppa, Fiz. Tekh. Poluprovodn. **28**, 407 (1994) [Semiconductors **28**, 246 (1994)].

[5] V. P. Kalinushkin, A. N. Buzynin, V. A. Yuryev, O. V. Astafiev, and D. I. Murin, Inst. Phys. Conf. Ser. **149**, 219 (1996).

[6] V. P. Kalinushkin, D. I. Murin, T. M. Murina *et al.*, Mikroelektronika **15**, 523 (1986).

[7] V. P. Kalinushkin, V. A. Yuryev, D. I. Murin, and M. G. Ploppa, Semicond. Sci. Technol. **7**, A255 (1992).

[8] V. P. Kalinushkin, V. A. Yur'ev, and D. I. Murin, Fiz. Tekh. Poluprovodn. **25**, 798 (1991) [Sov. Phys. Semicond. **25**, 483 (1991)].

[9] V. V. Voronkov, G. I. Voronkova, V. P. Kalinushkin, D. I. Murin, T. M. Murina, and A. M. Prokhorov, Fiz. Tekh. Poluprovodn. **18**, 938 (1984) [Sov. Phys. Semicond. **18**, 584 (1984)].

[10] S. E. Zabolotskiĭ, V. P. Kalinushkin, D. I. Murin, T. M. Murina, M. G. Ploppa, and A. M. Prokhorov, Fiz. Tekh. Poluprovodn. **21**, 1364 (1987) [Sov. Phys. Semicond. **21**, 830 (1987)].

[11] A. N. Buzynin, N. A. Butylkina, A. E. Luk'yanov, V. V. Osiko, V. M. Tatarintsev, and A. M. Éĭdenzon, Izv. Akad. Nauk SSSR, Ser. Fiz. **52**, 1387 (1988).

[12] A. N. Buzynin, S. E. Zabolotskiĭ, V. P. Kalinushkin, A. E. Luk'yanov, T. M. Murina, V. V. Osiko, M. G. Ploppa, V. M. Tatarintsev, and A. M. Éĭdenzon, Fiz. Tekh. Poluprovodn. **24**, 264 (1990) [Sov. Phys. Semicond. **24**, 161 (1990)].

[13] O. V. Astafiev, V. P. Kalinushkin, and V. A. Yuryev, Mater. Sci. Eng. B **34**, 124 (1995).

[14] O. V. Astaf'ev, V. P. Kalinushkin, and V. A. Yur'ev, Mikroelektronika **24**, 472 (1995).

[15] O. V. Astaf'ev, V. P. Kalinushkin, and V. A. Yur'ev, Pis'ma Zh. Tekh. Fiz. **21** (11), 52 (1995) [Tech. Phys. Lett. **21**, 420 (1995)].

[16] O. V. Astafiev, V. P. Kalinushkin, and V. A. Yuryev, Inst. Phys. Conf. Ser. **146**, 775 (1995).

[17] O. V. Astaf'ev, V. P. Kalinushkin, and V. A. Yur'ev, Mikroelektronika **25**, 41 (1996).

[18] O. V. Astafiev, V. P. Kalinushkin, and V. A. Yuryev, Inst. Phys. Conf. Ser. **149**, 361 (1996).

[19] O. V. Astafiev, V. P. Kalinushkin, V. A. Yuryev, A. N. Buzynin, and N. I. Bletskan, Mater. Res. Soc. Symp. Proc. **378**, 615 (1995).

[20] V. P. Kalinushkin, D. I. Murin, V. A. Yuryev, O. V. Astafiev, and A. I. Buvaltsev, in *Proceedings of the 2nd International Symposium on Advanced Laser Technologies,* Prague, 1993 [Proc. Soc. Photo-Opt. Instrum. Eng. **2332**, 146 (1994)].

[21] O. V. Astaf'ev, A. I. Buval'tsev, V. P. Kalinushkin, D. I. Murin, and V. A. Yur'ev, Poverkhnost' (4), 79 (1995).

Translated by P. Shelnitz

Molecular effect in the implantation of light ions in semiconductors

I. A. Abroyan and L. M. Nikulina

State Technical University, 195251 St. Petersburg, Russia
(Submitted February 26, 1997; accepted for publication March 5, 1997)
Fiz. Tekh. Poluprovodn. **31**, 1164–1167 (October 1997)

The accumulation of structural defects in Si during the implantation of monatomic and diatomic nitrogen ions under equivalent conditions, i.e., at the same energies per atom and flux densities of the atoms, is investigated. The molecular effect in the accumulation of defects is observed only at doses for which the damage level in the crystal lattice exceeds 0.15. Under these conditions each N_2^+ ion creates the same number of stable defects as do six N_1^+ ions. In our experiments (30 keV for N_1^+ and 60 keV for N_2^+ at room temperature) the amorphization doses are equal to 3.75×10^{15} and 1.25×10^{15} ions/cm^2 for N_1^+ and N_2^+, respectively. © *1997 American Institute of Physics.* [S1063-7826(97)00310-4]

1. INTRODUCTION. LITERATURE SURVEY

The molecular effect in the accumulation of radiation defects in semiconductors under the action of heavy ions (As, Cd, Sb, and Te) has been known for a long time (see, for example, Ref. 1) and has been satisfactorily explained using the displacement spike and thermal spike conceptions. In the case of heavy ions of any element, the molecular effect is manifested by the fact that an X_k^+ ion (k is the number of atoms of type X in the ion) creates $\gamma k N_a$ defects, where N_a is the number of defects created by a monatomic X ion with the same velocity, and the coefficient $\gamma>1$.

For light ions (with mass numbers $M\leqslant 10-20$) the situation is more complicated in regard to the experimental setup and the interpretation of the results, and the literature data are contradictory. The experimental complexity is attributed to the possible dependence of the defect introduction rate on the ion current density for light ions (see, for example, Ref. 2). For this reason, to achieve equivalent conditions for irradiation by X_k^+ ions ($k=1,2,3\ldots$), not only equality of the energies and doses per atom, but also equality of the flux densities expressed in atoms/(cm$^2\cdot$s) must be ensured. The theoretical interpretation of the molecular effect, if such an effect exists, is complicated by the fact that the density of the energy released in elastic collisions can be insufficient for displaying spikes when $M\leqslant 10-20$.

When Si was irradiated at $T=300$ K by C^+, CO^+, CO_2^+, and $(C_6H_6)^+$ ions in Ref. 3, a clearly expressed molecular effect was observed for all the ions [γ increased from $\gamma\simeq 3$ for CO^+ to $\gamma\simeq 15$ for $(C_6H_6)^+$]. A molecular effect was also observed for Ge and CO^+ and CO_2^+ ions $T=300$ K in Ref. 4 ($\gamma=1.5$ and $\gamma=2.6$, respectively). We note that the differences between the values of the nuclear charge Z and the mass number M for the C and O atoms imparts some uncertainty to the interpretation of the results in Refs. 3 and 4. In contrast to Refs. 3 and 4, Thompson and Walker[5] irradiated Si with nitrogen ions at $T=50$ K and did not notice any differences in the accumulation of defects for N_1^+ and N_2^+ when the energies (per atom) and doses were equal. Unfortunately, Thompson and Walker[5] did not concern themselves with the equality between the flux densities of the atoms in these experiments. The same criticism can also be addressed to Stevanovic *et al.*,[6] who reported the observation of a molecular effect with $\gamma=1.4$ in GaAs at 40 K. A dependence of the accumulation of defects on the flux density of the atoms may have been lacking in the experiments in Refs. 5 and 6 because of the low irradiation temperatures; however, it would have been worthwhile to specially verify this, especially in regard to the results in Ref. 5, where the dependence of the number of defects introduced on the ion dose was superlinear. Finally, Abroyan and Nikulina[7] observed a molecular effect when Si crystals containing structural defects that had been created preliminarily by implanting argon ions were bombarded at room temperature.

A molecular effect has also been observed using boron fluoride and phosphorous fluoride ions.[8–10] It is even more complicated to ensure the equivalence of molecular and atomic irradiations in work with such ions. For example, for BF_k^+ ions with an energy E [per a.m.u. or $E/(11+19k)$ per ion] and a current density j, simultaneous irradiation by B^+ and F^+ ions with energies $11E/(11+19k)$ and $19E/(11+19k)$, respectively and a current density j for B^+ and kj for F^+ would be equivalent. Such conditions were not ensured in Refs. 8–10. In the investigation in Ref. 8 Si was irradiated at $T=77$ K by BF_k^+ $(1\leqslant k\leqslant 3)$ and PF_k^+ $(1\leqslant k\leqslant 5)$ ions; unfortunately, neither the orientation of the beam relative to the crystal axes nor the current density were indicated. The damage excess γ was determined as the ratio of the number of defects created by a single molecular ion to the total number of defects created by the corresponding atomic ions. Grob *et al.*[8] scarcely observed a molecular effect for the diatomic ions ($\gamma=1$ for BF^+ and $\gamma=1.07$ for PF^+); however, when k was increased, γ reached values of 1.27 and 1.8 for the BF_3^+ and PF_5^+ ions. The molecular effect observed was interpreted in Ref. 8 as a manifestation of a displacement spike resulting from the two- and threefold overlap of subcascades, which allows the achievement of a defect concentration sufficient for the passage of Si into the atomic state in the overlap region.

In Refs. 9 and 10 Si was irradiated at room temperature by B^+, F^+, BF^+, and BF_2^+ ions. As far as we can tell from the text, equivalent irradiation conditions were not ensured in these studies (this refers to equality between the flux densities of the particles). In addition, the complex nonlinear de-

pendence of the number of defects on the ion dose Φ (see, for example, Ref. 11) was disregarded, the nonadditivity and noncommutativity of defect accumulation[12,13] were not stipulated, and the possibility of ion-stimulated annealing of the defects during irradiation first by heavier ions (F^+) and then by lighter ions (B^+)[14] was also disregarded. According to the authors' interpretation in Ref. 9, a molecular effect ($\gamma = 1.5 - 2.5$) was observed for the so-called surface defect maximum (at depths up to 25 nm from the surface) and was absent in the region of the bulk maximum (at $x = R_p$). Kotai *et al.*[10] observed a molecular effect ($\gamma > 1$) near the surface and a negative molecular effect ($\gamma < 1$) in the bulk.

Finally, in Ref. 15 silicon was irradiated at $T = 900$ K by C_k^- ions ($k = 1,2,3,4,6$, and 8) with energies of the order of 70 keV/a.m.u, i.e., 10–100 times greater than in the papers cited above. Irradiation equivalence (with respect to the flux density) was apparently not ensured. In addition, electron excitation can play a significant role in defect accumulation. Döbeli *et al.*[15] observed a negative molecular effect ($\gamma < 1$) for $k = 2,3,4$, and 6 and a positive molecular effect ($\gamma > 1$) for $k = 8$ at depths up to several hundred nanometers. According to their data, at the end of the ion range the number of defects per atom does not depend on the number of atoms in the cluster ion.

The foregoing analysis shows that to obtain unequivocal answers to the questions of whether the molecular effect exists, what type of ion (positive or negative) mediates it, and what mechanism underlies the effect we must ensure the equivalence of all the conditions for irradiation by atomic and molecular ions, i.e., equality of the kinetic energies of the free atoms and atoms within a molecular ion, equality of the flux densities and doses for atoms of all kinds in the molecular and atomic regimes, equality of the temperatures and irradiation times for atomic and molecular ions, and constancy of the orientation of the beams relative to the crystal axes. Of course, it is considerably easier to achieve all these conditions simultaneously when molecular ions consisting of atoms of a single element are used.

2. EXPERIMENT

In the present work Si(111) wafers were irradiated in the direction normal to the surface at room temperature by N_1^+ and N_2^+ ions with energies of 30 and 60 keV and current densities $j = 0.3$ and 0.15 $\mu A \cdot cm^{-2}$, respectively. Equivalent conditions were thus ensured for bombardment by the monatomic and diatomic nitrogen atoms. The implantation was carried out on a standard Iolla-2 implanter with a sector magnetic mass separator. To ensure irradiation uniformity along the surface, the target under the beam was scanned mechanically. The linear scan rate chosen corresponded to an ion-current pulse duration equal to 130 ms. The (111) plane of the wafers was deflected somewhat from the plane of the surface, so that a normal to the wafer surface would form an angle of the order of 3° with the $\langle 111 \rangle$ axis (rotation through $\sim 1.4°$ about the OO axis and rotation through 2.6° about the O_1O_1 axis) (see the inset in Fig. 1).

Profiles of the fraction of displaced atoms n_d with respect to the depth x were determined by anisotropic inelastic

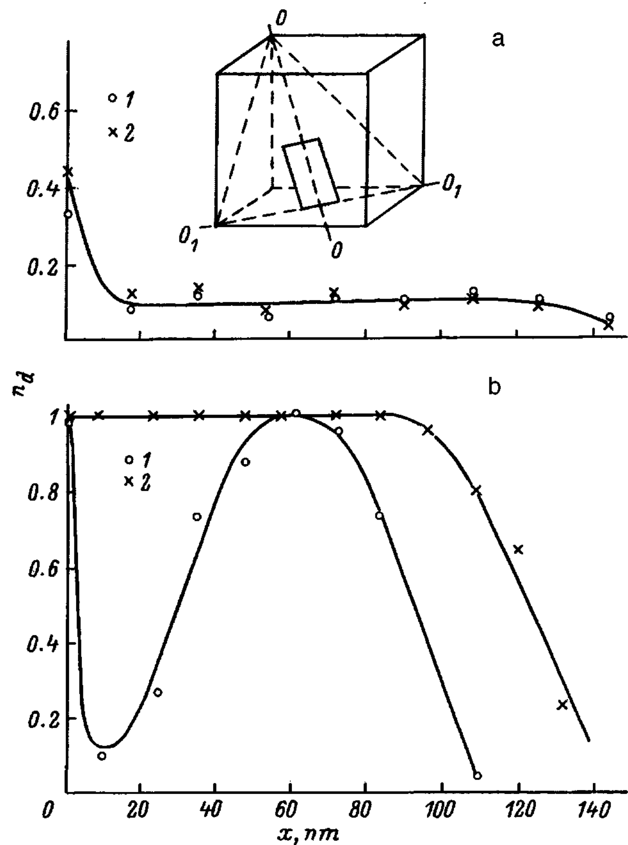

FIG. 1. Profile of the relative defect concentration n_d created by N_1^+ and N_2^+ ions with $E = 30$ keV/atom in Si at $T = 300$ K with respect to the depth x. The inset shows the orientation of the sample during irradiation. Values of the dose Φ, atoms/cm^2: a — 8.5×10^{14}, b — 3.75×10^{15}. Ions: *1* — N_1^+, *2* — N_2^+.

electron reflection measurements with layer-by-layer removal of thickness-calibrated Si layers (anodic oxidation followed by dissolution of the oxide in HF). The values of n_d were calculated according to the procedure in Ref. 16, which ensures satisfactory agreement between the results obtained by this method and by Rutherford backscattering spectroscopy.

Figure 1 presents some example $n_d(x)$ curves after the irradiation of Si samples by N_2^+ and N_1^+ ions in doses $\Phi = 8.5 \times 10^{14}$ atoms/cm^2 (a) and $\Phi = 3.75 \times 10^{15}$ atoms/cm^2 (b). It is seen that at the smaller dose (Fig. 1a) the atomic and molecular ions create the same number of defects. On the other hand, when $\Phi = 3.75 \times 10^{15}$ atoms/cm^2, the molecular N_2^+ ions created a continuous amorphous layer of thickness $80 - 90$ nm, while the value of n_d for the atomic N_1^+ ion reached the amorphous level only at the maximum of the defect depth profile.

Figure 2 shows plots of the dependence of the relative defect concentration at the maximum of the $n_d(x)$ profile on the dose of bombarding atoms. Curve *1* corresponds to the N_1^+ ions, and curve *2* corresponds to N_2^+. It follows from Fig. 2 that the two curves practically coincide at $\Phi < 2 \times 10^{15}$ atoms/cm^2, i.e., up to a damage level $n_d = 0.15$, and only then do they diverge strongly on the steeper portions of the curves. We note, incidentally, that the influence of the cur-

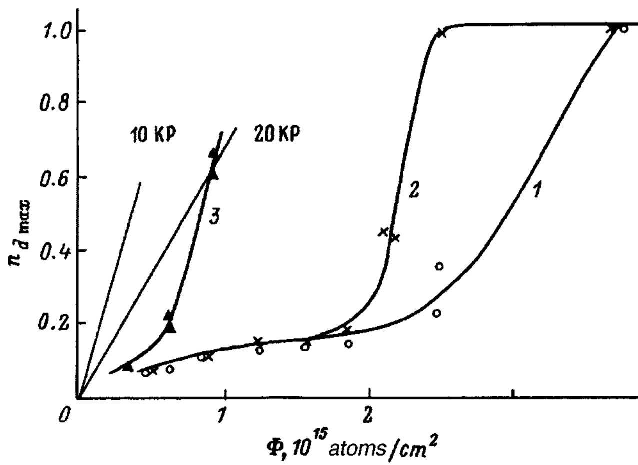

FIG. 2. Dependence of the relative concentration $n_{d\max}$ at the maximum of the depth profile of the defects on the dose Φ for N_1^+ (*1*) and N_2^+ ions (*2*, *3*). Current densities of the N_1^+ and N_2^+ ions j, μA/cm^2: *1* — 0.3, *2* — 0.15, *3* — 1. The straight lines labeled 10 KP and 20 KP show the slopes of the initial portions of the $n_{d\max}(\Phi)$ curves calculated in the Kinchin-Pease model for displacement thresholds equal to 10 and 20 eV, respectively.

rent density on defect accumulation is either totally absent or is strongly suppressed (see, for example, Ref. 17). This is also seen from a comparison of the slopes of curve *2* and curve *3* in Fig. 2. The latter was obtained when Si was bombarded by N_2^+ ions with an energy of 60 keV and $j=1$ μA/cm^2.

3. DISCUSSION OF RESULTS

Let us consider the possible mechanisms of the molecular effect as applied to our experiments.

1. The thermal spike and displacement spike conceptions, which have been used successfully in the case of heavy ions, are inapplicable for light ions, at least in their usual formulation. In fact, because of the low specific energy losses, the mean density of the energy released when N_1^+ ions are slowed in silicon does not exceed 0.1 eV per atom, and an energy greater than the heat of fusion, i.e., greater than 0.7–0.8 eV per atom, is required to display a thermal spike (the melting of Si in a microvolume). In addition to the low specific energy losses, the probability of the overlap of the individual cascades created by the atoms of a dissociated N_2^+ ion will be small because of the comparatively high probability of the scattering of light atoms (according to the estimate in Ref. 18, the volume of an individual cascade is 100 times smaller than the volume of the statistical cascade). This renders the displacement spike conception in its conventional form useless for explaining the molecular effect.

2. When a crystal is bombarded in a crystallographic direction with low indices, it can be expected that at certain depths a considerable part of the N_1^+ ions will still be moving in the channeling regime, while the flux of atoms from the molecular beam will already be randomized (the N_2^+ ions will dissociate in collisions, and scattering at angles exceeding the channeling angles will occur). Then, larger defects will be created by the molecular beam than by the beam of N_1^+ ions at these depths (this possibility was pointed out to us by A. I. Titov). We also note that the total number of defects was measured in most of the studies cited, while in our experiments the concentration at the maximum of the $n_d(x)$ profile was determined. However, such a mechanism for the molecular effect is unlikely in our experiments. In fact, the deflection angle of the beam from the $\langle 111\rangle$ axis was $\sim 3°$, i.e., it was almost equal to the channeling angle $\Psi_c=4°20'$, and the N_1^+ ions still had to traverse a distance of 60 nm in a heavily damaged crystal virtually without scattering in order to remain in the channeling regime.

3. The difference in damage accumulation during irradiation by molecular and atomic ions at $T=300$ K can be attributed to the thermal and ion-stimulated annealing of the defects created by N_1^+ and N_2^+ ions. Unfortunately, it is difficult to quantitatively evaluate the contribution of these processes to the observed effect.

4. As is seen from Fig. 2, the molecular effect begins to be manifested when the mean percentage of displaced atoms at the maximum of their depth profile reaches $\sim 15-20\%$. When $\Phi=2\times 10^{15}$ atoms/cm^2, the defect introduction rate $dn_d/d\Phi$ increases sharply, especially for the N_2^+ ions, and can exceed the calculated damage rate in the linear model. In Fig. 2 the straight lines labeled 10 KP and 20 KP show the slopes of the initial portions of the $n_{d\max}(\Phi)$ curves calculated in the Kinchin-Pease model under the assumption that the threshold atom displacement energies are equal to 10 and 20 eV. We note that the slopes of these lines practically coincide with the slopes of the steep portions of the $n_{d\max}(\Phi)$ curves for the N_2^+ and N_1^+ ions.

According to the current theory (see, for example, Refs. 11 and 17), damage accumulation occurs on the steep segments as a result of a spontaneous phase transition to the amorphous state in regions of the crystal where the defect concentration exceeds a limiting (threshold) value. Taking into account the latter circumstance and recalling that the only difference between molecular and atomic irradiation is the synchrony ($\Delta t\leqslant 10^{-15}$ s) of the entry of the atoms of a molecular ion into the crystal and the proximity (from 0 to 0.11 m) of their points of impingement, we believe that the following qualitative model of the phenomenon is reasonable. When $n_d>0.15$, the lattice is already prepared for the phase transition to the amorphous state. However, for such a transition to occur the inhomogeneously damaged matrix must still receive a certain amount of energy, which is needed to raise the concentration of structural defects to the instability threshold. All the individual subcascades created by atoms of the molecular current are located within the statistical cascade, i.e., within an ellipsoid of revolution with minor semiaxes measuring ~ 30 nm. The number of subcascades created simultaneously within such an ellipsoid by a N_2^+ ion is two time greater than the number for N_1^+.

As a result, the filling of the statistical cascade by simultaneously created defects increases nearly twofold, and the overlap of subcascades has not been ruled out. Such temporal and spatial correlation of the subcascades, which allows them to ''help'' one another to destroy the crystal, also leads to the appearance of the observed molecular effect.

We used similar ideas in Ref. 7 to discuss the results of the molecular effect for N_2^+ ions bombarding Si that was

preliminarily irradiated by argon ions. In Ref. 7 we advanced the hypothesis that a necessary condition for the molecular effect with light ions is readiness of the crystal to undergo a structural phase transition. This hypothesis has been directly confirmed here (see Fig. 2).

4. CONCLUSIONS

The requirements which ensure the equivalence of irradiation by comparatively light ($M \leqslant 20$ a.m.u.) atomic and molecular ions have been formulated. The accumulation of structural defects in Si during the implantation of N_1^+ and N_2^+ ions under equivalent conditions at $T = 300$ K has been investigated experimentally. It has been established that at low damage levels in the crystal lattice, where the relative concentration of defects is less than 15%, a single N_2^+ ion creates as many defects as two N_1^+ ions under equivalent conditions. When $n_d > 0.15$, the efficiency of the damage of Si by ions increases: along the steep ascent on the $n_d(\Phi)$ curve each N_2^+ ion creates about six times more defects than does a N_1^+ ion. The amorphization dose Φ_a, expressed in atoms/cm^2, for the implantation of N_2^+ ions is 1.5 times smaller than the value for N_1^+. These features of the action of molecular ions can be regarded as a result of a phase transition which occurs in the heavily damaged, but still crystalline matrix of the semiconductor.

We thank A. G. Kireev and M. V. Karaseva for their assistance in performing some of the measurements, A. B. Fadeev for irradiating the samples, and V. S. Belyakov and A. I. Titov for their interest in our research and some useful discussions.

[1] J. A. Davies, in *Ion Implantation and Beam Processing*, J. S. Williams and J. M. Poate (Eds.), Academic Press (1984).
[2] A. I. Titov, C. E. Christodoulides, G. Carter, and M. J. Nobes, Radiat. Eff. **41**, 109 (1979).
[3] J. A. Davies, G. Foti, L. M. Home, J. M. Mitchell, and K. B. Winterbon, Phys. Rev. Lett. **34**, 1441 (1975).
[4] G. Foti, G. Vitali, and J. A. Davies, Radiat. Eff. **32**, 187 (1977).
[5] D. A. Thompson and R. S. Walker, Nucl. Instrum. Methods **132**, 281 (1976).
[6] D. V. Stevanovic, N. P. Tognetti, G. Carter, C. E. Christodoulides, A. M. Ibrahim, and D. A. Thompson, Radiat. Eff. **71**, 91 (1983).
[7] I. A. Abroyan and L. M. Nikulina, Fiz. Tekh. Poluprovodn. **30**, 1893 (1995) [Semiconductors **30**, 990 (1995)].
[8] A. Grob, J. J. Grob, and A. Golanski, Nucl. Instrum. Methods Phys. Res. B **19/20**, 55 (1987).
[9] Li Xiagin, Lin Chenglu, Yang Gengin, Zhou Zuyao, and Zou Shichang, Nucl. Instrum. Methods Phys. Res. B **55**, 589 (1991).
[10] E. Kotai, N. Q. Khanh, and J. Gylai, in *Ion Beam Modification of Materials*, J. S. Williams, R. G. Elliman and M. C. Ridgway (eds.), Academic Press (1996), p. 823.
[11] I. A. Abroyan, Izv. Ross. Akad. Nauk, Ser. Fiz. **60** (7), 62 (1996).
[12] I. A. Abroyan and A. I. Titov, in *Proceedings of the 2nd Soviet-American Seminar on Ion Implantation* [in Russian], Inst. Fiz. Poluprovodn. Sib. Otd. Akad. Nauk SSSR, Novosibirsk (1979) p. 335.
[13] I. A. Abroyan and A. I. Titov, in *Ion Implantation in Semiconductors and Other Materials. Proceedings of the 7th International Conference, Vilnius, 25–28 September 1983* [in Russian], Vilnius (1985) p. 128.
[14] I. A. Abroyan, L. M. Nikulina, and A. I. Titov, Fiz. Tekh. Poluprovodn. **19**, 1030 (1985) [Sov. Phys. Semicond. **19**, 632 (1985)].
[15] M. Döbeli, F. Ames, R. M. Ender, M. Suter, H. A. Synal, and D. Vetterli, Nucl. Instrum. Methods Phys. Res. B **106**, 43 (1995).
[16] A. I. Titov, Doctoral Thesis, Leningrad Polytechnical Institute, Leningrad (1989).
[17] A. I. Titov and G. Carter, Nucl. Instrum. Methods Phys. Res. B **119**, 491 (1996).
[18] D. A. Thompson and P. S. Walker, Radiat. Eff. **37**, 113 (1978).

Translated by P. Shelnitz